



PHD

**Development of Graphene-based materials for engineering applications: Acoustic Absorbers and Supercapacitors
(Alternative Format Thesis)**

Rapisarda, Mario

Award date:
2022

Awarding institution:
University of Bath

[Link to publication](#)

Alternative formats

If you require this document in an alternative format, please contact:
openaccess@bath.ac.uk

Copyright of this thesis rests with the author. Access is subject to the above licence, if given. If no licence is specified above, original content in this thesis is licensed under the terms of the Creative Commons Attribution-NonCommercial 4.0 International (CC BY-NC-ND 4.0) Licence (<https://creativecommons.org/licenses/by-nc-nd/4.0/>). Any third-party copyright material present remains the property of its respective owner(s) and is licensed under its existing terms.

Take down policy

If you consider content within Bath's Research Portal to be in breach of UK law, please contact: openaccess@bath.ac.uk with the details. Your claim will be investigated and, where appropriate, the item will be removed from public view as soon as possible.



PHD

**Development of Graphene-based materials for engineering applications: Acoustic Absorbers and Supercapacitors
(Alternative Format Thesis)**

Rapisarda, Mario

Award date:
2022

Awarding institution:
University of Bath

[Link to publication](#)

Alternative formats

If you require this document in an alternative format, please contact:
openaccess@bath.ac.uk

Copyright of this thesis rests with the author. Access is subject to the above licence, if given. If no licence is specified above, original content in this thesis is licensed under the terms of the Creative Commons Attribution-NonCommercial 4.0 International (CC BY-NC-ND 4.0) Licence (<https://creativecommons.org/licenses/by-nc-nd/4.0/>). Any third-party copyright material present remains the property of its respective owner(s) and is licensed under its existing terms.

Take down policy

If you consider content within Bath's Research Portal to be in breach of UK law, please contact: openaccess@bath.ac.uk with the details. Your claim will be investigated and, where appropriate, the item will be removed from public view as soon as possible.

Development of Graphene-based
materials for engineering
applications: Acoustic Absorbers and
Supercapacitors



Mario Rapisarda

Department of Mechanical Engineering

University of Bath

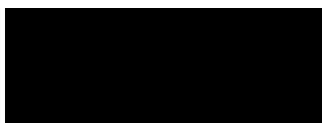
A Thesis submitted for the degree of
Doctor of Philosophy

May 2022

Copyright

Attention is drawn to the fact that copyright of this thesis rests with the author and copyright of any previously published materials included may rest with third parties. A copy of this thesis has been supplied on condition that anyone who consults it understands that they must not copy it or use material from it as licensed, permitted by law or with the consent of the author or other copyright owners, as applicable.

Signature of Author



*Obstacles are those frightful things you see
when you take your eyes off your goal*

Henry Ford

Acknowledgements

First and foremost, my gratitude goes to Prof. Michele Meo. He gave me the opportunity to start this beautiful journey, then he supported and guided me not only professionally, as my research supervisor, but also personally, as a mentor.

I would also like to show gratitude to Prof. Frank Marken, my second supervisor. Without his help and enthusiasm in showing me the secrets of electrochemistry, I would have not been able to accomplish many of the results presented in this thesis.

I am deeply grateful to Stefano, a colleague, a friend, and a brother. We shared memorable times inside and outside the University and supported each other during the hard moments. I am glad of having gone through this incredible experience with you.

A big thanks goes to Gian-Piero Malfense Fierro, Francesco Flora, Marco Boccaccio, Christos Andreades, Kostas Myronidis, Mario Emanuele De Simone, Fabrizio Bucciarelli, Salvatore Boccardi and Fulvio Pinto, the 2E 4.9 crew. You were all amazing colleagues and friends, and made our office a great place where to spend countless hours.

Thank you to my flatmates and all “Johnstone Street friends”, because when the PhD life is fun, studying and working become much easier. Grazie anche agli amici da Catania, che (a modo loro) hanno sempre saputo supportarmi. Grazie a Mari, Federico e Alessio, e alle interminabili telefonate con cui abbiamo condiviso gli alti e bassi della vita da forestieri.

Un ringraziamento speciale ai miei nonni, Mario e Tina, e a tutta la mia fantastica famiglia, per essere i miei più grandi sostenitori. Infine, il mio più profondo e sentito ringraziamento non può che andare ai miei genitori, Mimmo e Rosalba, e a mia sorella, Giuliana. Se ho raggiunto questo grande traguardo è soprattutto grazie a voi, che mai avete dubitato di me e che sempre mi siete stati vicino annullando ogni distanza. Voi siete stati la mia più grande forza.

Abstract

Graphene Oxide (GO) is one of the main candidates for the industrial production of graphene-derived materials. Thanks to the oxygen functional groups introduced during its synthesis from Graphite, it is readily processable in polar solvents (among which water stands out for its abundance and eco-friendliness), while maintaining some of the characteristics attributed to the peculiar hexagonal structure of pristine Graphene. A deep understanding of the chemico-physical properties of graphene-derived materials, and the way those are influenced by the various steps of their fabrication process, is therefore the key to fully exploit such materials in advanced engineering applications. The initial part of this thesis is therefore focused on the background of GO derived materials, from processing methods to characterisation techniques. Two different applications are then approached: light and compact porous absorbers and supercapacitors with active binder. In both the cases GO allows the development of environmentally friendly and scalable fabrication processes, matching with the current transition toward a greener more sustainable industry. More specifically, an ultralight aerogel obtained from a blend of GO and polyvinyl alcohol is proposed as a novel class of acoustic materials with tuneable and broadband sound absorption and sound transmission losses. The same material is then chemically modified to develop multifunctional properties, satisfying the advanced requirements of automotive and aerospace industries. On the other hand, this research work shows also how GO can actively contribute to the electrochemical performance of supercapacitors: as a stand-alone active binder in a first instance and then

in a hybrid gel with Starch, a biopolymer processable in water, for a fabrication procedure immediately transferrable to the industry. Additionally, both the approaches share the adoption of a conductive carbon paper derived from the thermal treatment of GO as current collector, for the fabrication of “all-graphene based” devices.

TABLE OF CONTENTS

Table of Contents	9
List of Figures	13
List of Tables.....	25
Chapter 1 Introduction	29
1.1 The Graphene family	29
1.2 Scope and Objectives	32
1.3 Outline of the Thesis	35
Chapter 2 Graphene-based materials	39
2.1 Graphene oxide and reduced graphene oxide	39
2.2 Reduction	42

2.2.1	<i>Thermal methods</i>	43
2.2.2	<i>Chemical methods</i>	45
2.3	Chemicophysical properties	46
2.4	Engineering applications	55
Chapter 3 Acoustic absorbers		57
3.1	Technological background.....	57
3.1.1	<i>History and basic principles of acoustics</i>	57
3.1.2	<i>Porous absorbers</i>	59
3.1.3	<i>Sound propagation</i>	61
3.1.4	<i>Evaluation of the acoustic properties</i>	63
3.1.5	<i>Semi-phenomenological modelling</i>	67
3.2	Sound insulation with Graphene-based porous absorbers	68
3.2.1	<i>Organic, inorganic and hybrid foams</i>	68
3.2.2	<i>Graphene-based foams</i>	71
Chapter 4 Supercapacitors		75
4.1	Technological background.....	75
4.1.1	<i>History and basic principles of capacitors</i>	75
4.1.2	<i>Supercapacitors</i>	79
4.1.3	<i>Evaluation of the electrochemical properties</i>	83
4.2	Improving supercapacitors technology with Graphene	86
4.2.1	<i>Chemically and thermally reduced GO</i>	87
4.2.2	<i>Binder-free electrodes from templated structures</i>	91
4.2.3	<i>Binder-free electrodes from carbonaceous nanocomposite</i>	94

Chapter 5 Graphene-based Acoustic Materials	99
5.1 Context	99
5.2 Ultralight aerogels for broadband and tuneable acoustic properties 102	
5.3 Multifunctional properties of modified graphene oxide composite aerogels	133
Chapter 6 Graphene-based Supercapacitors	170
6.1 Context	170
6.2 Binder-free supercapacitors with an innovative current collector 172	
6.3 Environmentally friendly and high-performance supercapacitors with a hybrid binder	206
Chapter 7 Conclusions and Future Works	252
7.1 Conclusions	252
7.2 Future Works	256
References	258

LIST OF FIGURES

Chapter 1 Introduction

Figure 1-1 – Main carbon allotropes: (a) Fullerene, (b) Carbon Nanotube, (c) Graphene, and (d) Graphite [5].	30
--	----

Chapter 2 Graphene-based materials

Figure 2-1 – Processing route from (a) Graphite to (d) rGO, with (b) GtO and (c) GO as intermediates [49].	42
Figure 2-2 – Digital pictures of GO dispersed in water and other organic solvents through bath ultrasonication. Top panel shows the dispersions immediately after sonication, while the bottom 3 weeks after sonication [16].	42
Figure 2-3 – Fabrication scheme and optical microscopy images of reduced and patterned GO films [62].	44

Figure 2-4 – (a) Digital pictures of GO and rGO respectively before and after AA treatment. (b) Representative Atomic Force Microscopy image of rGO sheet, showing single layers [70].	46
Figure 2-5 – Mechanism of structure formation and SEM images of aerogel microstructures [79].	48
Figure 2-6 – (a) FT-IR and (b) RS of GO before (1) and after AA reduction with increasing times (2-4) [69].	51
Figure 2-7 – Evolution of the 2D peak as a function of the number of layers evidenced by RS with 514 and 633 nm excitation wavelengths [92].	52
Figure 2-8 – XRD patterns of GO with different degrees of oxidation [36].	54
Figure 2-9 – XRD patterns of graphite, GO and graphene [101].	54

Chapter 3 Acoustic absorbers

Figure 3-1 – Different contributions of a sound wave incident to an acoustic surface.	59
Figure 3-2 – Different categories of porous absorbers [113].	60
Figure 3-3 – Impedance tube in two-microphone configuration.	65
Figure 3-4 – Impedance tube in four-microphone configuration. The four pressure amplitudes of the plane wave components (A, B, C, and D) are indicated.	66
Figure 3-5 – Illustration of cell opening mechanism and SEM images of PU with different cellular structure [122].	69
Figure 3-6 – (a) Comparison of sound absorption coefficient for different compositions of hybrid foams and (b) SEM image for the PU/PVDF/MWCNT foam exhibiting two immiscible phases in the material [130].	71

Figure 3-7 – (a) Illustration of sound absorption mechanism in directionally antagonistic graphene sound absorber and (b) absorption coefficient for different thicknesses [134]. 72

Figure 3-8 – Acoustic absorption performances and absorption mechanism for bubbled graphene monoliths manufactured with different densities [139]. 73

Chapter 4 Supercapacitors

Figure 4-1 – Sketch of Ragone plot for various energy storage and conversion devices. The indicated areas are rough guide lines [145]. 78

Figure 4-2 – Schematic representation of (a) conventional capacitor and (b) Electrical Double Layer capacitor (EDLC). (c) Example of EDL [148]. 80

Figure 4-3 – (a) CV of of rGO with TEA-BF₄ in AN electrolyte. (b) SEM and TEM imaging of rGO [8]. 88

Figure 4-4 – (a) Schematic illustration of graphene synthesis with CB as intercalating compounds. (b) SEM image showing CB particles on graphene surface. (c) GCD and (d) corresponding trend of specific capacitance for graphene/CB composite, compared with pure graphene [184]. 91

Figure 4-5 – (a) Schematic illustration of supercapacitor fabrication from direct laser reduction of GO. SEM images shows the exfoliation from GO to rGO. (b) Design and electrochemical performance of the all-solid-state device [75]..... 93

Figure 4-6 – Schematic diagrams with SEM images, electrochemical performance, and digital images of electrodes assembled exploiting rGO as an active binder when in composites with other carbon materials [197]..... 95

Figure 4-7 – (a) Schematic illustration of rGO providing adhesion on current collector. (b) TEM image showing rGO flake surrounding AC particle. (c) CV of EDLC assembled with rGO/AC electrodes and (d) comparison with traditional materials [199]. 97

Chapter 5 Graphene-based Acoustic Materials

Figure P1-1 – Schematic illustration of the ultralight GPAs. 110

Figure P1-2 – (a-e) DM and (f-o) SEM images of GO/PVA aerogels. PVA (a, f, k), GPA-1 (b, g, l), GPA-2 (c, h, m), GPA-3 (d, i, n), GO (e, j, o). Magnifications: (a-e) x20, (f-j) x500, and (k-o) x3000. Same scale bars apply to images with equal magnification. 110

Figure P1-3 – Physicochemical characterisation of GO/PVA aerogels: (a) FT-IR spectra and (b) XRD patterns. Wavenumbers attributable to GO are denoted in black (●), while those for PVA are in red (●)..... 112

Figure P1-4 – Effects of (a, b) GPA composition and (c, d) GPA-1 thickness on acoustic properties: (a, c) sound absorption and (b, d) sound transmission loss. Sample thickness is 25 mm when not studied as a variation (a, b). Key and average α and STL values are summarised in Table S2-2..... 114

Figure P1-5 – Effects of processing time and densities on acoustic properties of GPA-1 samples: (a) sound absorption and (b) sound transmission loss. Key and average α and STL values are summarised in Table S4. (c) Comparison of the average sound absorption coefficient, calculated in the 400 – 2500 Hz range, as a function of density for GPA-1 samples and other porous absorbers with comparable thickness previously reported in literature (Table S1-1). 115

Figure P1-6 – Semi-phenomenological analysis of GPA-1 samples with different processing times: (a) comparison between semi-analytical

model predictions (solid lines) and experimental measurements (markers) of the Sound Absorption Coefficient. (b) Flow Resistivity, (c) Tortuosity, (d) Viscous and Thermal Characteristic Lengths affected by processing time with Average Absorption Coefficient trend..... 117

Figure P1-7 – Diagram of ultralight GO/PVA aerogel fabrication process. 119

Figure P2-1 – Proposed chemical structure. Schematic diagrams of (a) unmodified and (b) modified GOP blends. 143

Figure P2-2 – Physicochemical characterisation of modified GOP aerogels. (a) XRD patterns, (b) FT-IR spectra, and (c) Raman spectra..... 146

Figure P2-3 – Physical structure and thermal behaviour of modified GOP aerogels. SEM imaging of (a, f) GO, (b, g) pl₂₀-GOP, (c, h) cl₁₀-GOP, (d, i) pl₂₀cl₁₀-GOP, and (e, j) rGOP. Magnifications: (a–e) ×200 (200 μm scalebar) and (f–j) ×1000 (50 μm scalebar). (k) Variation of thermal conductivity and density with chemical composition. (l) TGA and dTGA curves..... 149

Figure P2-4 – Acoustic properties of modified GOP aerogels. (a) Sound Absorption Coefficient and (b) Sound Transmission Loss..... 151

Figure P2-5 – Mechanical properties of modified GOP aerogels. (a) Static compression loading from 0 to 75% strain, (b) 2nd and (c) 10th cycles of the dynamic compression loading between 5 and 30% strain. (d, e) Trend of Energy Loss Coefficient and Maximum Compression Stress with cycle number. Same legend applies for all the panels. 153

Figure P2-6 – Piezoresistive behaviour of rGOP aerogels. (a) Stress-strain curve and trend of the normalised electrical resistance (R/R_0) and (b) relationship between the normalised electrical resistance change ($\Delta R/R_0$) and the strain during static compression testing. (c) Trend of $\Delta R/R_0$ during cyclic compression testing. (d) Relationship between $\Delta R/R_0$ and the strain during cyclic compression testing. 154

Figure P2-7 – Comparison of the multifunctional properties of the composite aerogels presented in the current work. The specific volume is calculated as the inverse of the density, the average value in the 500 – 1500 Hz range was taken for the sound absorption coefficient, the thermal resistivity is obtained from the inverse of the thermal conductivity, and the compressive stress is taken at 30% strain of the 10 th mechanical compression cycle. All values are proportionally scaled using the un-modified GOP as reference.....	157
Figure S2-1 – GOP aerogel manufacturing scheme. Modifications to the reference GOP can be distinguished by colors: plasticiser in orange, cross-linker in yellow and reducing agent in red.....	163
Figure S2-2 – Physicochemical characterisation of modified GOP aerogels. (a, c) XRD patterns and (b, d) FT-IR spectra of (a, b) pl _x -GOP and (c, d) cl _y -GOP with pure GO and PVA as reference. (e) Raman spectra of un-modified GOP with pure GO and PVA as reference.....	164
Figure S2-3 – Thermal stability of modified GOP aerogels. (a,b) TGA and (c,d) dTGA of (a,c) pl _x -GOP and (b,d) cl _y -GOP aerogels.....	165

Chapter 6 Graphene-based Supercapacitors

Figure P3-1 – (a, d) TEM and (b, e) FE-SEM images of: (a, b) CB_TT and (d, e) CB/GO_TT with the relative histograms of aggregates size distribution, (c) and (f) respectively (see Table P3-2 in the experimental section for the adopted nomenclature in this work). The term referred to the current collector has been omitted since it does not affect thermal treatment results.....	182
Figure P3-2 – Proposed schemes for (a) the 3D interconnected network consisting of CB and GO with TX100 molecules as dispersers and (b) the electrically conductive carbon nanocomposite consisting of CB and	

rGO with Non-Covalent Interactions (NCI) enhancing the adhesion with the current collector.	182
Figure P3-3 – (a) Raman spectra of the carbonaceous coatings with untreated CB included as reference; the onset shows the comparison between the untreated CB and GO. (b) XRD patterns of the carbonaceous coatings. The term referred to the current collector has been omitted since it does not affect thermal treatment results. ...	186
Figure P3-4 – (a) CVs at 50 mV s^{-1} between -2.7 and +2.7 V and (b) GCs at 0.5 and 1 A g^{-1} in a 1.5 M solution of TEMA-TFB in ACN of SCs made with CB/GO_AI_TT, CB/GO_AI_AD, CB_AI_TT, and CB_AI_AD (the GC profile of the latter is omitted as the internal resistance was too high to perform measurements with comparable specific currents with respect of the other samples).....	188
Figure P3-5 – (a) CVs and (b) GCs of SCs made with CB/GO_Gr_TT at different scan rates, from 50 to 500 mV s^{-1} , between -2.7 and +2.7 V and different specific currents, from 0.5 to 4 A g^{-1} , in a 1.5 M solution of TEMA-TFB in ACN.	190
Figure P3-6 – Ragone plot of specific power versus specific energy for SCs made with CB/GO_AL_TT, CB/GO_Gr_TT, CB_AI_TT and CB_Gr_TT.....	191
Figure P3-7 – Scheme of the manufacturing process showing also the electrochemical workstation. CB/rGO indicates the carbonaceous nanocomposite used as the active material. CE, RE, SE and WE indicate, respectively, Counter Electrode, Reference Electrode, Sensing Electrode and Working Electrode. Images by the author M. Rapisarda.....	196
Figure S3-1 – Qualitative comparison of the adhesion of the active material on the current collector and of its mechanical integrity between (a-d) CB/GO_Gr_TT and (e-h) CB_Gr_TT as samples were: (a) and (e), as	

taken out from the furnace; (b) and (f), tilted on a side; (c) and (g) tilted upside-down; (d) and (h), returned to horizontal position. A considerable amount of active material falling from the current collector is noticeable for the sample CB_Gr_TT while no material is detached from the sample CB/GO_Gr_TT. Images by the author M. Rapisarda..... 204

Figure S3-2 – (a) CVs and (b) GCs of SCs made with CB/GO_Al_TT at different scan rates, from 50 to 500 mV s⁻¹, between -2.7 and +2.7 V and different specific currents, from 0.5 to 4 A g⁻¹, in a 1.5 M solution of TEMA-TFB in ACN. 204

Figure S3-3 – (a) CVs and (b) GCs of SCs made with CB_Al_TT at different scan rates, from 50 to 500 mV s⁻¹, between -2.7 and +2.7 V and different specific currents, from 0.5 to 4 A g⁻¹, in a 1.5 M solution of TEMA-TFB in ACN. 205

Figure S3-4 – (a) CVs and (b) GCs of SCs made with CB_Gr_TT at different scan rates, from 50 to 500 mV s⁻¹, between -2.7 and +2.7 V and different specific currents, from 0.5 to 4 A g⁻¹, in a 1.5 M solution of TEMA-TFB in ACN. 205

Figure P4-1 – Schematic representation and electronic microscope imaging of GO-StC electrodes. (a) Schematic of GO-StC slurry preparation and of (b) GO-StC electrode. (c-h) SEM images showing: surface morphology of (c) GO-StC and (d) StC coatings (scale bar 100 μm) with higher magnification inset (scale bar 5 μm); AC and CB particles distribution in (e,f) GO-StC and (g,h) StC electrode materials (scale bars 2 μm and 500 nm). (i-o) TEM images of GO-StC electrode material showing: (i) starch particles attached to AC, (j) AC and CB particles distribution, (k) GO sheets at the base of the StC agglomerate (scale bars 200 nm), and (l) AC, (m) Starch, (n) CB and (o) GO magnified structures (scale bars 10 nm). 214

Figure P4-2 – Physicochemical characterisation (a) XRD patterns, (b) FT-IR and (c) RS spectra of GO-StC electrode material and GO-St-gel binder compared with reference materials. Red dashed, blue dotted and black dashed and dotted lines refer to AC, GO and St related features, respectively. “#” stands for “Amylose and Amylopectin”. (d) GO and (e) AC deconvolution results. Red solid and black dotted lines indicate experimental measurements and fitting results, respectively. (f) Variation of L_a with $I_D/(I_D+I_G)$ ratio. 218

Figure P4-3 – Thermal behaviour of GO-StC coatings. TGA and dTGA of (a) GO-St-gel, GO-St, GO, St and (b) GO-StC, StC, AC. (c) Variation of $I_D/(I_D+I_G)$ ratio and L_a with the temperature. SEM images showing development of cracks after thermal treatment of GO-StC electrodes at (d) 350 and (e) 550 °C (scale bars 100 μm). (f) TEM image showing reduced GO after thermal treatment at 350 °C (scale bar 2 nm)... 220

Figure P4-4 – Electrochemical characterisation of supercapacitors. (a) CV curves at a scan rate of 100 mV s⁻¹ and (b) GCD curves at a current density of 1 A g⁻¹ for GO-StC electrodes with varying GO amounts. (c) Variation of specific capacitance and equivalent series resistance (ESR) with GO amount. (d) CV curves at a scan rate of 100 mV s⁻¹ and (e) GCD curves at a current density of 1 A g⁻¹ for GO-StC electrodes with varying thermal treatment temperatures. (f) Variation of specific capacitance and ESR with the temperature. 223

Figure P4-5 – Electrochemical characterisation of optimised GO-StC electrodes. a CVs at scan rates of 10 to 400 mV s⁻¹ and (b) GCDs at current densities of 0.2 to 6 A g⁻¹ for GO-StC electrodes with 5% GO after thermal treatment at 350 °C (rGO-StC@350). (c) Variation of specific capacitance and ESR with current density and (d) Nyquist plots of rGO-StC@350 with dried-only GO-StC and StC electrodes (GO-StC@80 and StC@80) included for comparison. High-frequency

region magnified in the inset. Markers represents the experimental points, while solid lines the modelled behaviour with the simplified equivalent circuit (Figure S4-6). (e) Capacitance retention during the cycling at 4 A g^{-1} of rGO-StC@350 °C up to 17,000 cycles. Inset showing the comparison with GO-StC@80 and StC@80 up to 5,000 cycles. (f) Comparative bar chart expressing the high performance of the GO-St-gel (stacked bar colored in black, blue and red when referring to StC@80, GO-StC@80 and rGO-StC@350, respectively) among all alternative green binders processable in water (colored in green) and conventional binders of commercially available devices (colored in dark grey). Some non-biomaterial based greener alternatives have also been included as reference (colored in light grey). Water is used as the only solvent unless differently specified between brackets (*water is mixed with acetic acid). 226

Figure S4-1 – Electronic microscope imaging of GO-StC electrodes. (a-b) SEM images showing: surface morphology of (c) GO-StC and (d) StC coatings (scale bar $20 \mu\text{m}$). 247

Figure S4-2 – Physicochemical characterisation of GO-StC coatings at varying thermal treatment temperatures. (a) XRD patterns, (b) FT-IR and (c) RS spectra. 247

Figure S4-3 – Electrochemical characterisation of GO-StC electrodes with GO amount varying from 0 (StC) to 7.5%. (a, c, e, g, i, k) Cyclic Voltammetry Scans (CVs) and (b, d, f, h, j, l) Galvanostatic Charge Discharge Cycles (GCDs). Same legend applies for all CVs and all GCDs. Variation of (m) specific capacitance and (n) Equivalent Series Resistance (ESR) with current density. Same legend applies for both panels..... 248

Figure S4-4 – Electrochemical characterisation of GO-StC electrodes with thermal treatment temperatures varying from 80 to 550 °C. (a, c, e, g,

i, k) Cyclic Voltammetry Scans (CVs) and (b, d, f, h, j, l) Galvanostatic Charge Discharge Cycles (GCDs). Same legend applies for all CVs and all GCDs. Variation of (m) specific capacitance and (n) Equivalent Series Resistance (ESR) with current density. Same legend applies for both panels. 249

Figure S4-5 – Ragone plot of assembled SCs..... 250

Figure S4-6 – Impedance characterisation of supercapacitors. (a) Schematic of GO-StC symmetric cell with equivalent circuit elements assignment (R_{s1-2} are resistors accounting for leads, current collectors and interparticle series resistances; R_{s-el} accounts for the electrolyte series resistance; CPE_{int1-2} are constant phase elements accounting for interfacial non-ideal capacitances; R_{ct1-2} account for charge-transfer resistances at interfaces; W_{o1-2} are finite length-open Warburg elements accounting for the transmission-line behaviour of porous materials; CPE_{dl1-2} account for non-ideal double-layer capacitances [4]). (b) Simplified equivalent circuit for EIS fittings where $R_s=R_{s1}+R_{s2}+R_{s-el}$, $CPE_{dl}=(CPE_{dl1}+CPE_{dl2})/2$, $Z(R_{ct}-CPE_{int}-W_o)=Z(R_{ct1}-CPE_{int1}-W_{o1})+Z(R_{ct2}-CPE_{int2}-W_{o2})$. (c-d) Bode plots of rGO-StC@350 with dried-only GO-StC and StC electrodes (GO-StC@80 and StC@80) included for comparison. Markers represents the experimental points, while solid lines the modelled behaviour with the simplified equivalent circuit. Capacitors response frequency at a phase angle of -45° are specified. Variation of (e) Real and (f) imaginary part of complex capacitance for StC@80, GO-StC@80, and rGO-StC@350. Capacitors relaxation frequency (local maxima of C'') are specified. 250

Figure S4-7 – Flow diagram of rGO-StC electrodes fabrication process. 251

LIST OF TABLES

Chapter 1 Introduction

Chapter 2 Graphene-based materials

Chapter 3 Acoustic absorbers

Chapter 4 Supercapacitors

Table 4-1 – Examples of different porous carbons used for supercapacitors manufacturing.	82
---	----

Chapter 5 Graphene-based Acoustic Materials

Table P1-1 – Physical properties of all samples	109
Table P1-2 – Physical properties of GPA-1 samples for various processing times.....	110

Table S1-1 – Comparison of density, porosity, and sound absorption properties between GPA-1 samples from this work and other porous absorbers with comparable thickness previously reported in the literature.	127
Table S1-2 – Sound absorption and transmission properties for GPAs with different composition.	127
Table S1-3 – Sound absorption and transmission properties for GPA-1 samples with different thicknesses.	128
Table S1-4 – Sound absorption and transmission properties for GPA-1 samples obtained with different mixing times.	128
Table S2-1 – Comparison of density, porosity, sound absorption and thermal conductivity between modified GOP aerogels from this work and other aerogels with comparable thickness previously reported in the literature.	166

Chapter 6 Graphene-based Supercapacitors

Table P3-1 – Raman D to G band ratios, XRD Peak Positions, Lattice Spacing and Crystallite Sizes.	186
Table P3-2 – Summary of fabricated and tested supercapacitors samples with the adopted nomenclature.	195
Table S3-1 – Comparison of the four devices of Figure P3-6 in terms of active mass loading, capacitance and specific capacitance, with the values measured through GCs at specific currents ranging from 0.5 A g ⁻¹ to 4 A g ⁻¹	205
Table S4-1 – Slurry composition of different GO-StC and reference electrodes.	240
Table S4-2 – Main peaks positions and calculated structural parameters from XRD patterns of GO-StC, StC, AC, GO, GO-St-gel, GO-St, and	

St (Figure P4-2 – a of the manuscript). d , B and L_a are interplanar spacing in crystal lattice, line broadening at half-maximum intensity of the peak and crystallite lateral size, respectively.....	240
Table S4-3 – Main features and relative assignment from FT-IR spectra of GO, GO-St-gel, GO-St, and St (Figure P4-2 – b of the manuscript).	241
Table S4-4 – Interbands deconvolution of Raman spectra and resulting $I_D/(I_D+I_G)$ ratio of GO-StC, StC, AC, GO, GO-St-gel, and GO-St. Deconvolution result for GO is shown in Figure P4-2 – d of the manuscript, GO-St-gel and GO-St show similar fittings. Deconvolution result for AC is shown in Figure P4-2 – e of the manuscript, GO-StC and StC show similar fittings. x_c , w and l are peak position, full width at half height and peak height, respectively.	242
Table S4-5 – Starting, ending and peak temperatures of GO reduction and Starch degradation for GO-StC electrode material and GO-St-gel binder compared with reference materials (from TGA and dTGA analysis presented in Figure P4-3 – a-b of the manuscript).	243
Table S4-6 – Main peaks positions and calculated structural parameters from XRD patterns of GO-StC coatings thermally treated at varying temperatures (a). d , B and L_a are interplanar spacing in crystal lattice, line broadening at half-maximum intensity of the peak and crystallite lateral size, respectively.	243
Table S4-7 – Interbands deconvolution of Raman spectra and resulting $I_D/(I_D+I_G)$ ratio of GO-StC coatings thermally treated at varying temperatures (Figure S4-1 – c). x_c , w and l are peak position, full width at half height and peak height, respectively.	244
Table S4-8 – Electrodes coating specifications (mass loading, m_i ; thickness, h ; density, ρ) and resulting specific and volumetric capacitance (C and C_v , respectively; calculated at 0.2 A g^{-1}).....	244

Table S4-9 – Fitted values of the simplified equivalent circuit model (Figure S4-4 – b) and capacitor properties extrapolated from experimental data for StC@80, GO-StC@80, and rGO-StC@350 supercapacitor symmetric cells..... 245

Table S4-10 – Comparison of specific capacitance and capacitance retention for different supercapacitors obtained using alternative green binder processable in water and conventional binders of commercially available devices. Some non-biomaterial based alternatives have also been included as reference. Water is used as the only solvent unless differently specified between brackets..... 246

Chapter 1

INTRODUCTION

1.1 The Graphene family

Graphene is a carbon material consisting of a two-dimensional (2D) hexagonal lattice of sp^2 hybridized carbon atoms. It was experimentally discovered in 2004 thanks to the Nobel prize awarded work of Geim and Novoselov [1], following the discovery of zero-dimensional (0D) Fullerene in 1958 [2] and of one-dimensional (1D) Carbon Nanotubes in 1991 [3]. Particularly, graphene is considered the basic building block of the aforementioned synthetic carbon allotropes and also of three-dimensional (3D) Graphite, whose origin can be both natural and synthetic. The key difference between the allotropes is the different spatial arrangement of the 2D planes (Figure 1-1) [4].

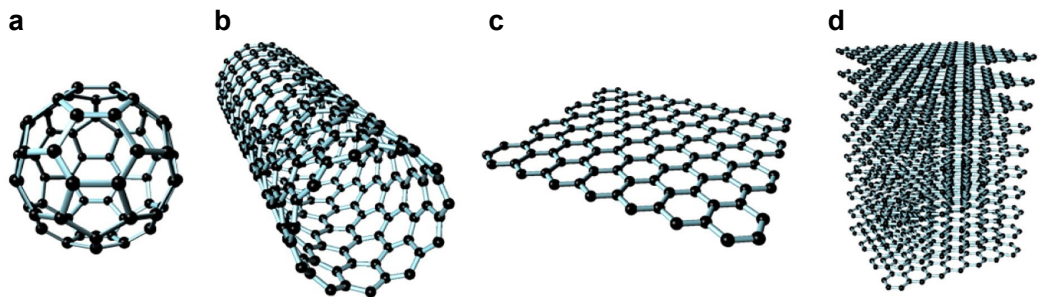


Figure 1-1 – Main carbon allotropes: **(a)** Fullerene, **(b)** Carbon Nanotube, **(c)** Graphene, and **(d)** Graphite [5].

Thanks to its outstanding mechanical [4], thermal [6] and electrical properties [1, 7], graphene is an ideal candidate to contribute to performance improvements of a wide range of applications, such as energy storage [8], noise control [9], polymeric composites [10], sensing [11], and water treatment [12]. Its large-scale use is however affected by a limited processing ability, due to the restacking tendency of individual graphene sheets, and consequently inhomogeneities and precipitation once dispersed into a matrix or a solvent.

Nowadays, there are four main routes that are being explored for the mass production of graphene-based materials: micro mechanical exfoliation of Graphite, Chemical Vapour Deposition (CVD), epitaxial growth, and Graphene Oxide (GO) reduction [13]. The latter is particularly considered as the most promising [14]. Thanks to its chemical structure, GO can form homogenous, stable and easy to be processed dispersions in water [15] or in organic solvents [16]. An important feature arising from GO processability, is its great versatility to be manufactured and templated in multi-dimensional assemblies with low cost and environmentally friendly processes. Examples are powders and quantum dots (0D) [17, 18], nanofibers and nanoribbons [19, 20], thin films on different substrates and free-standing papers (2D) [21, 22], and aerogels [23]. For the latter, GO can be either the only constituent or homogeneously blended with inorganic

materials and/or polymers [24]. Moreover, GO final properties can be tuned for specific engineering applications controlling its synthesis, processing and, eventually, reduction [25].

Given the great variety of works available in literature and the lack of homogeneity in the use of terms related to the wide family of materials derived from graphene, the definitions of greatest interest for a correct understanding of the current study are provided below. These are reported from the clarifying analysis done by Bianco et Al [26]:

- *Graphene* – single-atom-thick sheet of hexagonally arranged, sp²-bonded carbon atoms that is not an integral part of a carbon material, but is freely suspended or adhered on a foreign substrate. The lateral dimensions of graphene can vary from several nanometres to the macroscale (...).
- *Graphene oxide (GO)* – chemically modified graphene prepared by oxidation and exfoliation that is accompanied by extensive oxidative modification of the basal plane. Graphene oxide is a monolayer material with a high oxygen content, typically characterized by C/O atomic ratios less than 3.0 and typically closer to 2.0.
- *Graphite oxide (GtO)* – a bulk solid made by oxidation of graphite through processes that functionalize the basal planes and increase the interlayer spacing. Graphite oxide can be exfoliated in solution to form (monolayer) graphene oxide or partially exfoliated to form few-layer graphene oxide.
- *Reduced graphene oxide (rGO)* – graphene oxide (as above) that has been reductively processed by chemical, thermal, microwave, photo-chemical, photo-thermal or microbial/bacterial methods to reduce its oxygen content (...).

- *Graphene materials (also graphene-based materials, graphene nanomaterials, graphene-family nanomaterials)* – overarching terms for the collection of 2D materials defined above that contain the word “graphene”, including multi-layered materials (N less than about 10), chemically modified forms (GO, rGO), and materials made using graphene, graphene oxide, or another graphene material as a precursor. (...).

1.2 Scope and Objectives

The present research work aims to investigate the versatility of exploiting GO as a precursor for the manufacturing of graphene-based materials in multiple and integrated engineering applications. The way GO contributes on the final performance of such materials highly depends on how it is processed, from its synthesis to its dispersion in solvents, and to its reduction. These steps all highly affect the resulting chemico-physical properties, whose assessment with the appropriate characterisation techniques is then crucial to understand the underlying phenomena that lead to a certain behaviour of the final material. For these reasons, the first objective of the thesis is to investigate the background of graphene-based materials obtained from GO, by describing its chemical structure, processing methods, reduction approaches, characterisation techniques and chemico-physical properties.

The core of the research work is then addressed, with the discussion of the developed engineering applications using graphene-based materials. Two main engineering areas are investigated: acoustic materials and energy storage devices. The objectives of this section are:

1. To study and describe the state of the art of both technologies.

2. To define the gaps between the academic research and the industry, with a focus in readily scalable and environmentally friendly manufacturing processes.
3. To design and manufacture novel materials, building functioning prototypes for the corresponding application.
4. To critically evaluate and improve firstly developed methods and materials, leading to more advanced and/or functional prototypes.

The development of acoustic materials is the first engineering application considered for this thesis. The aim is to mitigate noise related issues that are of concern in many mechanical systems as industrial machineries, home appliances, vehicles of all nature, buildings and constructions. In particular, porous absorbers are a class of acoustic materials capable to reduce noise by the absorption of incident sound, mostly, and in part also from its reflection. Although traditional porous absorbers as cellular foams and fibrous materials are effective over a medium frequency range, that is between 800 and 2,000 Hz, in order to effectively reduce noise at lower frequencies their use is limited by the need of thick and heavy structures. In this thesis, the prototype of a thin and ultralight aerogel capable of broadband and tuneable acoustic properties is presented. It is obtained from a mixture of GO and poly(vinyl alcohol) (PVA) opportunely processed where water was used as the only solvent and thus allowing for a low cost and environmentally friendly manufacturing process. The presence of GO proves to be crucial for both the ability to template an ultralight structure and the development of the intriguing acoustic properties.

With the aim to further broaden the applicability of graphene aerogels in advanced engineering structures, chemical modification approaches to the manufacturing of GO and PVA aerogels are also proposed. Particularly, three chemical agents are used: glycerol (GLY) as a plasticiser,

glutaraldehyde (GA) as a cross-linker, and ascorbic acid (AA) as a reductant. Their use, stand-alone and/or in combination, enhances the cellular structure of the material guaranteeing mechanical robustness, acoustic and thermal insulation, and, when AA is used to promote GO reduction, piezoresistive properties.

The continuous growth in energy demand and the need of a more sustainable industry is raising the interest toward more efficient and sustainable energy storage devices; the latter are the focus of the second engineering challenge examined in the present research work. In particular, Supercapacitors (SCs) represent a viable solution thanks to their high current capabilities while maintaining long cycling life and high energy efficiency in a broad operating temperature range and with scalable designs. Their main drawback is a limited energy density, issue that researchers are addressing with multiple approaches consisting mostly in the improvement of the specific capacitance of the electrodes through novel active materials. Another issue related to SCs that have currently received only minor attention is the environmental impact caused by the use of hazardous chemicals during their manufacturing. Those are mostly due to the need of binders as fluoropolymers dispersed in organic solvents. On this regard, the present research work proposes two different approaches. The first consists in the fabrication of binder-free electrodes through the processing of a carbonaceous slurry composed of GO and Carbon Black (CB) using water as the only solvent. In such embodiment GO is initially responsible for the cohesion between carbon particles and for their adhesion on the substrate behaving as current collector, without the need of any additional binder. After a thermal treatment promoting its reduction, GO (now rGO) also actively participate to the improved electrochemical performances. Moreover, in the same study a rGO paper, derived from the thermal annealing of free-standing GO films, is proposed as an alternative

current collector for the manufacturing of lighter and “all-graphene based” devices.

The second approach investigated for the development of more environmentally friendly SCs consists in the use of a biopolymer processable in water, namely Starch (St), as green binder. Its properties are enhanced by the inclusion of GO which can, as introduced from the previous study, actively contribute to the electrochemical performances upon subjecting the electrodes to thermal treatment. Another feature inherited from the previous study is the use of the rGO paper as current collector, although more conventional Activated Carbons (AC) are used as active material with only limited inclusion of CB as conductive additive.

1.3 Outline of the Thesis

This thesis, in accordance with the alternative format, is outlined as follows.

Chapter 1 gives an overview on graphene-based materials, describing their origin, main advantages and disadvantages, and an appropriate nomenclature. The scope and the objectives of the thesis are also disclosed. Particularly, the context of the engineering applications investigated in this research work is introduced, and the role of GO in each is also briefly described.

Chapter 2 contains the background on graphene-based materials, backbone for a clear understanding of the engineering applications detailed in the following chapters. The synthesis and the structure of GO is initially described, as well as its most salient features. GO processing methods and the relationship with its precursor, GtO, and its eventual products, namely rGO, are also disclosed. The most important characterisation techniques

and the chemico-physical properties of graphene-based materials are then discussed. Finally, the engineering applications are introduced.

Chapter 3 and 4 presents the background on the two developed engineering applications, respectively focusing on porous absorbers as acoustic materials and EDLCs as energy storage devices. For both, the basic theory and concepts are initially disclosed. Then, the broader context in literature is disclosed. Finally, current research questions are highlighted, introducing how those will be addressed in the publications presented in the thesis.

The following chapters contain the core of this research work, which is exposed as a collection of scientific papers. They are grouped in the two investigated engineering applications. For each, a brief introduction describing their rationale and main results is provided.

Chapter 5 initially presents the study on the development of an ultralight GO/PVA aerogel as an acoustic material. The chemico-physical characterisation initially provide for the formation of the aerogel, then the acoustic properties are assessed. Furthermore, a semi-analytical approach is employed to find a correlation between the acoustic and non-acoustic properties of the material. The chapter continues with another, related, study where chemical modification approaches to the GO/PVA are proposed. After an evaluation of their chemico-physical properties, the modified aerogels were tested for multifunctional abilities such as acoustic and thermal insulation, elastic resiliency, and piezoresistivity.

Chapter 6 explores the two approaches adopted for the development of more environmentally friendly SCs. In the first GO completely substitute the binder, while in the second GO enhances the performance of Starch, used as an alternative green binder. Both exploit rGO paper as current

collector. The studies start with the characterisation of the chemico-physical properties, providing insights on the fabrication of the electrodes, and then focus on the electrochemical characterisation of the assembled devices.

Chapter 7 contains conclusive remarks and paves the basis for future works.

Chapter 2

GRAPHENE-BASED MATERIALS

2.1 Graphene oxide and reduced graphene oxide

GO is one of the main candidates to be used as precursor for the industrial scale production of graphene-derived materials [14]. It can be obtained with the so-called “exfoliation process” of GtO. In fact, GO and GtO are only distinguished by the number of layers of which they are made of: GO is, by definition, a monolayer material while GtO is a bulk solid [26]. The latter was first produced in 1859 by Brodie [27] during his studies on the structure of graphite, where he originally termed it as “Graphic Acid”. The synthesis of GtO was then improved by Staudenmaier in 1898 [28] and by Hummers and Offeman in 1958 [29]. For industrial and laboratory production, “Modified Hummers’ methods” are currently used, where small alterations with respect

to the original method are introduced to improve safety and scalability [30]. The process can be summarised as follows: a mixture of Sulphuric Acid and/or Phosphoric Acid (protonated solvent) with Potassium Permanganate (oxidizing agent) is used to oxidize Graphite; the obtained compound is diluted with water and treated with Hydrogen Peroxide to remove metal ions and then dried; the resulting solid is finally washed with diluted Hydrochloric Acid first and distilled water later to complete its purification.

The oxidation process of Graphite results into the introduction of several oxygen based functional groups (Figure 2-1 – a-b): Epoxide and Hydroxyl on basal planes and Carbonyl and Carboxyl on edges [31-34], among the others. Although several models have been reported in literature, being Lerf-Klinowski [31, 35] and Dékány [32] the more commonly accepted, GO structure is not precisely defined yet. This uncertainty arises from the nonstoichiometric atomic composition of the material and from variations in structure and properties of GtO when different oxidation methods or different Graphite sources are used [34, 36-38].

The oxygen containing functional groups are actually defects that interrupt the hexagonal lattice of sp^2 -hybridised carbon atoms in pristine graphene layers. The existence of structural defects, and the chemical behaviour of oxygen functionalities play a major role in the resulting features of the compound, whose can be streamlined as follows:

- Increase of the distance between adjacent graphene layers from $\sim 3.35 \text{ \AA}$ of Graphite to $6-10 \text{ \AA}$ of GtO, where the variation depends on different hydration levels [39];
- Hydrophilicity and consequently the ability of water and organic polar solvents to intercalate between interlayers spacing [16, 34];
- Low electrical and thermal conductivities [34, 40];

- Thermal instability [15, 41];
- Possibility to exploit surface-modifications reactions, and so to develop functionalised GO [42].

The intercalation of water allows GtO to be easily exfoliated to GO when sufficient mechanical energy is provided through sonication or high-speed stirring (Figure 2-1 – b-c). Paredes et Al [16] demonstrated that the best results in terms of successful exfoliation and long-term stability are reached in water dispersion, but also that other organic polar solvents, such as Dimethylformamide (DMF), N-Methyl-2-pyrrolidone (NMP), Tetrahydrofuran and Ethylene Glycol (EG), can be used with a similar outcome (Figure 2-2). This provides for the possibility to manufacture nanocomposites with matrices incompatible in aqueous dispersions and broadens viable approaches to functionalise GO and Graphene [34, 43-46].

The electrical and thermal conductivity of Graphene are given by the conjugated network of the hexagonal lattice of carbon atoms. In GO, the latter is interrupted by the oxygen functionalities, thus introducing phonon-scattering and decreasing carrier mobility [47]. In the reduction process of GO the aim is, ideally, to remove all the impurities previously introduced during the oxidation (i.e., removal of atomic-scale lattice defects and restoration of the conjugated network) while maintaining a stable dispersion in solution and/or an expanded structure (i.e., avoiding the restacking of graphene layers due to Van der Waals interactions) [34, 48]. The resulting product of GO reduction is, as previously anticipated, the rGO (Figure 2-1 – c-d). Although the transformation always leads to the presence of impurities, whose can arise from both the precursor and the reducing agent itself, the chemico-physical properties of rGO are, to some extent, similar to pristine Graphene. The two subsequent processes of oxidation and reduction of Graphite to obtain rGO may appear as redundant, however it's important to

highlight that such kind of processing allows to embrace the advantages of a top-down approach as scalability and cost-effectiveness while keeping some advantages commonly found in bottom-up approaches like the ability of performance tuning.

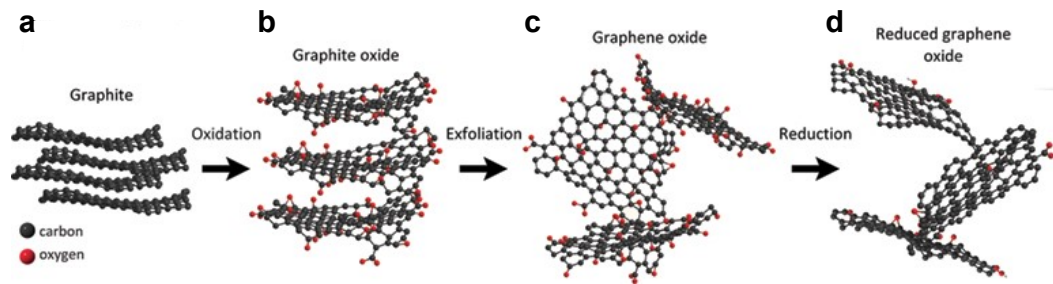


Figure 2-1 – Processing route from (a) Graphite to (d) rGO, with (b) GtO and (c) GO as intermediates [49].

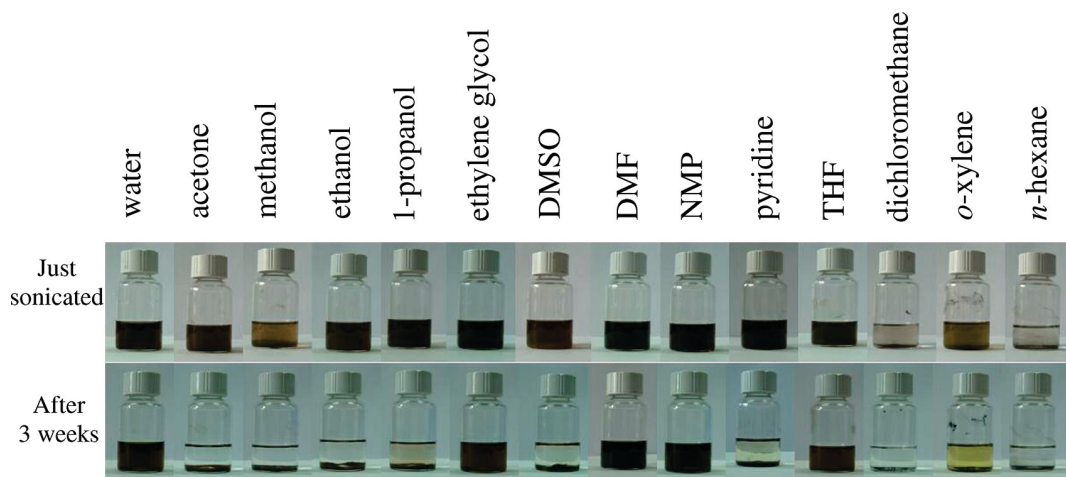


Figure 2-2 – Digital pictures of GO dispersed in water and other organic solvents through bath ultrasonication. Top panel shows the dispersions immediately after sonication, while the bottom 3 weeks after sonication [16].

2.2 Reduction

The reduction from GO to rGO can be achieved following several routes that can be categorised in two main families: thermal and chemical methods. The characteristics of each, as well as some examples are described in the following paragraphs.

2.2.1 Thermal methods

Thermal methods are based on the sudden evolution of CO₂ and CO with traces of H₂O, all in gaseous phase, which is generated by the decomposition of oxygen groups when GO or GtO are rapidly heated. Schniepp et al. [50], in one of the first report illustrating this behaviour, produced “functionalized single graphene sheets” (equivalent to rGO considering the nomenclature adopted for the current manuscript) through the application of an extremely rapid heating at 2,000 °C min⁻¹ (i.e., thermal annealing). McAllister et al. estimated, from the evaluation of the Hamaker constant, that a pressure of 2.5 MPa is sufficient to separate two stacked Graphene Oxide sheets [51]. In the same work, it is also shown that, by applying the equation of state, the gaseous expansion allows the development of a 40 MPa pressure at 200 °C, raising to 130 MPa at 1,000 °C. It is interesting to note that 200 °C corresponds to the decomposition temperature of oxygen-containing groups, as determined with TGA/DSC analysis [50]. If the heating is not quick enough, however, the lateral diffusion can relieve the pressure allowing Van der Waals forces to maintain the graphitic stacking [51]. Comparing the reaction and the diffusion time scale, McAllister et al. estimated a value of 550 °C as a lower limit of temperature for the exfoliation to occur [51]. Nevertheless, examples of successful reduction of GO to rGO at lower rates and temperature are reported in literature [52-56].

Another important factor during the thermal reduction is the atmosphere control: Oxygen presence should be minimized to reduce the etching effect at high temperature. For this reason, the reaction is usually performed in vacuum or inert atmosphere; alternatives are the use of reducing H₂ atmosphere for improved reduction or with carbonaceous source such as Ethylene for defect healing [48].

Besides conventional heating processes where the heating elements of ovens or furnaces are used as energy sources, it is also possible to find examples of Microwave Irradiation or Photo-Irradiation. The first has been effectively used to produce exfoliated graphite from either graphite intercalation compounds [57] or amorphous carbons [58] and recently proved to be as effective for the reduction of GO [59]. Its main advantage is a rapid and uniform heating that leads to high yields [60]. The photo-irradiation exploit the inability of carbon nanomaterials to dissipate the energy absorbed during the exposure to intense light source like Xeon flash [61] or laser [62], leading to quick and localized heating. The use of laser, particularly, is of great interest thanks to the possibility to finely control the reduction area, realizing two dimensional patterns with precision in the order of microns (Figure 2-3) [62]. Moreover, changing wavelength, power and exposure time, the reduction process is extremely governable [63, 64]. With a simulation of temperature dynamics Trusovas et al. [65] estimated an increase in the local temperature of a GO film up to 1,400 °C on the surface and up to 600 °C in a layer 300 nm under the surface, sufficient to generate the evolution of CO and CO₂ and thus the reduction of GO to rGO.

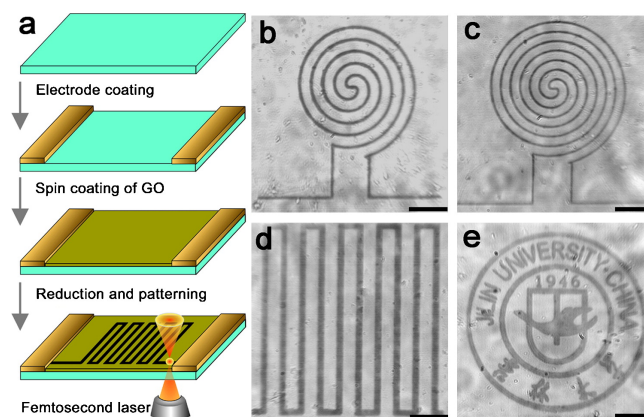


Figure 2-3 – Fabrication scheme and optical microscopy images of reduced and patterned GO films [62].

2.2.2 Chemical methods

Chemical methods use strong reducing agents coupled to mild heating to remove the oxygen groups. Due to the complexity of the involved reactions, several reaction mechanisms have been proposed but none of them are unequivocally recognized. Such processes have the advantages of a relatively mild working temperature and easiness to reach large-scale production. To be effective, a reducing agent should readily promote deoxygenation and at the same time have small to null reactivity with the solvent of the GO dispersion. One of the most commonly used reagent is Hydrazine: it was used for the reduction of GO by Kotov et al. even before the discovery of Graphene but the first report regarding the production of “Graphene” is from Stankovich et al. [15, 66]. Other reducing agents recently employed with similar or even better results are Sodium Borohydride (NaBH_4) [67], Hydroiodic Acid (HI) [68] and Ascorbic Acid (AA) [69, 70], among the others. AA is an ideal candidate for the development of a green process (Hydrazine is highly toxic) and allows also the production of more stable colloids (Figure 2-4) [69]. The drawbacks of chemical methods are the introduction of heteroatomic impurities, consisting of reaction by-products covalently attached to the planes of the resulting rGO, the selectiveness of the reducing agent toward specific functional groups that always lead to some Oxygen residue in the final product, and the toxicity of the reducing agent if green alternatives are not used [34].

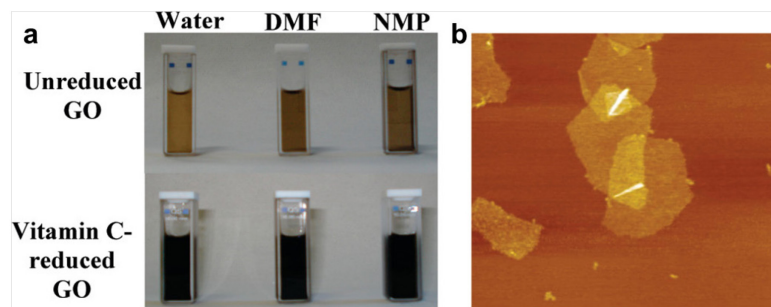


Figure 2-4 – (a) Digital pictures of GO and rGO respectively before and after AA treatment. **(b)** Representative Atomic Force Microscopy image of rGO sheet, showing single layers [70].

Other less conventional chemical approaches are Photocatalyst reduction, Electrochemical reduction and Solvothermal reduction [48]. The first employs material with photocatalytic activity like Titanium Dioxide to promote photo-chemical reactions when the colloidal solution is UV-irradiated [71]. In the electrochemical process the reduction is activated by electrons transfer between GO and the electrodes of the cell. Also for this reaction, the mechanisms is still unclear [34]. Ramesha and Sampath [72] showed that the reaction occur in a voltage range between -0.60 V and -0.87 V and that it is irreversible. Particularly, Electrophoretic Deposition was successfully applied to assemble rGO films [73]. The advantage of electrochemical methods is the non-use of any reducing agent but the scalability of the process still needs to be investigated [48]. In solvothermal processes a GO dispersion in water is heated in a sealed container, allowing the pressure to raise and the temperature of the water to go above the boiling point (i.e., reaching the supercritical state). In such conditions, water effectively becomes a green reducing agent [48, 74].

2.3 Chemicophysical properties

As described above, the production of rGO from bulk Graphite requires three major steps, that are Oxidation, Exfoliation and Reduction, and two significant intermediates, that are GtO and GO, are produced. In order to

optimise the manufacturing process and allow product performance tuning, the knowledge of a set of characterisation techniques to observe and measure changes in the chemical structure and in physical properties is then crucial.

The first technique that allows to qualitatively establish whether the reduction is successful or not is the visual inspection. GO colloidal dispersions, films and powders have a characteristic yellow-to-brown colour that switch to black after their reduction [74, 75]. In some cases, generally when thick films are assembled and then highly reduced, also a metallic lustre is given to the sample. It is determined by the variation in charge carrier conditions that alters light reflectivity [76].

Other visual techniques employ electron microscopes, as in Scanning Electron Microscopy (SEM) and Transmission Electron Microscopy (TEM) and in scanning force microscopes, particularly with Atomic Force Microscopy (AFM). SEM is useful for micrometer-scale morphology analysis of surfaces and cross-sections, depending on the assembly [15, 22]. From the work of Gao et al., as example, it is clearly possible to observe the morphological change and increased porosity after the laser patterned reduction [77]. The typical layered structure of graphene paper is instead evident in the report from Chen et al., [78]. Wang et al. adopted SEM to show GO ability to be templated in aerogels with well-organised structures by freeze-casting (Figure 2-5) [79]. TEM allows observations on the morphology and structure of single or few layers sheets, where a higher transparency is evidence of thinner sheets of GO [80]. This is useful to characterise the exfoliation or the reduction processes, as illustrated by Stobinski et al. [81]. Nanometer-scale morphology and atomic-scale structure can be probed with AFM, allowing the measurement of sheets thickness and lateral dimensions [69, 82]. Luo et al., exploited AFM to

assess the exfoliation degree or the agglomeration of GO and rGO sheets after their dispersion in solvents [83]. In addition, the same instrument was effectively used to assess the nanomechanical properties by Poot and van der Zant [84].

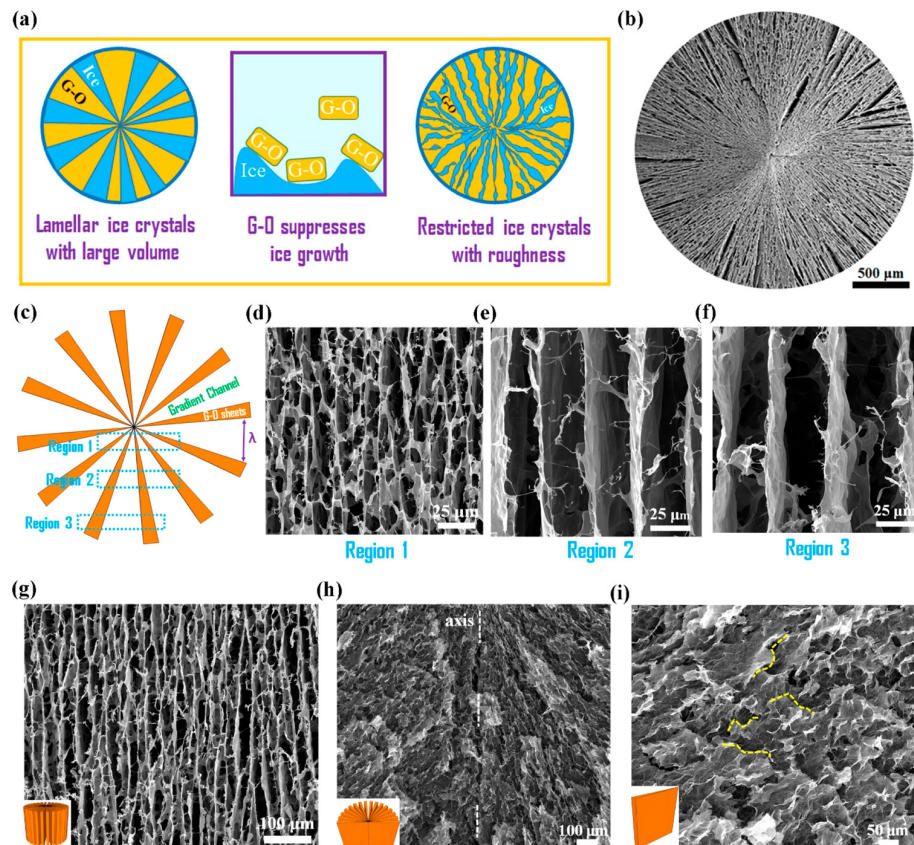


Figure 2-5 – Mechanism of structure formation and SEM images of aerogel microstructures [79].

The chemical structure and composition can be analysed by spectroscopy methods: “the science concerned with the investigation and measurement of spectra produced when materials interacts with or emits electromagnetic radiation” (Meer, 2018) [85]. The techniques that are more commonly used are X-Ray Photoelectron Spectroscopy (XPS), Fourier-Transform Infrared Spectroscopy (FT-IR), and Raman Spectroscopy (RS). In XPS the surface of a sample is irradiated by X-rays and, due to the photoemission phenomenon, electrons are emitted [86]. The number of

electrons and the relative kinetic energy are then measured and used to extrapolate the spectra. Particularly, XPS can be used to determine the ratio between Carbon and Oxygen atoms (C/O ratio) before and after the reduction process, with values within the 4:1 – 2:1 range and of about 12:1 for GO and rGO, respectively [48]. Moreover the binding energy of Carbon atoms bonding in different functional groups can be assessed: C-C bonding (π electrons from sp^2 hybridized atoms) at ~ 284.5 eV; C-O (epoxide and hydroxyl groups) at ~ 286 eV, C=O (carbonyl group) at ~ 287.8 eV, C-(O)O (carboxyl and carboxylate groups) at ~ 289 eV [48, 83]. When performed before and after the reduction, it allows to determine and quantify the oxygen impurities left in rGO.

In FT-IR a broadband infrared beam of light is exposed to the sample, the energy that the latter absorbs (i.e., the absorbance) at various wavelengths is then measured. As different types of bonds between different elements absorb the light uniquely, the molecular composition and structure of materials can be determined. FT-IR was effectively used by Hontoria-Lucas et al. to characterise the different functional groups of GO, and thus to confirm a successful oxidation of graphite as well as the extent of the process [87]. According to literature [87, 88], the typical features are the following: O-H stretching and deformation of hydroxyl groups within the $3200-3400\text{ cm}^{-1}$ and $1050-1250\text{ cm}^{-1}$ ranges, C=O stretching of carbonyl groups at $\sim 1720\text{ cm}^{-1}$, COOH stretching of carboxyl groups within $1650-1750\text{ cm}^{-1}$, C-O-C stretching of epoxy groups at ~ 1030 and 850 cm^{-1} . It is also possible to find a band at $\sim 1620\text{ cm}^{-1}$, attributable to either the C=C stretching of un-oxidized graphitic domains or the bending modes of adsorbed water [89]. Some Alkyl impurities may also be observed in the asymmetric and symmetric stretching of C-H bonds within the $2950-2800\text{ cm}^{-1}$ range. FT-IR allows also to study GO reduction and compare the effectiveness of different reducing methods by the evaluation of eventual

residual groups, which may be not completely removed after the process (Figure 2-6 – a) [69, 90]. In addition, FT-IR is a well-established method to monitor GO and rGO functionalisation effects [91]. Being composed of homo-nuclear molecular bonds, the technique is instead less effective for the characterisation of pristine graphene or graphite.

In RS a laser light is directed to the surface of the sample, from the interaction of the incident light with the molecules of the material a scattered light is then produced. This is made of two parts: the Rayleigh Scatter, unchanged in wavelength, and the Raman Scatter, scattered with different wavelengths depending on the chemical structure. Every molecule has a unique vibration, a fingerprint that is excited by the laser light. For graphene-based materials, the RS can be used to have information regarding the number and quality of layers, doping level and disorder [92]. This is possible because the spectra are characterized by three main features: the G band at $\sim 1580\text{ cm}^{-1}$, characteristic of E_{2g} primary in plane vibrating mode between pairs of sp^2 atoms in both rings and chains of molecules and associate with the stacking of the structure; the D band at $\sim 1360\text{ cm}^{-1}$, from A_{1g} breathing modes of sp^2 atoms in rings that describe the structural disorder; and the 2D band at $\sim 2700\text{ cm}^{-1}$, a second order overtone of the D band [34, 92]. The first two features are usually merged in their intensity ratio (I_D/I_G ratio), where higher values are associated to more disordered structures while in pristine graphene it approaches zero (Figure 2-6 – a) [92]. Its value as quantitative analysis of the oxidation/reduction degree is however questionable and XPS should be used for this purpose [83]. It is worth noting that for a rigorous evaluation of graphene-based material structural features with RS, also the existence of other bands should be taken into account and interbands fitting techniques may be used [93]. Ferrari and Basko disclosed on the effectiveness of RS as a tool to study graphene [94], in their work the effects of structural defects in graphene spectrum are particularly clarified. For the

estimation of the number of pristine graphene layers, both the G and the 2D bands can be evaluated. Gupta et al. first observed a linear proportionality between the number of layers and G peak intensity [95], while Wang et al. later provided an empirical correlation between the number of layers and G band position [96]:

$$\omega_G = 1581.6 + \frac{11}{(1 + n^{1.6})} \quad (1)$$

where ω_G is the position of the band in wavenumber and n is the number of layers. The accuracy of this formula is however susceptible from other phenomena causing the shift of the G band, such as mechanical strain, doping, and temperature [97, 98]. The 2D band can be similarly used by observing its position and shape: monolayer graphene presents a single sharp peak below 2700 cm^{-1} ; in bilayer sheets the peak is broader and around 2700 cm^{-1} ; when the sheets are made of more than five layers, the peak is broad and above 2700 cm^{-1} (Figure 2-7) [92].

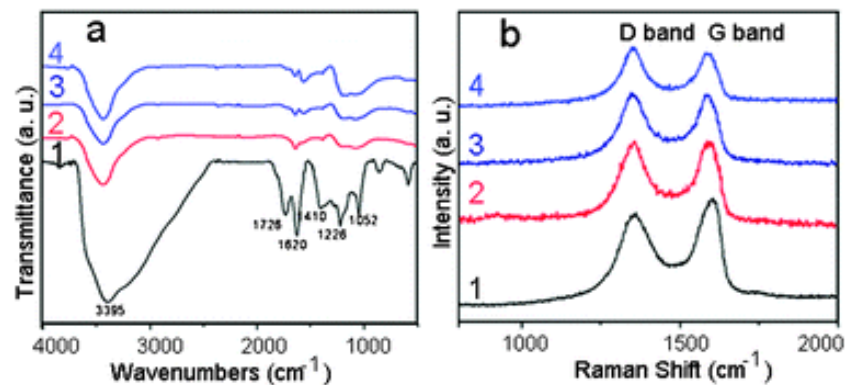


Figure 2-6 – (a) FT-IR and (b) RS of GO before (1) and after AA reduction with increasing times (2-4) [69].

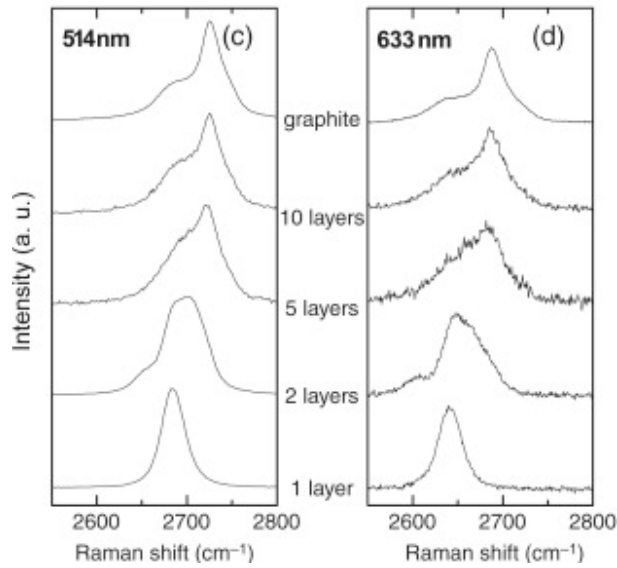


Figure 2-7 – Evolution of the 2D peak as a function of the number of layers evidenced by RS with 514 and 633 nm excitation wavelengths [92].

Depending on their nature, constitutive elements of solid materials can be arranged in a highly ordered structure, the so-called crystal lattice. When X-Rays having a wavelength similar to the spacing between lattice planes and a certain incident angle interact with it, a constructive interference is achieved if the spacing is an integer multiple of the wavelength. Then, X-Rays are reflected so that the angle of reflection is equal to the angle of incidence. This is the phenomenon diffraction, and it is the basic principle of X-Ray Diffractometry (XRD). Thanks to the application of Bragg's Law [99]:

$$d = \frac{\lambda}{2 \sin \theta} \quad (2)$$

where λ is the radiation wavelength and θ is the reflection angle of the crystalline phase under analysis, the interplanar distance d can be calculated. Every crystalline phase has a different reflection angle, so their patterns can be considered as fingerprints of the substance. Regarding XRD patterns of graphene-based materials, Graphite is commonly characterized by a (002) reflection peak at 2θ of 26.3° while in GtO a (001)

reflection peak is usually found within the 10 – 11° range [36]. Graphene and GO, being monolayer materials, cannot have any diffraction peaks but when few layers stacking are present, the (001) and (002) phases could be individuated and the interplanar spacing determined. Another feature observable in graphene-based materials is the (10) reflection at ~43° [81]. It derives from a turbostratic arrangement of graphene layers that leads to the merging of the (100) and (101) reflections, whose are instead present in ordered graphite at 42.22° and 44.39°, respectively [100]. Krishnamoorthy et al. documented the variation of XRD patterns for different oxidation degrees of Graphite [36]: the (001) and (002) phases coexist for lower oxidation degrees; the (002) then disappears to give space to a sharp (001) when the process is complete (Figure 2-8). Johra et al. used XRD as further proof of a successful reduction from GO to rGO (Figure 2-9) [101]. Moreover, with the application of Scherrer's formula [102], Stobinski et al. [81] estimated the number of Graphene and/or Oxidized Graphene layers as well as their height and average diameter. The formula is expressed as follows:

$$L = \frac{K\lambda}{B \cos \varphi} \quad (3)$$

where K is a shape factor, B is the line broadening at half-maximum intensity of the peak, and φ is the corresponding scattering angle of the feature under analysis. L represents main crystallite dimensions, which are the stacking height L_c , derived from the (002) peak using a shape factor of 0.89, and the lateral size L_a when a shape factor of 1.84 and the (10) reflection are used [103]. From the seminal work of Tuinstra and Koenig [104], it is worth noting the existence of a linear relationship between the I_D/I_G ratio and the inverse of L_a .

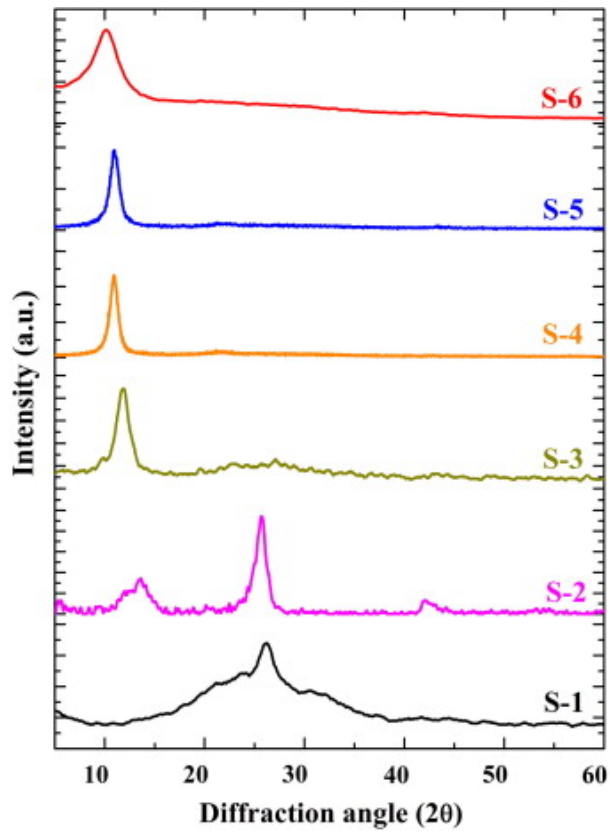


Figure 2-8 – XRD patterns of GO with different degrees of oxidation [36].

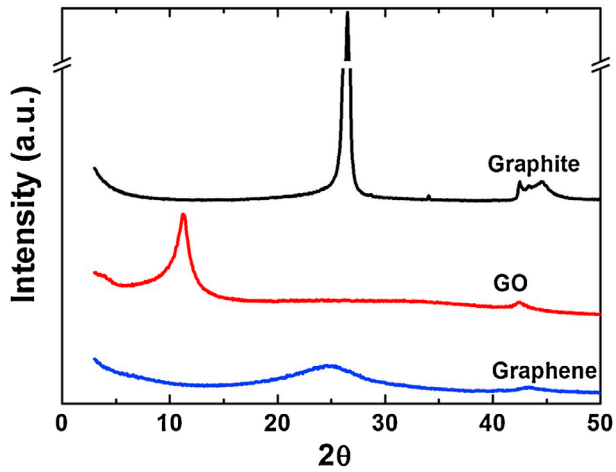


Figure 2-9 – XRD patterns of graphite, GO and graphene [101].

2.4 Engineering applications

The properties described in this chapter shape GO as an extremely versatile precursor for the development of graphene-based materials that can be specifically tailored for several engineering applications. One of the most important features is surely GO ability to form stable dispersions in water, which allow for scalable, low-cost, and environmentally friendly processes. The previously mentioned versatility arises from the possibility to exploit those processes to obtain different assemblies and blends with other inorganic materials or polymers.

One example is 3D aerogels, recently defined by Ziegler et al. as “a solid with meso- and macropores with diameters up to a few hundred nanometers and a porosity of more than 95% in which the dispersed phase is a gas” [105]. As it will later (Chapter 3) be described in detail, the working principle of porous sound absorbers consists in the dissipation of sound energy due to the friction of air particles through the pores of the material. Carefully tailored graphene-based aerogels represent therefore an ideal solution as acoustic materials.

Another example of assemblies obtainable from GO are powders, coatings and free-standing papers, whose electrical properties can be tuned through the reduction and conversion to rGO. It will later be described how porous carbons are one of the basic elements for electrodes fabrication and that the need of binders and organic solvents is the main cause of environmental issues and high processing costs. Due to the possibility to exploit the synergy of graphene-based materials with other carbon particles in easy to process carbonaceous nanocomposites, the just mentioned assemblies, where the need of binders can be removed or mitigated, represent a great opportunity for the technological development of more environmentally friendly SCs.

Chapter 3

ACOUSTIC ABSORBERS

3.1 Technological background

3.1.1 History and basic principles of acoustics

Studies on physical mechanisms governing the behaviour of sound waves in solid bodies were initially performed in the nineteenth century by renowned scientists such as Poisson, Stokes, Kirchhoff and Helmholtz. Their drive was the improvement of sound quality in wind instruments, with Kirchhoff, in particular, deriving an analytical solution for sound oscillations in organ pipes. He paved the basis of modern acoustic analysis in gases, porous materials and structures [106]. More recent developments came in the twentieth century with the founding of architectural acoustics by Sabine:

rooms acoustics became extremely important in theatres, cinemas and studios [107]. Nowadays, the interest toward acoustic materials has grown exponentially, due to both technological improvements and public concern about noise in everyday life, and has been extended to mechanical systems in industries, home appliances, vehicles, and civil buildings. In the last 50 years, initially due to health issues related to the use of asbestos-based materials and later for environmental issues related to the production of synthetic fibres, the focus is moving toward more environmentally friendly acoustic materials [108].

When a sound wave hits a surface, its associated energy can be considered as a combination of three contributions: reflection, absorption, and transmission; with incident energy always being conserved (Figure 3-1). The distribution between the three contributions depends on the acoustic properties of the material, with equal importance of the properties of the exposed surface and of the bulk. In order to achieve proper noise control, the aim of acoustic engineering is to manipulate sound propagation and maximise the desired contribution for the specific application. They are, in fact, generally related by inverse proportionality. As example, sound transmission through a material is one of the most important parameters in a noise reduction problem; conversely, materials characterised by low transmission generally reflect back most of incident energy. Differently, if a material is characterised by a high absorption, the incident energy would be mostly dissipated and only a relatively small part would be reflected. The problem of noise is generally related to a frequency spectrum, which, for convenience of analysis in this research work, will be split as follows: “low-frequency range” below 800 Hz, “mid-frequency range” between 800 and 2,000 Hz, and “high-frequency range” above 2,000 Hz [109].

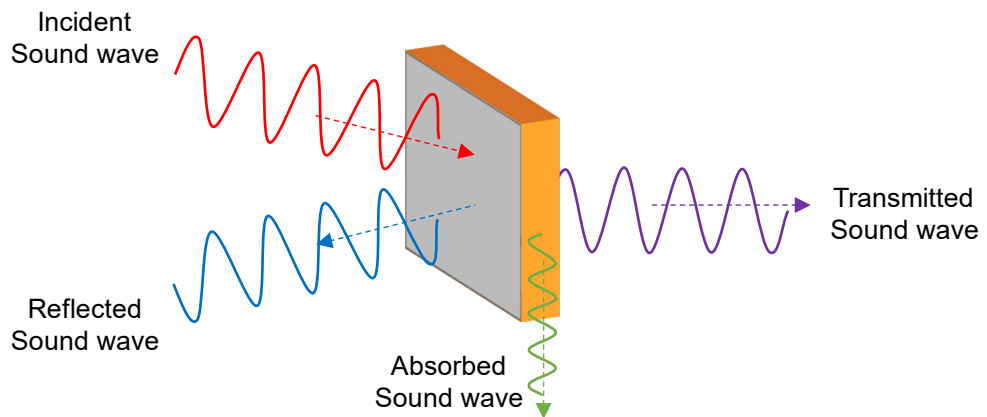


Figure 3-1 – Different contributions of a sound wave incident to an acoustic surface.

3.1.2 Porous absorbers

A particular class of acoustic materials is represented by porous absorbers: they are able to dissipate incident sound energy thanks to a network of interconnected pores, through which sound waves propagate. The friction of air, a viscous fluid, within the pores is responsible for most of energy dissipation (i.e., viscous effects localised in the boundary layer in proximity of pore's wall) with a smaller contribution from thermal conduction. Absorbers' performance is usually evaluated in terms of an Absorption Coefficient (α): it is defined as the ratio of energy absorbed by the material to the energy incident on its surface, and consequently varies between 0 (i.e., no absorption) and 1 (i.e., complete absorption). The thickness of porous absorbers highly influences α (other important parameters will be introduced and described in detail in the following paragraphs) in terms of both magnitude and frequency range where optimum performances are achieved. In particular, as sound dissipation is a quadratic function of frequency and optimum absorption is achieved where particle velocity is high, the required thickness to achieve significant absorption with common porous absorbers is generally 1/10 of the wavelength: this highly limits their practical use for low frequency absorption [110, 111].

Porous absorbers can be classified in three categories, depending on pores topology and related viscous effects on air: fibrous materials, where air goes through a complex and interconnected network of passages between the fibres; foams, characterised by a cellular structure where small and interconnected pockets of air can be formed; and granular materials whose porosity is derived by voids between the elements [109, 112]. For the scope of this research work, only foams (with aerogels being their subcategory) will be considered.

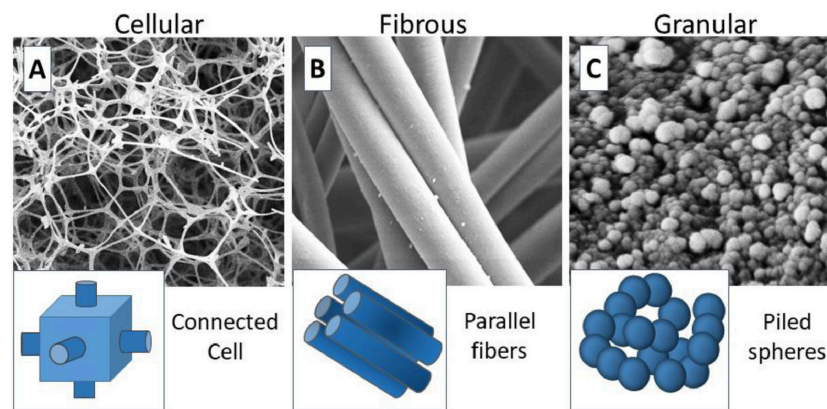


Figure 3-2 – Different categories of porous absorbers [113].

The acoustic behaviour of foams can be directly related to a set of so-called “non acoustic properties”, which are described as follows [114-116]:

- *Flow resistivity* (σ) – resistance offered from a porous material to an airflow, giving insights on boundary layer effects causing sound energy dissipation.
- *Open porosity* (ϕ) – fractional pore volume involved in sound propagation.
- *Tortuosity* (α_∞) – complexity of sound waves propagation paths through the absorber.
- *Viscous and thermal characteristic lengths* (Λ and Λ' , respectively) – viscous and thermal effects of pores shape on sound propagation.

- *Viscous and thermal permeabilities* (q_0 and q_0' , respectively) – Transport parameters expressing viscous and thermal interactions between air and pores structure of the material.

Those, thanks to the use of a semi-phenomenological fluid model that will be discussed in the following paragraphs, are extremely important for the understanding and/or the prediction of sound absorption capabilities of novel materials [109].

3.1.3 Sound propagation

Considering the propagation of a plane wave through an acoustic medium in the x direction, pressure (p) and particle velocity (u) are defined as follows:

$$p = Ae^{j(\omega t - kx)} \quad (4)$$

$$u = \frac{A}{\rho c} e^{j(\omega t - kx)} \quad (5)$$

where A is a constant related to the magnitude of the wave, $\omega = 2\pi f = kc$ is the angular frequency, k is the wavenumber, f is the frequency and c and ρ are the speed of sound and density of the medium, respectively. From the ratio of p and u , it is possible to derive an important property of the acoustic medium: the characteristic acoustic impedance ($z_c = \rho c$). It is real, and equal to 415 rayls for air, while complex for a porous material: the real and imaginary parts represent the characteristic resistance (i.e., energy losses) and reactance (i.e., phase changes), respectively. The sound propagation of a material can be predicted from the values of z_c and k , as well as from two other variables: the effective density (ρ_e) and the bulk modulus (K_e). The first expresses the density experienced by the acoustic waves, while the second is the ratio of the pressure applied to a material to the resultant relative change in volume. They can be related to z_c and k as follows:

$$z_c = \sqrt{K_e \rho_e} \quad (6)$$

$$k = \omega \sqrt{\frac{\rho_e}{K_e}} \quad (7)$$

For a plane wave incident to the interface between two acoustic media (being medium 1 air, characterised by k_1 and z_{c1} , and medium 2 an absorbent characterised by k_2 and z_{c2}) with an angle ψ (p_i), a reflected wave with an angle θ (p_r) and a transmitted wave with an angle ϕ (p_t) will be generated. Considering they have to satisfy the continuity of pressure (i.e., $p_r + p_i = p_t$), and applying Fermat's principle and Snell's law, a relationship between the angles can be obtained:

$$k_1 \sin(\psi) = k_2 \sin(\phi) \quad (8)$$

As the speed of sound in the absorbent is much lower than that in air, the angle of the transmitted wave will tend to zero.

In addition to α , that estimates energy variation on sound wave reflection, there are other three interrelated acoustic quantities of fundamental importance when the behaviour of absorbers is studied: surface impedance (as previously defined), admittance (β), and pressure reflection coefficient (R). Differently from α , they estimate magnitude and phase change on reflection. R and β are defined as follows:

$$R = \frac{p_r}{p_i} \quad (9)$$

$$\beta = \frac{1}{z_2} \quad (10)$$

Due to the continuity of particle velocity normal to the surface, R and z_2 can be related from the following equations:

$$R = \frac{\frac{z_2}{\rho_1 c_1} \cos(\psi) - 1}{\frac{z_2}{\rho_1 c_1} \cos(\psi) + 1} \quad (11)$$

$$\frac{z_2}{\rho_1 c_1} \cos(\psi) = \frac{1 + R}{1 - R} \quad (12)$$

Following the definition of α , it can be related with R as follows:

$$\alpha = 1 - |R|^2 \quad (13)$$

3.1.4 Evaluation of the acoustic properties

The acoustic properties of porous absorbers can be evaluated using an “impedance tube”: it consists in a controlled environment for sound waves propagation where the plane wave hypothesis can be assumed valid with negligible errors. This is obtained thanks to thick metal tube walls (i.e., high acoustic impedance), so that energy losses through the walls are minimised, with a constant cross-section and a smooth surface, so that sound attenuation due to tube material is minimised and any reflection is avoided. Sound waves in a wide spectrum of frequencies are generated by a loudspeaker placed in one end of the tube, they propagate down the tube and then interact with the sample under investigation. The result of this interactions is reflected or reflected and transmitted waves, depending on test set-up, that are captured by a set of microphones at specifically designed positions. The measurable frequency range is strictly related to the geometrical design of the tube as follows:

- The upper working frequency (f_u) is inversely proportional with tube inner diameter (d):

$$f_u \leq \frac{c}{2d} \quad (14)$$

- The lower working frequency (f_l) is instead inversely proportional with microphone spacing (s):

$$f_l \geq \frac{c}{20s} \quad (15)$$

The aim of the acoustic characterisation is to determine the Normal Incidence Sound Absorption Coefficient (α , as previously defined) and the Normal Incidence Sound Transmission Losses (STL). The so-called “transfer function method”, also described in international standards, is typically followed, where, for each of the two parameters, a specific tube set-up is required: α can be measured with a two-microphone configuration following the standard test method ASTM E1050 [117], while a four-microphone configuration following the ASTM E2611 is used for STL [118]. In a two-microphone configuration, the sample is placed in one end of the tube with a rigid back surface reflecting all soundwaves transmitted through the sample (Figure 3-3). The pressure (p) in the impedance tube can be split in two components, one related to the incident wave and one to the reflected:

$$p = A(e^{jkz} + Re^{-jkz}) \quad (16)$$

where A is a complex constant and R is the reflection coefficient. The two unknowns of the equation, namely the magnitude and phase of R , can be derived by measuring the pressure in two points (hence, two microphones in position z_1 and z_2) and applying the transfer function between the two (H_{12}):

$$H_{12} = \frac{p(z_2)}{p(z_1)} = \frac{e^{jkz_2} + Re^{-jkz_2}}{e^{jkz_1} + Re^{-jkz_1}} \quad (17)$$

The latter can be rearranged for R , so that α and also the normal incidence surface impedance (Z_s) of the sample can be calculated following equations (13) and (12), respectively:

$$R = \frac{H_{12}e^{jkz_1} - e^{jkz_2}}{e^{-jkz_2} - H_{12}e^{-jkz_1}} \quad (18)$$

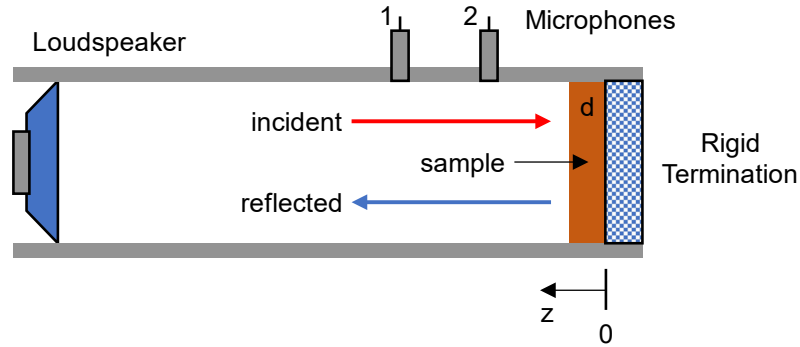


Figure 3-3 – Impedance tube in two-microphone configuration.

In a four-microphone configuration, the sample is placed between two symmetric tubes having two microphones each at symmetrical position with respect of the sample. Also, two different terminations are required: open and anechoic (Figure 3-4). Pressure and velocity on the left side can be derived from equations (19) and (20), while on the right side from (21) and (22):

$$p = Ae^{jkz} + Be^{-jkz} \quad (19)$$

$$u = \frac{1}{\rho c} (Ae^{jkz} - Be^{-jkz}) \quad (20)$$

$$p = Ce^{jkz} + De^{-jkz} \quad (21)$$

$$u = \frac{1}{\rho c} (Ce^{jkz} - De^{-jkz}) \quad (22)$$

with A , B , C , and D being the pressure amplitudes of the plane wave components in the tube (as described in Figure 3-4). They can be calculated from the following:

$$A = \frac{p(z_1)e^{-jkz_2} - p(z_2)e^{-jkz_1}}{2j \sin(k(z_1 - z_2))} \quad (23)$$

$$B = \frac{p(z_2)e^{-jkz_1} - p(z_1)e^{-jkz_2}}{2j \sin(k(z_1 - z_2))} \quad (24)$$

$$C = \frac{p(z_3)e^{-jkz_4} - p(z_4)e^{-jkz_3}}{2j \sin(k(z_3 - z_4))} \quad (25)$$

$$D = \frac{p(z_4)e^{-jkz_3} - p(z_3)e^{-jkz_4}}{2j \sin(k(z_3 - z_4))} \quad (26)$$

with $p(z_{1-4})$ being the pressures measured at the four microphones. Thanks to all the above equations, pressures and velocities on the front of the sample ($z = 0$) and on the back ($z = -d$) can be evaluated and summarised by the following transfer matrix:

$$\begin{bmatrix} p^a & p^o \\ u^a & u^o \end{bmatrix}_{z=0} = \begin{bmatrix} T_{11} & T_{12} \\ T_{21} & T_{22} \end{bmatrix} \begin{bmatrix} p^a & p^o \\ u^a & u^o \end{bmatrix}_{z=-d} \quad (27)$$

It is then clear that the four transfer matrix components, T_{11} , T_{12} , T_{22} , T_{21} , can be determined only if pressures and velocities are measured with both the anechoic (a) and open (o) terminations. The transmission loss is finally given by equation (28):

$$TL = 20 \log_{10} \left(\frac{1}{2} \left| T_{11} + \frac{T_{11}}{\rho c} + \rho c T_{21} + T_{22} \right| \right) \quad (28)$$

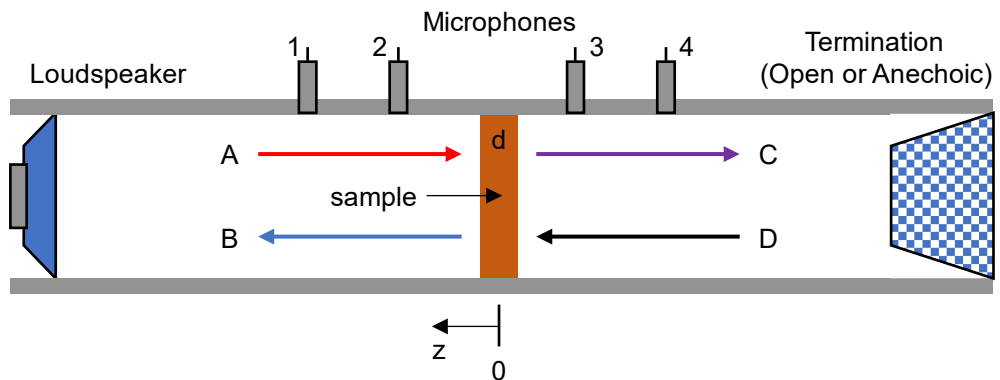


Figure 3-4 – Impedance tube in four-microphone configuration. The four pressure amplitudes of the plane wave components (A, B, C, and D) are indicated.

3.1.5 Semi-phenomenological modelling

The previously mentioned non-acoustic properties are crucial for the modelling of porous absorbers: mathematical models exploit them to estimate the surface impedance and the absorption coefficient of a given material. Particularly, models are used to relate the physical properties of the absorber to the sound propagation through it by the calculation of ρ_e and K_e . Equations (6) and (7) can then be used to determine Z_c and k , and finally of the normal incidence surface impedance (Z_s), R and α , as expressed in equations (29), (30), and (13) respectively:

$$z_s = -i z_c \cot(kd) \quad (29)$$

$$R = \frac{z_s - z_0}{z_s + z_0} \quad (30)$$

where z_0 is the acoustic impedance of air.

Several approaches can be followed for modelling, whose can be categorised in theoretical, empirical, and semi-phenomenological models. The first relies on the assumption of rigid material to apply the classical theories of sound propagation in small pores. The second relies on indirect fitting to derive the relationship between Z_c and k with σ , and are for this reason simple and effective, although they ignore the role microscopic properties of porous materials. Semi-phenomenological models overcome this limitation by the combination of both the theoretical and empirical approaches. For the purpose of this thesis, the Johnson-Champoux-Allard (JCA) model for porous materials was adopted [116, 119]. Equations (31) and (32) show the relationship between ρ_e and K_e with the non-acoustic properties of porous absorbers and physical properties of the acoustic medium:

$$\rho_e = \frac{\alpha_\infty \rho_0}{\phi} \left(1 + \frac{\sigma \phi}{i \omega \rho_0 \alpha_\infty} \sqrt{1 + \frac{4i \alpha_\infty^2 \eta \rho_0 \omega}{\sigma^2 \Lambda^2 \phi^2}} \right) \quad (31)$$

$$K_e = \frac{\gamma P_0}{\phi} \left[\gamma - (\gamma - 1) / \left(1 + \frac{8\eta}{i \Lambda'^2 N_{pr} \omega \rho_0} \sqrt{1 + \frac{i \rho_0 \omega N_{pr} \Lambda'^2}{16\eta}} \right) \right]^{-1} \quad (32)$$

where ρ_0 , η , γ , and N_{pr} are density, dynamic viscosity, ratio of the specific heat capacities, and Prandtl Number for air, respectively, while P_0 is the atmospheric pressure.

3.2 Sound insulation with Graphene-based porous absorbers

Foams are a class of porous absorbers characterised by a cellular structure, and thus with a high porosity, from which features such as low density, high surface area, and low cost of the material derives. This, specifically in the case of aerogels, allows their use for aerospace and automotive applications [120, 121]. The chemical composition is generally used to define a foam as organic, inorganic, or hybrid.

3.2.1 Organic, inorganic and hybrid foams

Organic foams are generally obtained from the polymerisation of an organic precursor in the presence of a blowing agent, with chosen reaction ingredients and parameters highly influencing the resulting cellular structure. A common example is polyurethane (PU) foam, of which Park et al. manipulated the microcellar geometry by adjusting the rheological properties during the foaming reaction [122]. Particularly, an optimised cellular openness of the 15% allowed to reach better sound absorbing performance with respect of a heavier foam (Figure 3-5). Besides PU, other resins can be used as precursors [123, 124]. Ye and co-workers recently

discussed a novel elastic urea-melamine-formaldehyde (UMF) foam exhibiting an interconnected network structure with increasing cell size and porosity for decreasing UF/MF mass ratio [125].

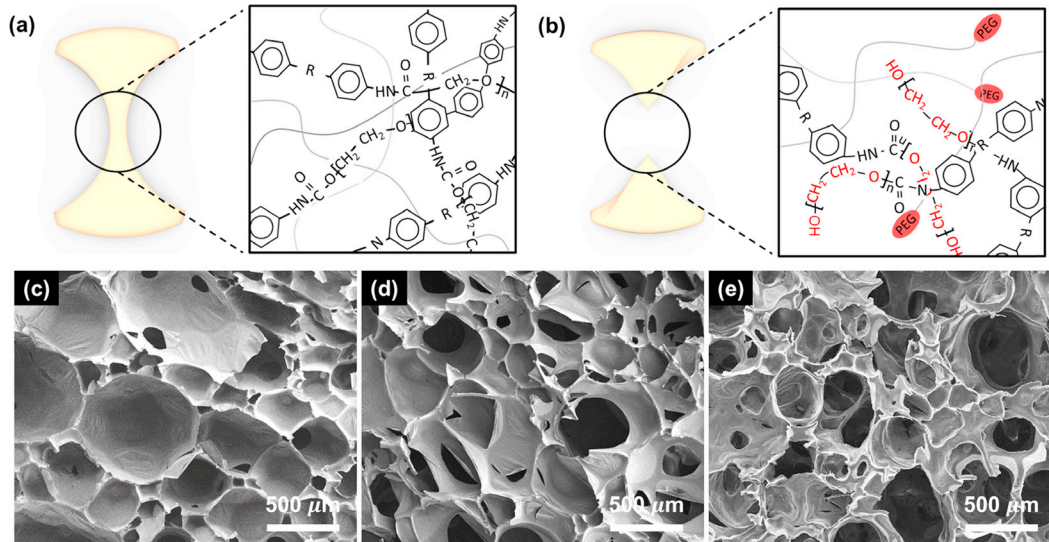


Figure 3-5 – Illustration of cell opening mechanism and SEM images of PU with different cellular structure [122].

With a completely different approach, Mosanenzadeh et al. developed a porous structure with microstructural gradation [126]. Salt (NaCl) was used as a particulate to template a Polylactide matrix, which was subsequently leached to fabricate open-cell foams. Particularly, they proved a 20% increase of the maximum sound absorption coefficient and a 9% increase of average absorbing capability when comparing the graded foam structure to the uniform one. In a similar manner, inorganic foams can also be manufactured. The inherent properties of inorganic material such as metal alloys [127], carbonaceous derivatives [128], and ceramics render them particularly suitable for harsh environments [129]. Additives such as polymer particles can be used as pore formers, and subsequently removed via the sintering process. In a recent research, the effects of processing parameters on the structure of a lightweight cellular ceramic foam were evaluated [129]. The results showed that a sample with larger pores had

superior sound absorption performance with respect of another with similar porosity but having smaller pores.

Recently, materials of different nature have been combined to obtain hybrid foams where additive compounds were used to control the cellular microstructure of polymeric matrices [112]. Statharas et al. realised a PU/PVDF/Multiwalled CNT (MWCNT) composite foam with enhanced sound absorption where the PVDF formed a separate phase in the PU scaffold, introducing interfacial damping and local piezoelectric damping effects (Figure 3-6 – a-b). MWCNT filaments, instead, facilitated the dissipation of electrical charges and consequently enhanced both the interfacial and local effects introduced from PVDF. Overall, the sound absorption coefficient had a substantial increase with respect of a conventional PU foam, by reaching 0.85 at 1,000 Hz [130]. Another example consists in the combination of cellulose nanofiber (CNF) and melamine foam (MF) to obtain a composite foam. A cyclic freezing-thawing process was used to obtain a hierarchical pore structure that enhanced the reflections and vibrations of sound waves. As a result, using an unmodified MF as comparison, sound absorption performance were enhanced of the 107% at 500 Hz and of the 80% in the 250 – 2,000 Hz range [131].

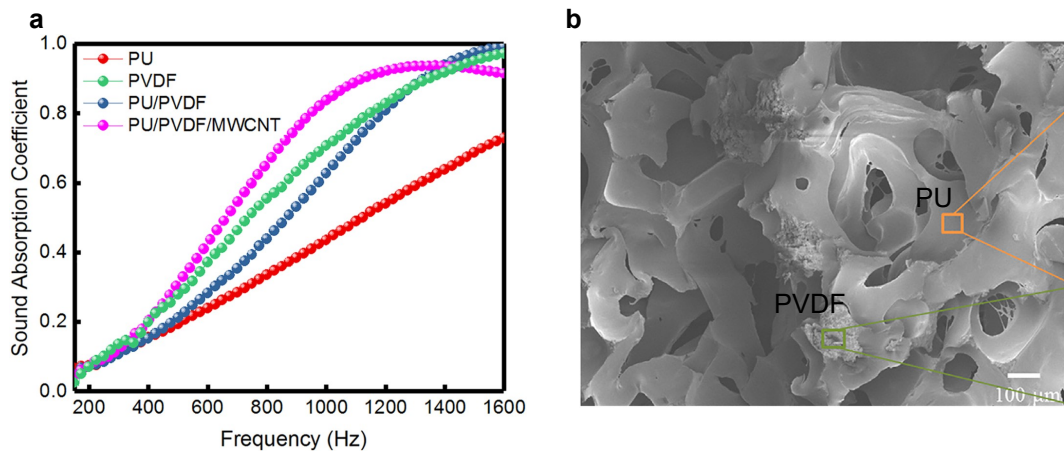


Figure 3-6 – (a) Comparison of sound absorption coefficient for different compositions of hybrid foams and **(b)** SEM image for the PU/PVDF/MWCNT foam exhibiting two immiscible phases in the material [130].

3.2.2 Graphene-based foams

Properties of graphene and derived materials, such as processability in different solvents, chemical and mechanical stability, and high surface area, can be conveniently exploited for porous sound absorptions thanks to hybrid foam fabrication approaches.

Wu et al. obtained graphene foams via CVD on a Nickel template, which was subsequently dip-coated with Polydimethylsiloxane (PDMS). The nickel template was finally etched to obtain porous hybrid foams. The sample characterised by a 51.5% of porosity showed the best sound absorption abilities, with a coefficient of 0.7 at 100 – 150 Hz. Those results were attributed to synergy of the viscoelastic damping properties of the PDMS matrix, the energy conversions from vibrational waves to heat of the graphene skeleton, and the friction induced at the graphene-PDMS interface [132].

Another method consists in the impregnation of conventional acoustic foams with GO. A melamine-supported GO foam showed an increase in flow resistivity and tortuosity, which allowed for a sound absorption

coefficient of 0.6 over 800 Hz [9]. Similarly, Li and co-workers obtained a semi-open cellular structure with small GO sheets interrupted by CNT. Thanks to the optimal non-acoustic properties, the composite foam exhibited an enhancement of the 100% and 20% over 250 – 1,600 Hz when compared to the pure MF or MF with GO only, respectively [133]. PU foam acoustic performance can as well be improved with GO impregnation, as demonstrated with the directionally antagonistic GO-PU hybrid aerogel from Oh et al. The structural orientation, obtained thanks to the freeze-drying process, increased the viscous friction and thermal conduction resulting in a broadband sound absorption coefficient of 0.6 at 1,000 Hz (Figure 3-7) [134, 135]. Furthermore, GO impregnation density can be controlled to optimise the sound absorbing properties to a specific frequency. In particular, a step-by-step vacuum assisted process aided by the evaluation of the non-acoustic properties was used to find the optimum impregnation, leading to an averaged sound absorption coefficient of 0.9 over a 800 – 6,300 Hz frequency range [136].

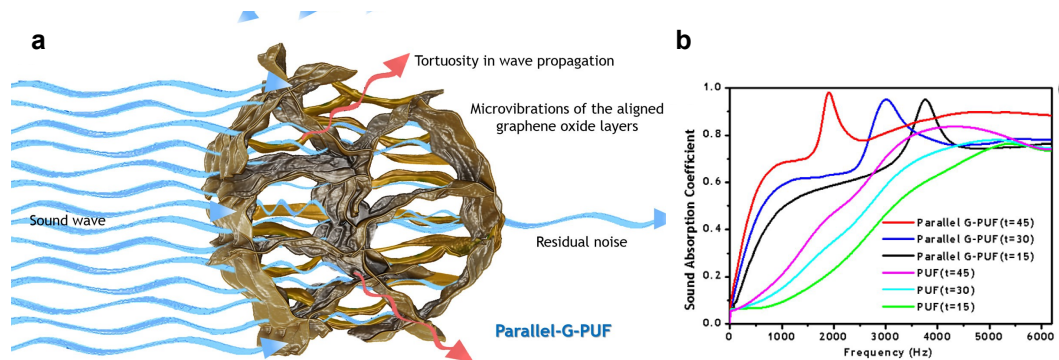


Figure 3-7 – (a) Illustration of sound absorption mechanism in directionally antagonistic graphene sound absorber and **(b)** absorption coefficient for different thicknesses [134].

Pinto et al., fabricated a hybrid structure with PU functionalised by either GO or graphene and aluminium open-cell (Al-OC) foam. The foam with a loading of 2.5 wt% GO showed the best sound absorption between 1,250 and 1,750 Hz, which was explained with an increased ability of foam cells to stretch, bend and buckle without deformation [137]. Porous ceramics

acoustic performance can also be enhanced by graphene-derived material, as showed with a coating of GO and styrene-butadiene rubber film. Particularly, the composite film improved the thermal viscous effect and extended the dissipation mechanism, allowing to reach a sound absorption coefficient of 0.3 in the range of 200 – 800 Hz and an enhancement of the average value within 500 – 2,000 Hz of 15.4% [138]. A rare example of carbon-only foam is found in the bubbled graphene monolith described by Lu et al., where a light material was obtained thanks to the use of a surfactant as bubbling agent and freeze-drying followed by thermal annealing as templating process. A normalised sound absorption coefficient of 0.9 was obtained within a range of 800 – 6,300 Hz, exploiting the high thermal conductivity of graphene and graphene bubbles walls vibration (Figure 3-8) [139].

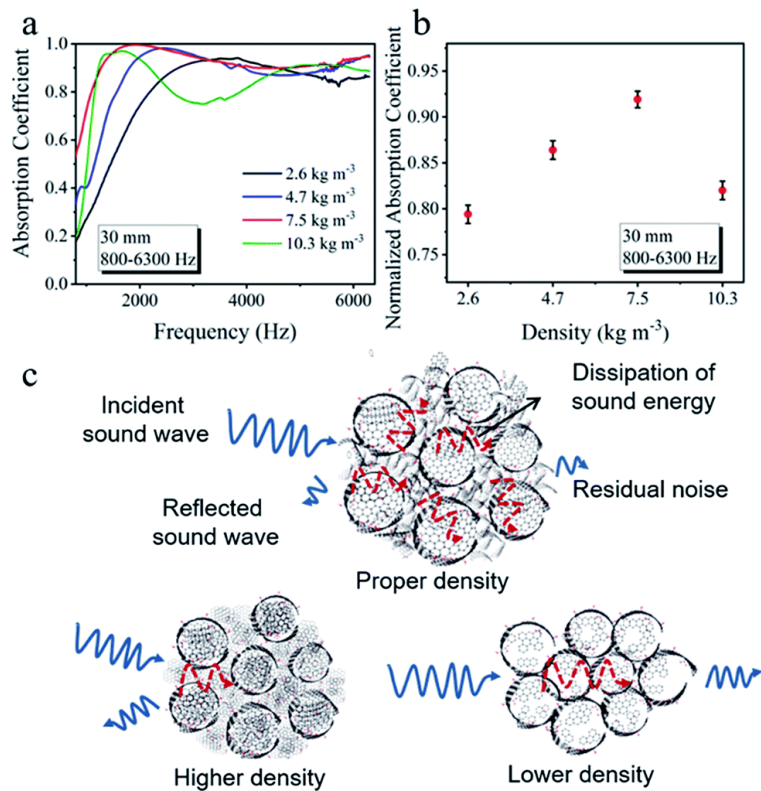


Figure 3-8 – Acoustic absorption performances and absorption mechanism for bubbled graphene monoliths manufactured with different densities [139].

In the presented research works, graphene role is only marginal and mostly related to the enhancement of sound absorption abilities of a main matrix, such as PDMS, MF, PU, Al-OC, and ceramics, through a modification of their non-acoustic properties. Although such enhancements are undoubtedly promising and could lead to technological improvement in the acoustic field, the use of graphene-derived materials as the main sound absorbing material was rarely discussed. This leaves room for novel developments in the field, with the aim to exploit more environmentally friendly processes, a better tunability of the material for specific applications and a more limited bulkiness of the resulting acoustic structure.

Chapter 4

Supercapacitors

4.1 Technological background

4.1.1 History and basic principles of capacitors

The first example of an electrical energy storage device, nowadays called “capacitor”, is the Leyden jar, and is dated to the eighteenth century. Although it immediately allowed the first experiments on capacitors, it was only in the nineteenth century that Helmholtz described the phenomenon of the double-layer capacitance and successfully applied Faraday’s law to explain the electrical charge storage [140]. The first practical application of this principle was demonstrated and patented by Becker in 1957 [141]: the patent described a device made of two porous carbon electrodes

submerged in an aqueous electrolyte with the development of an Electrical Double Layer (EDL) at the interface. Nine years later the Standard Oil Company, Cleveland, Ohio (SOHIO) applied the same concept but using a non-aqueous electrolyte with an operating voltage up to 4 V [142], outreaching Becker's capacitor limit of 1 V and laying the foundations for the development of moderns "Electrochemical Supercapacitors" (SCs). The name "Supercapacitor" is credited to the Nippon Electric Company (NEC) which, under SOHIO license, in 1971 marketed the first commercially successful SCs as low-power devices for power-supply backup of computer memories [143].

A capacitor is made of two conducting plates, called "electrodes", separated by an insulating material, called "dielectric". When an electric potential difference, (E), is applied between the two electrodes, opposite charges accumulate electrostatically on the surface of the conductive plates (Figure 4-2 – a). The ability of the system to store these charges, the capacitance (C), is defined as the ratio between the stored charges (Q) and the applied E :

$$C = \frac{Q}{E} \quad (33)$$

The unit of measure is the Farad (F): a capacitor with a capacitance of 1 F stores 1 Coulomb of charge with a potential difference of 1 Volt between the electrodes. For easiness of comparison, the capacitance is often normalized with respect to the mass (m), volume (v) or surface (a) of the electrodes or of the whole device, giving the Gravimetric (C_m), Volumetric (C_v) or Areal Capacitance (C_a), respectively:

$$C_m = \frac{C}{m} ; C_v = \frac{C}{v} ; C_a = \frac{C}{a} \quad (34)$$

In the case of an ideal parallel plate capacitor, C can be calculated as follows:

$$C = \varepsilon_0 \varepsilon_r \frac{A}{d} \quad (35)$$

where ε_0 is the permittivity of free space (equal to $8.85 \times 10^{-12} \text{ F}\cdot\text{m}^{-1}$), ε_r is the dielectric constant of the separating material, A is the surface area of the electrodes and d is the distance between them.

The performances of energy storage devices are commonly evaluated by their Energy (U), in Watt-hour (Wh) and Power (P) in Watt (W). While the first measures the amount of energy that can be stored, the second specify how quickly this energy can be delivered. In capacitors, they can be calculated from the following equations:

$$U = \frac{1}{2} CE^2 \quad (36)$$

$$P = \frac{E^2}{4 ESR} \quad (37)$$

where ESR is the “Equivalent Series Resistance”. These quantities are also usually normalized by the weight of the electrodes or of the whole device, obtaining the Specific Energy, in $W\cdot h\cdot kg^{-1}$, and the Specific Power, in $W\cdot kg^{-1}$. “Ragone plots” of Specific Power versus Specific Energy are a powerful tool for performance comparison between different electrical energy storage devices [144]. Figure 4-1 as example shows how SCs fill the gap between capacitors, characterized by high specific power but low specific energy, and batteries, with high specific energy but low specific power [145].

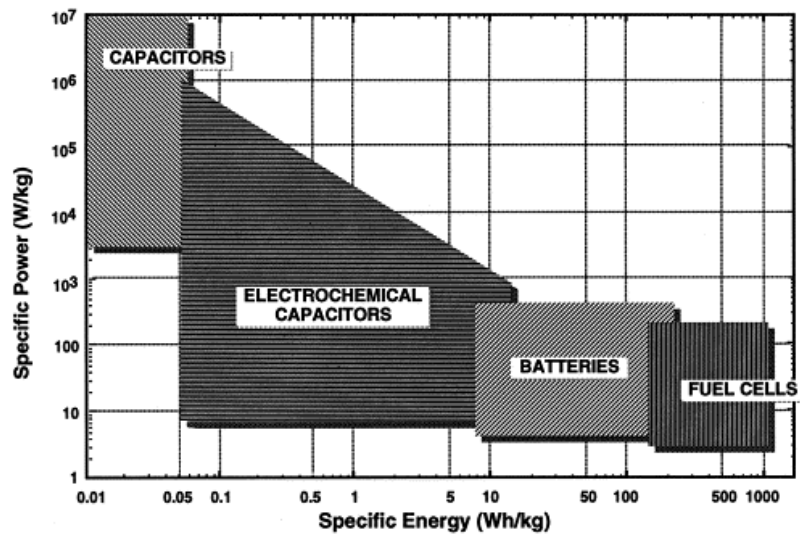


Figure 4-1 – Sketch of Ragone plot for various energy storage and conversion devices. The indicated areas are rough guide lines [145].

The *ESR* gathers the resistances of all the internal components of the device. It represents the main contribution to energy losses during charging and discharging and is crucial in power performance evaluation as it restricts the charge/discharge rate. Other important parameters for performance evaluation are the following:

- *Cycle life* – number of complete charge/discharge cycles that the device is able to support before its capacity falls under the 80% of the starting one, it highly depends on the reversibility of the mechanisms involved during the process.
- *Charge/discharge time* – time necessary to complete a full charge/discharge of the device, it depends on the time constant (τ) of the device:

$$\tau = ESR * C \quad (38)$$

- *Energy efficiency* – ratio of discharge to charge energies, it depends on the applied current, *ESR*, temperature, age of the device.

4.1.2 Supercapacitors

Depending on the mechanism of electrical energy storage, it is possible to distinguish three different classes of supercapacitors: Electrochemical Double-Layer Capacitors (EDLCs), where the energy is stored electrostatically and there are no Faradaic reactions involved; Pseudocapacitors, involving rapid and reversible Faradaic reactions; and Hybrid Capacitors, that are a combination of the previous two. For the scope of this research work, particular focus is given to EDLCs.

The working principle of EDLCs is similar to parallel plate capacitors, with the main difference being in their constituent: the electrodes are made of a conductive substrate, called “current collector,” and of a porous material, called “active material”, adhered on it; the dielectric is substituted with an electrolyte that soaks the active material and with a semi-permeable membrane, called “separator” (Figure 4-2 – b). The role of the current collector is to provide support to the active material and collect and transport electrons to/from it during the charge/discharge process. The electrolyte provides instead the ions, that are the charge carriers diffusing between the two electrodes. The separator electrically separates the electrodes preventing short circuit but allowing ions to diffuse from one electrode to the other. Due to these changes, the capacitance of SCs is much higher, increased by a factor of 10,000 or more, than that of common electric capacitors [146]. Looking at equation (35), this extreme increase derives from two main contributions:

- The area A of the electrodes is extended thanks to active materials characterised by a high Specific Surface Area (SSA), that in the case of porous carbons can reach values of over $2,000 \text{ m}^2 \text{ g}^{-1}$ [147].

- The electrical charges accumulate at the interface between the electrode and the electrolyte forming the EDL, with electrons at the electrode side and cations or anions at the electrolyte side of the interface (Figure 4-2 – c) [146]. The thickness of the double layer is in the order of few Angstroms, thus dramatically reducing the distance between the electrodes (the thickness of common dielectrics in electric capacitors is in the order of Microns) [146].

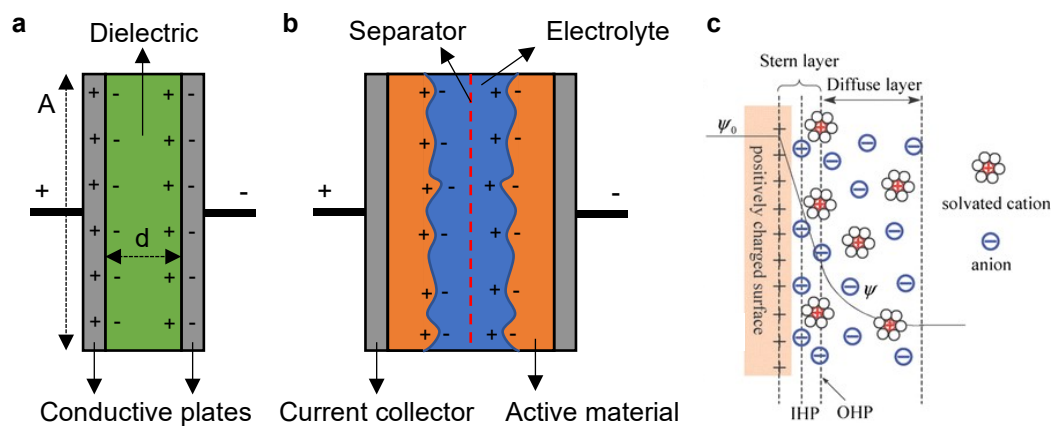


Figure 4-2 – Schematic representation of (a) conventional capacitor and (b) Electrical Double Layer capacitor (EDLC). (c) Example of EDL [148].

Due to the development of an EDL per electrode-electrolyte interface, when the electrochemical properties of the whole device are evaluated with a two-electrode configuration (as it will later be discussed), the two EDLs actually behave as two capacitors in series (C_1 and C_2). The total capacitance (C_{tot}) should then be calculated as follows:

$$C_{tot} = \frac{1}{\frac{1}{C_1} + \frac{1}{C_2}} = \frac{C_1 C_2}{C_1 + C_2} \quad (39)$$

Another important feature of EDLCs is that, since only non-Faradaic mechanism are involved, they can theoretically be charged and discharged any number of times, determining a high cycle life: up to 1×10^6 cycles of charge/discharge can be performed retaining a capacitance of the 80% with

respect of the initial state, three order of magnitudes more than batteries [149].

Since their first use in Becker's "low voltage electrolytic capacitor" [141], porous carbon materials, thanks to their high SSA, high chemical stability, good electrical conduction, and low cost are used in state of the art SCs. There are many forms of such materials, being Activated Carbon (ACs) [150, 151] the most commonly used for commercial applications while Carbon Aerogels (CAs) [152], Carbon Onions (CNOs) [153, 154], Carbon Nanotubes (CNTs) [155], Graphene and Graphene-derived [156, 157] are the most commonly evaluated for future improvements [156, 158, 159]. The main goal is to increase the specific energy but maintaining the characteristic high specific power and high cycle life: the first two are in the order of $\sim 10 \text{ Wh kg}^{-1}$ and $\sim 10 \text{ kW kg}^{-1}$, respectively, for state of the art supercapacitors [160]. The stored energy is much smaller than that of batteries but the power is at least two order of magnitudes higher ($\sim 200 \text{ Wh kg}^{-1}$ and $\sim 300 \text{ W kg}^{-1}$ for Lithium-Ion batteries [161]). Equation (36) shows that the energy can be increased acting on both the capacitance and the voltage, with a quadratic factor for the latter. According to equation (35), the capacitance increases proportionally with the SSA. It must be noted however that also the pore size and pore-size distribution, together with the wettability of the electrolyte on the active material, play a crucial role [146]. According to IUPAC, pores can be classified, depending on their sizes, in three groups: micropores ($< 2 \text{ nm}$); mesopores ($2 \text{ to } 50 \text{ nm}$) and macropores ($> 50 \text{ nm}$). Due to diffusion kinetic, while micropores lead to a larger surface area, bigger micropores and smaller mesopores, with size in the order of $1\text{-}2 \text{ nm}$, give most of the contribution to double layer capacitance [162, 163]. The voltage depends principally on the electrochemical stability of the used electrolyte. Table 4-1 shows some examples of porous carbons having

different SSA and assembled in cell using different electrolyte, with the resulting gravimetric capacitance.

Table 4-1 – Examples of different porous carbons used for supercapacitors manufacturing.

Porous Carbon	SSA [m² g⁻¹]	C_g [F g⁻¹]	Ref.
AC	~2,000	~100	[153]
CA	~2,400	~120	[152]
CNO	~800	~110	[154]
CNT	~100-500	~50-100	[155]
<i>Graphene based</i>	~1,500-3,000	~150-300	[156, 157]

Three different kinds of electrolytes can be distinguished: aqueous, with Sulphuric Acid (H₂SO₄), Phosphoric Acid (H₃PO₄), Potassium Hydroxide (KOH), and Sodium Sulphate (Na₂SO₄), among others, dissolved in water as ions providers; organic, with Tetraethylammonium Tetrafluoroborate (TEA-TFB) or Tetramethylammonium (TEMA)-TFB, among others, usually dissolved in Acetonitrile (ACN) or Propylene Carbonate (PC); and Ionic Liquids, with 1-Ethyl-3-methylimidazolium-TFB (EMIM-TFB) as example. Aqueous electrolytes are characterized by a limited operative voltage window of ±0.9-1.0 V, due to H₂ and O₂ evolution reactions [164], but they also have a high ion conductivity that is converted in a low *ESR*. Organic electrolytes are stable to higher voltage, up to 3.5 V, but they have a lower conductivity and volatility, and are also affected by toxicity, flammability and cost issues. Ionic liquids are also stable at high voltage, up to 3.5-4 V, and have a high ionic conductivity, without the environmental and safety issues that concerns organic electrolytes. Their application in SC is however still in the early stages and issues like wettability, polarization and temperature dependence of the viscosity are under investigation [162, 165]. With the aim to develop all-solid-state, flexible and leak-free SCs, a new class of electrolytes is lately being developed: gelled electrolytes. They consist in “a

mixture of solid polymers and liquid electrolytes that are formulated with the goal to obtain the mechanical properties of the solid polymer while retaining the ionic conductivity of the liquid electrolyte” (Mauger et al., 2017) [166]. The use of Polyvinyl Alcohol (PVA) with a H_3PO_4 or H_2SO_4 aqueous solution is one of the most common examples [75, 167], but also organic or ionic liquid based gel can be realized [168, 169].

For SCs electrodes fabrication, active materials are usually mixed with binders and conductive agents, such as CBs, to obtain a mixture, called “slurry”, which can be easily spread on current collectors’ surface to achieve a uniform and robust coating. Binders are typically non-conductive fluoropolymers, such as Polytetrafluoroethylene (PTFE) and Polyvinylidene Fluoride (PVDF), that require organic solvents such as NMP and ACN to be effectively dispersed. They have the fundamental role of providing cohesion between active material particles and any conductive additive, as well as their adhesion onto the current collector [170].

4.1.3 Evaluation of the electrochemical properties

Electrochemical properties of SCs can be evaluated using electrochemical workstations. These instruments are capable to operate in two basic modes: potentiostatic or galvanostatic. In the first case, the voltage difference between a Working Electrode (WE) and a Reference Electrode (RE) is controlled by regulating the current through a Counter Electrode (CE). In the second case, instead, the current is controlled by adjusting the voltage. Two different electrodes configuration may be used:

- *Three-electrode* – one EDLC electrode is connected to the WE lead of the electrochemical workstation, a reference electrode able to maintain a stable and constant potential during testing is connected to the RE lead, and an electrode capable to withstand large enough currents is connected to the CE lead.

- *Two-electrode* – the WE lead is connected to one electrode of the device under test, while the RE and CE leads are connected, together, to the other electrode.

Although the three-electrode configuration allows to accurately investigate the chemistry of the active material and the applicable potential window, it is not reliable for capacitance and resistance measurements. For this reason, the two-electrode configuration is generally recognised as the best way to evaluate the overall performances of EDLCs [146].

The aim of the electrochemical characterisation is to determine the three basic parameters, namely C , working potential window, and ESR , from which E and P can then be calculated following equation (37) and (38). For this purpose, two techniques are mostly exploited: Cyclic Voltammetries (CVs) and Galvanostatic Charge-Discharge Cycles (GCDs). The CV consists in the application of a linearly varying potential (E ; i.e., potential sweep) between two fixed extremes ($\Delta E = E_2 - E_1$; i.e., potential window) with a set speed of variation (ν ; i.e., sweep rate). The current response (i) is measured and plotted with respect of E , obtaining the “voltammogram”. Considering equation (33), C is obtained calculating Q from the absolute area inscribed by the voltammogram and dividing it by ΔE :

$$C = \frac{\int_{E_1}^{E_2} i(E) dE}{2\nu\Delta E} \quad (40)$$

In GCDs a constant current (i) is applied with simultaneous recording of the potential (E) response. In a first step, a positive i_c allows the charging of the cell under test; once a set voltage (E_c) is reached or a defined charging time (t_c) elapsed, the current is inverted (i_d) allowing the discharge until a set voltage (E_d) is reached or a defined discharging time (t_d) elapsed. A drop of potential, (E_{drop} ; i.e., iR drop), due to the ESR of the device, in the

instant the current is inverted is usually observed. Considering equation (33), C can be calculated from the following:

$$C = \frac{i \Delta t}{\Delta E} \quad (41)$$

where $\Delta t = t_c - t_d$ is the time required for the discharge and ΔE is the potential difference between the charged point, after the iR drop, and the discharged point ($\Delta E = E_c - E_{drop} - E_d$). The ESR is instead determined as follows:

$$ESR = \frac{E_{drop}}{\Delta i} \quad (42)$$

where $\Delta i = i_c - i_d$ is the current inversion. It is worth highlighting that in two-electrode configuration, the calculated C with the two as-described techniques is that of the whole device. When novel active materials are studied and compared with the state-of-the-art or results from other works available in literature, it is general practice to refer to the gravimetric specific capacitance (C_m) of the active material on one electrode; according to equation (34) and (39), C_m can be derived from C :

$$C_m = \frac{4 C}{m} \quad (43)$$

where m is the total mass of the active material in both electrodes. GCDs are also used to estimate the cycle life of a device, by evaluating the trend of C for a certain number of continuously repeated charge-discharge cycles.

Another characterisation technique performable with electrochemical workstations is the Electrochemical Impedance Spectroscopy (EIS). It allows to study the in-depth electrochemical behaviour of assembled cells and to create equivalent circuit models (i.e., a combination of basic elements such as capacitors, resistors and inductors, or more complex elements such as the so-called “Warburg”). In EIS, when the instrument is

operated in potentiostatic mode, the system is perturbed with an alternating voltage of small amplitude ($E(t)$), usually 5 or 10 mV, over a wide frequency (f) range, usually 10 mHz to 100 kHz, and the current response ($i(t)$) measured. Both can be expressed as follows:

$$E(t) = E_0 \sin \omega t \quad (44)$$

$$i(t) = i_0 \sin(\omega t + \phi) \quad (45)$$

where E_0 and i_0 are voltage and current amplitude, respectively, $\omega = 2\pi f$ is the angular frequency, and ϕ is the phase angle (i.e., the shift of current response with respect of excitation potential). The impedance (Z) is the ratio of voltage versus current and it is commonly represented in complex numbers notation:

$$Z(\omega) = \frac{E_0 \sin \omega t}{i_0 \sin(\omega t + \phi)} = Z'(\omega) - jZ''(\omega) \quad (46)$$

where Z' and Z'' are the real and imaginary parts, respectively. Results are generally presented in BODE plots (i.e., impedance magnitude ($|Z(\omega)|$) and ϕ versus $\log f$) and Nyquist plots (i.e., $-Z''$ versus Z').

4.2 Details on the model of the used electrochemical workstation, electrodes configuration, and testing parameters are provided in each of the two proposed research studies regarding SCs development. Improving supercapacitors technology with Graphene

Due the inherent properties of Graphene and derived compounds, such as chemical stability, electrical conductivity, surface area and mechanical strength, and thanks also to synthesis processes in continuous development, graphene-based materials are very promising for the development of next-generation supercapacitors [157]. A single layer of

pristine graphene, in particular, has a theoretical SSA of $2,675 \text{ m}^2 \text{ g}^{-1}$ and a specific capacitance of $\sim 550 \text{ F g}^{-1}$ [171]. Although such high values are hardly reached from fabricated electrodes, due to graphene layers aggregation and the introduction of defects and impurities caused by the required processing techniques, researchers keep exploring various approaches to exploit the maximum potential from graphene-based materials.

4.2.1 Chemically and thermally reduced GO

In their seminal work published in 2008, Ruoff and co-workers were the first to present a graphene-based supercapacitor [8]. They assembled the electrodes using rGO obtained from hydrazine reduction as active material and PTFE as binder, achieving specific capacitances of 135 and 99 F g^{-1} in aqueous (KOH) and organic (TEA-BF₄/ACN) electrolytes, respectively (Figure 4-3 – a). It is worth noting that such high electrochemical performances were achieved despite the partial agglomerations of graphene layers that led to a relatively moderate SSA of $705 \text{ m}^2 \text{ g}^{-1}$ (Figure 4-3 – b). Nowadays, the number of research studies regarding graphene-based material for supercapacitors have grown, and keep growing, exponentially, exploring different methods to reduce GO and by templating it in different assemblies [172]. Ramachandran et al. reported a specific capacitance of 265 F g^{-1} in an aqueous KCl electrolyte by using NaBH₄ as reducing agent [173], which led to a less severe restacking of graphene layers and thus an enhanced ion transport and diffusion. Other research groups tried greener alternative to limit the use of toxic and expensive agents. As example, sodium carbonate (Na₂CO₃) was effectively used by Jin et al. obtaining a specific capacitance of 228 F g^{-1} in KOH [174]. They confirmed Na₂CO₃ ability to eliminate oxygen containing groups and the formation of only few layers, around 10, graphene sheets.

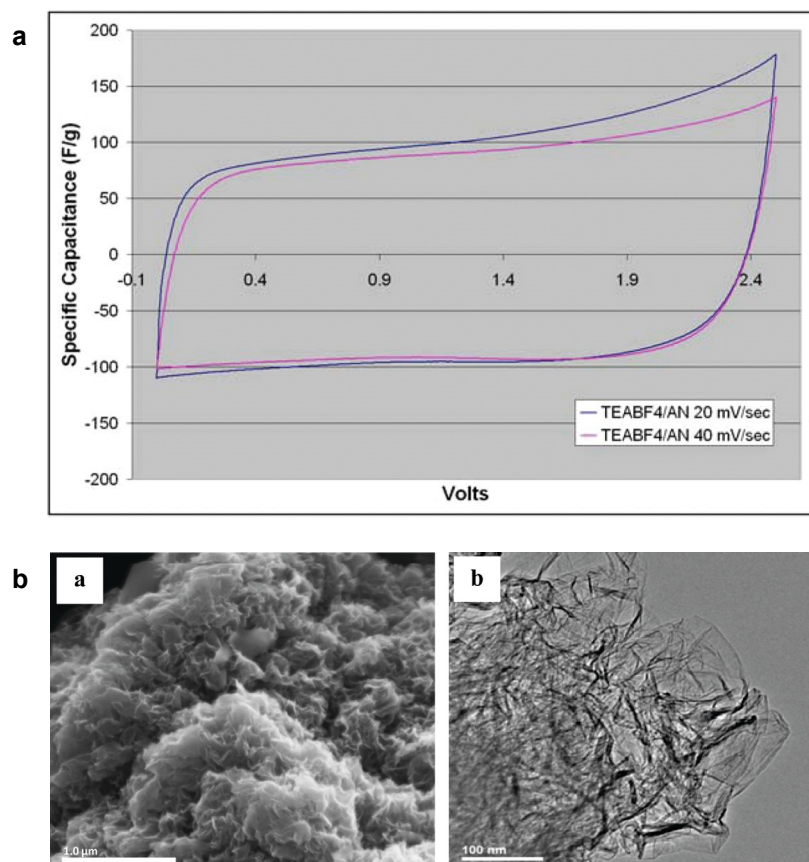


Figure 4-3 – (a) CV of of rGO with TEA-BF₄ in AN electrolyte. **(b)** SEM and TEM imaging of rGO [8].

Toxicity issues are inherently absent in the case of thermal reduction, which proved to be as effective as hydrazine for supercapacitors application. In particular, Vivekchand et al. obtained a specific capacitance of 117 F g⁻¹ in H₂SO₄ from rGO synthesised at 1,050 °C, which was characterised by only 3-6 graphene layers and a SSA of 925 m² g⁻¹ [175]. The high temperature, however, can limit practical applications in industry; this inspired Lv et al. for a vacuum promoted low-temperature exfoliation, at 200 °C, that led to specific capacitances of 264 and 122 F g⁻¹ in aqueous (KOH) and organic electrolytes (MeEt₃N-BF₄/ACN), respectively [176]. These values are interestingly high if related to the relatively low SSA of 368 m² g⁻¹, behaviour that was justified with an optimised aggregation of graphene layers due to the reduction in vacuum. Although methods for the

low-temperature reduction of dry powders are appealing, in solution methods may still be favourable for large scale productions, and thus researchers attempted to exploit the benefits of both. Several solvothermal approaches were developed, as the one-step synthesis in water in in Sci et al. work, or in Zhu et al. exfoliation and subsequent reduction in Propylene Carbonate (PC), with the assembled SCs exhibiting 139 (in KOH aqueous electrolyte) and 120 F g⁻¹ (in TEA-BF₄/PC organic electrolyte), respectively [52, 177]. In the latter, the solvothermal approach prevented the precipitation in PC solvent of the rGO, which was characterised by 2-10 graphene layers, thus facilitating the following steps for electrodes fabrication.

Microwave irradiation, being a convenient and rapid heating source, was likewise exploited as a potential route for large-scale synthesis of rGO to be used as active material in EDLC electrodes. It was initially adopted as an aid in chemical reduction [178] and then by direct heating dry powders. With the latter, Zhu et al. synthesised “worm-like” and only few-layer thick graphene sheets with a SSA of 463 m² g⁻¹. The resulting specific capacitance was of 191 F g⁻¹ using KOH electrolyte [59]. The same research group later demonstrated the benefits of graphene activation by mixing the microwave exfoliated GO with KOH and heating at 800 °C in inert atmosphere. The high specific capacitance of 166 F g⁻¹ in BMIM-BF₄/ACN electrolyte was achieved [179]. The activation process was found to be responsible for a continuous 3D network with curved and atom-thick walls forming a balanced distribution of micro and meso pores, thus leading to the large SSA of up to 3,100 m² g⁻¹.

Another method to overcome the issue of a generally limited SSA in graphene-based materials consists in the use of intercalation compounds that prevent the agglomeration of graphene layers (Figure 4-4 – a) [180]. Si

and Samulski demonstrated the ability of Platinum nanoparticles to adhere on graphene layers and behave as spacers [181]. The SSA was 20 times larger than commonly dried graphene (from 44 to 862 m² g⁻¹) and led to a specific capacitance of 269 F g⁻¹ in H₂SO₄ electrolyte. Zhang et al. evaluated the effects of different surfactants on graphene layers agglomeration during hydrazine reduction [182]; tetrabutylammonium hydroxide (TBAOH) was found to be the most effective yielding to the specific capacitance of 194 F g⁻¹ in H₂SO₄ electrolyte, thanks also to the enhanced wettability of graphene surface. Other promising materials to be used as spacers are other nano/micro/meso-porous carbons such as Carbon Nanotubes (CNTs), CBs, and mesoporous carbon spheres [183-185]. In Yan et al. work, CB particles inhibited the agglomeration of graphene layers and improved both electrolyte-electrode accessibility and electrode conductivity, leading to the specific capacitance of 175 F g⁻¹ in KOH (from 123 F g⁻¹ of the un-spaced graphene) (Figure 4-4) [184].

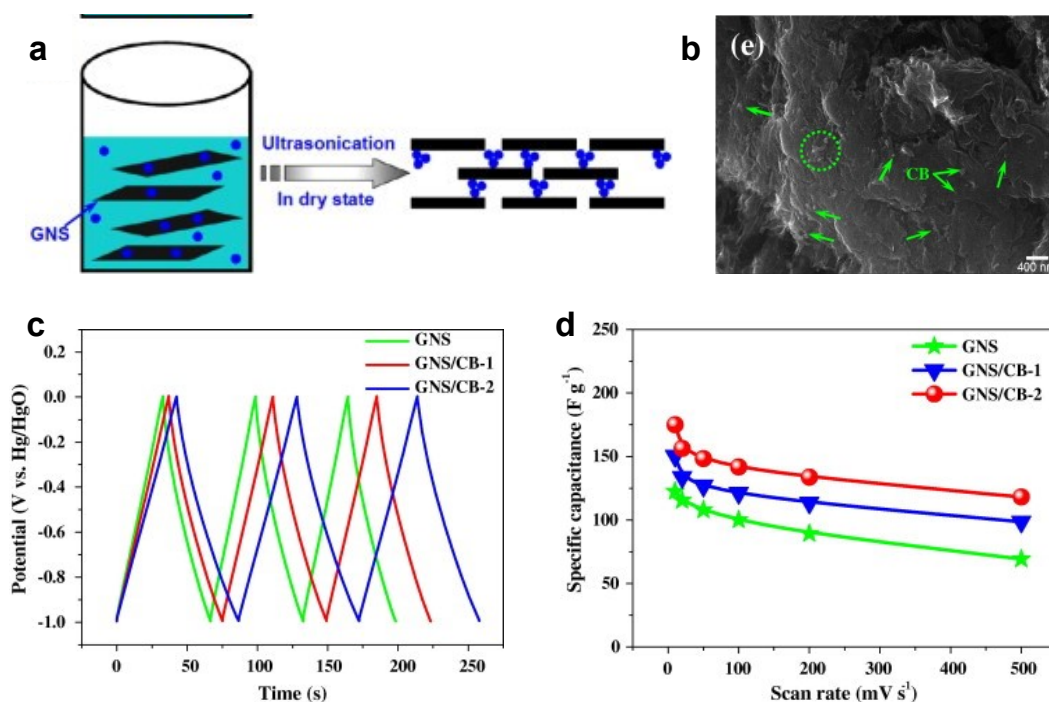


Figure 4-4 – (a) Schematic illustration of graphene synthesis with CB as intercalating compounds. (b) SEM image showing CB particles on graphene surface. (c) GCD and (d) corresponding trend of specific capacitance for graphene/CB composite, compared with pure graphene [184].

4.2.2 Binder-free electrodes from templated structures

As discussed in the previous chapters, another intriguing feature of graphene-based materials, particularly in those derived from GO aqueous dispersions, is their ability to be templated as free-standing (i.e., not needing mechanical and electrical support of current collectors) and multi-dimensional structures, such as fibres and ribbons (1D) [186], films and yarns (2D) [75], expanded films, and aerogels (3D) [187, 188]. This inspired researchers to fabricate binder-free electrodes that overcome the issues related with the use of binders, as well as innovative devices such as flexible and/or microscale SCs [189, 190]. For this purpose, hybrid structures derived from the combination of graphene with electrically conducting polymers, were also considered [191]. It is worth noting, however, that due to the inherent properties of conductive polymers, a pseudocapacitive behaviour may also be introduced. Gao and co-workers used AA to reduce

a GO/CNT mixture solution in proper moulds to obtain composite fibres, then they introduced polypyrrole (PPy) to improve electrochemical performances and stretchable PU as structural support and self-healing agent [192]. The reported volumetric capacitance is of 25.9 F cm^{-3} with a $\text{H}_3\text{PO}_4/\text{PVA}$ gel electrolyte. Electrochemical performances of the device were unaffected by its stretching at up to 300% the original length and capable to resist to three cutting/healing cycles while retaining the 54% of the initial capacitance.

With a ground-breaking work, El-Kady et al. demonstrated the possibility to produce flexible and mechanically robust EDLC interdigitated electrodes by direct laser reduction of thin GO film (Figure 4-5 – a) [75]. The as obtained laser-scribed graphene possess the high SSA of $1520 \text{ m}^2 \text{ g}^{-1}$ thanks to the simultaneous reduction and exfoliation of GO sheets that prevents the agglomeration of graphene sheets; the generated open network yields to a specific capacitance of 202, 265, and 276 F g^{-1} in aqueous (H_3PO_4), organic ($\text{TEA-BF}_4/\text{ACN}$), or ionic liquid (EMIM-BF_4) electrolytes. They also assembled an all-solid-state device by using a $\text{H}_3\text{PO}_4/\text{PVA}$ gel electrolyte that retains about the 95% of the initial capacitance after 1,000 bending cycles (Figure 4-5 – b). In another approach exploiting free-standing GO films, Niu et al. prepared rGO foams with a “leavening strategy” involving hydrazine vapor [188]. The generated open porous network, made of graphene layers with cross-links preventing their restacking, possessed a specific capacitance of 110 F g^{-1} in aqueous (H_2SO_4) electrolyte, much higher than the 17 F g^{-1} reported for compact rGO films, and the capability to withstand bending while maintaining almost unvaried electrochemical performances.

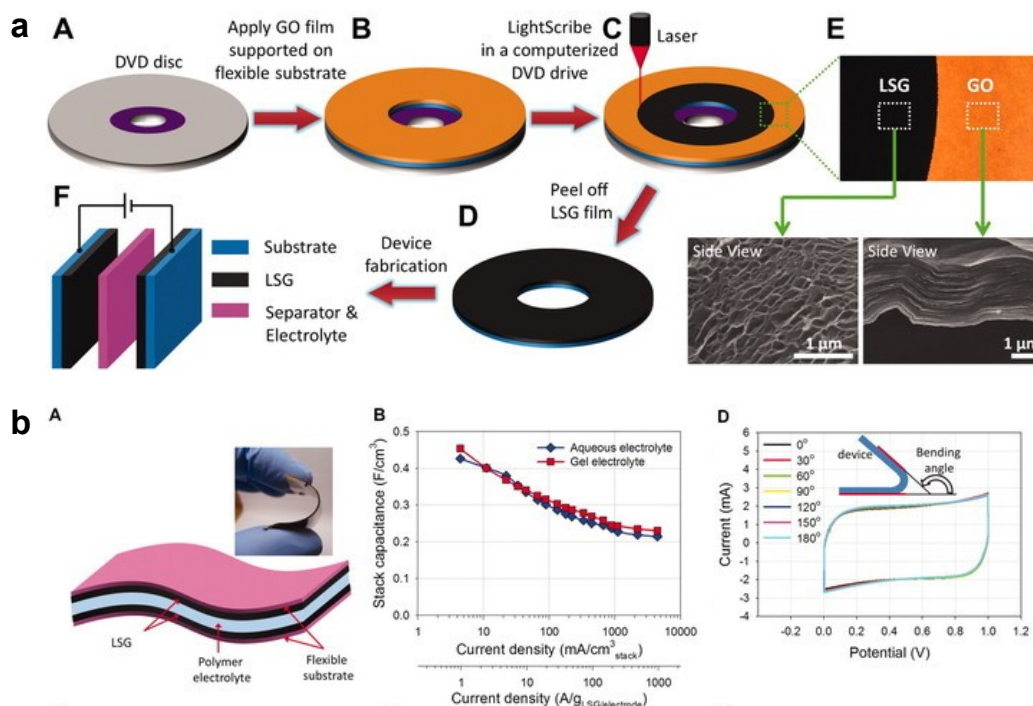


Figure 4-5 – (a) Schematic illustration of supercapacitor fabrication from direct laser reduction of GO. SEM images shows the exfoliation from GO to rGO. **(b)** Design and electrochemical performance of the all-solid-state device [75].

Along with films, aerogels attracted a lot of interest for the fabrication of free-standing SC electrodes with high specific capacitance, exploiting the inherent low weight of such assemblies. Zang et al. adopted a solvothermal method in an optimised Ethylene glycol and water system to synthesise holey graphene sheets with nanopores of 1.5-5 nm. Such sheets served as building blocks for aerogels having a SSA of 528 m² g⁻¹ and showing a specific capacitance of 178 F g⁻¹ in KOH aqueous electrolyte [193]. With a similar approach but using AA as reducing agent, Chong and co-workers optimised the graphene sheets size and stacking by acting on sonication time; the as-formed aerogel showed a relatively low SSA of 190 m² g⁻¹ but were yet capable to deliver enhanced electrochemical properties, as demonstrated by the specific capacitance of 182 F g⁻¹ with KOH aqueous electrolyte [194]. In a recent study, Wang et al. assembled binder-free and compact SCs from a room-temperature assembly of 3D porous graphene

frameworks, where they exploited polyoxometalates (POM) as cross-linker and hydrazine as reductant [195]. The final mechanically flexible, electrically conducting, and compact films were directly used as densely stacked SC electrodes, achieving a specific capacitance of 205 and 157 F g⁻¹ in H₂SO₄ aqueous and PVA gel electrolytes, respectively. It is worth noting, however, that the electrochemical performances were enhanced by the pseudocapacitive contribution of POM.

4.2.3 Binder-free electrodes from carbonaceous nanocomposite

Although all the previously mentioned studies described the possibility to manufacture binder-free and/or flexible devices characterised by a high specific capacitance, it is important to observe that complex manufacturing techniques involving multi-step procedures and/or hazardous chemicals were often required. In larger-scale manufacturing processes, this would represent issues in terms of both actual feasibility and costs, as well as in terms of environmental impact. The potential use of pseudocapacitive materials was also briefly mentioned, and although the great benefits in terms of energy storage capabilities, the use of such materials would limit the cycle life of the devices [196]. For the above reasons, a different and novel approach consist in the manufacturing of carbonaceous nanocomposite where graphene-based materials act as “active binders” when mixed with porous carbons (Figure 4-6) [197-200]. In other words, in such embodiments graphene-based materials would simultaneously provide cohesion between active material particles, their adhesion onto current collectors and would also actively participate, by enhancing them, in electrochemical processes [201].

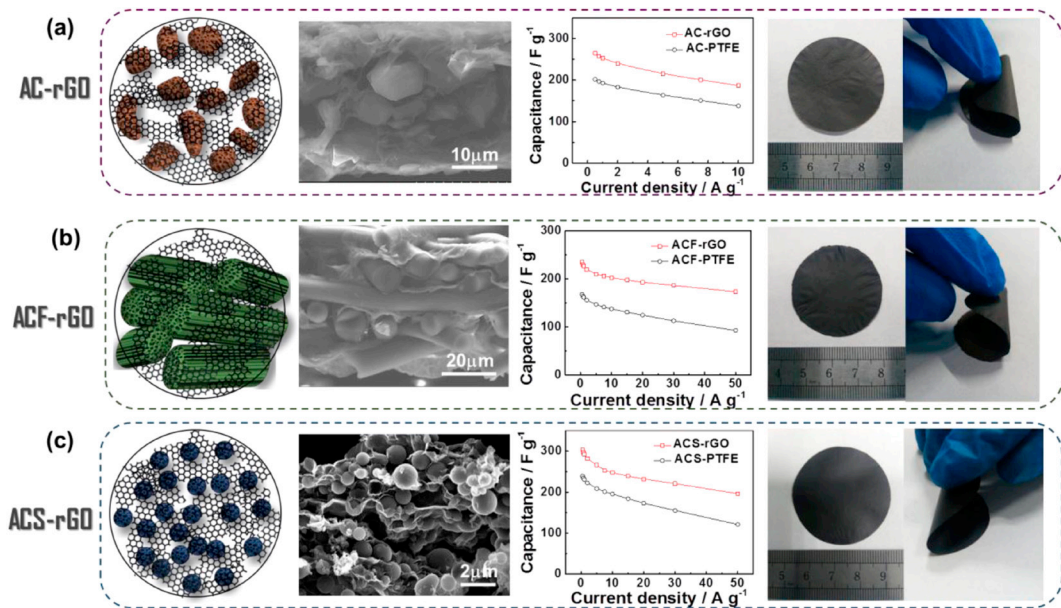


Figure 4-6 – Schematic diagrams with SEM images, electrochemical performance, and digital images of electrodes assembled exploiting rGO as an active binder when in composites with other carbon materials [197].

Xu et al. investigated the ability of rGO to be used as a binder when mixed with carbons of different morphologies. The process involved the blending of an aqueous GO solution and pre-dispersed carbons in dimethylformamide (DMF), which was followed by vacuum assisted filtration and subsequent drying and thermal reduction in inert atmosphere at 300 °C [197]. The as-prepared free-standing electrodes with hierarchical porous carbon (HPC, in a mass ratio of 4:1 with rGO), thanks to the 3D conductive network with a SSA of 2,561 m² g⁻¹, yielded the high specific capacitance of 321 F g⁻¹; to be compared with the already high values of 251 F g⁻¹ and 2,201 m² g⁻¹ of HPC with conventional PTFE binder. Jang and co-workers similarly demonstrated good capacitive performance of biomass-derived activated carbons with rGO binder [198]. In their optimised process (with rGO being the 2 wt% of the whole mass), carbon particles were added to a GO aqueous dispersion that was subsequently coated on a carbon paper as current collector and thermally annealed at 300 °C. The assembled devices showed an ultra-high specific capacitance of 512 F g⁻¹ in KOH

aqueous electrolyte, which was attributed by the authors to the preservation of the high surface area of the porous carbons in electrically conductive networks formed by the rGO binder, the pseudocapacitance contribution due to residual oxygen functional groups, and the improved wettability from the electrolyte. Galhena et al. proposed instead a 1:10 mixture of GO with AC in PC solvent, which was subsequently coated on Al current collector and heated at 300 °C in inert atmosphere and low pressure to promote the conversion to rGO [199]. The residual oxygen functionalities were considered responsible for the adhesive properties, through non-covalent interactions, of rGO with both AC particles and current collector, and allowed for a specific capacitance of 79.8 F g⁻¹ in TEA-BF₄/PC electrolyte (Figure 4-7). In a recent work from Skrypnichuk et al., activated rGO was used as active material with CNTs as electrically conductive binder. Those were dispersed in water thanks to GO aid, and fumed silica was added as rheology-modifying and thickening additive. All the components were step-wise mixed with high-shear ball milling in a 10:1:1:1 ratio, coated on a flexible steel current collector and then thermally annealed at 200 °C [200]. The reported specific capacitances are of 180 and 140 F g⁻¹ in aqueous (KOH) and organic (TEA-BF₄/ACN) electrolyte, respectively. Those high values were ascribed to the preservation of the 3D structure of activated rGO, and to the improved contact between material grains thanks to CNTs.

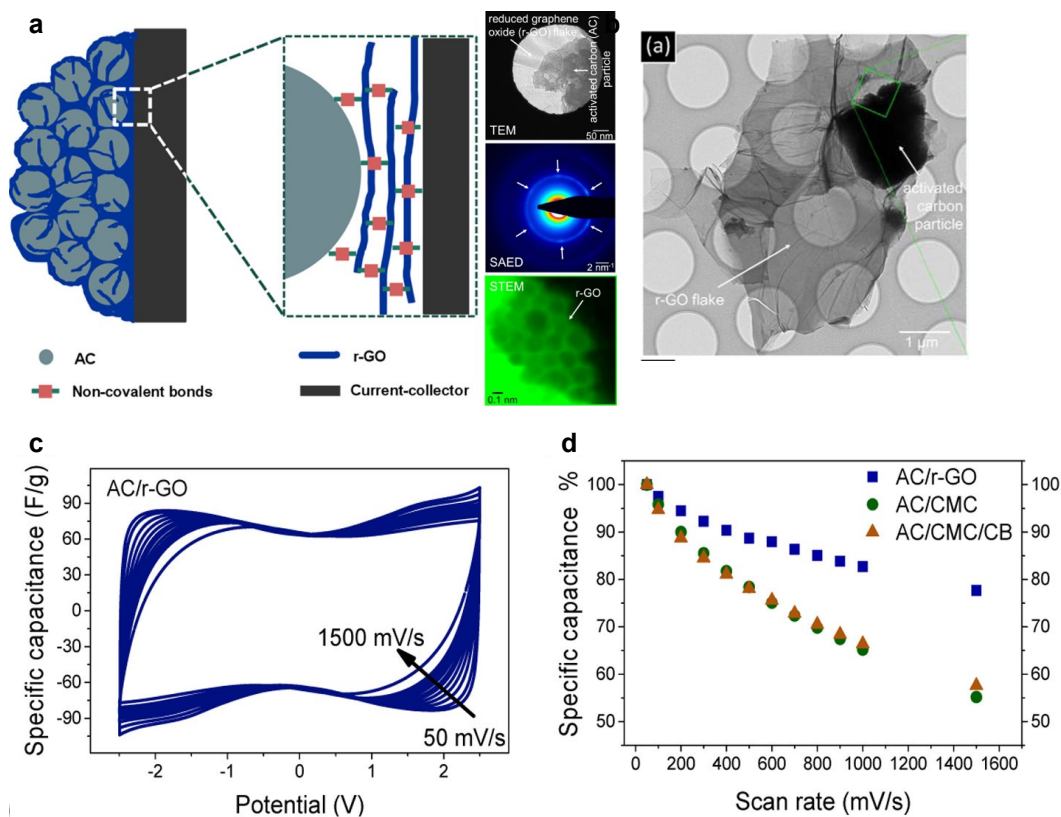


Figure 4-7 – (a) Schematic illustration of rGO providing adhesion on current collector. (b) TEM image showing rGO flake surrounding AC particle. (c) CV of EDLC assembled with rGO/AC electrodes and (d) comparison with traditional materials [199].

This literature survey shows how graphene-based materials were effectively exploited as active materials in traditional electrodes, by templating them in free-standing electrodes, or, more recently, as alternative and active binders. In most of the reported studies, however, the scalability of the manufacturing steps from laboratory to industry, the potential costs, and environmental impacts deriving by the use of exotic and/or hazardous chemicals and other raw materials were hardly considered. In particular, it was only in the last few years that researchers started to assess processes where graphene-based materials allow water to be used as the only solvent for the dispersion of both active material and, eventually, binder. It is thus believed that graphene-based materials can further be evaluated and optimised for the development of environmentally

friendly SCs, exploiting them to obtain water-based slurries that can potentially be processed with current industrial manufacturing techniques.

Chapter 5

GRAPHENE-BASED MATERIALS **ACOUSTIC**

5.1 Context

The issue of noise pollution caused by low frequency sound emissions of industrial machineries, home appliances, vehicles of all nature, buildings and constructions have drawn great attention toward more efficient sound insulating methods. In the aerospace and automotive industries, for instance, primary and secondary structures have generally strict boundaries in terms of weight and size, whose limit the applicability of traditional porous absorbers. The latter, in fact, proved to be bulky and heavy in the low-mid frequency range ($< 2,000$ Hz). Although great advance was obtained with

hybrid porous absorbers consisting of an organic matrix loaded with inorganic compounds, a density $< 30 \text{ kg m}^{-3}$ was rarely obtained. Additionally, meagre attention was posed toward the eco-friendliness of both manufacturing processes and used materials. Surprisingly, although the inherent properties of chemical and mechanical stability, high surface area and easiness of processability, graphene-based materials deriving from GO were only recently studied for sound absorption application and only to a limited extent.

With the aim to fill the literature gaps discussed above, the first research paper of this collection proposes a new class of ultralight and subwavelength-thin porous absorbers with high, broadband, and tuneable sound absorption and sound transmission loss. Particularly, aerogels with an extremely low density (down to 2.10 kg m^{-3}) were manufactured starting from the high-shear mixing of GO and PVA blends in water, then embedded in a honeycomb (HC) core, freeze-cast, and finally freeze-dried. The first step was crucial for the incorporation of air bubbles, the consecutive freeze-casting-drying allowed to maintain the templated structure, while the embedding in HC core demonstrated the readiness for the application of the proposed material in secondary structures for the aerospace industry. Moreover, in addition to the evaluation of the physicochemical and acoustic properties, a semi-phenomenological model was for the first time applied to evaluate the relationship between the so-called “non-acoustic properties” of the material and the energy dissipation mechanism of soundwaves when travelling through it.

Besides the need of porous absorbers to be light and thin, advanced structures for aerospace and automotive applications are generally required to provide multiple functionalities. On this regard, aerogels deriving from GO suspensions in water can also be functionalised by their combination with

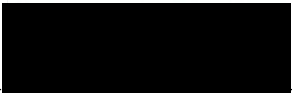
other chemical substances and/or by the removal of oxygen groups to restore the electrical properties of graphene. However, despite applications of functionalised aerogels were described in many fields, such as water treatment, energy storage, and stress-strain sensing, complex synthesis methods with exotic chemicals, or the need of specific conditions to achieve optimal performances, have limited their scale-up and practical use.

Therefore, the previously discussed aerogels obtained from GO and PVA blends were the starting point of further developments pointing toward multifunctional materials, which are discussed in the second and last journal paper of the collection regarding graphene-based acoustic materials. In particular, a preliminary evaluation of the thermal and mechanical properties allowed to define which modifications would have been more beneficial. In fact, while the thermal properties were already satisfactory, an unbalance between the bulky PVA molecules and the lighter GO sheets and the absence of stable cross-links between the two components, was found to be the cause of a poor elastic resilience. The issue was tackled through a double chemical modification: the addition of glycerol as plasticising agent, to soften the intermolecular forces along PVA chains, and of glutaraldehyde as cross-linking agent. Correspondingly, the impact of such modifications to the chemico-physical structure and to the thermal, acoustic and mechanical properties was evaluated. Furthermore, a third modification was proposed: the partial removal of oxygen groups through using ascorbic acid as a green reducing agent. The resulting aerogel was characterised by a piezoresistive behaviour and, as a major impact the other properties was not evidenced, it could be considered for the fabrication of multifunctional structure to be applied in advanced engineering applications.

5.2 Ultralight aerogels for broadband and tuneable acoustic properties

The statement of Authorship Form and the paper can be found next, followed by the relevant supplementary information.

This declaration concerns the article entitled:	
<i>Ultralight aerogels for broadband and tuneable acoustic properties</i>	
Publication status (tick one)	
Draft Manuscript <input type="checkbox"/> Submitted <input type="checkbox"/> In Review <input type="checkbox"/> Accepted <input type="checkbox"/> Published <input checked="" type="checkbox"/>	
Publication details (reference)	https://doi.org/10.1038/s41598-021-90101-0
Copyright status (tick the appropriate statement)	
I hold the copyright for this material <input type="checkbox"/>	
Copyright is retained by the publisher, but I have been given permission to replicate the material here <input checked="" type="checkbox"/>	
Candidate's contribution to the paper (provide details, and also indicate as a percentage)	<p>The candidate contributed to / considerably contributed to / predominantly executed the...</p> <p>Formulation of ideas: 80% <i>I proposed the idea of ultra-high shear mixing a blend of GO and PVA to obtain a light aerogel for acoustic application to Prof. M. Meo, who actively contributed and approved the research work.</i></p> <p>Design of methodology: 80% <i>I designed the experimental campaign, with Dr. G.P. Malfense Fierro contributing for acoustic properties evaluation. I also proposed the use of the semi-phenomenological model, after discussion with Dr. G.P. Malfense Fierro. He helped in his implementation.</i></p> <p>Experimental work: 90% <i>I manufactured and characterised all the samples, Dr. G.P. Malfense Fierro helped for the acoustic properties.</i></p> <p>Presentation of data in journal format: 80%</p>

	<i>I defined paper structure, wrote the first draft and designed the figures. Dr. G.P. Malfense Fierro contributed for the discussion on acoustic properties and semi-phenomenological analysis. Prof. M. Meo reviewed the manuscript and supported in the submission and publication process.</i>		
Statement from Candidate	This paper reports on original research I conducted during the period of my Higher Degree by Research candidature.		
Signed			Date 15/02/2022

Ultralight Graphene Oxide/Polyvinyl Alcohol Aerogel for broadband and tuneable acoustic properties

Mario Rapisarda¹, Gian-Piero Malfense Fierro¹, and Michele Meo^{1,*}

¹*University of Bath, Department of Mechanical Engineering, Bath, BA27AY, UK*

**Corresponding author*

Abstract

An ultralight Graphene Oxide (GO)/Polyvinyl Alcohol (PVA) Aerogel (GPA) is proposed as a new class of acoustic materials with tuneable and broadband sound absorption and sound transmission losses. The interaction between GO sheets and PVA molecules is exploited in our environmentally friendly manufacturing process to fabricate aerogels with hierarchical and tuneable porosity embedded in a honeycomb scaffold. The aerogels possess an enhanced ability to dissipate sound energy, with an extremely low density of 2.10 kg m^{-3} , one of the lowest values ever reported for acoustic materials. We have first experimentally evaluated and optimised the effects of composition and thickness on the acoustic properties, namely sound absorption and sound transmission losses. Subsequently, we have employed a semi-analytical approach to evaluate the effect of different processing times on acoustic properties and assessed the relationships between the acoustic and non-acoustic properties of the materials. Over the 400 – 2500 Hz range, the reported average sound absorption coefficients are as high as 0.79, while the average sound transmission losses can reach 15.8 dB. We envisage that our subwavelength thin and light aerogel-based materials will possess other functional properties such as fire resistance and

EMI shielding, and will prove to be novel acoustic materials for advanced engineering applications.

1. Introduction

The development of innovative acoustic materials has been of huge interest in the past decades, in particular porous absorbers have been extensively studied and adopted for several engineering applications [1]. Traditional porous absorbers such as cellular foams [2-4] and fibrous materials [4-6] exhibit good sound absorption abilities over a medium frequency range (i.e., 800 – 2000 Hz), but they are typically bulky and heavyweight at lower frequencies, limiting their application. Porous absorbers dissipate sound energy due to two main mechanisms: viscous friction on pore walls and thermal losses within pores [7, 8]. The understanding of sound absorption capabilities of these materials relies on the prediction of their effective density (ρ_e) and bulk modulus (K_e), that can be achieved with a semi-phenomenological fluid model developed by Johnson-Champoux-Allard (JCA) [9, 10]. The model relates the sound propagation through porous materials to their non-acoustic properties, which are porosity (ϕ), flow resistivity (σ), tortuosity (α_∞), viscous (Λ) and thermal (Λ') characteristic lengths. Therefore, tailored absorption of porous materials requires accurate measurement of these factors, linked to a precise manufacturing process. Porous absorbers can be distinguished by chemical composition as organic, hybrid, or inorganic [4], with a recent growing interest in the use of carbon-based materials [11, 12]. Graphene Oxide (GO) is an ideal candidate for engineering novel absorbers, thanks to its peculiar chemical structure consisting of a two-dimensional (2D) lattice of sp^2 hybridised carbon atoms with oxygen functionalities [13]. The main advantages of GO are its capability to form stable suspensions in water [14] and to be templated in various assemblies such as aerogels [15] with low cost and in

environmentally friendly processes. GO has been evaluated for applications including water treatment [16], energy storage [17], composite reinforcements [18], EMI shielding [19], and thermal insulation with fire-retardancy [20]. Acoustic-related properties have recently been described [8, 12, 21]. Nine et al. [21] developed a hybrid foam with GO supported by Melamine where it promoted an increase in air-flow resistivity and tortuosity leading to a sound absorption coefficient of 0.6 over 800 Hz with a sample thickness of 26 mm. Similarly, Oh et al. [12] fabricated a directionally antagonistic Graphene Polyurethane aerogel with a broadband absorption coefficient over 0.6 above 1000 Hz with a sample thickness of 30 mm. An example of carbon-only foam is found in the work of Lu et al. [8], where a bubbled GO solution was freeze-cast and thermally reduced. A Bubbled Graphene Monolith was obtained, with a normalised absorption coefficient of 0.9 in the 800 – 6300 Hz range with a sample thickness of 30 mm and a density of 7.5 kg m^{-3} . While these results achieve broadband absorption with thin structures, the pursuit of tuneable, lighter, and higher absorbing materials is still of fundamental and practical importance.

Herein we present a new class of ultralight and subwavelength thin acoustic aerogels with high, broadband, and tuneable sound absorption and sound transmission loss. These are manufactured by ultra-high shear mixing blends of GO and Polyvinyl Alcohol (PVA) which are then embedded in a honeycomb (HC) core, freeze-cast, and finally freeze-dried. This process allows the incorporation of air bubbles in a templated structure that leads to the ultralight GO/PVA Aerogels (GPAs). PVA has many favourable characteristics such as high chemical resistance, good optical and physical properties [22], low toxicity [23] and high biodegradability [24]. In addition, its water solubility and cross-linking ability renders it an ideal candidate to form homogeneous solutions with GO. While alterations of blend composition produce aerogels with different physicochemical

characteristics, variations in the time of ultra-high shear mixing changes the structural characteristics. Both directly affect the efficiency of sound dissipation through the material and, consequently, shape the JCA model as a powerful tool for the understanding of the acoustic behaviour of GPAs. Digital Microscopy (DM), Scanning Electron Microscopy (SEM), Fourier-Transform Infrared Spectroscopy (FT-IR) and X-Ray Diffractometry (XRD) are used to characterise the physical and chemical properties of the aerogels. The Normal Absorption Coefficient (α) and the Normal Incident Sound Transmission Loss (*STL*) are measured to determine the acoustic properties of the proposed material, evaluating and optimising the effects of composition, thickness and processing time. The JCA model is used to predict the physical parameters of the aerogels, identify the effects of the shear mixing process and ultimately provide information to tune the acoustic properties of the absorbers. To the best of our knowledge, no reports have been published discussing the acoustic behaviour of functionalised GO aerogels based on semi-analytical models, or describing their sound transmission losses. The ultralight aerogels manufactured in this work possess high broadband sound absorption, with the optimised GPA potentially being the lightest porous absorber on record at this time.

2. Results

2.1. Formation of ultralight GO/PVA aerogels

GO is hydrophilic due to oxygen functionalities such as epoxy, hydroxyl and carboxyl groups which are found on its basal planes and edges [25]. A polar solvent such as water can intercalate between GO interlayer spacings [13, 26], leading to stable suspensions. Likewise, thanks to hydroxyl functionalities, PVA is also hydrophilic and water-soluble [27]. As shown in Figure P1-1 – a, when GO suspensions and PVA solutions are mixed in water, homogeneous blends can be obtained due to hydrogen bonds

between the molecules of the two components [28, 29]. Figure P1-1 – b pictures air bubble entrapment (i.e., foaming) after ultra-high shear mixing of the blends. This is a result of the low interfacial tension of PVA, whereas foam stability is improved by changes to surface elasticity and viscosity due to the presence of GO [30-32]. Increasing the amount of GO increases foaming capability, until a critical concentration of solids leads to bulk clustering of particles that destabilises the foam [33]. After a stable hydrogel is obtained, it is possible to maintain the templated structure and to embed it in a Nomex HC core. Figure P1-1 – c-d shows the subsequent freeze-casting and freeze-drying processes: the structure is first frozen unidirectionally from the bottom (i.e., cold surface) to the top (i.e., surface exposed to the atmosphere), resulting in ice crystals growing vertically and pushing the bigger and lighter air bubbles upward; it is then dried through sublimation as pressure and temperature inside the drying chamber are below the triple point. Figure P1-1 – d presents the resulting aerogel characterised by a hierarchical porosity. Micro-porosity is generated by the exclusion of particles, polymeric molecules, or a mixture of them, from the nucleation and growth of small ice crystals due to extremely low temperature exposure (i.e., about -190 °C thanks to the use of Liquid Nitrogen as freezing medium) [34]. Macro-porosity is instead induced by air bubbles previously entrapped.

In Table P1-1 GPAs of different composition are compared with pure GO and PVA aerogels. Blends having PVA as the more abundant component have been excluded as the resulting aerogels did not possess acceptable structural robustness. The variation in the amount of PVA in the starting blend leads to both macroscopic (Figure P1-2 – a-e, DM) and microscopic (Figure P1-2 – f-o, SEM) differences in morphology. GPA-1 and GPA-2 possess a similar micro-porous structure, with the first showing the largest macroscopic entrapment of air bubbles. GPA-3 exhibits no bubbles

and a bulkier micro-structure, similar to pure GO. The transition from light to bulky structures is reflected by the physical properties of the aerogels, of which GPA-1 is the lightest with a density of 5.11 kg m⁻³ and a porosity of 99.32% (Table P1-1). A processing time of 15 min is used for the initial blends, as it represents the optimum state of air entrapment, homogenisation and structural robustness in the resulting aerogel. However, the time of ultra-high shear mixing controls air entrapment in the foamed blends, and in so doing, tunes the structural properties of the aerogels to maximise sound energy dissipation. The 1:1 ratio blend shows the best tuning ability in the time interval of 5 – 20 minutes, with the resulting physical properties summarised in Table P1-2. Notably, an ultralight aerogel characterised by a density of 2.10 kg m⁻³ and a porosity of 99.72% is obtained with precisely 5 minutes of processing. GPAs are among the lightest acoustic materials reported in the literature so far (see Table S1-1 of Supplementary Information), guaranteeing a small weight increase with respect to the HC core that is as little as the 3.43% for the lightest sample (Table P1-1 and Table P1-2).

Table P1-1 – Physical properties of all samples

Sample	GO:PVA ratio	Density (kg m⁻³)	Φ (%)	Weight increase on HC core (%)
<i>PVA</i>	0:1	43.80	96.5	71.55
<i>GPA-1</i>	1:1	5.11	99.32	8.34
<i>GPA-2</i>	2:1	7.80	98.68	12.74
<i>GPA-3</i>	3:1	7.59	98.71	12.41
<i>GO</i>	1:0	5.80	97.77	11.83

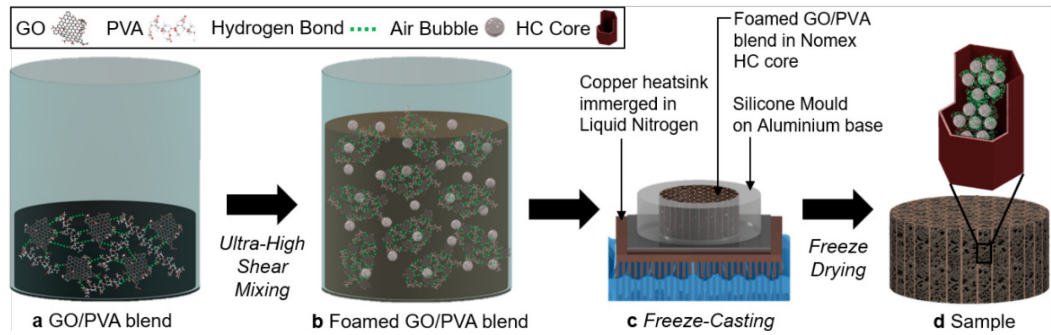


Figure P1-1 – Schematic illustration of the ultralight GPAs.

Table P1-2 – Physical properties of GPA-1 samples for various processing times.

Processing time (min)	Density (kg m ⁻³)	Φ (%)	Weight increase on HC core (%)
5	2.10	99.72	3.43
10	4.38	99.42	7.16
15	5.11	99.32	8.34
20	7.41	99.23	12.11

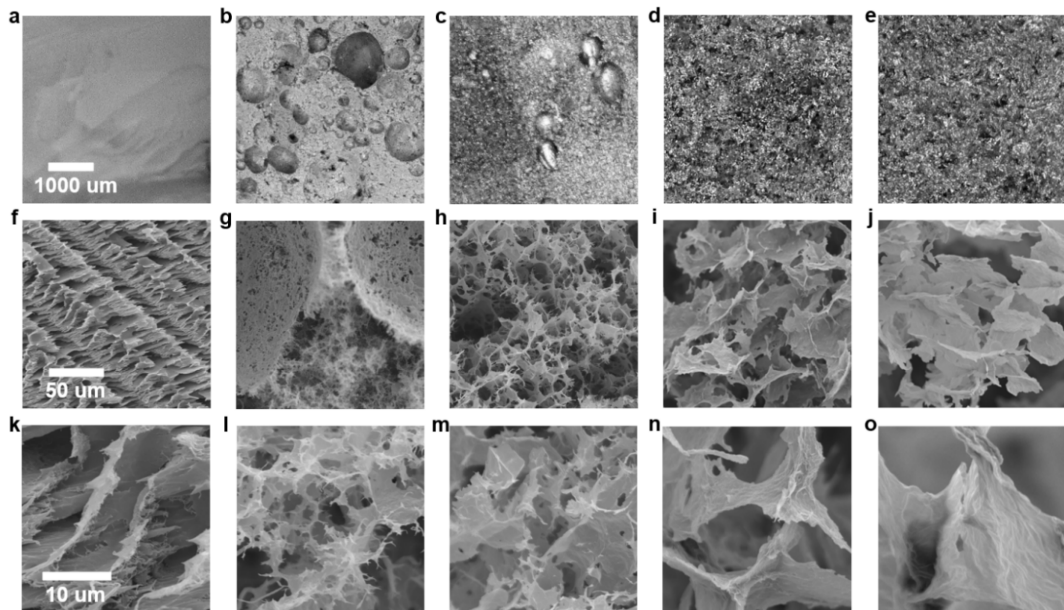


Figure P1-2 – (a-e) DM and (f-o) SEM images of GO/PVA aerogels. PVA (a, f, k), GPA-1 (b, g, l), GPA-2 (c, h, m), GPA-3 (d, i, n), GO (e, j, o). Magnifications: (a-e) x20, (f-j) x500, and (k-o) x3000. Same scale bars apply to images with equal magnification.

2.2. Physicochemical characterisation

Figure P1-3 – a shows the FT-IR spectra for all the samples. The main features observable in the GO spectrum are the O-H stretching and deformation of hydroxyl groups at 3351 and 1373 cm^{-1} , coupled with the C-OH stretching at 1217 and 1160 cm^{-1} , the C=O stretching of carbonyl groups at 1718 cm^{-1} , and the C-O-C stretching of epoxy groups at 1033 cm^{-1} [35-38]. The peaks at 3194 and 1615 cm^{-1} are respectively due to the stretching and deformation of adsorbed water molecules [38]. On the other hand, the main features of the PVA spectrum are the O-H stretching and deformation at 3307 and 1377 cm^{-1} , the asymmetric and symmetric stretching of C-H at 2941 and 2911 cm^{-1} respectively, the C-H₂ bending at 1418 cm^{-1} , the C-O-C stretching at 1089 cm^{-1} , and the C-C stretching at 845 cm^{-1} [39-41]. As GO/PVA blends exhibit the features of both the components, with intensities proportional to their relative mass ratios, the homogeneous mixing and stability of the samples can be assumed. Additionally, a shift of O-H related features around 3351, 1373, 1217, and 1160 cm^{-1} confirms the formation of hydrogen bonds between the oxygen groups on GO sheets and the hydroxyl groups of PVA molecules [42-44].

From XRD patterns presented in Figure P1-3 – b, GO shows its characteristic peak associated with the (001) carbon crystalline phase at 10.80° and the (100) reflection related to the longitudinal dimension of the structural elements at 42.45° [45, 46]. The introduction of increasing PVA amounts in the blends affects the (001) peak causing its reduction in intensity and sharpness. This indicates a lower degree of crystallinity and a possible decrease in the size of crystallites. A shift toward lower 2θ values can also be observed, indicating that the interactions between PVA molecules and GO sheets lead to a more expanded structure. According to Bragg's law [47], the interplanar distance (d) between GO layers increases from 8.19 Å for pristine GO to the maximum of 16.20 Å for GPA-1. The PVA

main reflection (101) peak appearing at 19.36° is not visible in the patterns for GPAs, which is the sign of a completely amorphous phase [48].

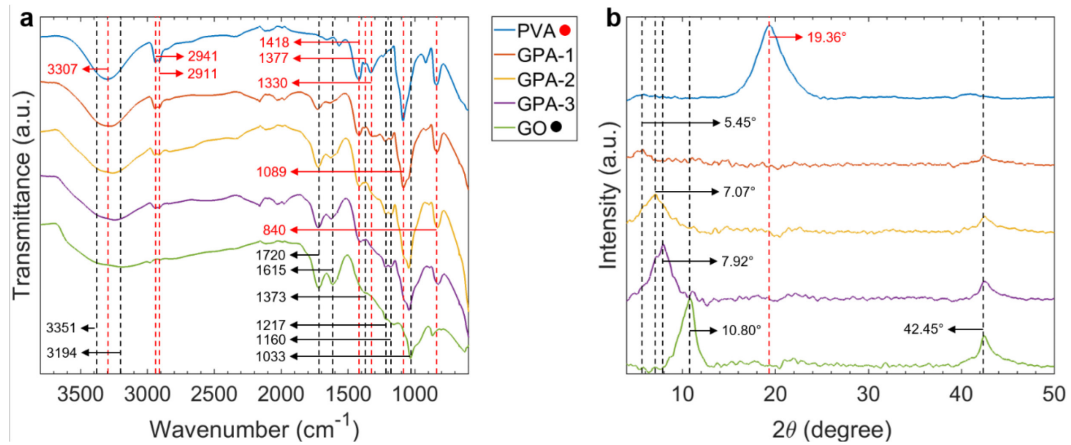


Figure P1-3 – Physicochemical characterisation of GO/PVA aerogels: **(a)** FT-IR spectra and **(b)** XRD patterns. Wavenumbers attributable to GO are denoted in black (●), while those for PVA are in red (●).

2.3. Optimisation of the acoustic properties

Figure P1-4 – a-b presents the variation of α and STL for different compositions of GPAs as a function of frequency. As PVA inclusion increases, the absorption curves are flattened and shift toward lower frequencies than pure GO. This leads to higher absorption in the low frequency range (i.e., below 1200 Hz), with $\alpha > 0.4$ from 500 Hz for GPA-1 and GPA-2. GPA-3 and pure GO outperform in the high frequency range (i.e., above 1200 Hz), and have similar performances to other GO foams reported in the literature [8]. This behaviour is related to changes in the physical structure of the aerogel. In particular, the macrostructure of GPA-1 and GPA-2 exhibits large pores (Figure P1-2 – b-c) that result to an increased porosity and a reduced flow resistivity. The average sound absorption coefficients ($\bar{\alpha}$) for all the GPA samples fall in the 0.74 and 0.77 range. A PVA inclusion higher than 75 wt% (GPA-1 and GPA-2) results in improved transmission loss performances (Figure P1-4 – b), with GPA-1 having the highest average loss (\overline{STL}) of 13.2 dB. The STL generally reflects

the damping properties attributed to the cross-sectional distribution of large and small pores within the aerogel (Figure P1-2 – g), and therefore sound attenuation through the material [49]. The relation between α and the Reflection Coefficient (R), $\alpha = 1 - |R|^2$, further justifies this behaviour as higher transmission losses are expected from a structure showing lower absorption and, consequently, higher reflections.

GPA-1 was chosen as the optimum composition as it possesses high sound absorption and sound transmission losses while being the lightest aerogel. Figure P1-4 – c-d shows the effect of adjusting the thickness from 12.5 to 37.5 mm on both α and STL . The increase in aerogel thickness improves sound absorption at lower frequencies as expected, with the 37.5 mm thick sample achieving $\alpha > 0.6$ from 500 Hz upwards with a peak of $\alpha = 0.96$ at 948 Hz. \overline{STL} follows the same behaviour and reaches 15.7 dB for 37.5 mm thickness.

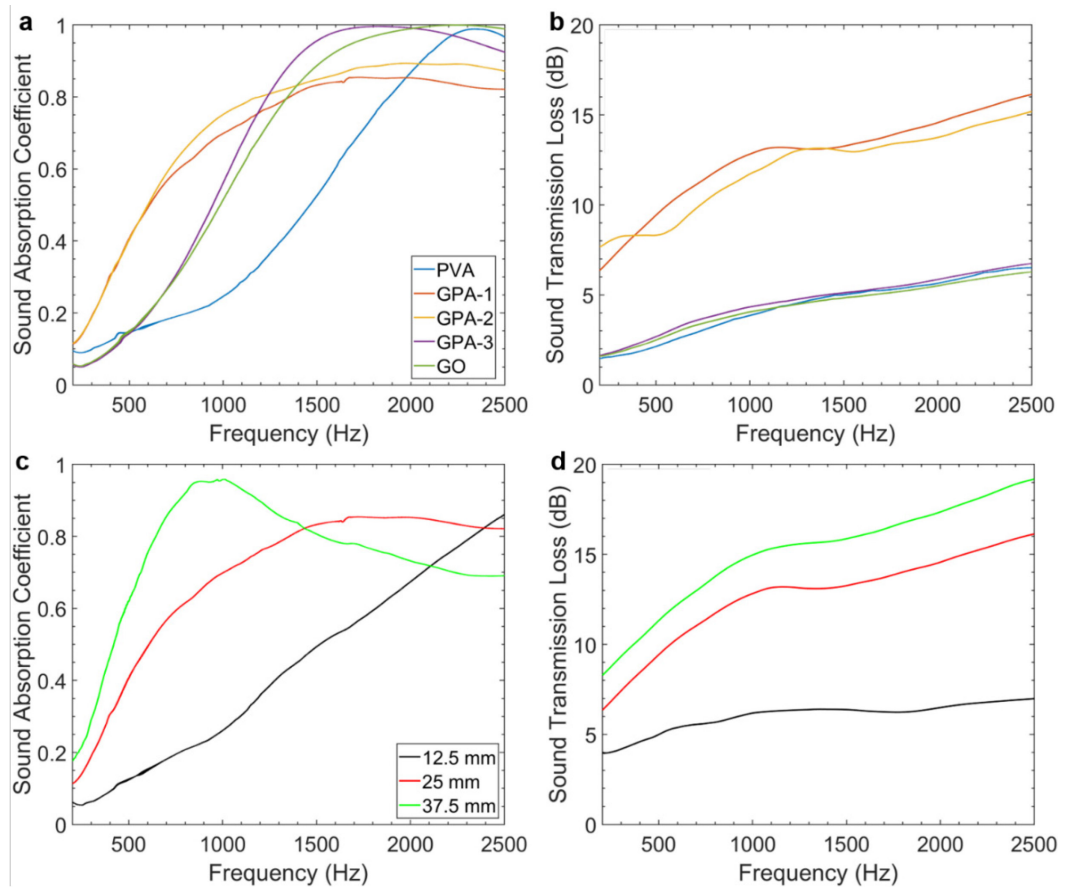


Figure P1-4 – Effects of (a, b) GPA composition and (c, d) GPA-1 thickness on acoustic properties: (a, c) sound absorption and (b, d) sound transmission loss. Sample thickness is 25 mm when not studied as a variation (a, b). Key and average α and STL values are summarised in Table S2-2.

The next optimisation step is the evaluation of processing time and, consequently, porosity on acoustic properties of GPA-1. Figure P1-5 – a shows that an increasing porosity leads to higher sound absorption of the proposed structure over the frequency range investigated. In particular, the lightest aerogel obtained with 5 min of processing time results in a density of 2.10 kg m^{-3} and a porosity of 99.72% achieving $\bar{\alpha} = 0.79$. As sound waves travel from large to smaller pores (Figure P1-2 – g), air velocity increases and sound energy is dissipated due to friction [50-51]. Figure P1-5 – b depicts an increase of the transmission loss as aerogels become bulkier. The heaviest aerogel (7.41 kg m^{-3}) has the best result with $\overline{STL} = 15.8 \text{ dB}$.

Furthermore, Figure P1-5 – c compares $\bar{\alpha}$ and density values of GPA-1 aerogels with other porous absorbers previously reported, demonstrating their superior acoustic properties while guaranteeing extremely low densities.

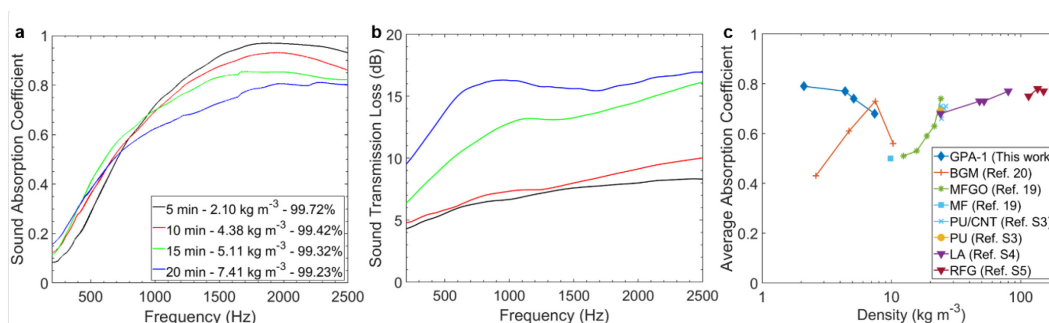


Figure P1-5 – Effects of processing time and densities on acoustic properties of GPA-1 samples: **(a)** sound absorption and **(b)** sound transmission loss. Key and average α and STL values are summarised in Table S4. **(c)** Comparison of the average sound absorption coefficient, calculated in the 400 – 2500 Hz range, as a function of density for GPA-1 samples and other porous absorbers with comparable thickness previously reported in literature (Table S1-1).

2.4. Semi-phenomenological analysis

The effects of processing time on the physical structure of GPA-1 and the resulting acoustic behaviour are further investigated using the JCA semi-phenomenological approach. The equivalent fluid model is fitted to measured results considering three experimentally derived parameters (ϕ , σ and α_∞) and two unknown parameters (Λ and Λ'). The predicted sound absorption coefficient curves have an average error $< 1\%$ when compared to the experimental results (Figure P1-6 – a), suggesting a good fit to the non-acoustic properties of the aerogels. For different processing times, the density and the non-acoustic properties change, and the complex interactions between these parameters lead to the observed shift in GPA-1 sound absorption. Porosity is directly proportional to the volume of air available to sound waves [52] and positively contributes to sound energy dissipation. However, it is crucial to highlight that the non-acoustic properties are not independent (i.e., a change in one parameter will cause

a change in the others). An inverse trend of $\bar{\alpha}$ with respect of σ can be observed from Figure P1-6 – b. In particular, the best performing sample (5 min of processing time) shows $\bar{\alpha} = 0.79$ for $\sigma = 33,981 \text{ N s m}^{-4}$. The flow resistivity is a measure of the porous material's resistance to an airflow and can thus give an idea of the extent of sound energy dissipation due to boundary layer effects within the material [52]. However, if the resistivity is too high the sound wave incident to the material would meet a relatively high impedance surface leading to high reflection due to the impedance mismatch and thus to low sound absorption [53]. This is in agreement with *STL* results previously reported (Figure P1-5 – b). The variation in α_{∞} shown in Figure P1-6 – c is within a relatively small range of 1.31 – 1.66, except for the 15 min sample. The tortuosity is a measure of the complexity of the propagation path of sound waves through the material, where more complex paths usually lead to higher sound absorption. However, no direct correlation is exhibited between $\bar{\alpha}$ and α_{∞} for the experimental aerogels. Λ increases with processing time from the minimum value of 29 μm to the maximum of 97 μm (Figure P1-6 – d). The viscous characteristic length is defined as “the surface-to-pore volume ratio of the pore-solid interface” [9] and is thus proportional to the microscopic dimensions of pores. Smaller values lead to increased viscous effects and thus to an improved dissipation of sound energy, explaining the acoustic behaviour pictured in Figure P1-6 – a. Finally, the variation of Λ' (between 154 and 202 μm) is a function of thermal losses at high frequencies [52] and thus has limited effect on sound absorption over the range investigated (Figure P1-6 – d).

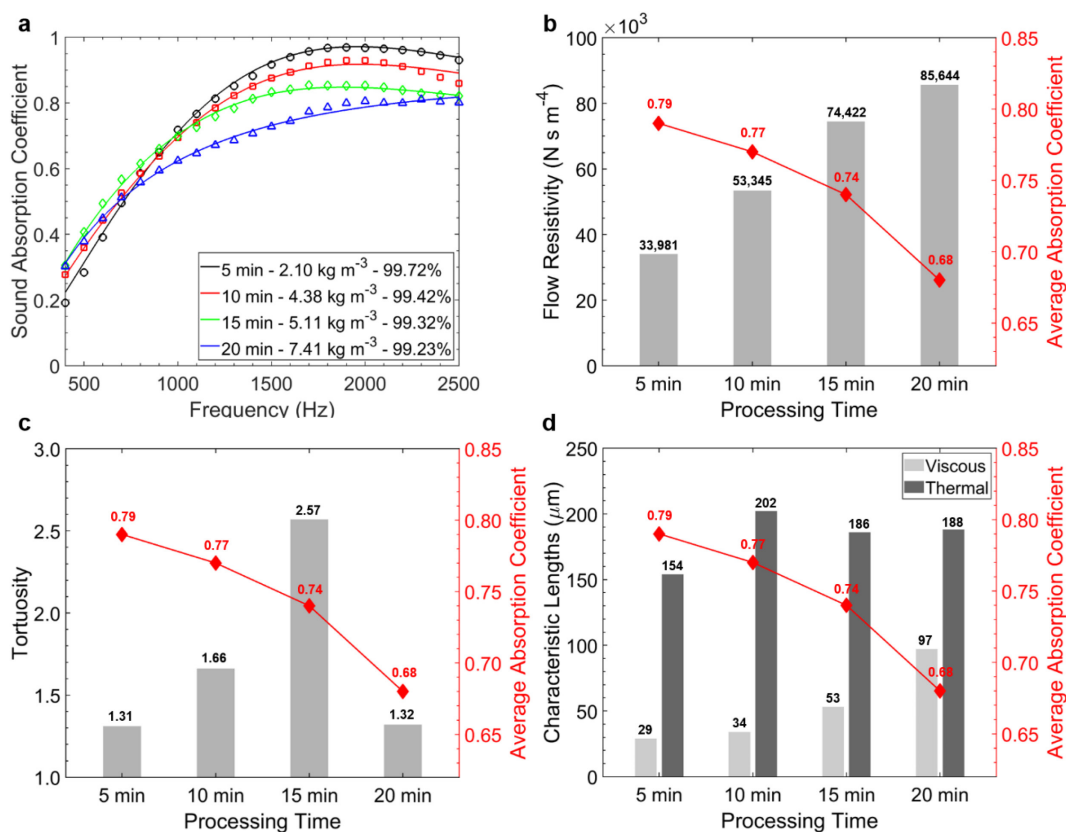


Figure P1-6 – Semi-phenomenological analysis of GPA-1 samples with different processing times: **(a)** comparison between semi-analytical model predictions (solid lines) and experimental measurements (markers) of the Sound Absorption Coefficient. **(b)** Flow Resistivity, **(c)** Tortuosity, **(d)** Viscous and Thermal Characteristic Lengths affected by processing time with Average Absorption Coefficient trend.

3. Discussion

In conclusion, we have developed a novel ultralight aerogel for the design of thin and light materials with excellent acoustic properties. We have exploited the chemical properties of GO/PVA blends and a specific environmentally friendly manufacturing process to embed the aerogels in structural HC cores. The physicochemical characterisation has demonstrated the effects of the blend composition on the physical properties of the material, the existence of hydrogen bonds between GO sheets and PVA molecules and the ability of the two components to form a homogeneous and expanded structure. We have also evaluated the effects

of composition, thickness, and processing time on the acoustic properties of the proposed material. Thanks to the hierarchical porosity, the resulting absorber is endowed with the advantages of a density as low as 2.10 kg m^{-3} , and tuneable sound absorption and transmission functionality. The novel aerogel-based structures provide a solution for the development of acoustic materials in structural engineering applications requiring high sound absorption and sound transmission losses as well as excellent mechanical stiffness and strength. Additionally, the inherent potential of GO to unlock multifunctional features such as EMI shielding and fire-retardancy may prompt advanced applications in the aerospace and power generation industries.

4. Methods

4.1. Materials

Graphite Oxide (GtO) powder was supplied by Xiamen TOB New Energy, PVA (98-99% hydrolyzed, medium molecular weight) was purchased from Sigma Aldrich. Deionized MilliQ® water was used throughout all the experiments. All the chemicals were used as received without further treatment or purification.

4.2. Sample fabrication

The fabrication process is schematised in Figure P1-7. GtO was dispersed in water (8 mg mL^{-1}) and exfoliated to form a GO suspension through probe sonication (Dr. Hielscher GmbH UP100H, with an amplitude of 80% and continuous pulsing) for 40 minutes under constant magnetic stirring and in an ice bath to ensure a homogeneous process with controlled temperature. A PVA solution (5 wt%) was obtained by dissolving the raw polymer in water: the system was heated up to $90 \text{ }^{\circ}\text{C}$ on a hot plate with continuous magnetic stirring until the solution became clear. Blends of GO and PVA were then

obtained with ultra-high shear mixing (IKA Ultra-Turrax T25) at 20,000 rpm for 15 minutes in a typical blend, or with varying processing times for porosity optimisation purposes. Proper amounts of the two components were mixed so that the designed mass ratio could be reached (Table P1-1).

Aerogels were obtained with unidirectional freeze-casting of the blends in a Nomex HC core with the aid of a silicone mould having an aluminium plate as base directly placed on a copper heat sink immersed in liquid nitrogen. Templated structures were finally freeze-dried (LTE LyoTrap Mini) for 96h, leaving the GPAs embedded in the Nomex core. Samples consisting of pure GO suspension and pure PVA solution were also manufactured as reference material.

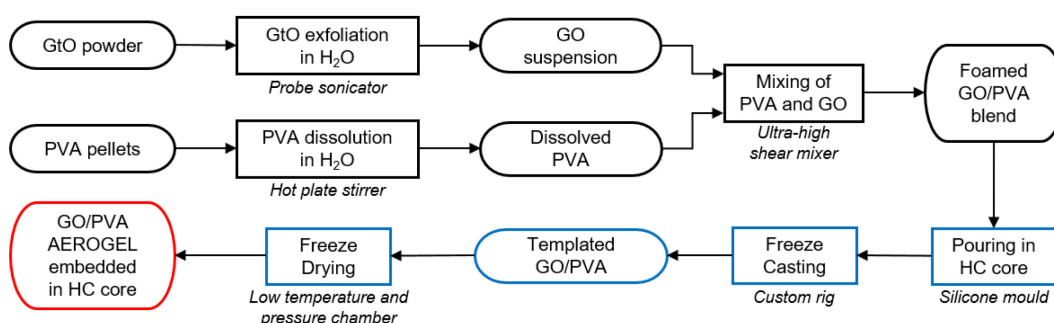


Figure P1-7 – Diagram of ultralight GO/PVA aerogel fabrication process.

4.3. Characterisation

The composition of the starting blend determined the morphology of the aerogels, evaluated with DM (Keyence VHX 6000) and SEM (Hitachi SU3900). Chemical structure was evaluated by Fourier-Transform Infrared Spectroscopy (FT-IR, Perkin-Elmer Frontier FTIR Spectrometer) with a liquid nitrogen cooled MCT detector from 400 to 4000 cm^{-1} . The crystalline structure of the blends was finally analysed with X-Ray Diffractometry (XRD, STOE STADI P) in the range of $2\theta = 4 - 50^\circ$ at room temperature using a Cu-K α generator with 1.54 Å wavelength. XRD data were additionally processed to calculate the interplanar distance d between GO layers using

Bragg's law [47] as expressed in equation (P1-1), where λ is the radiation wavelength and θ is the reflection angle of the (001) phase.

$$d = \lambda / 2 \sin \theta \quad (\text{P1-1})$$

The density of the samples (ρ_s) was calculated from their weight and volume. The porosity of each sample was calculated as expressed in equation (P1-2), where ρ_{GO} and ρ_{PVA} are the densities of bulk GO (0.26 g cm⁻³) and PVA (1.25 g cm⁻³), respectively, while w_{GO} and w_{PVA} are the mass percentages of the two components in the blend.

$$\phi = \left(1 - \frac{\rho_s}{w_{GO}\rho_{GO} + w_{PVA}\rho_{PVA}} \right) \times 100 \quad (\text{P1-2})$$

The coefficients expressing acoustic performances, α and STL , were measured following the standard test methods ASTM [54] and ASTM E2611 [55], respectively. Detailed experimental procedures can be found in Supplementary Information.

Detailed information on the measurement of the non-acoustic properties can be found in Supplementary Information. Briefly, porosity was evaluated using the density of the aerogels as expressed in equation (P1-2), flow resistivity was indirectly determined from impedance tube measurements according to equation (S1-9) [55-57], tortuosity was experimentally derived from equation (S1-10) using an ultrasonic time-of-flight method [58], and finally viscous and thermal characteristic lengths were obtained by applying an inverse identification method [59, 60].

References

1. Arenas, J. & Crocker, M. Recent Trends in Porous Sound-Absorbing Materials. *Sound & vibration* **44**, 12-17 (2010).

2. Gwon, J. G., Kim, S. K. & Kim, J. H. Sound absorption behavior of flexible polyurethane foams with distinct cellular structures. *Materials & Design* **89**, 448-454, doi:<https://doi.org/10.1016/j.matdes.2015.10.017> (2016).
3. Lu, T. J., Chen, F. & He, D. Sound absorption of cellular metals with semiopen cells. *The Journal of the Acoustical Society of America* **108**, 1697-1709, doi:10.1121/1.1286812 (2000).
4. Cao, L., Fu, Q., Si, Y., Ding, B. & Yu, J. Porous materials for sound absorption. *Composites Communications* **10**, 25-35, doi:<https://doi.org/10.1016/j.coco.2018.05.001> (2018).
5. Seddeq, H. S., Aly, N. M., Marwa A, A. & Elshakankery, M. Investigation on sound absorption properties for recycled fibrous materials. *Journal of Industrial Textiles* **43**, 56-73, doi:10.1177/1528083712446956 (2013).
6. Chen, W., Liu, S., Tong, L. & Li, S. Design of multi-layered porous fibrous metals for optimal sound absorption in the low frequency range. *Theoretical and Applied Mechanics Letters* **6**, 42-48, doi:<https://doi.org/10.1016/j.taml.2015.12.002> (2016).
7. Hyuk Park, J. *et al.* Cell openness manipulation of low density polyurethane foam for efficient sound absorption. *Journal of Sound and Vibration* **406**, 224-236, doi:<https://doi.org/10.1016/j.jsv.2017.06.021> (2017).
8. Lu, B. *et al.* High performance broadband acoustic absorption and sound sensing of a bubbled graphene monolith. *Journal of Materials Chemistry A* **7**, 11423-11429, doi:10.1039/C9TA02306B (2019).
9. Johnson, D. L., Koplik, J. & Dashen, R. Theory of dynamic permeability and tortuosity in fluid-saturated porous media. *Journal of Fluid Mechanics* **176**, 379-402, doi:10.1017/S0022112087000727 (1987).
10. Champoux, Y. & Allard, J. F. Dynamic tortuosity and bulk modulus in air-saturated porous media. *Journal of Applied Physics* **70**, 1975-1979, doi:10.1063/1.349482 (1991).
11. Wu, Y. *et al.* Graphene foam/carbon nanotube/poly(dimethyl siloxane) composites as excellent sound absorber. *Composites Part A: Applied Science and Manufacturing* **102**, 391-399, doi:<https://doi.org/10.1016/j.compositesa.2017.09.001> (2017).
12. Oh, J.-H., Kim, J., Lee, H., Kang, Y. & Oh, I.-K. Directionally Antagonistic Graphene Oxide-Polyurethane Hybrid Aerogel as a

- Sound Absorber. *ACS Applied Materials & Interfaces* **10**, 22650-22660, doi:10.1021/acsami.8b06361 (2018).
13. Dreyer, D. R., Park, S., Bielawski, C. W. & Ruoff, R. S. The chemistry of graphene oxide. *Chemical Society Reviews* **39**, 228-240, doi:10.1039/B917103G (2010).
 14. Zhu, Y. *et al.* Graphene and Graphene Oxide: Synthesis, Properties, and Applications. *Advanced Materials* **22**, 3906-3924, doi:<https://doi.org/10.1002/adma.201001068> (2010).
 15. He, Y. *et al.* An environmentally friendly method for the fabrication of reduced graphene oxide foam with a super oil absorption capacity. *Journal of Hazardous Materials* **260**, 796-805, doi:<https://doi.org/10.1016/j.jhazmat.2013.06.042> (2013).
 16. Wang, J. *et al.* Graphene Oxide as an Effective Barrier on a Porous Nanofibrous Membrane for Water Treatment. *ACS Applied Materials & Interfaces* **8**, 6211-6218, doi:10.1021/acsami.5b12723 (2016).
 17. Rapisarda, M., Damasco, A., Abbate, G. & Meo, M. Carbon Black and Reduced Graphene Oxide Nanocomposite for Binder-Free Supercapacitors with Reduced Graphene Oxide Paper as the Current Collector. *ACS Omega* **5**, 32426-32435, doi:10.1021/acsomega.0c04530 (2020).
 18. Wang, C. *et al.* Silver nanoparticles/graphene oxide decorated carbon fiber synergistic reinforcement in epoxy-based composites. *Polymer* **131**, 263-271, doi:<https://doi.org/10.1016/j.polymer.2017.10.049> (2017).
 19. Yan, D.-X. *et al.* Structured Reduced Graphene Oxide/Polymer Composites for Ultra-Efficient Electromagnetic Interference Shielding. *Advanced Functional Materials* **25**, 559-566, doi:<https://doi.org/10.1002/adfm.201403809> (2015).
 20. Wicklein, B. *et al.* Thermally insulating and fire-retardant lightweight anisotropic foams based on nanocellulose and graphene oxide. *Nature Nanotechnology* **10**, 277-283, doi:10.1038/nnano.2014.248 (2015).
 21. Nine, M. J. *et al.* Graphene Oxide-Based Lamella Network for Enhanced Sound Absorption. *Advanced Functional Materials* **27**, 1703820, doi:<https://doi.org/10.1002/adfm.201703820> (2017).
 22. Shi, R. *et al.* The effect of citric acid on the structural properties and cytotoxicity of the polyvinyl alcohol/starch films when molding at high

- temperature. *Carbohydrate Polymers* **74**, 763-770, doi:<https://doi.org/10.1016/j.carbpol.2008.04.045> (2008).
23. DeMerlis, C. C. & Schoneker, D. R. Review of the oral toxicity of polyvinyl alcohol (PVA). *Food and Chemical Toxicology* **41**, 319-326, doi:[https://doi.org/10.1016/S0278-6915\(02\)00258-2](https://doi.org/10.1016/S0278-6915(02)00258-2) (2003).
 24. Matsumura, S., Kurita, H. & Shimokobe, H. Anaerobic biodegradability of polyvinyl alcohol. *Biotechnology Letters* **15**, 749-754, doi:10.1007/BF01080150 (1993).
 25. Dikin, D. A. *et al.* Preparation and characterization of graphene oxide paper. *Nature* **448**, 457-460, doi:10.1038/nature06016 (2007).
 26. Paredes, J. I., Villar-Rodil, S., Martínez-Alonso, A. & Tascón, J. M. D. Graphene Oxide Dispersions in Organic Solvents. *Langmuir* **24**, 10560-10564, doi:10.1021/la801744a (2008).
 27. Adawa, H. & Deneault, C. Chemical Modification of Poly(Vinyl Alcohol) in Water. *Applied Sciences* **5**, 840-850, doi:10.3390/app5040840 (2015).
 28. Liang, J. *et al.* Molecular-Level Dispersion of Graphene into Poly(vinyl alcohol) and Effective Reinforcement of their Nanocomposites. *Advanced Functional Materials* **19**, 2297-2302, doi:<https://doi.org/10.1002/adfm.200801776> (2009).
 29. Bao, C., Guo, Y., Song, L. & Hu, Y. Poly(vinyl alcohol) nanocomposites based on graphene and graphite oxide: a comparative investigation of property and mechanism. *Journal of Materials Chemistry* **21**, 13942-13950, doi:10.1039/C1JM11662B (2011).
 30. Georgieva, D., Cagna, A. & Langevin, D. Link between surface elasticity and foam stability. *Soft Matter* **5**, 2063-2071, doi:10.1039/B822568K (2009).
 31. Murray, B. S. & Ettelaie, R. Foam stability: proteins and nanoparticles. *Current Opinion in Colloid & Interface Science* **9**, 314-320, doi:<https://doi.org/10.1016/j.cocis.2004.09.004> (2004).
 32. Kim, J. *et al.* Graphene Oxide Sheets at Interfaces. *Journal of the American Chemical Society* **132**, 8180-8186, doi:10.1021/ja102777p (2010).
 33. Vijayaraghavan, K., Nikolov, A. & Wasan, D. Foam formation and mitigation in a three-phase gas-liquid-particulate system. *Advances in Colloid and Interface Science* **123-126**, 49-61, doi:<https://doi.org/10.1016/j.cis.2006.07.006> (2006).

34. Qian, L. & Zhang, H. Controlled freezing and freeze drying: a versatile route for porous and micro-/nano-structured materials. *Journal of Chemical Technology & Biotechnology* **86**, 172-184, doi:<https://doi.org/10.1002/jctb.2495> (2011).
35. Hontoria-Lucas, C., López-Peinado, A. J., López-González, J. d. D., Rojas-Cervantes, M. L. & Martín-Aranda, R. M. Study of oxygen-containing groups in a series of graphite oxides: Physical and chemical characterization. *Carbon* **33**, 1585-1592, doi:[https://doi.org/10.1016/0008-6223\(95\)00120-3](https://doi.org/10.1016/0008-6223(95)00120-3) (1995).
36. Guo, H.-L., Wang, X.-F., Qian, Q.-Y., Wang, F.-B. & Xia, X.-H. A Green Approach to the Synthesis of Graphene Nanosheets. *ACS Nano* **3**, 2653-2659, doi:10.1021/nn900227d (2009).
37. Stankovich, S., Piner, R. D., Nguyen, S. T. & Ruoff, R. S. Synthesis and exfoliation of isocyanate-treated graphene oxide nanoplatelets. *Carbon* **44**, 3342-3347, doi:<https://doi.org/10.1016/j.carbon.2006.06.004> (2006).
38. Titelman, G. I. *et al.* Characteristics and microstructure of aqueous colloidal dispersions of graphite oxide. *Carbon* **43**, 641-649, doi:<https://doi.org/10.1016/j.carbon.2004.10.035> (2005).
39. Prosanov, I. Y. & Matvienko, A. A. Study of PVA thermal destruction by means of IR and Raman spectroscopy. *Physics of the Solid State* **52**, 2203-2206, doi:10.1134/S1063783410100318 (2010).
40. Blout, E. R. & Karplus, R. The Infrared Spectrum of Polyvinyl Alcohol. *Journal of the American Chemical Society* **70**, 862-864, doi:10.1021/ja01182a504 (1948).
41. Mansur, H. S., Sadahira, C. M., Souza, A. N. & Mansur, A. A. P. FTIR spectroscopy characterization of poly (vinyl alcohol) hydrogel with different hydrolysis degree and chemically crosslinked with glutaraldehyde. *Materials Science and Engineering: C* **28**, 539-548, doi:<https://doi.org/10.1016/j.msec.2007.10.088> (2008).
42. Salavagione, H. J., Martínez, G. & Gómez, M. A. Synthesis of poly(vinyl alcohol)/reduced graphite oxide nanocomposites with improved thermal and electrical properties. *Journal of Materials Chemistry* **19**, 5027-5032, doi:10.1039/B904232F (2009).
43. Li, C., She, M., She, X., Dai, J. & Kong, L. Functionalization of polyvinyl alcohol hydrogels with graphene oxide for potential dye removal. *Journal of Applied Polymer Science* **131**, doi:<https://doi.org/10.1002/app.39872> (2014).

44. Qi, X., Yao, X., Deng, S., Zhou, T. & Fu, Q. Water-induced shape memory effect of graphene oxide reinforced polyvinyl alcohol nanocomposites. *Journal of Materials Chemistry A* **2**, 2240-2249, doi:10.1039/C3TA14340F (2014).
45. Krishnamoorthy, K., Veerapandian, M., Yun, K. & Kim, S. J. The chemical and structural analysis of graphene oxide with different degrees of oxidation. *Carbon* **53**, 38-49, doi:<https://doi.org/10.1016/j.carbon.2012.10.013> (2013).
46. Popova, A. N. Crystallographic analysis of graphite by X-Ray diffraction. *Coke and Chemistry* **60**, 361-365, doi:10.3103/S1068364X17090058 (2017).
47. Bragg, W. H. & Bragg, W. L. The reflection of X-rays by crystals. *Proceedings of the Royal Society of London. Series A, Containing Papers of a Mathematical and Physical Character* **88**, 428-438, doi:doi:10.1098/rspa.1913.0040 (1913).
48. Ricciardi, R., Auriemma, F., De Rosa, C. & Lauprêtre, F. X-ray Diffraction Analysis of Poly(vinyl alcohol) Hydrogels, Obtained by Freezing and Thawing Techniques. *Macromolecules* **37**, 1921-1927, doi:10.1021/ma035663q (2004).
49. Fahy, F. & Gardonio, P. *Sound and structural vibration: radiation, transmission and response: second edition*. (Academic Press, 2007).
50. Bonfiglio, P. & Pompoli, F. A single measurement approach for the determination of the normal incidence transmission loss. *The Journal of the Acoustical Society of America* **124**, 1577-1583, doi:10.1121/1.2951605 (2008).
51. Han, F., Seiffert, G., Zhao, Y. & Gibbs, B. Acoustic absorption behaviour of an open-celled aluminium foam. *Journal of Physics D: Applied Physics* **36**, 294-302 (2003).
52. Cox, T. & D'Antonio, P. *Acoustic absorbers and diffusers: theory, design and application*. (Routledge Taylor & Francis, 2009).
53. Kleiner, M. *Acoustics and Audio Technology, Third Edition*. (J. Ross Publishing, 2011).
54. ASTM E1050-19, Standard Test Method for Impedance and Absorption of Acoustical Materials Using a Tube, Two Microphones and a Digital Frequency Analysis System, ASTM International, West Conshohocken, PA, 2019,. doi:10.1520/E1050-19.
55. ASTM E2611-19, Standard Test Method for Normal Incidence Determination of Porous Material Acoustical Properties Based on the

Transfer Matrix Method, ASTM International, West Conshohocken, PA, 2019,.

56. Tao, J., Wang, P., Qiu, X. & Pan, J. Static flow resistivity measurements based on the ISO 10534.2 standard impedance tube. *Building and Environment* **94**, 853-858, doi:<https://doi.org/10.1016/j.buildenv.2015.06.001> (2015).
57. Doutres, O., Salissou, Y., Atalla, N. & Panneton, R. Evaluation of the acoustic and non-acoustic properties of sound absorbing materials using a three-microphone impedance tube. *Applied Acoustics* **71**, 506-509, doi:<https://doi.org/10.1016/j.apacoust.2010.01.007> (2010).
58. Allard, J. F., Castagnede, B., Henry, M. & Lauriks, W. Evaluation of tortuosity in acoustic porous materials saturated by air. *Review of Scientific Instruments* **65**, 754-755, doi:10.1063/1.1145097 (1994).
59. Atalla, Y. & Panneton, R. Inverse acoustical characterization of open cell porous media using impedance tube measurements. *Canadian Acoustics* **33**, 11-24 (2005).
60. Fellah, Z. E. A., Mitri, F. G., Fellah, M., Ogam, E. & Depollier, C. Ultrasonic characterization of porous absorbing materials: Inverse problem. *Journal of Sound and Vibration* **302**, 746-759, doi:<https://doi.org/10.1016/j.jsv.2006.12.007> (2007).

Supplementary Information

Table S1-1 – Comparison of density, porosity, and sound absorption properties between GPA-1 samples from this work and other porous absorbers with comparable thickness previously reported in the literature.

^A The average was calculated in the 400 – 2500 Hz range.

Name	Density (kg m ⁻³)	Porosity (%)	Thickness (mm)	Average ^A Absorption Coefficient	Ref.
<i>GPA-1</i>	2.10 – 7.80	98.61 – 99.72	25	0.68 – 0.79	This work
<i>BGM</i>	2.6 – 10.3	up to 99.7	30	0.43 – 0.73	[1]
<i>MFGO</i>	12.39 – 24.12	-	26	0.51 – 0.74	[2]
<i>Commercial MF</i>	9.84	-	26	0.50	[2]
<i>PU/CNT foams</i>	23.37 – 26.31	~95	30	0.66 – 0.71	[3]
<i>Commercial PU</i>	23.87	~95	30	0.69	[3]
<i>Lignin Aerogels</i>	24 – 80	94 – 98.4	-	0.68 – 0.77	[4]
<i>RFG</i>	115 – 150	94 – 95.4	30	0.75 – 0.77	[5]

Table S1-2 – Sound absorption and transmission properties for GPAs with different composition.

^A The average was calculated in the 400 – 2500 Hz range.

Sample	Peak Freq (Hz)	Peak		500 Hz		1000 Hz		2000 Hz		Average ^A	
		α	α	STL (dB)	α	STL (dB)	α	STL (dB)	$\bar{\alpha}$	\overline{STL} (dB)	
<i>PVA</i>	2339	0.99	0.15	2.1	0.25	3.9	0.87	5.65	0.54	4.6	
<i>GPA-1</i>	1734	0.85	0.41	9.4	0.70	12.8	0.85	14.57	0.74	13.2	
<i>GPA-2</i>	1970	0.89	0.41	8.3	0.75	11.7	0.89	13.75	0.77	12.4	
<i>GPA-3</i>	1827	1.00	0.15	2.7	0.56	4.3	0.99	5.86	0.74	4.9	
<i>GO</i>	2244	1.00	0.15	2.5	0.51	4.1	0.99	5.51	0.72	4.6	

Table S1-3 – Sound absorption and transmission properties for GPA-1 samples with different thicknesses.

^A The average was calculated in the 400 – 2500 Hz range.

Sample	Peak		500 Hz		1000 Hz		2000 Hz		Average ^A	
	Freq (Hz)	α	α	<i>STL</i> (dB)	α	<i>STL</i> (dB)	α	<i>STL</i> (dB)	$\bar{\alpha}$	\overline{STL} (dB)
12.5 mm	2500	0.86	0.13	5.0	0.26	6.2	0.67	6.49	0.46	6.2
25 mm	1735	0.85	0.41	9.4	0.70	12.8	0.85	14.57	0.74	13.2
37.5 mm	948	0.96	0.62	11.3	0.96	15.0	0.73	17.36	0.79	15.7

Table S1-4 – Sound absorption and transmission properties for GPA-1 samples obtained with different mixing times.

^A The average was calculated in the 400 – 2500 Hz range.

Sample	Peak		500 Hz		1000 Hz		2000 Hz		Average ^A	
	Freq (Hz)	α	α	<i>STL</i> (dB)	α	<i>STL</i> (dB)	α	<i>STL</i> (dB)	$\bar{\alpha}$	\overline{STL} (dB)
5 min	1885	0.97	0.29	5.5	0.72	6.7	0.97	8.00	0.79	7.3
10 min	1952	0.93	0.36	5.8	0.69	7.3	0.93	9.13	0.77	8.0
15 min	1735	0.85	0.41	9.4	0.70	12.8	0.85	14.57	0.74	13.2
20 min	2284	0.81	0.38	13.7	0.62	16.3	0.80	16.11	0.68	15.8

Methods used to measure acoustic properties.

The aerogels were acoustically characterised through measurements of two key parameters: the Normal Absorption Coefficient (α) and the Normal Incident Sound Transmission Loss (*STL*). For the first, the standard test method ASTM E1050 [6] was followed. Briefly, samples of the composite structure were placed in one end of a two microphone impedance tube having an internal diameter of 50.8 mm with a rigid back surface, while a loudspeaker generating a broadband random signal was mounted at the other end. The coefficient α was then estimated as expressed in equation (S1-1):

$$\alpha = 1 - |R|^2 \quad (\text{S1-1})$$

Where R is the Complex Reflection Coefficient measured on the incident surface of the sample following the transfer function method [6].

The sound transmission losses were instead evaluated according to the standard test method ASTM E2611 [7]. The procedure is similar to the determination of α , but the transfer functions were calculated for four microphones, with two of them mounted each side of the sample, and two different terminations, anechoic and open. The STL was then estimated with equation (S1-2):

$$STL = 10 \log_{10} \left(\frac{1}{\tau} \right) \quad (\text{S1-2})$$

where τ is the sound transmission coefficient.

Equivalent fluid model of porous absorbers.

The acoustic behaviour of GPA-1 samples, specifically in terms of sound absorption ability, was studied with a semi-phenomenological approach following the Johnson-Champoux-Allard (JCA) model for porous materials [8, 9]. The effective density (ρ_e) and effective bulk modulus (K_e) relate the physical properties of the absorber to the sound propagation through it, and are calculated as expressed in equations (S1-3) and (S1-4):

$$\rho_e = \frac{\alpha_\infty \rho_0}{\phi} \left(1 + \frac{\sigma \phi}{i \omega \rho_0 \alpha_\infty} \sqrt{1 + \frac{4i \alpha_\infty^2 \eta \rho_0 \omega}{\sigma^2 \Lambda^2 \phi^2}} \right) \quad (\text{S1-3})$$

$$K_e = \frac{\gamma P_0}{\phi} \left[\gamma - (\gamma - 1) / \left(1 + \frac{8\eta}{i \Lambda'^2 N_{pr} \omega \rho_0} \sqrt{1 + \frac{i \rho_0 \omega N_{pr} \Lambda'^2}{16\eta}} \right) \right]^{-1} \quad (\text{S1-4})$$

where ρ_0 , η , γ , and N_{pr} are density, dynamic viscosity, ratio of the specific heat capacities and Prandtl Number for air, respectively, while P_0 is the atmospheric pressure. The remaining parameters (i.e., the non-acoustic

properties of porous materials) are porosity (ϕ), flow resistivity (σ), tortuosity (α_∞), viscous (Λ) and thermal (Λ') characteristic lengths.

The characteristic impedance (Z_c) and wavenumber (k_c) can then be determined from equation (S1-5) and (S1-6), respectively:

$$Z_c = \sqrt{K_e \rho_e} \quad (\text{S1-5})$$

$$k_c = \omega \sqrt{\frac{\rho_e}{K_e}} \quad (\text{S1-6})$$

These equations allow the calculation of the normal incidence surface impedance (Z_s), R and α , as expressed in equations (S1-7), (S1-8) and (S1-1), respectively.

$$Z_s = -i Z_c \cot(k_c d) \quad (\text{S1-7})$$

$$R = \frac{Z_s - Z_0}{Z_s + Z_0} \quad (\text{S1-8})$$

Methods to measure the non-acoustic properties.

The porosity was calculated as expressed by equation (P1-2) in the manuscript.

The flow resistivity was indirectly measured from the low frequency acoustic behaviour of the samples in a standard impedance tube with two different terminations (i.e., anechoic and open), according to equation (S1-9) [10, 11]:

$$\sigma = \lim_{\omega \rightarrow 0} [-\text{Im}(Z_c k_c)] \quad (\text{S1-9})$$

where Z_c and k_c were evaluated following the transfer matrix approach detailed in the standard test method ASTM E2611 [7].

The tortuosity was determined with ultrasonic wave speed measurements in a sample saturated by air, according to equation (S1-10) [12]:

$$\alpha_{\infty} = \left(\frac{C_0}{C}\right)^2 (1 - 2\varphi) \quad (\text{S1-10})$$

where the ratio of celerity in free air over velocity inside the porous material (C_0/C) was calculated from the increase of the time of flight of a short ultrasonic pulse sent at 50 kHz between two transducers when a sample of the material was inserted. The loss angle (φ) was derived from the pulse signal damping.

The viscous and thermal characteristic lengths were finally obtained using an inverse identification method [13, 14]: The sound absorption coefficient predicted by the JCA model was fitted to the acoustical experimental data by varying Λ and Λ' and keeping all the other non-acoustic properties fixed to the experimentally or indirectly derived values.

Supplementary References


1. Lu, B. *et al.* High performance broadband acoustic absorption and sound sensing of a bubbled graphene monolith. *Journal of Materials Chemistry A* **7**, 11423-11429, doi:10.1039/C9TA02306B (2019).
2. Nine, M. J. *et al.* Graphene Oxide-Based Lamella Network for Enhanced Sound Absorption. *Advanced Functional Materials* **27**, 1703820, doi:<https://doi.org/10.1002/adfm.201703820> (2017).
3. Hasani Baferani, A., Katbab, A. A. & Ohadi, A. R. The role of sonication time upon acoustic wave absorption efficiency, microstructure, and viscoelastic behavior of flexible polyurethane/CNT nanocomposite foam. *European Polymer Journal* **90**, 383-391, doi:<https://doi.org/10.1016/j.eurpolymj.2017.03.042> (2017).
4. Wang, C. *et al.* Cellulose as an adhesion agent for the synthesis of lignin aerogel with strong mechanical performance, Sound-absorption and thermal Insulation. *Scientific Reports* **6**, 32383, doi:10.1038/srep32383 (2016).

5. Sun, Z., Shen, Z., Ma, S. & Zhang, X. Sound absorption application of fiberglass recycled from waste printed circuit boards. *Materials and Structures* **48**, 387-392, doi:10.1617/s11527-013-0190-6 (2015).
6. ASTM E1050-19, Standard Test Method for Impedance and Absorption of Acoustical Materials Using a Tube, Two Microphones and a Digital Frequency Analysis System, ASTM International, West Conshohocken, PA, 2019,. doi:10.1520/E1050-19.
7. ASTM E2611-19, Standard Test Method for Normal Incidence Determination of Porous Material Acoustical Properties Based on the Transfer Matrix Method, ASTM International, West Conshohocken, PA, 2019,.
8. Johnson, D. L., Koplik, J. & Dashen, R. Theory of dynamic permeability and tortuosity in fluid-saturated porous media. *Journal of Fluid Mechanics* **176**, 379-402, doi:10.1017/S0022112087000727 (1987).
9. Champoux, Y. & Allard, J. F. Dynamic tortuosity and bulk modulus in air-saturated porous media. *Journal of Applied Physics* **70**, 1975-1979, doi:10.1063/1.349482 (1991).
10. Tao, J., Wang, P., Qiu, X. & Pan, J. Static flow resistivity measurements based on the ISO 10534.2 standard impedance tube. *Building and Environment* **94**, 853-858, doi:<https://doi.org/10.1016/j.buildenv.2015.06.001> (2015).
11. Doutres, O., Salissou, Y., Atalla, N. & Panneton, R. Evaluation of the acoustic and non-acoustic properties of sound absorbing materials using a three-microphone impedance tube. *Applied Acoustics* **71**, 506-509, doi:<https://doi.org/10.1016/j.apacoust.2010.01.007> (2010).
12. Allard, J. F., Castagnede, B., Henry, M. & Lauriks, W. Evaluation of tortuosity in acoustic porous materials saturated by air. *Review of Scientific Instruments* **65**, 754-755, doi:10.1063/1.1145097 (1994).
13. Atalla, Y. & Panneton, R. Inverse acoustical characterization of open cell porous media using impedance tube measurements. *Canadian Acoustics* **33**, 11-24 (2005).
14. Fellah, Z. E. A., Mitri, F. G., Fellah, M., Ogam, E. & Depollier, C. Ultrasonic characterization of porous absorbing materials: Inverse problem. *Journal of Sound and Vibration* **302**, 746-759, doi:<https://doi.org/10.1016/j.jsv.2006.12.007> (2007).

5.3 Multifunctional properties of modified graphene oxide composite aerogels

The statement of Authorship Form and the paper can be found next, followed by the relevant supplementary information.

This declaration concerns the article entitled:	
<i>Multifunctional thermal, acoustic and piezoresistive properties of in situ modified composite aerogels with graphene oxide as the main phase.</i>	
Publication status (tick one)	
Draft Manuscript <input type="checkbox"/> Submitted <input type="checkbox"/> In Review <input type="checkbox"/> Accepted <input checked="" type="checkbox"/> Published <input type="checkbox"/>	
Publication details (reference)	Not available
Copyright status (tick the appropriate statement)	
I hold the copyright for this material <input type="checkbox"/>	
Copyright is retained by the publisher, but I have been given permission to replicate the material here <input checked="" type="checkbox"/>	
Candidate's contribution to the paper (provide details, and also indicate as a percentage)	The candidate contributed to / considerably contributed to / predominantly executed the... Formulation of ideas: 90% <i>I presented the idea of chemical modification of the aerogels to Prof. M. Meo, who approved with some suggestions.</i> Design of methodology: 100% <i>I designed both manufacturing and characterisation plans.</i> Experimental work: 100% <i>I manufactured and characterised all the samples.</i> Presentation of data in journal format: 90% <i>I defined paper structure, wrote the first draft and designed the figures. Prof. Meo reviewed the manuscript and supported in the submission and publication process.</i>

Statement from Candidate	This paper reports on original research I conducted during the period of my Higher Degree by Research candidature.		
Signed			Date 16/07/2022

Multifunctional Thermal, Acoustic and Piezoresistive Properties of In Situ Modified Composite Aerogels with Graphene Oxide as the Main Phase

Mario Rapisarda¹ and Michele Meo^{1,*}

¹*University of Bath, Department of Mechanical Engineering, Bath, BA27AY, UK*

**Corresponding author*

Abstract

Automotive and aerospace industries require advanced materials capable of multifunctional abilities while guaranteeing limited weight and volume, and a simple processing. On this context, cellular materials as graphene-based aerogels represent a promising solution. In this study, chemical modification approaches of graphene oxide and polyvinyl alcohol (GOP) aerogels are presented. The combination of a plasticising agent, glycerol, and of a cross-linking agent, glutaraldehyde, is exploited to obtain a mechanically balanced and robust cellular structure. As modified GOP aerogels show high elastic resilience (energy loss coefficient of 29% and 5 kPa of compressive strength at 30% strain, after the 10th compression cycle), low thermal conductivity (0.0424 W mK⁻¹), and high sound absorption (average coefficient of 0.72 between 500 and 1500 Hz), while maintaining a low density of 6.51 kg m⁻³ and a maximum thickness of 25 mm. Moreover, chemically reduced GOP (rGOP) aerogels are also synthesised. They are characterised by the additional feature of piezoresistive behaviour, with only a marginal impact on the other properties. For these reasons, modified GOP

and rGOP aerogels are promising candidates for the fabrication of multifunctional structures to be applied in advanced engineering applications.

1. Introduction

In the last decade, thanks to the inherent properties of high porosity, large surface area, and low density, aerogels have been extensively studied for aerospace and automotive applications [1, 2]. In addition, advanced structures for these industries are usually required to provide multiple functionalities while respecting limited weight and size and, additionally, should derive from cheap and easy to process materials [3]. A particular class of aerogels derives from graphene oxide (GO) suspensions in water, which are able to self-assemble in three-dimensional microstructures thanks to oxygen groups functionalising the hexagonal lattice of carbon atoms [4]. Although pristine GO aerogels have already been successfully used for environmental applications [5, 6], they can further be functionalised by their combination with other chemical substances [7]. As a result, specific properties can be tuned and optimised. As examples, Wan et al. developed efficient visible-light photocatalysts by functionalising GO with C_3N_4 [8], while Lihui and co-authors incorporated GO into alginate matrix to enhance oil/seawater separation [9]. Moreover, oxygen functionalities can be chemically or thermally removed, making reduced GO (rGO) aerogels electrically conductive [10]. This allowed the development of supercapacitive performance [11], piezoresistive properties [12], or electromagnetic absorption [13]. Despite the described intriguing results, complex synthesis methods, the need of exotic chemicals, or the achievement of high performance only in highly specific conditions, have however limited GO aerogels scale-up and practical use.

In our previous work, we presented an environmentally friendly manufacturing process for the fabrication of ultralight aerogels from optimised blends of GO and polyvinyl alcohol (PVA) [14]. Although very promising sound insulation performances were demonstrated, the study was lacking the inspection of other fundamental properties such as thermal stability and conductivity and mechanical strength. From preliminary evaluations it was found that the unbalance between the bulky PVA molecules and the light GO sheets, and the absence of stable cross-links between the two components was limiting the development of an organised cellular structure with high elastic resilience. Modification approaches of GO and PVA blends (GOP) were then evaluated. The enhancement due to the reduced intermolecular forces along PVA polymer chains after the addition of a plasticizer was demonstrated by Cobos et al., by adding Glycerol (GLY) to chitosan/GO nanocomposites [15], and by Hwang et al, improving the electromechanical performance thanks to dibutyl adipate and GO inclusion in PVC gels [16]. In addition, Zheng et al. proved cross-links formation between the hydroxyl groups present in PVA and hydroxylated carbon nanotubes using Glutaraldehyde (GA) successfully [17]. With a similar proposed mechanism, GA showed cross-linking capabilities between PVA molecules and rGO sheets for the fabrication of water-induced self-recoverable graphene aerogels for water treatment [18].

Herein, modified GOP composite aerogels with multifunctional abilities were fabricated by ultra-high shear mixing promoted foaming followed by freeze-casting and freeze-drying. Two modification agents, GLY and GA, were used to enhance the cellular structure of the material. The first was chosen for its ability to relax the molecular interactions between bulky PVA molecules, while the second allows cross-links formation between GO sheets and PVA molecules. Such enhancements were confirmed by a chemico-physical characterisation of GOP aerogels with varying amounts of

the modification agents. Optimised amounts were chosen for their combined use and multiple abilities of thermal and acoustic insulation and of elastic resiliency were demonstrated. A chemically reduced GOP (rGOP) composite aerogel was also fabricated, which additionally proved piezoresistive properties.

Although the use of GLY to enhance the structure of PVA composite, of GA as a medium for the cross-linking of PVA or GO composite materials, and of AA as GO reducing agent was previously discussed in the literature, to the best of our knowledge the combined and optimized use of the aforementioned agents was never considered in composite aerogels where GO represent the main phase. The novelty of the current work consists therefore in the ability to integrate the modifications approach in the manufacturing process of the ultralight GO and PVA aerogels previously presented, with the only additional step of cross-linking and reduction before the freeze-casting-drying. Such approach allowed the enhancement of the cellular structure of the composite aerogel guaranteeing lightness, mechanical robustness, acoustic and thermal insulation, and, when AA is used to promote GO reduction, piezoresistive properties.

In the result and discussion section, the fabrication and optimization of modified GOP aerogels is firstly discussed. The role and effects of the two modification agents, GLY and GA, and of the reducing agent, AA, during the manufacturing process is described, and further confirmed through a chemicophysical characterization. The multifunctional properties of the composite aerogel are then presented in the following paragraphs, starting from a physical and thermal analysis, followed by the characterization of the acoustic behavior and by the evaluation of the mechanical performance. Finally, a detailed explanation of the piezoresistive properties is discussed in the last paragraph.

2. Materials and methods

2.1. Materials

Powdered Graphite Oxide was purchased from Xiamen TOB New Energy, PVA pellets (98-99% hydrolyzed, medium molecular weight), GA solution (grade II, 25% in H₂O), and AA (anhydrous) were obtained from Sigma Aldrich, GLY (99.6%) and H₂SO₄ solution (0.1 M) were supplied by Fisher Scientific. Deionized MilliQ[®] was used throughout all the experiments. All the chemicals were used as received without further treatment or purification.

2.2. Precursors preparation

A GO suspension in water (8 mg mL⁻¹) was obtained via probe sonication (Dr. Hielscher GmbH UP100H) of GtO for 40 min under vigorous magnetic stirring and in an ice bath. PVA pellets were dissolved in water (5 wt%) through magnetic stirring at a temperature of 90 °C for 4 h. Pre-plasticised PVA was obtained similarly, by adding the plasticising agent, GLY, to the PVA solution in proper amounts after 2 h of hot stirring.

2.3. Synthesis of modified GO aerogels

The modified GOP aerogels were synthesised with proper adjustments to the previously reported method of ultra-high shear mixing and unidirectional freeze-casting of GO and PVA blends [14]. Typically, the two components were mixed in a 1:1 ratio with low-shear magnetic stirring for 1 h, followed by 5 min of ultra-high shear mixing (IKA Ultra-Turrax T25) at 13,000 rpm. The foamed blends were then embedded in Nomex HC cores and freeze-casted cores with the aid of silicone moulds, which were placed on an aluminium heat-sink submerged in liquid nitrogen. Finally, the ice-templated structures were freeze-dried (LTE LyoTrap Mini) for 96 h. Plasticised GO aerogels were obtained similarly but using a pre-plasticised PVA with GLY

content of 5, 10, 20, and 30 wt%_{GLY[PVA]} (denoted as pl_x-GOP, where *x* indicates the concentration of GLY with respect of PVA weight). Cross-linked GOP aerogels were synthesised with the following additional steps: the cross-linking agent, GA, was added to the PVA solution in varying amounts of 7.5, 10, 12.5, and 15 wt%_{GA[GO+PVA]}, with H₂SO₄ as catalyst (6 wt%_{H₂SO₄[GA]}); in addition, prior to freeze-casting the foamed blends were cross-linked in oven at 60 °C for 4 h and then cooled down to ambient temperature. The as-obtained aerogels are denoted as cl_y-GOP, where *y* indicates the concentration of GA with respect of GO and PVA weight. Furthermore, both the described modification approaches were combined in plasticised and cross-linked GOP aerogels: they were obtained as described for cl_y-GOP, upon using the pre-plasticised PVA. Optimised amounts of GLY (20 wt%_{GLY[PVA]}) and of GA (10 wt%_{GA[GO+PVA]}) were determined from a preliminary evaluation of the physicochemical properties of pl_x-GOP and cl_y-GOP aerogels. The sample is denoted as pl₂₀cl₁₀-GOP. Finally, aerogels where GO was chemically reduced were manufactured as reported for pl₂₀cl₁₀-GOP, with the addition of the reducing agent, AA, to GO, prior to its mixing with pre-plasticised PVA. A 4:1 mass was chosen and 10 min of bath ultrasonication were applied to ensure an intimate dispersion. The sample was denoted as rGOP, with the “pl₂₀cl₁₀-” appendix omitted for the sake of clarity. Modification procedures are summarised in Figure S2-1.

2.4. Physicochemical characterisation

The surface morphology and structure of the modified GOP aerogels were evaluated with Scanning Electron Microscopy (SEM, Hitachi SU3900). Fourier Transform Infrared Spectroscopy (FT-IR, Perkin-Elmer Frontier FTIR Spectrometer) and Raman Spectroscopy (Renishaw inVia Raman microscope, 532 nm laser source) were used to investigate the chemical structure. The crystalline phases were analysed by transmission powder x-

ray diffractometry (XRD, STOE STADI P, CuK α generator). From the latter, the interplanar distance (d) was calculated according to Bragg's law (Equation (P2-1)) [19]:

$$d = \frac{\lambda}{2 \sin \theta} \quad (\text{P2-1})$$

where λ is the radiation wavelength and θ is the reflection angle of the characteristic (001) feature. The density (ρ_s) of each sample was estimated from their weight and volume.

2.5. Evaluation of multifunctional properties

The thermal properties of the modified aerogels were evaluated by thermogravimetric analysis (Setaram SETSYS Evolution 16 TGA/DTA) and thermal conductivity measurements (Hot Disk TPS 500 S) with the transient plane source method. The acoustic behaviour was investigated by sound absorption coefficient (α) and sound transmission losses (STL) measurements with a custom-built impedance tube following the standard test methods ASTM E1050 and ASTM E2611 [20, 21], respectively. The mechanical performance was characterised by in-plane compression testing (Instron 3369, 100 N loadcell) with both static (0 to 70% strain with a speed of 10 mm min⁻¹) and dynamic loadings (10 cycles between 5 and 30% strain at 10 mm min⁻¹). For rGOP aerogels only, the electrical conductivity between the top and bottom surfaces was simultaneously measured: the connection with a digital multimeter (Keysight 34450A) was realised by two electrodes made of Cu tape and Ag conductive paste. The normalised electrical resistance (\bar{R}) and the normalised electrical resistance change ($\bar{\Delta R}$), defined as expressed in Equations (P2-2) and (P2-3), were calculated to evaluate the piezoresistive behaviour:

$$\bar{R} = \frac{R_i}{R_0} \quad (\text{P2-2})$$

$$\overline{\Delta R} = \frac{R_i - R_{i-1}}{R_{i-1}} \quad (\text{P2-3})$$

where R_i , R_0 and R_{i-1} are electrical resistance values at the instant i , at the start of the testing, and at the instant $i - 1$, respectively.

3. Results

3.1. Fabrication and optimisation of modified GOP aerogels

The possibility to prepare aerogels from GO homogeneous suspensions derives from their ability to self-assemble in 3D structures when unidirectionally frozen. As the bottom surface of the mould is exposed to a very low temperature (i.e., during the contact with the aluminium heatsink at ~ -190 °C thanks to the use of liquid nitrogen), small ice crystals nucleate and grow vertically pushing the solid suspension at their boundaries and thus allowing for the formation of a templated structure. The ice can subsequently be extracted promoting its sublimation (i.e., in drying chambers where temperature and pressure are below the triple point of water), and the remaining solid GO structure is held by Van der Waals forces acting among GO sheets. With the aim to obtain aerogels satisfying the following criteria: tuneable porosity and shape, lightweight yet mechanically robust, and capable of multifunctional properties, GO can be functionalised with other chemical compounds. It was previously demonstrated that PVA can be mixed with GO in homogeneous blends thanks to hydrogen bonds between their molecules (Figure P2-1 – a). Moreover, the peculiar physical properties of such blends allow the controlled inclusion of air bubbles during an ultra-high shear mixing step, leading to an ultralight aerogel with hierarchical porosity [14]. In order to further tune the structure and improve the mechanical robustness of the

aerogels, a plasticising and a cross-linking agent, GLY and GA respectively, were also introduced in the blend for this study. As schematised in Figure P2-1 – b, the two agents would affect the chemical structure of GOP with GLY weakening the interactions between PVA molecules and with GA providing cross-linking sites between PVA molecules and GO sheets.

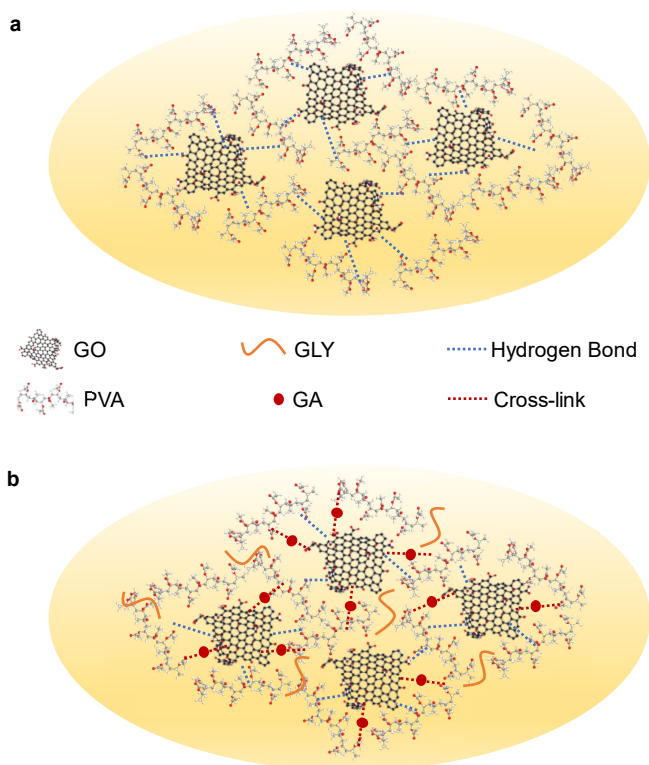


Figure P2-1 – Proposed chemical structure. Schematic diagrams of (a) un-modified and (b) modified GOP blends.

An optimised amount for each of the two agents was chosen on the basis of a physicochemical characterisation and of a qualitative analysis of blends processability and resulting aerogel robustness. XRD patterns in Figure S2-2 – a show the shift of the (001) crystalline phase of from 10.67° of GO to 4.67° of GOP, indicating a more expanded structure due to the intercalation of PVA molecules [22, 23]: according to Bragg's law, reported in Equation (P2-1), the interplanar distance between GO sheets increases from 8.28 to 18.90 Å. It is also possible to observe a negligible effect of GLY

inclusion in various amounts to pl_x -GOP crystalline structure. Figure S2-2 – b presents FT-IR spectra, which prove the existence of hydrogen bonds between the oxygen groups of GO and the hydroxyl functionalities of PVA [24, 25]. Moreover, it is shown that increasing amounts of GLY cause a proportional weakening and shift of the C-O-C stretching of PVA around 1083 cm^{-1} , thus indicating a successful interaction of the plasticiser with PVA molecules [26]. As pictured in Figure S2-2 – c, GA inclusion in cl_y -GOP has instead a marked impact on the crystalline structure. Particularly, the (101) peak of PVA disappears and the (001) feature of GO becomes sharper and shifts to lower degrees proportionally with GA amount: from 4.67° of GOP to 3.52° of $cl_{7.5}$ -GOP, down to 3.05° for cl_{15} -GOP. Both the phenomena confirm that GA effectively act as cross-linker between GO sheets and PVA molecules, resulting in a more expanded structure (d increasing from 18.90 \AA of GOP, to $25.07\text{-}28.93\text{ \AA}$ depending on GA amount) with the PVA phase now completely amorphous [27]. Accordingly, FT-IR spectra in Figure S2-2 – d show the formation of acetal bridges between pendant OH groups in the region between 3000 and 2800 cm^{-1} and of ether chemical bonds between 1000 and 1150 cm^{-1} , proportionally as well with included GA amount [28, 29]. In terms of processability, GLY addition up to the $20\text{ wt}\%_{GLY[PVA]}$ led to an increase of the viscosity of the blend, consequently resulting in an improved stability of entrapped air bubbles. Conversely, in pl_{30} -GOP the too high viscosity led to difficulties in the control of the ultra-high shear mixing. Starting from the $10\text{ wt}\%_{GLY[PVA]}$, also the mechanical robustness improved with a marked reduction of the brittle behaviour characterising the un-modified GOP aerogel. For cl_y -GOP blends the foaming process resulted negatively affected (i.e., decreased stability of entrapped air bubbles) by GA inclusion already in the smallest amount of $7.5\text{ wt}\%_{GA[GO+PVA]}$ and proportionally worsened for higher amounts until no air bubbles could be entrapped in cl_{15} -GOP. Besides, the mechanical robustness was highly improved with a remarkable elastic behaviour for

concentration of GA up to the 10 wt%_{GA[GO+PVA]}, while higher concentrations of GA led to an excessively bulky and brittle structure.

Due to the aforementioned reasons, the amounts of 20 wt%_{GLY[PVA]} and of 10 wt%_{GA[GO+PVA]} were chosen as optimum values for the manufacturing of pl₂₀cl₁₀-GOP aerogels where the two modification approaches were combined. The latter blend composition was also used for the fabrication of modified aerogels with improved electrical properties, thanks to the reduction of GO promoted by the used of AA as reducing agent. From XRD patterns in Figure P2-2 – a it is possible to observe a further expansion of the crystalline structure from 26.03 Å (3.39°) of cl₁₀-GOP to 28.19 Å (3.13°) of pl₂₀cl₁₀-GOP, while after the reduction rGOP shows only a slight restacking to 26.82 Å (3.29°). Figure P2-2 – b presents the FT-IR spectra where the presence of both GLY interaction with PVA molecules and ether cross-links between GO sheets and PVA molecules promoted by GA is confirmed. In rGOP spectrum, it is possible to observe the reduction of oxygen related features such as hydroxyl groups vibration and deformation at around 3400 cm⁻¹ and at 1413 cm⁻¹, respectively, and alkoxide, epoxide, and peroxide groups vibrations between 1050 and 900 cm⁻¹ [30, 31]. Moreover, a new band is visible at 1576 cm⁻¹, which is attributable to the aromatic C=C stretching and thus to the restoration of the sp² lattice [32]. Raman spectra of Figure P2-2 – b were collected to obtain more insights on GO reduction and its effects on the carbonaceous structure, while no significant differences are observed upon addition of GLY and GA to the unmodified GOP. In particular, pristine GO shows two main bands at 1352 cm⁻¹ (D) and 1606 cm⁻¹ (G) and secondary scatterings between 2680 and 3200 cm⁻¹ (Figure S2-2 – e). The first two are associated to the A_{1g} breathing mode caused by structural disorder and to the E_{2g} vibrating mode of ordered graphite crystallites [33]. They can be quantitatively analysed and compared with the calculation of the ratio of their intensities, the I_D/I_G ratio, which is an

index of the structural disorder [34]. Three additional interbands can also be considered for a more exact deconvolution of the signal: the D^* at $\sim 1140\text{ cm}^{-1}$, associated to sp^2 - sp^3 bonds at the edge of the hexagonal lattice of carbon atoms, the D'' at $\sim 1540\text{ cm}^{-1}$, due to amorphous regions with interstitial defects; and D' at $\sim 1620\text{ cm}^{-1}$, a phonon mode caused by crystal defects [35]. All the previously described features are observed in both unmodified GOP and in $pl_{20}cl_{10}$ -GOP aerogels, without significant differences. PVA main features, which are shown at 1440 and 2914 cm^{-1} (Figure S2-2 – e), result absent in all the aerogels, explainable with the amorphous nature of PVA intercalated phase as well as with the much higher intensity of the signal generated by carbonaceous structure [36]. It is crucial to observe the behaviour of the I_D/I_G ratio, which is equal to 0.88 in both GOP and $pl_{20}cl_{10}$ -GOP but sharply increases to 1.03 in rGOP. The latter is a clear sign of a successful reduction of GO to rGO during which the oxygen functionalities are removed by their reaction with AA, leading to a partially increased disorder in the structure but most importantly to the restoration of the hexagonal lattice of sp^2 carbon atoms which will be responsible to the improved electrical properties [37].

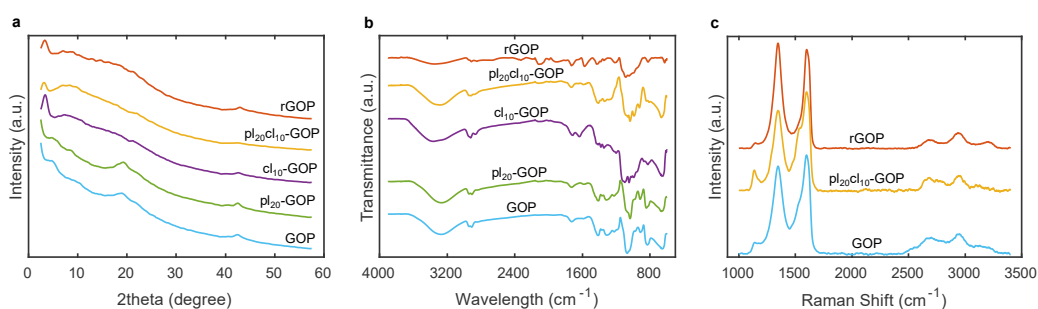


Figure P2-2 – Physicochemical characterisation of modified GOP aerogels. (a) XRD patterns, (b) FT-IR spectra, and (c) Raman spectra.

3.2. Physical and thermal properties

The surface morphology of cryogenically fractured aerogels is pictured in Figure P2-3. From low magnification images (Figure P2-3 – a-e), the

hierarchical porosity derived from the inclusion of air bubbles during the ultra-high shear mixing is visible for all samples although with some differences. Particularly, the stabilising effect of GLY and the detrimental one of GA on air bubbles during the processing is highlighted in Figure P2-3 – b-c, respectively. When both the agents are included in pl₂₀cl₁₀-GOP, the two opposing effects appear balanced (Figure P2-3 – d), while no differences with respect of the latter can be appreciated in rGOP (Figure P2-3 – e). Observing higher magnification images (Figure P2-3 – f-i), while GLY inclusion leads to a more ordered pore geometry and to more defined walls with respect of the un-modified GOP (Figure P2-3 – f-g), the cross-links in cl₁₀-GOP results in a bulkier structure with less interconnection between the pores (Figure P2-3 – h). The presence of both the agents leads to an interconnected porous structure, although with bigger pores with respect of GOP or pl₂₀-GOP (Figure P2-3 – i). Figure P2-3 – j shows that pl₂₀cl₁₀-GOP and rGOP structures are similar, but with thicker pore walls for the latter.

The variation of the physicochemical structure of modified aerogels directly affects their density and thermal conductivity (Figure P2-3 – k). Particularly, the unmodified GOP shows the lowest values for both: 2.10 kg m⁻³ and 0.0374 W mK⁻¹. The addition of 20 wt%_{GLY}[PVA] or 10 wt%_{GA}[GO+PVA] causes an increase for both the properties, with a bigger impact from GA (8.51 kg m⁻³ and 0.0413 W mK⁻¹). Interestingly when combined in pl₂₀cl₁₀-GOP, the modifying agents leads to an intermediate density of 6.51 kg m⁻³, thanks to the increased porosity, while the thermal conductivity reaches 0.0424 W mK⁻¹, explainable with the cross-linked pore walls. GO reduction severely affected both density and thermal conductivity, showing values of 19.92 kg m⁻³ and 0.0479 W mK⁻¹, respectively. The first is due to a reduced ability of the blend to stabilise air bubbles after the addition of AA, while the

second derives the partial restoration of the carbon lattice after the removal of oxygen functionalities.

The thermal stability of the aerogels was also evaluated with TGA and derivative analysis (dTGA). As pictured in Figure S2-3, the thermal reduction of GO in GOP starts at a lower temperature (156 °C) with respect of pure GO (184 °C) but at a slower rate, PVA degradation is instead almost hindered and shifted from 268 °C (sharp peak) to ~330-416 °C (broad peak, due to the merging with other thermal events). GLY addition causes a shift of both GO reduction and PVA degradation to slightly lower temperature and higher rates, proportionally with its amount (Figure S2-3 – a). In cly-GOP, the cross-linking has the same average effect of slightly delaying GO reduction and increasing PVA degradation rate (Figure S2-3 – b). The addition of both the modification agents has a positive effect on the thermal stability up to 300 °C (GO reduction region), while PVA degradation starts at lower temperature (Figure P2-3 – I). Those results are in accordance with previous observations of GLY molecules weakening PVA chemical structure and GA forming cross-links between oxygen functionalities of GO and PVA. Due to the previous chemical reduction, oxygen groups of GO were already partially stripped and thus the thermal reduction of GO during rGOP thermal analysis had a much smaller rate. For the same reason, above 200 °C the almost complete removal of oxygen groups, which are the sites for GO interactions and cross-links with PVA molecules, led to a more severe degradation.

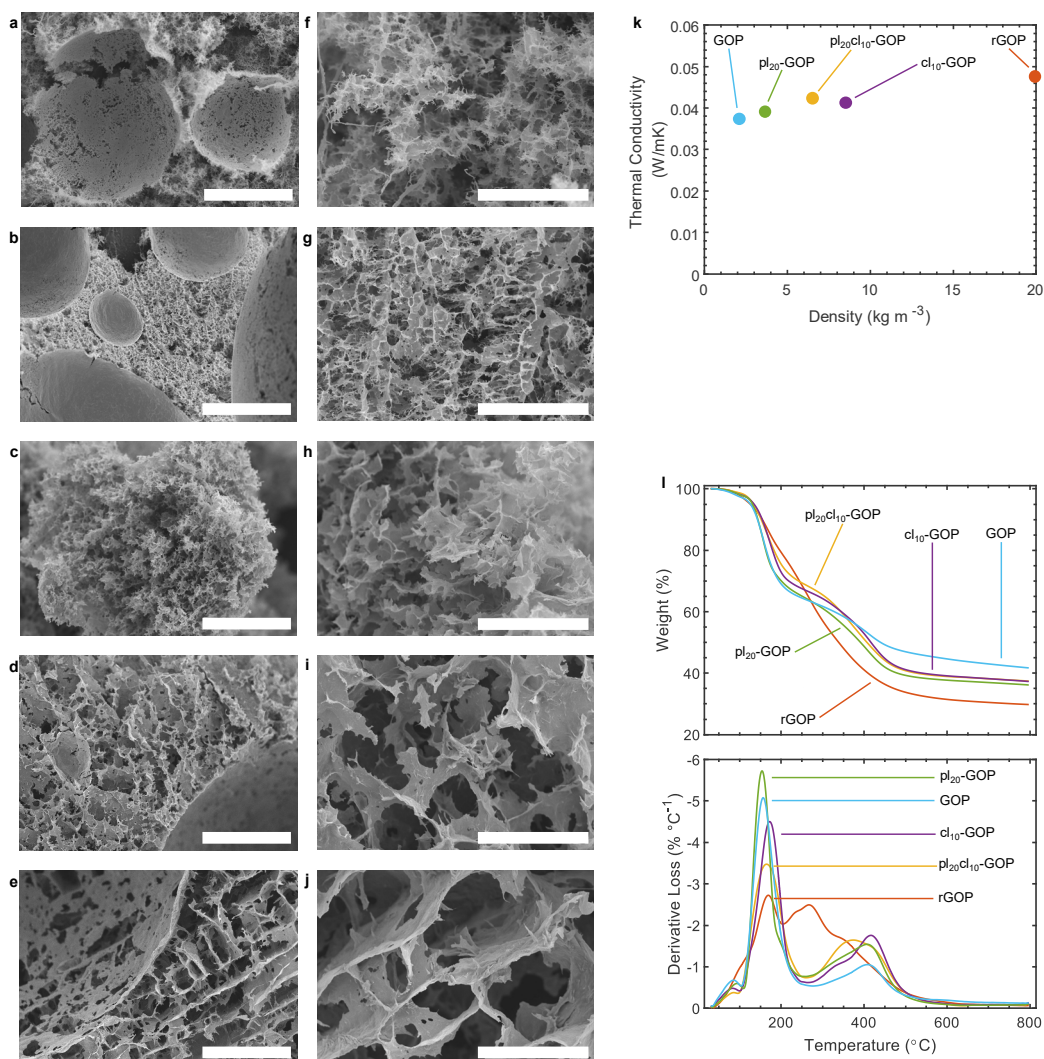


Figure P2-3 – Physical structure and thermal behaviour of modified GOP aerogels. SEM imaging of (a, f) GO, (b, g) pl₂₀-GOP, (c, h) cl₁₀-GOP, (d, i) pl₂₀cl₁₀-GOP, and (e, j) rGOP. Magnifications: (a–e) $\times 200$ (200 μm scalebar) and (f–j) $\times 1000$ (50 μm scalebar). (k) Variation of thermal conductivity and density with chemical composition. (l) TGA and dTGA curves.

3.3. Acoustic properties

The acoustic properties of modified GOP aerogels with a thickness of 25 mm are presented in Figure P2-4, where the effects of the different physicochemical structures are clearly visible in the variation of both α and STL with the frequency. The higher plasticity of pl₂₀-GOP causes a severe drop of sound absorption abilities above 500 Hz, while the increased

stiffness due to cross-linking in cl₁₀-GOP is reflected in a shift of the absorption peak to lower frequencies, at the cost of a 10% reduction of α (with respect of the un-modified GOP) in the low frequency region between 500 and 800 Hz. The combined effects of GLY and GA in pl₂₀cl₁₀-GOP leads instead to the best absorption performance up to 1500 Hz. The structural changes during GO reduction determine a shift of rGOP absorption peak to higher frequencies and an optimal behaviour in the mid-high frequency range between 1000 and 2500 Hz. For a direct comparison of the applicability of the modified aerogels as absorbing acoustic material, an average sound absorption coefficient ($\bar{\alpha}$) in the low-mid range between 500 and 1500 Hz was calculated. The best result of 0.72 was achieved by pl₂₀cl₁₀-GOP, immediately followed by the unmodified GOP with 0.68. pl₂₀-GOP and rGOP are the samples suffering most the structural modifications, with values of 0.54 and 0.59, respectively.

Transmission losses were similarly evaluated through an averaged coefficient in the 500-1500 Hz range (\overline{STL}). Considering the relation between α and the Reflection coefficient (R), $\alpha = 1 - |R|^2$, and that higher transmission losses can be predicted from a structure showing higher reflections [38], the best performance is expectedly found in pl₂₀-GOP with a very high \overline{STL} value of 15.54 dB. The values for the other samples fall instead in a range between 4.07 dB (rGOP) and 6.71 dB (GOP). The described acoustic behaviour can be explained by the cross-sectional distribution of large and small pores within the aerogels, which affects the damping properties of the different structures and in turn sound attenuation through the material [39]. Correspondingly, the numerical simulation conducted by Xie et al. suggest that slow-sound propagation could be achieved in subwavelength composite aerogels with inhomogeneous structure [40]. Those results well fit with the described physical structure

and acoustic behavior of modified GOP aerogels, with particular evidence in the effects of the addition of the plasticizing agent seen in pl20-GOP.

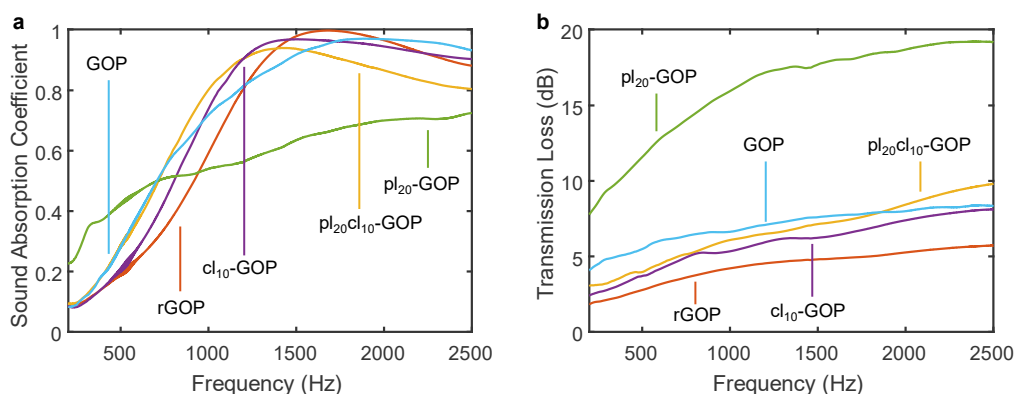


Figure P2-4 – Acoustic properties of modified GOP aerogels. (a) Sound Absorption Coefficient and **(b)** Sound Transmission Loss.

3.4. Mechanical properties

The mechanical properties of the manufactured aerogels were quantified through static in-plane compression tests up to 70 % strain. Three different regions can be distinguished in the stress-strain curves pictured in Figure P2-5 – a: an elastic region for strain below 20 %, a plateau region for strain between 20 and 50 %, and a densification region for strain above 50 %. Moreover, no signs of structural failure can be observed. A reduction of the compressive strength with respect of the un-modified GOP reference is found in pl₂₀-GOP, as a consequence of the plasticising agent interaction with PVA molecules. Conversely, cross-links created between GO and PVA thanks to GA addition allow for a marked improvement of cl₁₀-GOP compressive performance. Both the agents synergically determine a further improvement in pl₂₀cl₁₀-GOP mechanical strength. A different behaviour is instead seen in rGOP, where the partial loss of cross-links due to GO reduction leads to reduced elastic and plateau region, now up to the 40 % of strain, whereas the bulkier structure is responsible for the highest compression strength in the densification region.

To further evaluate the structural robustness of the modified aerogels, dynamic testing with 10 loading-unloading cycles of in-plane compression up to 30 % strain were performed, with the 2nd and 10th cycles pictured in Figure P2-5 – b-c, respectively. Hysteresis loops can be observed, indicating a resilient nature of the aerogels with energy dissipation due to the buckling of pore walls, friction and adhesion between the molecules, and formation of micro-fractures in the first cycles. These phenomena can be analysed with the variation of the energy loss coefficient and maximum compression strength with cycle number (Figure P2-5 – d-e). All the aerogels show a similar behaviour with the energy loss decreasing in the first 4 cycles, before reaching more stable values. The absence of cross-links and the structural integrity entrusted only to the secondary π - π interactions between GO sheets and hydrogen bonds between GO and PVA is responsible for the low resiliency and low maximum compression strength of un-modified GOP, with GLY plasticising effects on PVA molecules causing a further worsening. Nevertheless, the formation of cross-links promoted by GA dramatically improves both the properties in cl₁₀-GOP, with a further enhancement after the combined modifications in pl₂₀cl₁₀-GOP. Accordingly, it possible to speculate that plasticising molecules weakens PVA stiff nature and enable GO sheets and thus pore walls to bend and buckle more freely under compression. For the same reason, rGOP resiliency is not affected although the partial loss of cross-links determines a slight reduction of the compression strength in the plateau region.

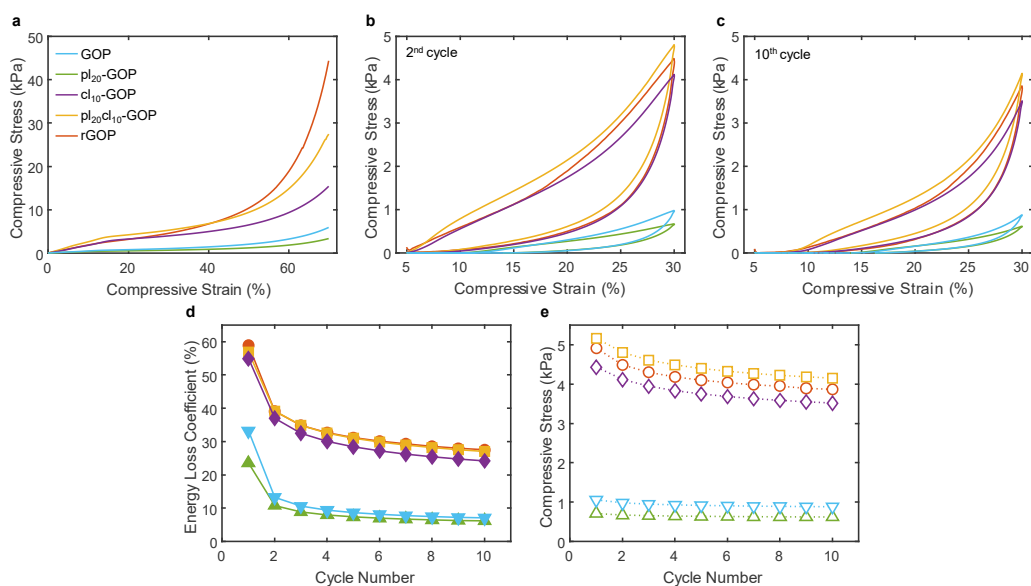


Figure P2-5 – Mechanical properties of modified GOP aerogels. (a) Static compression loading from 0 to 75% strain, **(b)** 2nd and **(c)** 10th cycles of the dynamic compression loading between 5 and 30% strain. **(d, e)** Trend of Energy Loss Coefficient and Maximum Compression Stress with cycle number. Same legend applies for all the panels.

3.5. rGOP aerogel piezoresistive properties

The partial restoration of the hexagonal lattice of sp² carbon atoms occurring during GO chemical reduction, is responsible for improved electrical properties in rGOP aerogels. Particularly, by monitoring the electrical resistance during compression tests it was possible to observe an intriguing piezoresistive behaviour. Two parameters, \bar{R} and $\overline{\Delta R}$, were analysed for this purpose (see Methods for more information). The trend of \bar{R} compared to the stress-strain curve during the static testing is shown in Figure P2-6 – a, with a 92.3 % decrease at 70 % of strain. This is due to the densification of the structure (i.e., reduction of distance between rGO sheets) and the formation of new contacts points between pore walls. Moreover, a linear relationship between $\overline{\Delta R}$ and the strain is found in the elastic and plateau region, after which the trend becomes exponential (Figure P2-6 – b). The initial steep variation is due to an increase of the contact area of the electrodes, while the anomalous variation around 65 %

strain can be attributed to a densification phenomenon. During dynamic testing, the small variation of $\overline{\Delta R}$ value further confirms the resilience of rGOP aerogels structure (Figure P2-6 – c). Additionally, from Figure P2-6 – d it is interesting to observe how after the first cycles, $\overline{\Delta R}$ can precisely track the cycling of the applied strain.

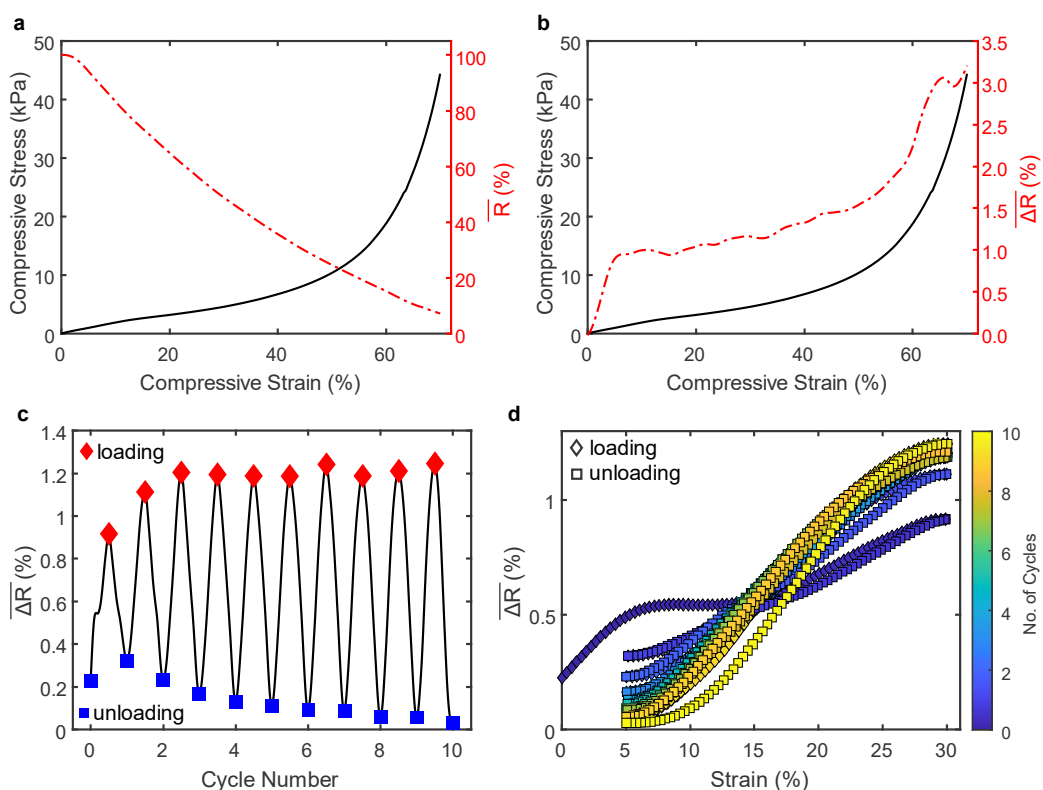


Figure P2-6 – Piezoresistive behaviour of rGOP aerogels. (a) Stress-strain curve and trend of the normalised electrical resistance (R/R_0) and **(b)** relationship between the normalised electrical resistance change ($\Delta R/R_0$) and the strain during static compression testing. **(c)** Trend of $\Delta R/R_0$ during cyclic compression testing. **(d)** Relationship between $\Delta R/R_0$ and the strain during cyclic compression testing.

4. Discussion

In this work, an in-situ modification approach for graphene aerogels obtained from foamed blends of GO and PVA was proposed. The aim was to keep and, eventually, tune the main features of the reference aerogel (GOP), such as the lightweight, the hierarchical porosity, the sound and

thermal insulating abilities, while improving the mechanical robustness, and as shown for rGOP, extend the functionalities thanks to the piezoresistive behaviour. Two modification agents were adopted, a plasticiser (GLY) and a cross-linker (GA). Their effects on the physicochemical structure, due to the interaction with and between rGO sheets and PVA molecules, were studied and optimised. Both the agents were introduced to the blends through specifically designed additional steps that didn't affect the processability (i.e., ability to include and stabilise air-bubbles during the ultra-high shear mixing) and the fabrication process in general (i.e., possibility to embed the aerogel in structural HC cores). Thanks to this approach, the pl₂₀cl₁₀-GOP aerogel benefitted of the modifications in terms of sound absorption abilities in the critical range of 500-1500 Hz, showing an increased average absorption coefficient of 0.72 while keeping a very low thermal conductivity of 0.0424 W mK⁻¹. Most importantly, the optimised sample showed a three-fold improvement of the compressive strength and of the energy loss coefficient during static and dynamic mechanical testing, respectively. Even though the modification causes an increase of the density of the material, now reaching 6.51 kg m⁻³, the presented pl₂₀cl₁₀-GOP aerogel is still one of the lightest ever reported in literature and yet being able to be used as a robust sound and heat insulator within structural HC cores (Table S2-1) [14, 17, 41-50].

It is crucial to mention that the adopted modification approach also allows the tuning of aerogels final properties for a specific application, with two examples that can be given from this research work. The first one is the pl₂₀-GOP aerogel where the weakening action of GLY molecules to PVA stiff phase led to the assembly of a more ordered pores geometry and a plastic mechanic behaviour. This was reflected in the sound transmission abilities, where the extremely high \overline{STL} value of 15.54 dB and a maximum of almost 20 dB reached at 2500 Hz were recorded, thanks to the improved

damping properties. Contemporary, the density and the thermal conductivity of the assembled aerogel (3.65 kg m^{-3} and 0.0391 W mK^{-1} , respectively) only marginally increased with respect of the un-modified reference. The as described features renders the pl_{20} -GOP aerogel an ideal candidate for applications where high transmission loss and thermal insulation are desired, while maintaining an extremely low weight. Slightly different is the case of the rGOP aerogel, where the chemical reduction of GO obtained through the addition of AA as reducing agent caused substantial changes in the physicochemical structure and, consequently, the properties. The most important consequence of oxygen functionalities loss in GO sheets and, therefore, of the partial restoration of the hexagonal lattice of carbon atoms was undoubtedly the unlocked ability of electrical conductivity. This in turn allowed for the piezoresistive properties of the rGOP aerogel: the shortening/elongation of the distance between rGO sheets and the formation/clearing of new contact points between pore walls led to the possibility to track the strain status during the compression/release phase of the mechanical testing through the variation of the measured electrical resistance between the electrodes. Nevertheless, the same aerogel is capable of remarking sound absorption abilities in the mid frequency range (i.e., α never below 0.9 between 1250 and 2500 Hz) and low thermal conductivity (0.0479 W mK^{-1}). A comparison of the multifunctional properties between presented composite aerogels is pictured in Figure P2-7.

Although further studies will be conducted to improve the mechanical robustness for a higher number of compression cycles and limit the increase in density, the presented modification method of GO and PVA blends allows the fabrication of multifunctional GOP aerogels that can be employed in aerospace, automotive and marine transport, as well as in building and construction.

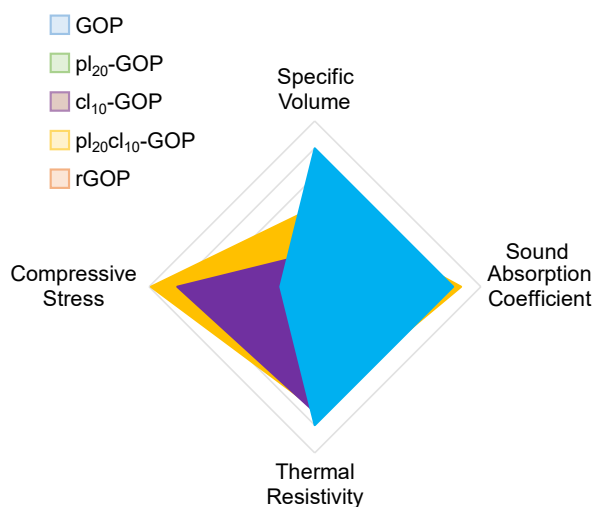


Figure P2-7 – Comparison of the multifunctional properties of the composite aerogels presented in the current work. The specific volume is calculated as the inverse of the density, the average value in the 500 – 1500 Hz range was taken for the sound absorption coefficient, the thermal resistivity is obtained from the inverse of the thermal conductivity, and the compressive stress is taken at 30% strain of the 10th mechanical compression cycle. All values are proportionally scaled using the un-modified GOP as reference.

References

- [1] N. Bheekhun, A.R. Abu Talib, M.R. Hassan, Aerogels in Aerospace: An Overview, *Advances in Materials Science and Engineering* 2013 (2013) 406065.
- [2] S. Alwin, X. Sahaya Shajan, Aerogels: promising nanostructured materials for energy conversion and storage applications, *Materials for Renewable and Sustainable Energy* 9(2) (2020) 7.
- [3] K.K. Sairajan, G.S. Aglietti, K.M. Mani, A review of multifunctional structure technology for aerospace applications, *Acta Astronautica* 120 (2016) 30-42.
- [4] C. Wang, X. Chen, B. Wang, M. Huang, B. Wang, Y. Jiang, R.S. Ruoff, Freeze-Casting Produces a Graphene Oxide Aerogel with a Radial and Centrosymmetric Structure, *ACS Nano* 12(6) (2018) 5816-5825.
- [5] X. Mi, G. Huang, W. Xie, W. Wang, Y. Liu, J. Gao, Preparation of graphene oxide aerogel and its adsorption for Cu²⁺ ions, *Carbon* 50(13) (2012) 4856-4864.

- [6] H. Hsu, C. Kuo, J. Jehng, C. Wei, C. Wen, J. Chen, L. Chen, Application of Graphene Oxide Aerogel to the Adsorption of Polycyclic Aromatic Hydrocarbons Emitted from the Diesel Vehicular Exhaust, *Journal of Environmental Chemical Engineering* 7(6) (2019) 103414.
- [7] X.-M. Han, K.-W. Zheng, R.-L. Wang, S.-F. Yue, J. Chen, Z.-W. Zhao, F. Song, Y. Su, Q. Ma, Functionalization and optimization-strategy of graphene oxide-based nanomaterials for gene and drug delivery, *Am J Transl Res* 12(5) (2020) 1515-1534.
- [8] W. Wan, S. Yu, F. Dong, Q. Zhang, Y. Zhou, Efficient C₃N₄/graphene oxide macroscopic aerogel visible-light photocatalyst, *Journal of Materials Chemistry A* 4(20) (2016) 7823-7829.
- [9] Y. Li, H. Zhang, M. Fan, P. Zheng, J. Zhuang, L. Chen, A robust salt-tolerant superoleophobic alginate/graphene oxide aerogel for efficient oil/water separation in marine environments, *Scientific Reports* 7(1) (2017) 46379.
- [10] S. Pei, H.-M. Cheng, The reduction of graphene oxide, *Carbon* 50(9) (2012) 3210-3228.
- [11] W. Si, X. Wu, J. Zhou, F. Guo, S. Zhuo, H. Cui, W. Xing, Reduced graphene oxide aerogel with high-rate supercapacitive performance in aqueous electrolytes, *Nanoscale Research Letters* 8(1) (2013) 247.
- [12] Y. Ma, Y. Yue, H. Zhang, F. Cheng, W. Zhao, J. Rao, S. Luo, J. Wang, X. Jiang, Z. Liu, N. Liu, Y. Gao, 3D Synergistical MXene/Reduced Graphene Oxide Aerogel for a Piezoresistive Sensor, *ACS Nano* 12(4) (2018) 3209-3216.
- [13] F. Wu, A. Xie, M. Sun, Y. Wang, M. Wang, Reduced graphene oxide (RGO) modified spongelike polypyrrole (PPy) aerogel for excellent electromagnetic absorption, *Journal of Materials Chemistry A* 3(27) (2015) 14358-14369.
- [14] M. Rapisarda, G.-P. Malfense Fierro, M. Meo, Ultralight graphene oxide/polyvinyl alcohol aerogel for broadband and tuneable acoustic properties, *Scientific Reports* 11(1) (2021) 10572.
- [15] M. Cobos, B. González, M.J. Fernández, M.D. Fernández, Chitosan-graphene oxide nanocomposites: Effect of graphene oxide nanosheets and glycerol plasticizer on thermal and mechanical properties, *Journal of Applied Polymer Science* 134(30) (2017) 45092.
- [16] T. Hwang, Z. Frank, J. Neubauer, K.J. Kim, High-performance polyvinyl chloride gel artificial muscle actuator with graphene oxide and plasticizer, *Scientific Reports* 9(1) (2019) 9658.

- [17] Q. Zheng, A. Javadi, R. Sabo, Z. Cai, S. Gong, Polyvinyl alcohol (PVA)–cellulose nanofibril (CNF)–multiwalled carbon nanotube (MWCNT) hybrid organic aerogels with superior mechanical properties, *RSC Advances* 3(43) (2013) 20816-20823.
- [18] S. Ye, Y. Liu, J. Feng, Low-Density, Mechanical Compressible, Water-Induced Self-Recoverable Graphene Aerogels for Water Treatment, *ACS Applied Materials & Interfaces* 9(27) (2017) 22456-22464.
- [19] W.H. Bragg, W.L. Bragg, The reflection of X-rays by crystals, *Proceedings of the Royal Society of London. Series A, Containing Papers of a Mathematical and Physical Character* 88(605) (1913) 428-438.
- [20] A. International, ASTM E1050-19, Standard Test Method for Impedance and Absorption of Acoustical Materials Using a Tube, Two Microphones and a Digital Frequency Analysis System, 2019.
- [21] A. International, ASTM E2611-19., Standard Test Method for Normal Incidence Determination of Porous Material Acoustical Properties Based on the Transfer Matrix Method, 2019.
- [22] K. Krishnamoorthy, M. Veerapandian, K. Yun, S.J. Kim, The chemical and structural analysis of graphene oxide with different degrees of oxidation, *Carbon* 53 (2013) 38-49.
- [23] A.N. Popova, Crystallographic analysis of graphite by X-Ray diffraction, *Coke and Chemistry* 60(9) (2017) 361-365.
- [24] C. Bao, Y. Guo, L. Song, Y. Hu, Poly(vinyl alcohol) nanocomposites based on graphene and graphite oxide: a comparative investigation of property and mechanism, *Journal of Materials Chemistry* 21(36) (2011) 13942-13950.
- [25] J. Liang, Y. Huang, L. Zhang, Y. Wang, Y. Ma, T. Guo, Y. Chen, Molecular-Level Dispersion of Graphene into Poly(vinyl alcohol) and Effective Reinforcement of their Nanocomposites, *Advanced Functional Materials* 19(14) (2009) 2297-2302.
- [26] S. Shi, X. Peng, T. Liu, Y.-N. Chen, C. He, H. Wang, Facile preparation of hydrogen-bonded supramolecular polyvinyl alcohol-glycerol gels with excellent thermoplasticity and mechanical properties, *Polymer* 111 (2017) 168-176.
- [27] R. Ricciardi, F. Auriemma, C. De Rosa, F. Lauprêtre, X-ray Diffraction Analysis of Poly(vinyl alcohol) Hydrogels, Obtained by Freezing and Thawing Techniques, *Macromolecules* 37(5) (2004) 1921-1927.

- [28] H.S. Mansur, C.M. Sadahira, A.N. Souza, A.A.P. Mansur, FTIR spectroscopy characterization of poly (vinyl alcohol) hydrogel with different hydrolysis degree and chemically crosslinked with glutaraldehyde, *Materials Science and Engineering: C* 28(4) (2008) 539-548.
- [29] A.L. Ahmad, N.M. Yusuf, B.S. Ooi, Preparation and modification of poly (vinyl) alcohol membrane: Effect of crosslinking time towards its morphology, *Desalination* 287 (2012) 35-40.
- [30] K.K.H. De Silva, H.-H. Huang, M. Yoshimura, Progress of reduction of graphene oxide by ascorbic acid, *Applied Surface Science* 447 (2018) 338-346.
- [31] J. Zhang, H. Yang, G. Shen, P. Cheng, J. Zhang, S. Guo, Reduction of graphene oxide vial-ascorbic acid, *Chemical Communications* 46(7) (2010) 1112-1114.
- [32] M. Cobos, M.J. Fernández, M.D. Fernández, Graphene Based Poly(Vinyl Alcohol) Nanocomposites Prepared by In Situ Green Reduction of Graphene Oxide by Ascorbic Acid: Influence of Graphene Content and Glycerol Plasticizer on Properties, *Nanomaterials* 8(12) (2018) 1013.
- [33] F. Tuinstra, J.L. Koenig, Raman Spectrum of Graphite, *The Journal of Chemical Physics* 53(3) (1970) 1126-1130.
- [34] A. Cuesta, P. Dhamelinourt, J. Laureyns, A. Martínez-Alonso, J. M. D. Tascón, Comparative performance of X-ray diffraction and Raman microprobe techniques for the study of carbon materials, *Journal of Materials Chemistry* 8(12) (1998) 2875-2879.
- [35] S. Claramunt, A. Varea, D. López-Díaz, M.M. Velázquez, A. Cornet, A. Cirera, The Importance of Interbands on the Interpretation of the Raman Spectrum of Graphene Oxide, *The Journal of Physical Chemistry C* 119(18) (2015) 10123-10129.
- [36] M. Goumri, J.W. Venturini, A. Bakour, M. Khenfouch, M. Baitoul, Tuning the luminescence and optical properties of graphene oxide and reduced graphene oxide fonctionalized with PVA, *Applied Physics A* 122(3) (2016) 212.
- [37] H.C. Schniepp, J.-L. Li, M.J. McAllister, H. Sai, M. Herrera-Alonso, D.H. Adamson, R.K. Prud'homme, R. Car, D.A. Saville, I.A. Aksay, Functionalized Single Graphene Sheets Derived from Splitting Graphite Oxide, *The Journal of Physical Chemistry B* 110(17) (2006) 8535-8539.

- [38] T. Cox, P. d'Antonio, *Acoustic absorbers and diffusers: theory, design and application*, Crc Press 2016.
- [39] F.J. Fahy, P. Gardonio, *Sound and structural vibration: radiation, transmission and response*, Elsevier 2007.
- [40] Xie, Y.; Zhou, B.; Du, A., Slow-sound propagation in aerogel-inspired hybrid structure with backbone and dangling branch. *Advanced Composites and Hybrid Materials* 2021, 4 (2), 248-256.
- [41] B. Lu, L. Lv, H. Yang, J. Gao, T. Xu, G. Sun, X. Jin, C. Shao, L. Qu, J. Yang, High performance broadband acoustic absorption and sound sensing of a bubbled graphene monolith, *Journal of Materials Chemistry A* 7(18) (2019) 11423-11429.
- [42] M.J. Nine, M. Ayub, A.C. Zander, D.N.H. Tran, B.S. Cazzolato, D. Losic, Graphene Oxide-Based Lamella Network for Enhanced Sound Absorption, *Advanced Functional Materials* 27(46) (2017) 1703820.
- [43] C. Simón-Herrero, N. Peco, A. Romero, J.L. Valverde, L. Sánchez-Silva, PVA/nanoclay/graphene oxide aerogels with enhanced sound absorption properties, *Applied Acoustics* 156 (2019) 40-45.
- [44] X. Li, Z. Yang, K. Li, S. Zhao, Z. Fei, Z. Zhang, A flexible silica aerogel with good thermal and acoustic insulation prepared via water solvent system, *Journal of Sol-Gel Science and Technology* 92(3) (2019) 652-661.
- [45] Q.B. Thai, R.O. Chong, P.T.T. Nguyen, D.K. Le, P.K. Le, N. Phan-Thien, H.M. Duong, Recycling of waste tire fibers into advanced aerogels for thermal insulation and sound absorption applications, *Journal of Environmental Chemical Engineering* 8(5) (2020) 104279.
- [46] C. Wang, Y. Xiong, B. Fan, Q. Yao, H. Wang, C. Jin, Q. Sun, Cellulose as an adhesion agent for the synthesis of lignin aerogel with strong mechanical performance, Sound-absorption and thermal Insulation, *Scientific Reports* 6(1) (2016) 32383.
- [47] Y. Si, X. Wang, L. Dou, J. Yu, B. Ding, Ultralight and fire-resistant ceramic nanofibrous aerogels with temperature-invariant superelasticity, *Science Advances* 4(4) (2018) eaas8925.
- [48] Pornea, A. G. M.; Puguán, J. M. C.; Ruello, J. L. A.; Kim, H., Multifunctional Dual-Pore Network Aerogel Composite Material for Broadband Sound Absorption, Thermal Insulation, and Fire Repellent Applications. *ACS Applied Polymer Materials* 2022, 4 (4), 2880-2895
- [49] Thai, Q. B.; Le-Cao, K.; Nguyen, P. T. T.; Le, P. K.; Phan-Thien, N.; Duong, H. M., Fabrication and optimization of multifunctional

nanoporous aerogels using recycled textile fibers from car tire wastes for oil-spill cleaning, heat-insulating and sound absorbing applications. *Colloids and Surfaces A: Physicochemical and Engineering Aspects* 2021, 628, 127363.

- [50] Nie, Z.-J.; Wang, J.-X.; Huang, C.-Y.; Feng, J.-F.; Fan, S.-T.; Tan, M.; Yang, C.; Li, B.-J.; Zhang, S., Hierarchically and wood-like cyclodextrin aerogels with enhanced thermal insulation and wide spectrum acoustic absorption. *Chemical Engineering Journal* 2022, 446, 137280.

Supplementary Information

1. Supplementary figures

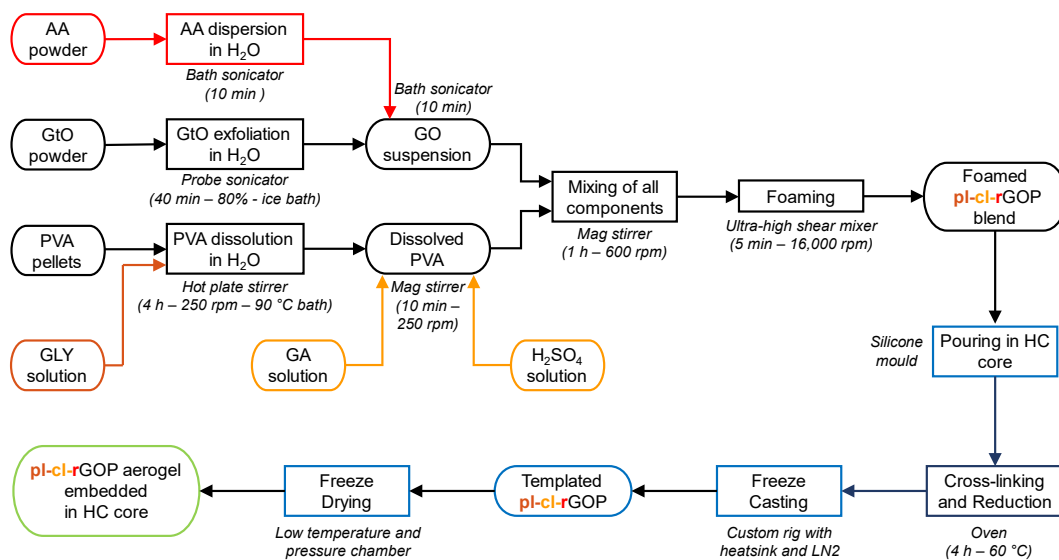


Figure S2-1 – GOP aerogel manufacturing scheme. Modifications to the reference GOP can be distinguished by colors: plasticiser in orange, cross-linker in yellow and reducing agent in red.

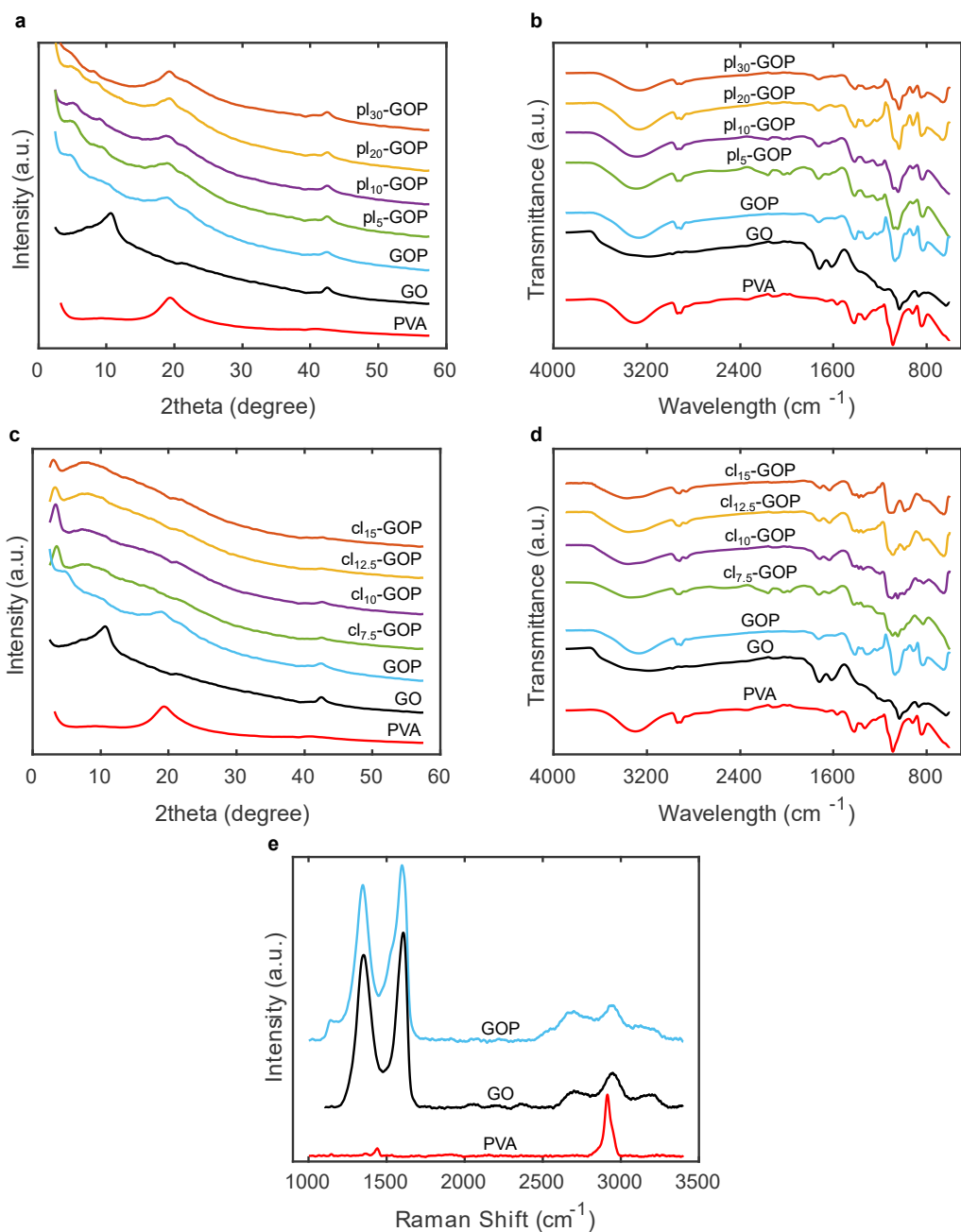


Figure S2-2 – Physicochemical characterisation of modified GOP aerogels. (a, c) XRD patterns and **(b, d)** FT-IR spectra of **(a, b)** pl_x-GOP and **(c, d)** cl_y-GOP with pure GO and PVA as reference. **(e)** Raman spectra of un-modified GOP with pure GO and PVA as reference.

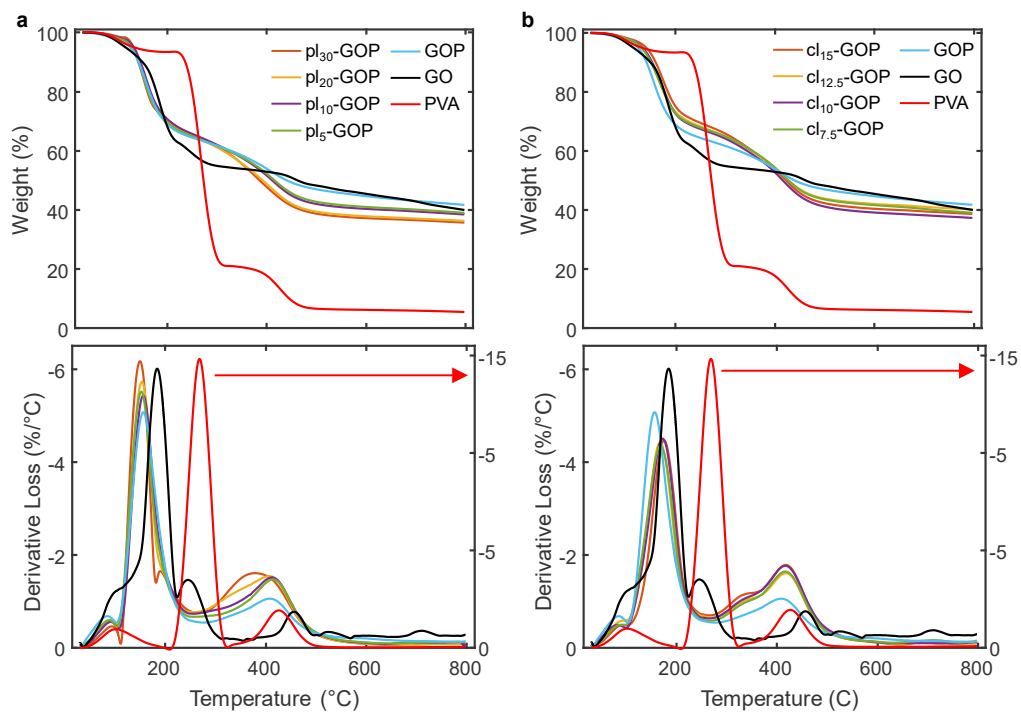


Figure S2-3 – Thermal stability of modified GOP aerogels. (a,b) TGA and (c,d) dTGA of (a,c) pl_x -GOP and (b,d) cl_y -GOP aerogels.

2. Supplementary tables

Table S2-1 – Comparison of density, porosity, sound absorption and thermal conductivity between modified GOP aerogels from this work and other aerogels with comparable thickness previously reported in the literature.

^A The average was calculated in the 500 – 1500 Hz range.

Name	Density (kg m ⁻³)	Thickness (mm)	Average ^A Absorption Coefficient	Thermal conductivity (W mK ⁻¹)	Ref.
Mod. GOP	3.65 – 19.92	25	0.54 – 0.72	0.0391	This work
GOP	2.10	25	0.68	0.0374	This work, [1]
BGM	2.6 – 10.3	30	0.33 – 0.74 [800-1500 Hz]	-	[2]
MFGO	12.39 – 24.12	26	0.40 – 0.69	-	[3]
GONPVA	-	20	0.71	0.0255	[4]
MTES	53 – 70	12	0.226	0.022 – 0.026	[5]
RA	57 – 126	30	0.43 – 0.55	0.035 – 0.049	[6]
Lignin Aerogels	24 – 80	-	0.47 – 0.77	0.128 – 0.174	[7]
CNFAs	0.5 – 10	15	-	0.025 – 0.032	[8]
PVA/CNF/MWCNT	20.13 – 30.62	-	-	0.028 – 0.030	[9]
CAP	20 - 70	20	0.57	0.031	[10]
NRA	25	30	0.61	0.035	[11]
BRAA	11.05	30	0.60	0.016	[12]

3. Supplementary references

- [1] M. Rapisarda, G.-P. Malfense Fierro, M. Meo, Ultralight graphene oxide/polyvinyl alcohol aerogel for broadband and tuneable acoustic properties, *Scientific Reports* 11(1) (2021) 10572.
- [2] B. Lu, L. Lv, H. Yang, J. Gao, T. Xu, G. Sun, X. Jin, C. Shao, L. Qu, J. Yang, High performance broadband acoustic absorption and sound sensing of a bubbled graphene monolith, *Journal of Materials Chemistry A* 7(18) (2019) 11423-11429.
- [3] M.J. Nine, M. Ayub, A.C. Zander, D.N.H. Tran, B.S. Cazzolato, D. Losic, Graphene Oxide-Based Lamella Network for Enhanced Sound Absorption, *Advanced Functional Materials* 27(46) (2017) 1703820.
- [4] C. Simón-Herrero, N. Peco, A. Romero, J.L. Valverde, L. Sánchez-Silva, PVA/nanoclay/graphene oxide aerogels with enhanced sound absorption properties, *Applied Acoustics* 156 (2019) 40-45.
- [5] X. Li, Z. Yang, K. Li, S. Zhao, Z. Fei, Z. Zhang, A flexible silica aerogel with good thermal and acoustic insulation prepared via water solvent system, *Journal of Sol-Gel Science and Technology* 92(3) (2019) 652-661.
- [6] Q.B. Thai, R.O. Chong, P.T.T. Nguyen, D.K. Le, P.K. Le, N. Phan-Thien, H.M. Duong, Recycling of waste tire fibers into advanced aerogels for thermal insulation and sound absorption applications, *Journal of Environmental Chemical Engineering* 8(5) (2020) 104279.
- [7] C. Wang, Y. Xiong, B. Fan, Q. Yao, H. Wang, C. Jin, Q. Sun, Cellulose as an adhesion agent for the synthesis of lignin aerogel with strong mechanical performance, Sound-absorption and thermal Insulation, *Scientific Reports* 6(1) (2016) 32383.
- [8] Y. Si, X. Wang, L. Dou, J. Yu, B. Ding, Ultralight and fire-resistant ceramic nanofibrous aerogels with temperature-invariant superelasticity, *Science Advances* 4(4) (2018) eaas8925.
- [9] Q. Zheng, A. Javadi, R. Sabo, Z. Cai, S. Gong, Polyvinyl alcohol (PVA)–cellulose nanofibril (CNF)–multiwalled carbon nanotube (MWCNT) hybrid organic aerogels with superior mechanical properties, *RSC Advances* 3(43) (2013) 20816-20823.
- [10] A.G.M. Pornea, J.M.C. Puguán, J.L.A. Ruello, H. Kim, Multifunctional Dual-Pore Network Aerogel Composite Material for Broadband Sound Absorption, Thermal Insulation, and Fire Repellent Applications, *ACS Applied Polymer Materials* 4(4) (2022) 2880-2895.

- [11] Q.B. Thai, K. Le-Cao, P.T.T. Nguyen, P.K. Le, N. Phan-Thien, H.M. Duong, Fabrication and optimization of multifunctional nanoporous aerogels using recycled textile fibers from car tire wastes for oil-spill cleaning, heat-insulating and sound absorbing applications, *Colloids and Surfaces A: Physicochemical and Engineering Aspects* 628 (2021) 127363.
- [12] Z.-J. Nie, J.-X. Wang, C.-Y. Huang, J.-F. Feng, S.-T. Fan, M. Tan, C. Yang, B.-J. Li, S. Zhang, Hierarchically and wood-like cyclodextrin aerogels with enhanced thermal insulation and wide spectrum acoustic absorption, *Chemical Engineering Journal* 446 (2022) 137280.

Chapter 6

GRAPHENE-BASED SUPERCAPACITORS

6.1 Context

As introduced in the previous chapters, the fabrication of SC electrodes usually requires the use of binders. Specifically, they allow to meet the requirements of satisfactory cohesion among active material particles and their adhesion on the current collector. Fluoropolymers (mostly PTFE and PVDF), due to their wide electrochemical stability and easiness of processing, are the most commonly used for this purpose. They are however not electrically conductive, representing thus a “dead mass” that does not contribute to the electrochemical performances. Additionally, in

order to achieve homogeneous slurries that can be easily coated on current collectors, they need to be dispersed in organic solvents, with an increase in cost, fabrication process complexity, and environmental impact of the devices. Since graphene discovery, thanks to the unique electrical properties and high SSA, several approaches were attempted to exploit its derivate materials for the manufacturing of novel SCs. Moreover, in the last years particular attention was posed on the use of graphene-based materials as free-standing electrodes, or as alternative and active binders. However, an effective scalability of fabrication processes was rarely taken into account, especially considering that in most of the cases exotic and/or hazardous chemicals were required.

The first research work of the paper collection regarding graphene-based supercapacitors finds its inspiration in the just described context. Particularly, a carbonaceous composite consisting of GO and CB was obtained from a slurry where water was used as a low-cost and environmentally friendly solvent. GO presence was, in a first stage, crucial to guarantee a homogeneous dispersion of carbon particles. Then, the electrical conductivity was restored thanks to a thermal reduction step, which allowed the resulting rGO to actively contribute to the electrochemical performance. Moreover, the same work presents a novel use of a rGO paper, obtained from the thermal annealing of GO, as the current collector. This led to a double advantage with respect of traditional Aluminium collectors: an enhanced adhesion and electric charges transfer from the carbonaceous coating, and a reduced overall weight.

It was proved that GO can potentially be used as an active binder with a carbon characterised by a high SSA (such as the Black Pearls® 2000) as the active material and a graphene-based current collector. A further analysis of the electrochemical performances however revealed that,

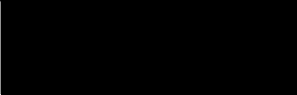
besides the limited specific capacitance, a low efficiency was also affecting the fabricated supercapacitors. In order to mitigate these issues and, eventually, develop materials and a fabrication procedure immediately transferrable to the industry, a different approach was followed for the second research article regarding graphene-based supercapacitors.

In particular, the ability of GO to behave as a dispersing agent first, and to actively contribute to the electrochemical performance after its reduction to rGO, was again exploited, as well as the rGO paper as current collector. Differently from the previous work, a binder was also introduced. With the aim to maintain the environmental friendliness of the process and the use of water as the only solvent, starch was used as an alternative green binder. The main novelty consisted in the gelation of an optimised mixture of starch and GO, thanks to which it was possible to fabricate homogeneous and robust carbonaceous coatings. A physicochemical characterisation confirmed the constructive interactions between the two components, and the corresponding effects on coatings structure and morphology. The electrochemical evaluation revealed instead how the ability of the proposed binder to provide cohesion between the active materials and adhesion on the rGO collector was translated to a fast and efficient electrical charge storage and release process. The latter was distinctively enhanced by GO presence, and furtherly boosted by its reduction after an optimised thermal treatment.

6.2 Binder-free supercapacitors with an innovative current collector

The statement of Authorship Form and the paper can be found next, followed by the relevant supplementary information.

This declaration concerns the article entitled:	
<i>Carbon Black and Reduced Graphene Oxide Nanocomposite for Binder Free Supercapacitors with Reduced Graphene Oxide Paper as the Current Collector</i>	
Publication status (tick one)	
Draft Manuscript <input type="checkbox"/> Submitted <input type="checkbox"/> In Review <input type="checkbox"/> Accepted <input type="checkbox"/> Published <input checked="" type="checkbox"/>	
Publication details (reference)	https://doi.org/10.1021/acsomega.0c04530
Copyright status (tick the appropriate statement)	
I hold the copyright for this material <input type="checkbox"/>	
Copyright is retained by the publisher, but I have been given permission to replicate the material here <input checked="" type="checkbox"/>	
Candidate's contribution to the paper (provide details, and also indicate as a percentage)	<p>The candidate contributed to / considerably contributed to / predominantly executed the...</p> <p>Formulation of ideas: 60% <i>I defined the idea of a carbonaceous nanocomposite of rGO and CB as a binder-free supercapacitor electrode, with integrative support from Dr. A. Damasco, and I also proposed the use of the rGO paper as current collector. Prof. M. Meo and Prof. G. Abbate participated in the discussion and approved the project.</i></p> <p>Design of methodology: 90% <i>I designed the experimental campaign, with Dr. A. Damasco contributing for electrochemical properties evaluation.</i></p> <p>Experimental work: 60% <i>I manufactured all the samples with Dr. A. Damasco. I characterised all the samples, Dr. A. Damasco helped for the electrochemical properties.</i></p> <p>Presentation of data in journal format: 70% <i>I defined paper structure, wrote the first draft and designed the figures. Dr. A. Damasco contributed for the discussion on electrochemical properties and methodology. Prof. M. Meo and Prof. G. Abbate</i></p>

	<i>reviewed the manuscript. Prof. M. Meo supported in the submission and publication process.</i>		
Statement from Candidate	This paper reports on original research I conducted during the period of my Higher Degree by Research candidature.		
Signed			Date 15/02/2022

Carbon Black and Reduced Graphene Oxide Nanocomposite for Binder Free Supercapacitors with Reduced Graphene Oxide Paper as the Current Collector

Mario Rapisarda¹, Achille Damasco², Giancarlo Abbate² and Michele Meo^{1,*}

¹University of Bath, Department of Mechanical Engineering, Bath, BA27AY, UK

²Dipartimento di Scienze Fisiche “Ettore Pancini”, Università degli Studi di Napoli “Federico II”, Via Cintia, 80126, Naples, Italy

**Corresponding author*

Abstract

Reduced Graphene Oxide (rGO) is an ideal candidate for the improvement of Supercapacitors (SCs) performances due to its industrial-ready manufacturing process and easiness to process. In this work, rGO was used as an active binder for the manufacturing of Carbon Black (CB) and rGO based SCs. Being able to form stable suspension in water, Graphene Oxide (GO) was initially exploited as dispersing agent to fabricate a homogeneous slurry with CB having exclusively water as a low-cost and environment-friendly solvent. After the casting on a suitable substrate, the material was subjected to thermal treatment allowing the reduction of GO to rGO, which was successively confirmed by a chemical-physical analysis. An innovative current collector, consisting in a high quality rGO paper, was also proposed ensuring an improved adhesion between the active material and the substrate and a reduction of the whole weight with respect of devices

fabricated using common metallic current collectors. Due to the interesting electrochemical performances, with the high specific power of 32.1 kW kg^{-1} and a corresponding specific energy of 8.8 Wh kg^{-1} at a current of 1 A g^{-1} , and the improved manufacturing process, the described “all-graphene based” device represents a valuable candidate for the future of SCs.

1. Introduction

The scientific research about SCs, being them energy storage devices offering excellent performances when charge and/or discharge speeds are crucial, [1] has a huge and growing interest. Moreover, SCs can work at low temperatures and carry out many charge and discharge cycles (till one million). Examples of SCs applications are emergency opening systems in buses and planes, UPS systems, KERS and Stop-Start technology in cars (especially hybrids) and the partial replacement of batteries in trucks.¹ They also operate in energy intermittence protection systems in wind or solar power generation plants, [2, 3] in the energy recovery apparatus of overhead cranes and hoists, in the rail transportation industry, [4] and, recently, also in mobile devices, for powerful flashes and wi-fi [5, 6].

rGO is a graphene-like material produced from a reduction reaction of GO [7, 8]. The latter is a functionalized graphene sheet having oxygen functional groups such as hydroxyl and carboxyl or epoxide that disrupt the conjugated network of sp^2 -hybridized carbon atoms, which is the peculiarity determining the great electronic and thermal properties of pristine graphene [9-12]. Through the process of reduction, these groups can be stripped away and the hexagonal lattice of carbon atoms recovered. For this reason, rGO is a good electrical conductor, even if not fully comparable with pristine graphene [13] the removal of the oxygen-containing groups causes topological defects affecting the electrical and thermal properties [14]. There

are however different methods to improve the reduction process and to prevent topological defects in the wide literature about rGO [15-20]. Nowadays, one of the most common ways to obtain graphene-like materials relies on the oxidation of graphite to obtain Graphite Oxide (GtO) [21, 23]. From GtO, sheets of GO can be produced as intermediates thanks to a mechanical exfoliation [10]. Besides, also the direct rGO production is possible [15, 16]. In numerous works, the choice of GO arises from two important advantages: it is readily soluble in water and it can be reduced in both physical, providing energy with heat or laser, [16, 17] and chemical ways [18]. However, due to the presence of oxygen functionalities, GO is an electric insulator and, therefore, the effectiveness of the reduction process becomes crucial when rGO is used in energy storage devices as SCs.

Since all kinds of commercial or experimental SCs have a high specific power, the main aim of current scientific researches focuses on the improvement of the amount of stored energy, which is nowadays about one tenth of the energy of a battery with the same mass [24]. Nonetheless, the stored energy is not the only margin of improvement: the manufacturing process, and in particular its cost, scalability and environmental impact, are important to give to new SCs a concrete impingement on the technological progress. Furthermore, the final weight of the devices may be crucial for applications in the automotive and aerospace field, as well as in portable electronics. In a SC electrode, the “active material” (i.e., the material responsible for electrical charges storage and usually consisting of porous carbons characterized by a high specific surface area like Activated Carbons (AC) and CB powders) needs to adhere to a “current collector” (i.e., the material allowing electrical current flow and usually consisting of Aluminum (Al) sheets) by the use of a binder. In most cases, especially in commercial SCs, the binder is a glue consisting of polymers as

Polytetrafluoroethylene and Polyvinylidene Fluoride [25, 26]. They both provide good adhesion and electrochemical stability, however, being electrically insulating polymers, they also represent a high-resistance component in the electrode. In addition, such polymers, together with the organic solvents required to obtain homogeneous slurries suitable for the coating of current collectors, are expensive and dangerous for the environment. Binders therefore represent a dead mass that is convenient to be reduced. An alternative to common binders is identified in conductive polymers as Polyaniline nanofibers, which can be used to fabricate freestanding electrodes or as a support for carbon nanotubes [27]. Their practical use is however limited by the manufacturing method: electrospinning is not readily scalable to industrial processes. In the work of Galhena et al., [20] rGO was adopted as an alternative binder with good results. However, as in other studies [28, 29], the use of toxic and expensive organic solvents was still necessary, especially for the Electrical Double Layer Capacitors (EDLCs; i.e., a type of SCs relying only on electrostatic charge storage). In Hybrid SCs (HSCs; i.e., a type of SCs consisting of a battery-like Faradic electrode and a EDLC-like non-Faradic electrode) an aqueous electrolyte was used for a rGO-based nanocomposite electrode [30-32]. For the latter, the Faradic electrode can be made with a metal-organic or metal-sulfidic nano-structure while the EDLC electrode can be made with carbon nanotubes evenly distributed in graphene sheets [30-32]. As the reported HSCs show promising performances, they are valuable for the future of SCs. Moreover, thanks to their hybrid nature, they can also benefit from newly developed electrodes for EDLCs based on rGO.

In this work, the fabrication of binder-free electrodes for EDLCs based on a nanocomposite of CB and rGO is proposed. A water-based slurry of CB and GO was coated to a current collector and then thermally treated through a tube furnace to promote the reduction of GO. rGO formation was

confirmed by a chemico-physical characterization, while its ability to behave as an “active binder” (i.e., as a material that ensure adhesion of the nanocomposite to the substrate with direct contribution to the final performance) was proved by an electrochemical characterization. In addition, an innovative use of a current collector consisting of a high quality rGO paper was also tested. It derives from a high-temperature thermal treatment of GO and allowed a double advantage with respect of conventional Al collectors: an improved adhesion with the nanocomposite active material under exam, thanks to materials’ affinity, and a reduced weight, thanks to a density of 1.2 g cm^{-3} against the 2.7 g cm^{-3} with a comparable thickness. The promising performances of the as obtained samples, showing the high specific power of 32.1 kW kg^{-1} and a corresponding specific energy of 8.8 Wh kg^{-1} at a current of 1 A g^{-1} , together with the cheap, environmental-friendly and scalable process adopted, the “all-graphene based” device described in this study represents a valuable candidate for the future of SCs.

2. Results and Discussion

2.1. Chemico-physical characterization

The carbon nanocomposite behaving as the active material of the SCs electrodes proposed in this research work was obtained, as described in detail in the experimental section, with a GO aided homogenization of CB particles previously suspended in a mixture of water and Triton X-100 (TX100). The carbonaceous coatings obtained after the drying of the slurries were physically and chemically characterized to investigate the effects of the GO in the resulting nanocomposite and confirm the reduction of GO to rGO when thermal treatment to the CB/GO slurry was applied.

CB is characterized by a hierarchical morphology with particles and aggregates: particles are the fundamental building block, but they are very rarely found in isolation due to Van der Waals interactions that exert a driving force for their aggregation [33]. While the initial size of pristine CB particles used for this research work ranges between 20 and 50 nm [34], Transmission Electron Microscopy (TEM) images of the thermally treated carbonaceous coating obtained from the CB-only suspension in the H₂O/TX100 solution (CB_TT) show that CB particles are disrupted and reduced in size, with values ranging from 10 to 20 nm (Figure P3-1 – a). Moreover, an average agglomerate size of 69 nm was estimated from the Field Emission Scanning Electron Microscopy (FE-SEM) image in Figure P3-1 – b (as depicted from the histogram with the size distribution in Figure P3-1 – c). Such value is slightly smaller than in usual CB aggregates (which ranges between 85 and 500 nanometers) [33]. Both the phenomena suggest that the use of TX100 effectively aids the dispersion of the carbonaceous particles in water but signs of inhomogeneity and defects in the structure of the material are still clearly visible (Figure P3-1 – b). When the GO is added into the slurry, the resulting thermally treated nanocomposite (CB/GO_TT) is homogeneous and less defective (as pictured from SEM in Figure P3-1 – e). The role of the TX100 is to pre-disperse CB in water and then to subsequently allow an intimate intercalation of GO sheets between CB particles. TX100 is a surfactant characterized by amphiphilic molecules with a hydrophilic region, consisting of Polyethylene Oxide chains, and a hydrophobic region, consisting of aromatic hydrocarbon chains. These are partially adsorbed by the carbon, with the non-covalent π - π interaction between the aromatic rings and external graphene layers on the surface of CB particles having an important function, while the hanging Polyethylene Oxide hydrophilic tails determine steric stabilization of CB particles against the Van der Waals forces that tend instead to aggregate them [35]. In GO, thanks to the hydrophilic

behavior of oxygen functional groups, water molecules can intercalate between graphene interlayer spacings, leading to stable suspensions in water [36]. When the latter is added to the pre-dispersed CB mixture in water, the GO sheets could wrap CB particles and thus generate an interconnected 3D network (as imaged from TEM in Figure P3-1 – d and illustrated in Figure P3-2 – a) preventing CB to flocculate into bigger clusters and thus leading to smaller agglomerates (as confirmed by the estimated average size of 48 nm depicted in Figure P3-1 – f). As water evaporates in ambient condition, the 3D structure is maintained but it is very likely that some of its molecules would get trapped due to the strong non-covalent interactions with the CB/GO/TX100 complex. Moreover, the electrically insulating GO sheets lead to poor electrical conductivity in the electrodes while the adsorbed TX100 molecules affects electrolyte ions diffusion. Thus, poor electrochemical performances are expected from the ambient dried samples. On the other side, when high temperatures are applied, two simultaneous phenomena lead to the formation of a highly electrically conductive carbon nanocomposite with free to access pores for electrolyte ions diffusion and enhanced adhesion thanks to non-covalent interactions with the current collector, as schematized in Figure P3-2 – b, from which remarkable electrochemical performances are likely to be developed. The first phenomenon is the thermal reduction of non-electrically conductive GO to form conductive rGO, discussed in the following paragraphs with the supporting Raman Spectroscopy and X-Ray Diffractometry (XRD) results, while the second is the complete evaporation of TX100: the latter is possible when the critical temperature of 310 °C is reached under inert atmosphere, as demonstrated by Mitsuda et al [37].

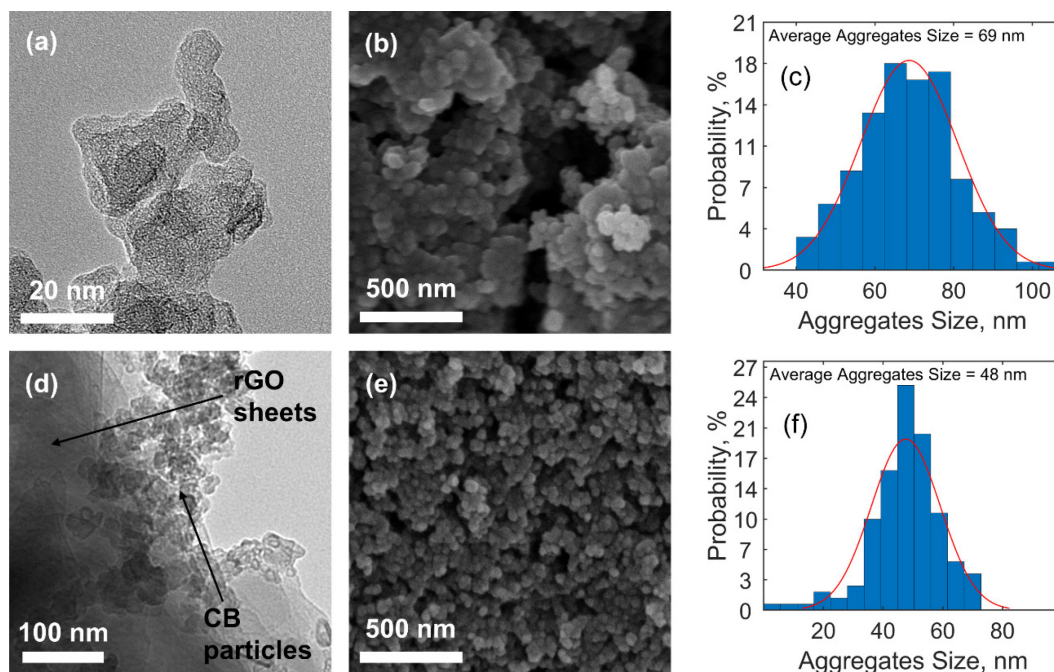


Figure P3-1 – (a, d) TEM and (b, e) FE-SEM images of: (a, b) CB_TT and (d, e) CB/GO_TT with the relative histograms of aggregates size distribution, (c) and (f) respectively (see Table P3-2 in the experimental section for the adopted nomenclature in this work). The term referred to the current collector has been omitted since it does not affect thermal treatment results.

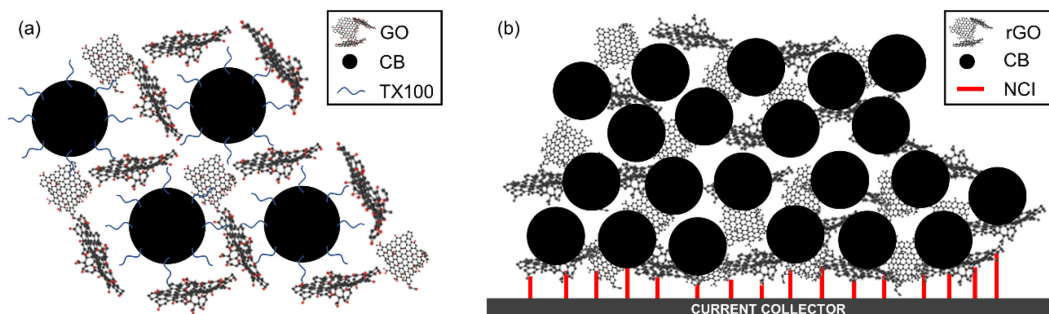


Figure P3-2 – Proposed schemes for (a) the 3D interconnected network consisting of CB and GO with TX100 molecules as dispersers and (b) the electrically conductive carbon nanocomposite consisting of CB and rGO with Non-Covalent Interactions (NCI) enhancing the adhesion with the current collector.

The Raman Spectra of all the carbonaceous coatings (Figure P3-3 – a) show the existence of the G band, arising from the primary vibrations mode of sp^2 atoms in rings and chains and which is a characteristic of all graphitic materials, at $\sim 1600\text{ cm}^{-1}$ and of the D band, arising from breathing modes of sp^2 atoms induced by defects and disorder in the crystalline structure, at

$\sim 1345\text{ cm}^{-1}$. These two features can be merged in their peak intensity ratio (I_D/I_G) to analyze the structure quality, where higher values of the ratio correspond to an increased disorder [38, 39]. The as calculated values for the materials under examination are reported in Table P3-1. The pristine CB and GO were included for reference purpose, with the higher intensity of GO peaks, explainable with a smaller crystallites size. Their I_D/I_G ratios of, respectively, 1.08 and 0.96, reveal instead their expected disordered structures. The material resulting from the ambient dried CB-only suspension in the TX100/H₂O solution shows a marginal increase in intensity of the peaks, explainable with the reduction in size of CB agglomerates during the processing in presence of the TX100. Moreover, as the I_D/I_G ratio is only slightly reduced to 1.06, the overall disorder of crystallites structure can be assumed as unaffected. The thermally treated suspension CB_TT is almost unvaried in both peaks' intensity and I_D/I_G ratio (equal to 1.08), confirming that the CB is inert at 550 °C with Ar atmosphere. On the other hand, the nanocomposite obtained from the ambient dried CB/GO slurry is characterized by higher peaks' intensity and a I_D/I_G ratio of 0.96, proving that GO sheets in solution successfully helps the disaggregation and stabilization of CB agglomerates in smaller particles, leading to a homogeneous mixture and thus confirming our previous assumption and TEM and FE-SEM results. When the thermal treatment is applied, oxygen functional groups and intercalated water are eliminated, releasing Carbon Dioxide (CO₂), Carbon Monoxide (CO) and water vapor, and thus the conjugated network of the hexagonal lattice of carbon atoms is restored [40]. The last is the mechanism governing the electrical conductivity of graphene [13] and the transition from the electrical insulating behavior of GO toward the conductive one of rGO is confirmed by the electrochemical tests that will be described later. The generated rGO sheets show a higher degree of disorder as depicted by the I_D/I_G ratio of 1.04,

value in between those of the CB/GO nanocomposite after ambient drying (CB/GO_AD) and CB_TT, due to vacancies and topological defects on graphene layers after the release of CO₂ and CO [40]. The successful reduction of GO to rGO is furthermore proved by the increased intensity of 2nd order scatterings, around the graphene-associated 2D band at ~2700 cm⁻¹ [41], which also shows turbostratic arrangements of graphene layers [38].

XRD patterns of the CB/GO nanocomposite and of the processed CB only carbonaceous material used as reference, before and after thermal treatment, are presented in Figure P3-3 – b. They all show a broad peak at around 22.97°, attributable to the (002) Carbon lattice and downshifted with respect of the ordered structure of graphite where the same peak is sharp and shown at 26.38° [42]. According to Bragg's law [43], reported in equation (P3-47), the interplanar spacing d_{002} in CB_GO_AD has a measured value of 4 Å, which is higher than the counterpart without the addition of GO (CB_AD), as observable from the values summarized in Table P3-1, and thus suggesting a more expanded and amorphous 3D structure of the nanocomposite (as compared to the 3.38 Å of crystalline graphite). When the thermal treatment is applied, d_{002} is almost unvaried for the CB only carbonaceous material, while it is contracted to a value of 3.77 Å for CB_GO_TT. This is a result of the reduction of GO to rGO which leads to the reorganization of the structure toward a more ordered fashion. Other important Carbon features are the (100) and (101) lattice peaks, usually shown in graphite at 2θ values of, respectively, 42.22° and 44.39° [42], which, for all the tested carbonaceous coatings, are merged into the broad (10) peak at around 43.64°. The latter is a consequence of turbostratic arrangements of graphene layers [42]. According to Scherrer equation (P3-48) [44], the two main crystallite dimensions, which are the stacking height L_C and the crystallite lateral size L_A , can be estimated from,

respectively, the (002) peak, using a shape factor of 0.89, and the (10) peak, with shape factor of 1.84 [45]. From their values, reported in Table P3-1, it is possible to notice the difference in both the sizes between the two ambient dried samples, with and without the addition of GO. L_C and L_A result instead comparable after the thermal treatment. The bigger stacking height in CB/GO_AD than in CB_AD can be explained, in accordance with the interplanar spacing behavior, with an expanding effect of intercalated GO layers. In the CB only material, almost no difference is measured in both L_C and L_A passing from the ambient dried to the thermally treat sample. In the CB/GO nanocomposite, however, a sharp decrease of L_C and a simultaneous increase of L_A are registered after the thermal treatment. These results are evidence of a hybrid structure, composed by an ordered graphitic state and an amorphous state, for the carbonaceous nanocomposite under investigation, which is typical in amorphous carbon as CB but influenced by GO intercalation. The amorphous subphase is promoted over the crystalline one in the ambient dried sample (due to a higher interplanar spacing and to a bigger crystallite size) while, after the application of the thermal treatment, the reduction of GO to rGO causes an opposite effect favoring the crystalline subphase (due to the reduced spacing and the smaller crystallite size).

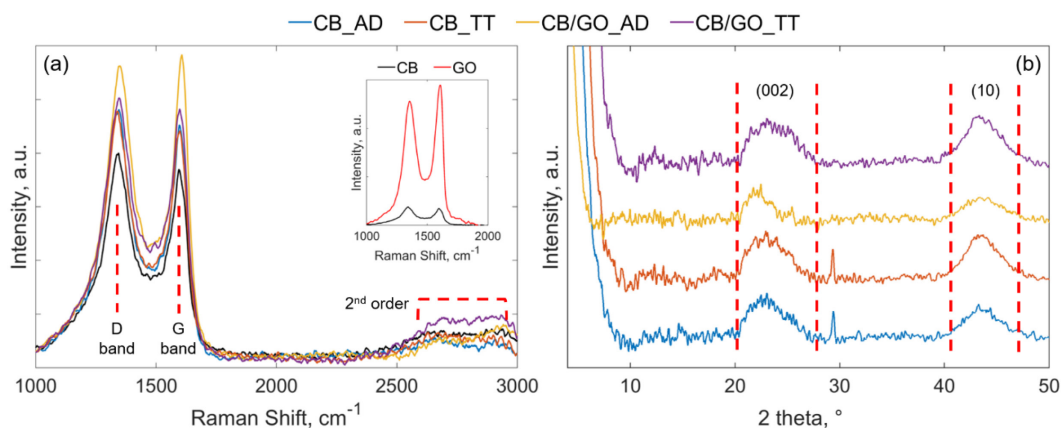


Figure P3-3 – (a) Raman spectra of the carbonaceous coatings with untreated CB included as reference; the onset shows the comparison between the untreated CB and GO. (b) XRD patterns of the carbonaceous coatings. The term referred to the current collector has been omitted since it does not affect thermal treatment results.

Table P3-1 – Raman D to G band ratios, XRD Peak Positions, Lattice Spacing and Crystallite Sizes.

Sample	I _D /I _G ratio	(002) [2θ]	(10) [2θ]	d ₀₀₂ [Å]	L _c [Å]	L _A [Å]
CB_AD	1.06	23.01	43.63	3.86	18.6	40.4
CB_TT	1.08	23.09	43.63	3.85	18.1	42.1
CB/GO_AD	0.96	22.23	43.70	4.00	27.3	36.3
CB/GO_TT	1.04	23.55	43.60	3.77	17.8	41.0

2.2. Electrochemical characterization

Figure P3-4 – a–b show the Cyclic Voltammeteries (CVs) and Galvanostatic Cycles (GCs) of SCs made with the CB/GO slurry before and after thermal treatment. Also, the CVs and GCs of SCs made with the CB only slurry before and after thermal treatment are reported for comparison. In Figure P3-4 – a, CVs are recorded using a scan rate of 50 mV s⁻¹ in a potential range from -2.70 V to +2.70 V; in Figure P3-4 – b, GCs curves obtained with a specific current of 0.5 A g⁻¹ for CB/GO_AI_AD and of 1 A g⁻¹ for CB/GO_AI_TT and CB_AI_TT. In the latter case, the different specific currents are justified as follows: using the same specific current (0.5 or 1 A g⁻¹) for all the samples, CB/GO_AI_TT and CB_AI_TT curve would be much

longer than that of CB/GO_AI_AD, leading to the impossibility to observe the trend of the latter. In Figure P3-4 – a–b, the differences between CB/GO_AI_AD and CB/GO_AI_TT prove that only with thermal treatment of GO an active material suitable for SCs can be achieved. The area under the CV curve of the thermally treated sample, CB/GO_AI_TT, is 18 times wider than the untreated one, CB/GO_AI_AD. In fact, the values of C_s calculated using the equations (P3-49) and (P3-50), reported in the experimental section are, respectively, 47.7 and 2.7 F g⁻¹ for a scan rate of 100 mV s⁻¹. Observing Figure P3-4 – a–b, while at first glance the sample without GO in the starting slurry, CB_AI_TT, show even better electrochemical performances, it should be noted that it actually lacks of other crucial properties, as adhesion on current collector and mechanical stability, as showed in Figure S3-1 of Supporting Information. This behavior arises from the absence of any binder and, as a consequence, such active material can hardly be considered for the manufacturing of SCs. As for GCs, for the non-thermally treated sample, the non-linearity of the graph was too high to conduct any measurements, while it is almost linear in the discharge curve of the sample annealed at 550 °C (showing a C_s of 27.4 F g⁻¹ for a specific current of 1 A g⁻¹, calculated using the equations (P3-52) and (P3-50)). These results are a consequence of the thermal GO reduction for two reasons: since GO is an insulating material, it hinders charge transfer inside pores (a tension drop in the discharge curve is also dominant in the CB/GO_AI_AD sample); moreover, the oxygen-containing groups of GO can lead to faradic reactions during the charge/discharge process, deviating from EDLC behavior and thus explaining the non-linearities in the curve and the leakage. While the tests shown in Figure P3-4 – a–b highlight the effectiveness of the GO reduction procedure (1 h at 550 °C under Ar flow), more tests were carried out on the sample of main interest for the current work, CB/GO_Gr_TT, as described in the following paragraph and pictured in Figure P3-5 – a–b. The resulting curves of the electrochemical

characterization of samples used as reference, manufactured as described in the experimental section, are reported in the Supporting Information (Figure S3-2, Figure S3-3, Figure S3-4). The active mass loading, necessary to extrapolate the specific capacitance from the cell capacitance, calculated from direct measurements performed with the electrochemical workstation according to equations (P3-49), (P3-50) and (P3-52), are also reported in the Supplementary Information (Table S3-1).

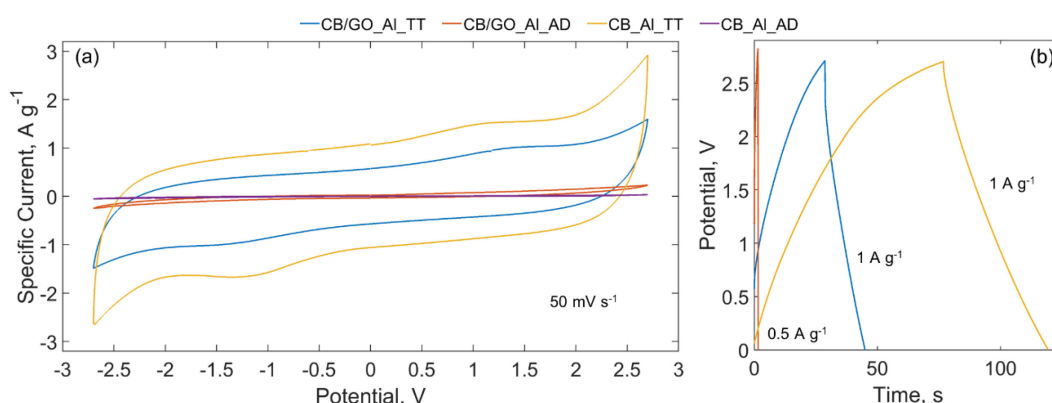


Figure P3-4 – (a) CVs at 50 mV s⁻¹ between -2.7 and +2.7 V and (b) GCs at 0.5 and 1 A g⁻¹ in a 1.5 M solution of TEMA-TFB in ACN of SCs made with CB/GO_AI_TT, CB/GO_AI_AD, CB_AI_TT, and CB_AI_AD (the GC profile of the latter is omitted as the internal resistance was too high to perform measurements with comparable specific currents with respect of the other samples).

Figure P3-5 – a shows CVs between -2.70 and +2.70 V at 50, 100, 300, and 500 mV s⁻¹. The rectangular shape of these graphs proves reversibility of charge/discharge after GO reduction (i.e., electrostatic behavior only). To study the effect on specific power and adhesion in an almost “all-graphene-based SC”, the trend in GCs was also analyzed. In Figure P3-5 – b charge/discharge curves at 0.5, 1, 2, and 4 A g⁻¹ are showed. Their analysis gives a specific capacitance range of 22.5–37.2 F g⁻¹ and a specific energy range of 6.3–10.5 Wh kg⁻¹, while the resulting specific power range is of 28.8–32.9 kW kg⁻¹ (Equivalent Series Resistance, ESR, of 30.2–26.5 Ω), calculated using, respectively, equations (P3-51) and (P3-54). The specific capacitance values are lower with respect of other available works in literature because of CB nature [46]: even though the

used CB powder for the manufacturing of the carbonaceous coatings under examination (BP® 2000) is characterized by a high Specific Surface Area (SSA) of $1216 \text{ m}^2 \text{ g}^{-1}$, its micropore volume is only $0.21 \text{ cm}^3 \text{ g}^{-1}$ [47]. For the more commonly used AC, in which the SSA ranges from 1000 to $2000 \text{ m}^2 \text{ g}^{-1}$, the micropore volume can reach $0.78 \text{ cm}^3 \text{ g}^{-1}$ [48]. As in a micropore (i.e., in a pore that has a less than 20 \AA diameter) there are more electric charges than in a larger pore with same area because of the ions losing the solvation sphere of the solvent, CB's SSA is less efficiently exploited in comparison to that of AC. However, it should be noted that the coupling of rGO and CB allows the optimization of other aspect of an EDLC, as shown in this research work.

The linearity of the curve from 1 A g^{-1} and above is another sign of an almost purely electrostatic behavior of this SC configuration (apart from a difference between the time of charge and discharge at 0.5 A g^{-1} due to leakage effects at low currents). In particular, at 1 A g^{-1} a specific power of 32.1 kW kg^{-1} was obtained. Since this result is correlated with a specific energy of 8.8 Wh kg^{-1} , the SC under analysis is hence above the common limits of commercial SC (with a maximum of 10 kW kg^{-1} of power and under 10 Wh kg^{-1} of energy) [49]. The energy value derives from a combination of a specific capacitance of 31.1 F g^{-1} with a highly optimized electrolyte as Triethyl methylammonium-Tetrafluoroborate (TEMA-TFB) in Acetonitrile (ACN). This electrolyte uses an organic solvent with high working tension and good conductivity, in addition TEMA-TFB ions entail cycle stability (even if this electrolyte is toxic and flammable) [50].

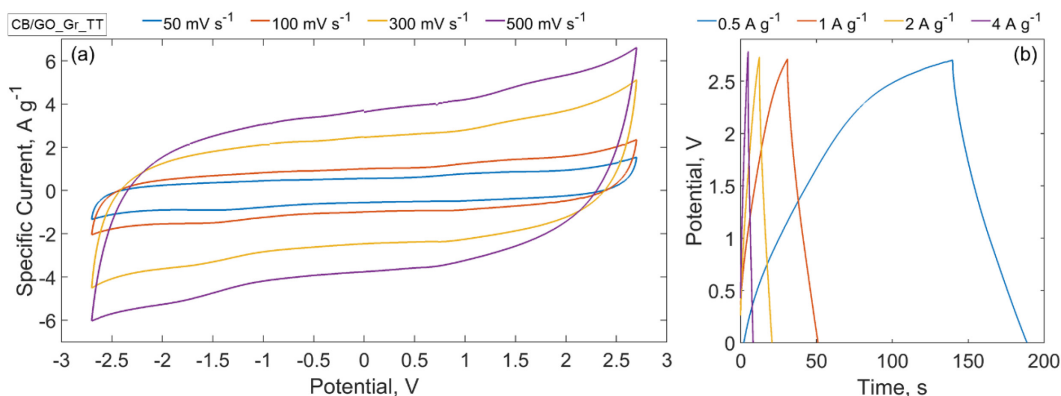


Figure P3-5 – (a) CVs and (b) GCs of SCs made with CB/GO_Gr_TT at different scan rates, from 50 to 500 mV s⁻¹, between -2.7 and +2.7 V and different specific currents, from 0.5 to 4 A g⁻¹, in a 1.5 M solution of TEMA-TFB in ACN.

Figure P3-6 shows a comparison of SCs in the Ragone plot (i.e., a plot of the specific power versus the specific energy). It shows that, while the specific energy ranges are superimposable, when the current collector is made with rGO there is an improvement in specific power with the same electrode. A possible explanation of this improvement could be in a different interaction of rGO in the active material when coated on a current collector consisting of the same material, as the rGO paper, rather than a metal sheet, as Al foil: in the studied electrodes, the adhesion derives from interactions between the non-removed oxygen-containing groups of rGO with the substrate surface [20]. While Al is a metal with an easy tendency to oxidize that often requires chemical etching to allow carbon coating, rGO paper does not need etching to form this bonding since, chemically, it is almost pure carbon. This is particularly true for the used rGO paper collector because, as an XRD analysis on this material showed in our previous work [51], it is characterized by a high degree of reduction of GO. Moreover, the rGO paper does not involve a discontinuity between two different materials (as for the Al-carbon interface) for the current flow during the charge/discharge process.

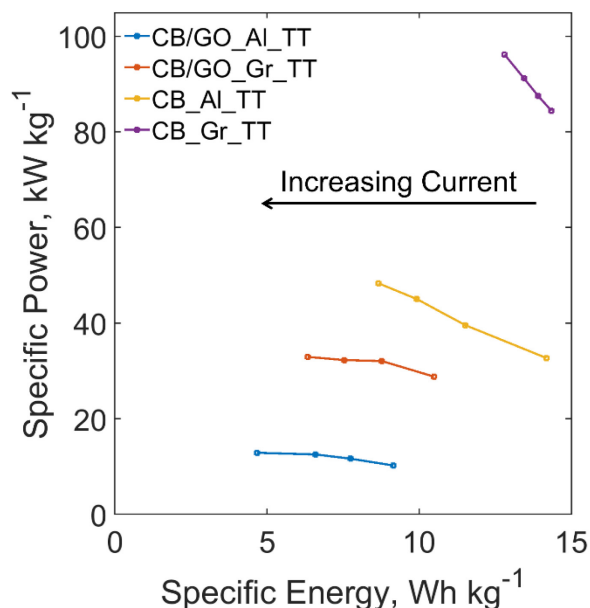


Figure P3-6 – Ragone plot of specific power versus specific energy for SCs made with CB/GO_Al_TT, CB/GO_Gr_TT, CB_Al_TT and CB_Gr_TT.

Surprisingly, Figure P3-6 shows also that the two analogous samples fabricated from the active material slurry prepared without the addition of GO perform better in both specific energy and power, in ostensible contradiction with Galhena et al [20]. It is however crucial to point out that this kind of active material had a very weak adhesion, on both Al and rGO paper current collectors, that led to an extreme fragility of the as fabricated electrodes and thus to an easiness to break when assembling SCs samples (see Figure S3-1 of Supplementary Information). Consequently, while these electrodes without rGO as active binder could be adopted for the manufacturing of very small devices with a delicate assembling process, they would unquestionably be not scalable. Nevertheless, CB_Al_TT and CB_Gr_TT samples show in a clearer way that the specific power of a SC with an rGO-based current collector surpasses that of an Al-based one by a factor of almost two (for the maximum recorded values, the specific powers are respectively 98.9 kW kg^{-1} and 49.4 kW kg^{-1} due to ESR of 2.8 and 10.0Ω). Since rGO paper mass density is less than one half of Al mass density (1.2 g cm^{-3} against 2.7 g cm^{-3}), a device as the sample

CB/GO_Gr_TT could reach a fourfold increase of the specific power when compared to a common SC, with a doubled specific energy. For the sake of clearness, this estimate omits the weight of the separator, the electrolyte and of all the connectors of which a complete device is made of.

2.3. Conclusions

In this study, a binder-free electrode was successfully manufactured using water as the only cheap and ecological solvent and GO as an alternative active binder that led to the formation of a homogeneous CB/GO nanocomposite. The material was subjected to a high temperature (550 °C) thermal treatment to reduce GO to rGO and thus unlock its ability to actively contribute to electrical energy storage performances. The reduction effectiveness was confirmed by the increase of the I_D/I_G ratio from 0.96 to 1.04 before and after, respectively, the thermal treatment, as depicted by Raman studies and confirmed by the XRD analysis, with the reduction of the interlayer spacing d_{002} from 4.00 to 3.77 Å. The electrochemical characterization showed interesting results with a high specific power of 32.1 kW kg⁻¹ and a corresponding specific energy of 8.8 Wh kg⁻¹ at a specific current of 1 A g⁻¹. The latter demonstrates that the development of a cheap, environmental-friendly and scalable manufacturing process unlocked by the complete removal of polymeric binders and organic solvents in the slurry preparation process and also the use of an innovative light-weight and high quality current collector based on rGO, for the fabrication of an “all-graphene based” device represents a valuable path for future improvements of the SCs industry.

3. Experimental section

3.1. Materials

CB powder (Black Pearls® 2000) was supplied by Cabot Corporation, TX100 (Laboratory Grade), regenerated cellulose membrane filters (Whatman RC55), TEMA-TFB and ACN were purchased from Sigma-Aldrich while GtO powder was acquired from XIAMEN TOB NEW ENERGY TECHNOLOGY Co. Deionized water (MilliQ®), was used throughout all the experiments. All chemicals were used as received without further purification.

3.2. Preparation of the CB/GO slurry

CB powder (1660 mg) was added in a solution of water (13 mL) and TX100 (46.5 μL , corresponding to 50 mg) and mixed as follows: 30 min of bath ultrasonication and subsequently 2 h of magnetic stirring. The resulting CB suspension in water was then mixed with a GO dispersion of 166 mg in 20.75 mL of water (8 mg mL⁻¹) with the aid of a ultrasonication bath. A homogeneous CB/GO (34 mg mL⁻¹) slurry was finally obtained after 12 h of further mixing using a magnetic stirrer. A CB-only slurry (34 mg mL⁻¹), without the addition of GO, was also prepared as reference.

The TX100 was mixed in water with the aid of a sonicating bath in a specific amount so that its concentration with respect of the CB is the 3 wt%. The volume of the GO dispersion in water, previously obtained by ultrasonic exfoliation of 1200 mg of GtO in 150 mL of water, was fixed in order to achieve a mass ratio of GO:CB=1:10.

3.3. Preparation of the rGO paper.

The rGO paper used as current collector was prepared following the procedure described in our previous work [51], briefly: a GO solution in

water was casted on a Polyethylene Terephthalate film and dried for 24 h in ambient condition to obtain a GO Film. The latter was annealed at a temperature of 1300 °C for 3h under Argon (Ar) atmosphere and rolled to obtain a free-standing paper with a controlled thickness of 40 μm and density of 1.2 g cm⁻³.

3.4. Fabrication of the EDLCs.

The as prepared slurries were coated on all the surface of the rGO paper serving as current collector using the doctor blade technique, a common Al sheet was also used as current collector for reference purposes. The coated collectors where heated at 550 °C for 1 h under Ar atmosphere. Finally, squares of 1 cm side were cut and used as electrodes of the supercapacitor samples. Non-thermally treated electrodes, subjected instead to ambient condition drying for 24 h after the coating, were used as reference.

For each SC sample, two identical electrodes were laminated in sandwich configuration using the regenerated cellulose membrane as separator and a 1.5 M solution of TEMA-TFB in ACN as electrolyte (0.5 mL). Heat-sealable laminating pouches and Copper tape for more robust electrical connections to the current collector (the conductive tape is never in contact with the active material) were used to finish the fabrication. A total of 6 different samples were manufactured and tested; the adopted nomenclature and the relative features are summarized in Table P3-2, while a summarizing scheme of the whole manufacturing process is shown in Figure P3-7.

Table P3-2 – Summary of fabricated and tested supercapacitors samples with the adopted nomenclature.

¹AD is the abbreviation of Ambient Drying, TT is the abbreviation of Thermally Treated, Gr is used to refer to the rGO paper used as current collector.

Sample¹	Slurry Composition	Current Collector	Thermal Treatment
<i>CB_Al_AD</i>	CB-only in TX100/H ₂ O	Al	No
<i>CB_Al_TT</i>	CB-only in TX100/H ₂ O	Al	Yes
<i>CB_Gr_TT</i>	CB-only in TX100/H ₂ O	rGO paper	Yes
<i>CB/GO_Al_AD</i>	CB/GO in TX100/H ₂ O	Al	No
<i>CB/GO_Al_TT</i>	CB/GO in TX100/H ₂ O	Al	Yes
<i>CB/GO_Gr_TT</i>	CB/GO in TX100/H ₂ O	rGO paper	Yes

3.5. Chemico-physical characterization.

For easiness of analysis, powder samples of the coating were scratched from the current collectors of each electrode type and then treated depending on the characterization technique. TEM (JEOL JEM-2100Plus) and FE-SEM (JSM-6301F FESEM by JEOL) were used to characterize the structures and morphologies particles and agglomerates constituting the carbonaceous nanocomposite. The powdered samples were subsequently sonicated and drop-casted on TEM grids for TEM analysis, while they were deposited on conductive carbon adhesive tabs for FE-SEM analysis. The obtained images from TEM and FE-SEM were then processed with the software “Image J” to extrapolate the features of interest.

Chemical properties were investigated through Raman Spectroscopy (inVia Raman Microscope by Renishaw) using a 532 nm laser source (IK Series He-Cd).The crystalline structure of the blends was analyzed with

Transmission Powder XRD (STOE STADI P) using a Cu-K α generator with 1.54 Å of wavelength. The powdered samples were deposited on regular microscope slides for Raman spectra collection, while they were mounted on specific sample holders for XRD measurements. XRD data were processed to obtain the interplanar spacing d in crystal lattices, following Bragg's law (P3-47) [43], and to estimate crystallite size L , using the Scherrer equation (P3-48) [44]:

$$d = \frac{\lambda}{2 \cdot \sin \theta} \quad (\text{P3-47})$$

$$L = \frac{K\lambda}{B \cdot \cos \varphi} \quad (\text{P3-48})$$

where λ is the radiation wavelength, θ is the scattering angle of the corresponding lattice, K is a shape factor, B is the line broadening at half maximum intensity of the peak, φ is the corresponding scattering angle.

3.6. Electrochemical characterization

The electrochemical performances of SC samples fabricated as previously described were evaluated using a μ AUTOLAB-BIII-FRA2 electrochemical workstation by Metrohm in two electrodes configuration (Figure P3-7). Two different techniques were exploited, all using the aforementioned workstation: CV and GCs.

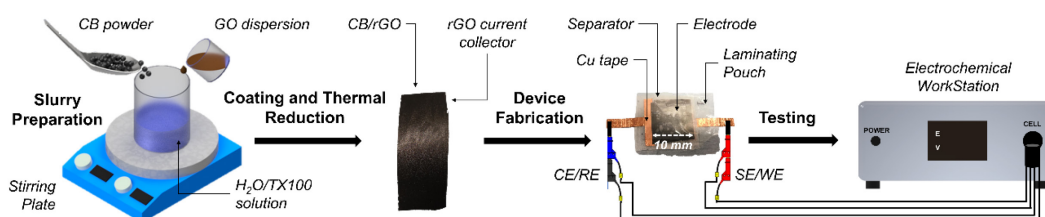


Figure P3-7 – Scheme of the manufacturing process showing also the electrochemical workstation. CB/rGO indicates the carbonaceous nanocomposite used as the active material. CE, RE, SE and WE indicate, respectively, Counter Electrode, Reference Electrode, Sensing Electrode and Working Electrode. Images by the author M. Rapisarda.

CV curves were analyzed, and the following formula was applied to calculate cell capacitances C :

$$C = \frac{1}{2\nu\Delta E} \oint I(E)dE = [F] \quad (\text{P3-49})$$

where ν is the scan rate, ranging from 50 to 500 mV s⁻¹ in current tests, E is the potential expressed in Volts (V) with ΔE as the potential excursion, between -2.7 V and 2.7 V (to better verify an EDLC behavior of the samples, as previously discussed), and the integral represents the area inside the curve which corresponds to the charge accumulated in the SC (with a factor of 0.5 that normalize the repeated area of the CV curve due to opposite sign scans). The specific capacitance C_s was obtained as follows:

$$C_s = 4 \times \frac{C}{m} = \left[\frac{F}{g} \right] \quad (\text{P3-50})$$

where C is the capacitance of the cell measured in the electrochemical tests while m is the mass of both electrodes expressed in grams (g). The multiplier of 4 adjusts the capacitance of the cell and the combined mass of two electrodes to the capacitance and mass of a single electrode, because each electrode has mass of $m/2$ and an EDLC is equivalent to two SC in series with half the capacitance of a single electrode. Moreover, the specific energy U_s was determined with the following:

$$U_s = \frac{1}{2 \times 3.6 \times m} C E_{max}^2 = \left[\frac{Wh}{kg} \right] \quad (\text{P3-51})$$

where E_{max} is the maximum applied potential and 3.6 is a factor used for the conversion of the energy from Joule to Watt-hour (Wh) and of the mass from grams to kilograms (kg).

GCs curves were obtained using a specific current of 0.5, 1, 2 and 4 A g⁻¹, in the potential range of 0–2.70 V. The capacitance was also calculated through the discharging part of the GCs curves by the formula:

$$C = \frac{I\Delta t}{\Delta E} = [F] \quad (\text{P3-52})$$

where I is the constant discharging current, expressed in Ampere, and Δt is the time interval, in seconds, of the discharge potential range ΔE . The specific capacitance and the specific energy were determined as in the previous case. Furthermore, the ESR can be estimated through the initial tension drop δE of the GC according to the following formula:

$$ESR = \delta E 2I = \Omega \quad (\text{P3-53})$$

The specific power P_s of SCs depends on the ESR and the maximum reached tension during the test as expressed in the following equation:

$$P_s = \frac{E_{max}^2}{4 \times ESR \times m} = \left[\frac{kW}{kg} \right] \quad (\text{P3-54})$$

The specific capacitance and the specific energy from the two tests just described usually show comparable results. However, thanks to the extra information obtainable from GCs, a Ragone plot can also be drawn to picture the trade-off between energy and power of electrical energy storage devices.

Acknowledgements

We acknowledge Prof. Frank Marken, Dr. Elena Madrid and Budi Riza Putra Putra of the Department of Chemistry of the University of Bath for their hospitality and advices. We acknowledge also in the same university Dr. Salman Shahid of the Department of Chemical Engineering for sharing its experiences about carbon and surfactants. Finally, we acknowledge the

Material and Chemical Characterisation Facility (MC²) at University of Bath (<https://doi.org/10.15125/mx6j-3r54>) for technical support and assistance in this work.

References

1. Abbate G., S. E., Damasco A. , Supercapacitor for Future Energy Storage. In *Sustaining Resources for Tomorrow. Green Energy and Technology*; Stagner J., Ting DK. (eds), Springer, Cham: 2020.
2. Abbey, C.; Joos, G., Supercapacitor Energy Storage for Wind Energy Applications. *IEEE Transactions on Industry Applications* **2007**, *43* (3), 769-776.
3. Hassanalieragh, M.; Soyata, T.; Nadeau, A.; Sharma, G., UR-SolarCap: An Open Source Intelligent Auto-Wakeup Solar Energy Harvesting System for Supercapacitor-Based Energy Buffering. *IEEE Access* **2016**, *4*, 542-557.
4. Ghaviha, N.; Campillo, J.; Bohlin, M.; Dahlquist, E., Review of Application of Energy Storage Devices in Railway Transportation. *Energy Procedia* **2017**, *105*, 4561-4568.
5. Song, Z.; Hou, J.; Hofmann, H.; Li, J.; Ouyang, M., Sliding-mode and Lyapunov function-based control for battery/supercapacitor hybrid energy storage system used in electric vehicles. *Energy* **2017**, *122*, 601-612.
6. Carignano, M. G.; Costa-Castelló, R.; Roda, V.; Nigro, N. M.; Junco, S.; Feroldi, D., Energy management strategy for fuel cell-supercapacitor hybrid vehicles based on prediction of energy demand. *Journal of Power Sources* **2017**, *360*, 419-433.
7. Stobinski, L.; Lesiak, B.; Malolepszy, A.; Mazurkiewicz, M.; Mierzwa, B.; Zemek, J.; Jiricek, P.; Bieloshapka, I., Graphene oxide and reduced graphene oxide studied by the XRD, TEM and electron spectroscopy methods. *Journal of Electron Spectroscopy and Related Phenomena* **2014**, 145-154.
8. Compton, O. C.; Nguyen, S. T., Graphene oxide, highly reduced graphene oxide, and graphene: versatile building blocks for carbon-based materials. *Small* **2010**, *6* (6), 711-23.
9. Lorf, A.; He, H.; Forster, M.; Klinowski, J., Structure of Graphite Oxide Revisited. *The Journal of Physical Chemistry B* **1998**, *102* (23), 4477-4482.

10. Dreyer, D. R.; Park, S.; Bielawski, C. W.; Ruoff, R. S., The chemistry of graphene oxide. *Chemical Society Reviews* **2010**, *39* (1), 228-240.
11. Novoselov, K. S.; Geim, A. K.; Morozov, S. V.; Jiang, D.; Zhang, Y.; Dubonos, S. V.; Grigorieva, I. V.; Firsov, A. A., Electric Field Effect in Atomically Thin Carbon Films. *Science* **2004**, *306* (5696), 666-669.
12. Balandin, A. A., Thermal properties of graphene and nanostructured carbon materials. *Nature Materials* **2011**, *10* (8), 569-581.
13. Pei, S.; Cheng, H.-M., The reduction of graphene oxide. *Carbon* **2012**, *50* (9), 3210-3228.
14. Bagri, A.; Mattevi, C.; Acik, M.; Chabal, Y. J.; Chhowalla, M.; Shenoy, V. B., Structural evolution during the reduction of chemically derived graphene oxide. *Nature Chemistry* **2010**, *2* (7), 581-587.
15. El-Kady, M. F.; Kaner, R. B., Scalable fabrication of high-power graphene micro-supercapacitors for flexible and on-chip energy storage. *Nature Communications* **2013**, *4* (1), 1475.
16. Yang, H.; Kannappan, S.; Pandian, A. S.; Jang, J.-H.; Lee, Y. S.; Lu, W., Nanoporous graphene materials by low-temperature vacuum-assisted thermal process for electrochemical energy storage. *Journal of Power Sources* **2015**, *284*, 146-153.
17. Jeong, H.-K.; Lee, Y. P.; Jin, M. H.; Kim, E. S.; Bae, J. J.; Lee, Y. H., Thermal stability of graphite oxide. *Chemical Physics Letters* **2009**, *470* (4), 255-258.
18. De Silva, K. K. H.; Huang, H. H.; Joshi, R. K.; Yoshimura, M., Chemical reduction of graphene oxide using green reductants. *Carbon* **2017**, *119*, 190-199.
19. Zhu, Y.; Stoller, M. D.; Cai, W.; Velamakanni, A.; Piner, R. D.; Chen, D.; Ruoff, R. S., Exfoliation of Graphite Oxide in Propylene Carbonate and Thermal Reduction of the Resulting Graphene Oxide Platelets. *ACS Nano* **2010**, *4* (2), 1227-1233.
20. Galhena, D. T. L.; Bayer, B. C.; Meyer, J. C.; Hofmann, S.; Amaratunga, G. A. J., Reduced Graphene Oxide as a Monolithic Multifunctional Conductive Binder for Activated Carbon Supercapacitors. *ACS Omega* **2018**, *3* (8), 9246-9255.
21. Brodie, B. C., XIII. On the atomic weight of graphite. *Philosophical Transactions of the Royal Society of London* **1859**, *149*, 249-259.
22. Hummers, W. S.; Offeman, R. E., Preparation of Graphitic Oxide. *Journal of the American Chemical Society* **1958**, *80* (6), 1339-1339.

23. Chen, J.; Yao, B.; Li, C.; Shi, G., An improved Hummers method for eco-friendly synthesis of graphene oxide. *Carbon* **2013**, *64*, 225-229.
24. Rolison, D. R.; Nazar, L. F., Electrochemical energy storage to power the 21st century. *MRS Bulletin* **2011**, *36* (7), 486-493.
25. Abbas, Q.; Pajak, D.; Frąckowiak, E.; Béguin, F., Effect of binder on the performance of carbon/carbon symmetric capacitors in salt aqueous electrolyte. *Electrochimica Acta* **2014**, *140*, 132-138.
26. Chmiola, J.; Largeot, C.; Taberna, P.-L.; Simon, P.; Gogotsi, Y., Desolvation of Ions in Subnanometer Pores and Its Effect on Capacitance and Double-Layer Theory. *Angewandte Chemie International Edition* **2008**, *47* (18), 3392-3395.
27. Simotwo, S. K.; DelRe, C.; Kalra, V., Supercapacitor Electrodes Based on High-Purity Electrospun Polyaniline and Polyaniline–Carbon Nanotube Nanofibers. *ACS Applied Materials & Interfaces* **2016**, *8* (33), 21261-21269.
28. Xu, B.; Wang, H.; Zhu, Q.; Sun, N.; Anasori, B.; Hu, L.; Wang, F.; Guan, Y.; Gogotsi, Y., Reduced graphene oxide as a multi-functional conductive binder for supercapacitor electrodes. *Energy Storage Materials* **2018**, *12*, 128-136.
29. Choi, J.-H.; Lee, C.; Cho, S.; Moon, G. D.; kim, B.-s.; Chang, H.; Jang, H. D., High capacitance and energy density supercapacitor based on biomass-derived activated carbons with reduced graphene oxide binder. *Carbon* **2018**, *132*, 16-24.
30. Xu, S.; Liu, R.; Shi, X.; Ma, Y.; Hong, M.; Chen, X.; Wang, T.; Li, F.; Hu, N.; Yang, Z., A dual CoNi MOF nanosheet/nanotube assembled on carbon cloth for high performance hybrid supercapacitors. *Electrochimica Acta* **2020**, *342*, 136124.
31. Xu, S.; Su, C.; Wang, T.; Ma, Y.; Hu, J.; Hu, J.; Hu, N.; Su, Y.; Zhang, Y.; Yang, Z., One-step electrodeposition of nickel cobalt sulfide nanosheets on Ni nanowire film for hybrid supercapacitor. *Electrochimica Acta* **2018**, *259*, 617-625.
32. Xu, S.; Wang, T.; Ma, Y.; Jiang, W.; Wang, S.; Hong, M.; Hu, N.; Su, Y.; Zhang, Y.; Yang, Z., Cobalt Doping To Boost the Electrochemical Properties of Ni@Ni₃S₂ Nanowire Films for High-Performance Supercapacitors. *ChemSusChem* **2017**, *10* (20), 4056-4065.
33. (ICBA), I. C. B. A., Carbon Black User's Guide: Safety, Health & Environmental Information. 2016.

34. Weingarth, D.; Drumm, R.; Foelske-Schmitz, A.; Kötz, R.; Presser, V., An electrochemical in situ study of freezing and thawing of ionic liquids in carbon nanopores. *Physical Chemistry Chemical Physics* **2014**, *16* (39), 21219-21224.
35. González-García, C. M.; González-Martín, M. L.; Gómez-Serrano, V.; Bruque, J. M.; Labajos-Broncano, L., Determination of the Free Energy of Adsorption on Carbon Blacks of a Nonionic Surfactant from Aqueous Solutions. *Langmuir* **2000**, *16* (8), 3950-3956.
36. Paredes, J. I.; Villar-Rodil, S.; Martínez-Alonso, A.; Tascón, J. M. D., Graphene Oxide Dispersions in Organic Solvents. *Langmuir* **2008**, *24* (19), 10560-10564.
37. Mitsuda, K.; Kimura, H.; Murahashi, T., Evaporation and decomposition of Triton X-100 under various gases and temperatures. *Journal of Materials Science* **1989**, *24* (2), 413-419.
38. Pimenta, M. A.; Dresselhaus, G.; Dresselhaus, M. S.; Cançado, L. G.; Jorio, A.; Saito, R., Studying disorder in graphite-based systems by Raman spectroscopy. *Physical Chemistry Chemical Physics* **2007**, *9* (11), 1276-1290.
39. Ferrari, A. C., Raman spectroscopy of graphene and graphite: Disorder, electron-phonon coupling, doping and nonadiabatic effects. *Solid State Communications* **2007**, *143* (1), 47-57.
40. Schniepp, H. C.; Li, J.-L.; McAllister, M. J.; Sai, H.; Herrera-Alonso, M.; Adamson, D. H.; Prud'homme, R. K.; Car, R.; Saville, D. A.; Aksay, I. A., Functionalized Single Graphene Sheets Derived from Splitting Graphite Oxide. *The Journal of Physical Chemistry B* **2006**, *110* (17), 8535-8539.
41. Ferrari, A. C.; Meyer, J. C.; Scardaci, V.; Casiraghi, C.; Lazzeri, M.; Mauri, F.; Piscanec, S.; Jiang, D.; Novoselov, K. S.; Roth, S.; Geim, A. K., Raman Spectrum of Graphene and Graphene Layers. *Physical Review Letters* **2006**, *97* (18), 187401.
42. Krishnankutty, N.; Vannice, M. A., Effect of Pretreatment on Surface Area, Porosity, and Adsorption Properties of a Carbon Black. *Chemistry of Materials* **1995**, *7* (4), 754-763.
43. Bragg, W. H.; Bragg, W. L., The reflection of X-rays by crystals. *Proceedings of the Royal Society of London. Series A, Containing Papers of a Mathematical and Physical Character* **1913**, *88* (605), 428-438.

44. P., S., Bestimmung der Größe und der inneren Struktur von Kolloidteilchen mittels Röntgenstrahlen. *Nachrichten von der Gesellschaft der Wissenschaften zu Göttingen, Mathematisch-Physikalische Klasse* **1918**, 1918, 98-100.
45. Biscoe, J.; Warren, B. E., An X-Ray Study of Carbon Black. *Journal of Applied Physics* **1942**, 13 (6), 364-371.
46. Naoi, K.; Simon, P., New Materials and New Configurations for Advanced Electrochemical Capacitors. *Journal of The Electrochemical Society* **2008**, 17 (1), 34-37.
47. Mydul Islam, A. K. M.; Hwang, J.-I.; Lee, S.-E.; Kim, J.-E., Comparative study of carbon black and activated carbon adsorbents for removal of carbofuran from aqueous solution. *Desalination and Water Treatment* **2016**, 57 (45), 21512-21523.
48. Shiraishi, S., Highly-Durable Carbon Electrode for Electrochemical Capacitors. *Boletín del Grupo Español del Carbón* **2013**, 28, 18-24.
49. Simon, P.; Gogotsi, Y., Materials for electrochemical capacitors. *Nat Mater* **2008**, 7 (11), 845-54.
50. Xia, L.; Yu, L.; Hu, D.; Chen, G. Z., Electrolytes for electrochemical energy storage. *Materials Chemistry Frontiers* **2017**, 1 (4), 584-618.
51. Rapisarda, M.; Meo, M., Multifunctional reduced graphene oxide coating on laminated composites. *Materials Today: Proceedings* **2020**.

Supplementary Information

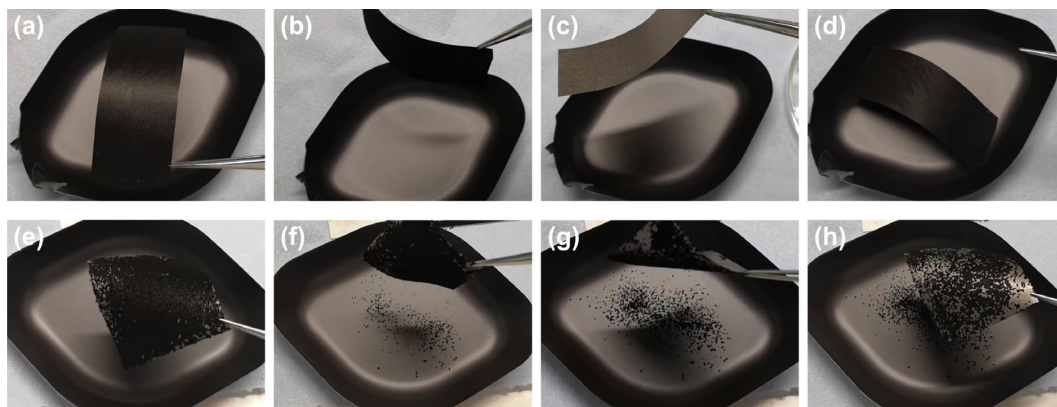


Figure S3-1 – Qualitative comparison of the adhesion of the active material on the current collector and of its mechanical integrity between (a-d) CB/GO_Gr_TT and (e-h) CB_Gr_TT as samples were: (a) and (e), as taken out from the furnace; (b) and (f), tilted on a side; (c) and (g) tilted upside-down; (d) and (h), returned to horizontal position. A considerable amount of active material falling from the current collector is noticeable for the sample CB_Gr_TT while no material is detached from the sample CB/GO_Gr_TT. Images by the author M. Rapisarda.

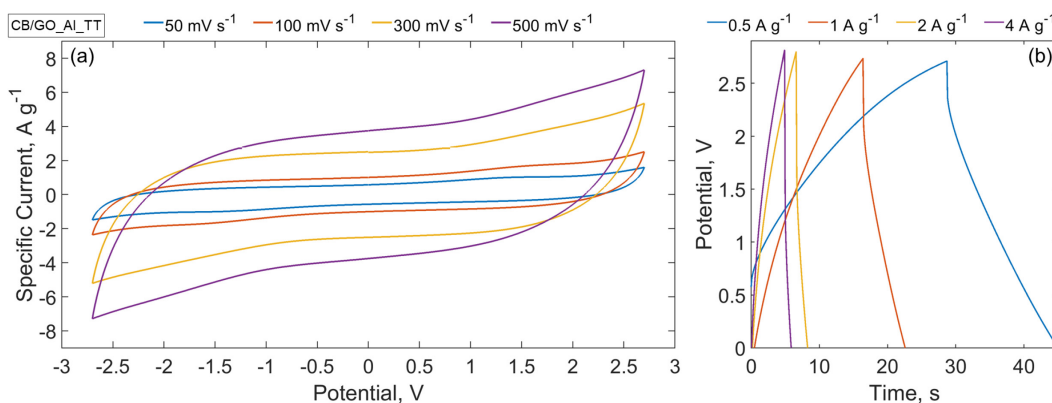


Figure S3-2 – (a) CVs and (b) GCs of SCs made with CB/GO_Al_TT at different scan rates, from 50 to 500 mV s⁻¹, between -2.7 and +2.7 V and different specific currents, from 0.5 to 4 A g⁻¹, in a 1.5 M solution of TEMA-TFB in ACN.

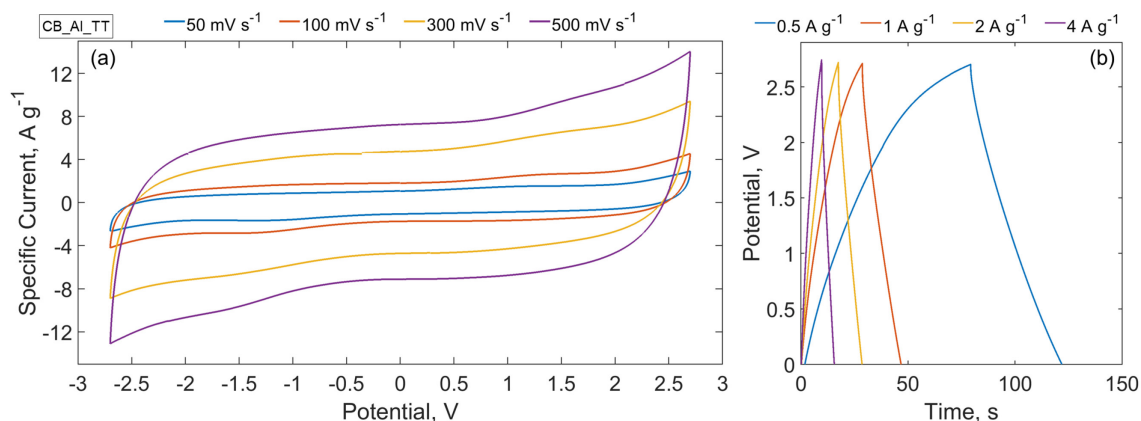


Figure S3-3 – (a) CVs and (b) GCs of SCs made with CB_Al_TT at different scan rates, from 50 to 500 mV s^{-1} , between -2.7 and +2.7 V and different specific currents, from 0.5 to 4 A g^{-1} , in a 1.5 M solution of TEMA-TFB in ACN.

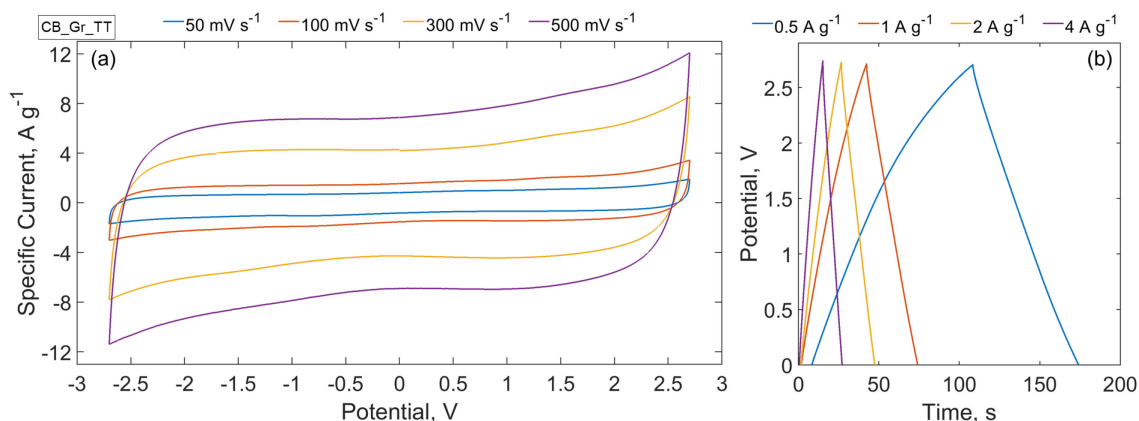


Figure S3-4 – (a) CVs and (b) GCs of SCs made with CB_Gr_TT at different scan rates, from 50 to 500 mV s^{-1} , between -2.7 and +2.7 V and different specific currents, from 0.5 to 4 A g^{-1} , in a 1.5 M solution of TEMA-TFB in ACN.

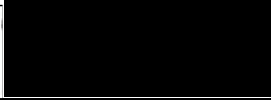
Table S3-1 – Comparison of the four devices of Figure P3-6 in terms of active mass loading, capacitance and specific capacitance, with the values measured through GCs at specific currents ranging from 0.5 A g^{-1} to 4 A g^{-1} .

Sample	Active mass [mg]	Capacitance range [mF]	Specific Capacitance range [F g^{-1}]
CB_Al_TT	3.68	31.6-51.6	34.3-56.1
CB_Gr_TT	3.33	42.2-47.3	50.6-56.7
CB/GO_Al_TT	3.16	13.1-25.6	16.6-32.4
CB/GO_Gr_TT	2.33	13.1-21.7	22.5-37.2

6.3 Environmentally friendly and high-performance supercapacitors with a hybrid binder

The statement of Authorship Form and the paper can be found next, followed by the relevant supplementary information.

This declaration concerns the article entitled:	
<i>Graphene Oxide and Starch Gel as a Hybrid Binder for Environmentally Friendly High-Performance Supercapacitors</i>	
Publication status (tick one)	
Draft Manuscript <input type="checkbox"/> Submitted <input type="checkbox"/> In Review <input type="checkbox"/> Accepted <input type="checkbox"/> Published <input checked="" type="checkbox"/>	
Publication details (reference)	https://doi.org/10.1038/s42004-021-00604-0
Copyright status (tick the appropriate statement)	
I hold the copyright for this material <input type="checkbox"/>	
Copyright is retained by the publisher, but I have been given permission to replicate the material here <input checked="" type="checkbox"/>	
Candidate's contribution to the paper (provide details, and also indicate as a percentage)	<p>The candidate contributed to / considerably contributed to / predominantly executed the...</p> <p>Formulation of ideas: 80% <i>I proposed the idea on the use of a rGO and Starch gel as an environmentally friendly binder for the manufacturing of supercapacitor electrodes, with Prof. F. Marken contributing to its final formulation. Prof. M. Meo participated in the discussions and approved the project.</i></p> <p>Design of methodology: 100% <i>I designed both manufacturing and characterisation plans.</i></p> <p>Experimental work: 100% <i>I manufactured and characterised all the samples.</i></p> <p>Presentation of data in journal format: 90%</p>

	<i>I defined paper structure, wrote the first draft and designed the figures. Prof. F. Marked participated in electrochemical properties discussion and reviewed the manuscript. Prof. M. Meo reviewed the manuscript and supported in the submission and publication process.</i>		
Statement from Candidate	This paper reports on original research I conducted during the period of my Higher Degree by Research candidature.		
Signed			Date 15/02/2022

Graphene Oxide and Starch Gel as a Hybrid Binder for Environmentally Friendly High-Performance Supercapacitors

Mario Rapisarda¹, Frank Marken², Michele Meo^{1,*}

¹*Department of Mechanical Engineering, University of Bath, Bath, BA27AY, UK*

²*Department of Chemistry, University of Bath, Bath, BA27AY, UK*

**Corresponding author*

Abstract

Alternative green binders processable in water are being investigated for the development of more efficient and sustainable supercapacitors. However, their electrochemical performances have fallen within or below the average of commercially available devices. Herein, an optimised gelled mixture of graphene oxide (GO) and starch, a biopolymer belonging to the family of polysaccharides, is proposed. The molecular interactions between the two components enhance electrodes structure and morphology, as well as their thermal stability. GO, thanks to its reduction that is initially triggered by reactions with starch and further progressed by thermal treatment, actively contributes to the charge storage process of the supercapacitors. The optimised electrodes can deliver a specific capacitance up to 173.8 F g⁻¹ while providing good rate capabilities and long-term stability over 17,000 cycles. These are among the best electrochemical performances achieved by environmentally friendly supercapacitors using a biomaterial as a binder.

1. Introduction

The on-going growth in global energy demand and the current transition toward a greener more sustainable industry are driving the research for the development of more efficient and sustainable energy storage devices [1]. A viable solution is represented by electrochemical double-layer capacitors (EDLCs), a type of supercapacitors accumulating and delivering electrical energy by ultra-fast electrostatic charge storage and release in the electrical double layer. Their rapid charge/discharge, high power density, cycling life, energy efficiency, broad operating temperature range, and scalable design allow EDLCs use in either electronic and portable devices, as well as for transportation and stationary applications [2]. Although their well-known drawback is a limited energy density, extensively addressed via multiple approaches [3-6], concerns over the environmental impact of EDLC electrodes manufacturing process are only recently arising. In particular, commonly used binders are fluoropolymers as poly(tetrafluoroethylene) and poly(vinylidene fluoride) dispersed in organic solvents as *N*-methyl-2-pyrrolidone and acetonitrile. Both binder and solvent represent a major cost [7] and, especially, the main source of danger to the environment[8-10]. For this reason, alternative binders consisting of biopolymers processable in water (i.e., “green binders” that are intrinsically renewable and biodegradable) could ultimately lead to cheaper and more environmentally friendly devices [11, 12]. In fact, they would allow for a reduction in the complexity of the coating process, as there would be no need for a solvent entrapment and recovery system during the drying, and a mitigation of risks of environmental pollution, thanks to the complete absence of toxic compounds.

Starch (St) is an inexpensive and readily available biopolymer belonging to the class of polysaccharides. It is composed of two types of

molecules, the linear and helical amylose and the branched amylopectin, which distribution depends on the native biomass. Non-edible potatoes are commonly used and lead to ~20 wt% amylose and ~80 wt% amylopectin [13]. For the peculiar physicochemical structure, starch represents an ideal candidate as a green binder [12, 14, 15]. While amylose behaves as conventional synthetic polymers and allows hydrophobic binding [16], amylopectin proved to be the key to overcome brittleness and shrinkage of coatings [15]. Although being naturally insoluble in water, starch becomes easily processable upon heating at its gelatinisation temperature (~60–80 °C) due to the swelling of its granules and the solubilisation of amylose [17].

Varzi, Passerini and Ruschhaupt [15, 18] proved that starch, or its mixture with guar gum, could effectively be used as alternative green binder, superseding carboxymethyl cellulose (i.e., the state of the art aqueous and non-fluorinated binder alternative [18]) issue of low mass loadings due to brittleness and shrinkage upon drying. They reported a specific capacitance of ~50 F g⁻¹ in an organic electrolyte within a potential window of 0–2.5 V. Their work inspired Jeżowski and Kowalczewski [14] to develop a starch-based conductive glue for an optimised coating process that improved high power performances, reporting an energy density of ~20 Wh kg⁻¹ at ~10 kW kg⁻¹ within 0–2.5 V. It is worth noting, however, that the findings of the aforementioned studies mostly rely on qualitative evaluations, and that the reported electrochemical performance falls within or below the average of commercially available devices [19].

Graphene Oxide (GO) is a functionalised form of graphene having oxygen groups, such as hydroxyl, carbonyl, alkoxy and epoxy, which disrupts the conjugated network of the sp² lattice of carbon atoms [20, 21]. The latter is responsible for the remarkable electronic and thermal properties reported for pristine graphene [22, 23]. GO is capable of forming

stable suspensions in water and can be templated in various assemblies with low cost and in environmentally friendly processes [24]. This allows its use for various applications such as aerogels for acoustic absorption [25] and water treatment [26], free-standing papers for multifunctional polymeric composites [27] and EMI shielding [28], and carbonaceous composites for SC electrodes [29]. In particular, Choi et al. recently exploited the inclusion of 2 wt% reduced GO (rGO) as an active binder in biomass derived Activated Carbons (ACs), where the remarkable electrochemical performances were attributed to the development of electrically conductive networks formed by the rGO binder and the pseudocapacitance contribution due to residual oxygen functional groups [30]. GO was also used as the precursor to fabricate crumpled graphene papers by Zhao and co-workers, where the excellent rGO mechanical stability was the key to fabricate all-solid-state and stretchable SCs for un-conventional electronic devices (i.e., wearables and portable) [31]. Moreover, the ability of oxygen groups on GO sheets to interact with polymers have been exploited to improve their electrical and mechanical properties, as well as their thermal stability [32]. In particular, biocomposites of starch and GO have recently been investigated [33-35].

In this study, a hybrid green binder was obtained from the gelation of an optimised mixture of starch and GO (GO-St-gel). Hydrogen bonds between amylose, amylopectin, and oxygen functionalities on GO sheets were formed during the water processing and an extended thermal stability was achieved, as revealed from a physicochemical characterisation. The proposed binder, after its mixing in water with ACs and Carbon Blacks (CBs), was capable to form homogeneous carbonaceous coatings (GO-StC) with a 3D morphology that enhanced the charge transfer process in the manufactured electrodes. GO actively contributed to the electrochemical performance (hence “hybrid”) due to its partial reduction

that started during the gelation, and that was later optimised thanks to a further thermal treatment. The assembled symmetrical EDLCs provided a high specific capacitance of 173.8 F g^{-1} , good rate capabilities, and a remarkable long-term stability with a capacitance retention of 93.1% after 17,000 charge/discharge cycles. Considering also that the electrodes were fabricated following an industrial-ready manufacturing process, the hybrid and green GO-St-gel binder presented in this work is an ideal candidate for the development of environmentally friendly and high-performance energy storage devices.

2. Results and discussion

2.1. Fabrication and characterisation of GO-StC electrodes

GO-StC electrodes were fabricated by a conventional method consisting of three main steps. The synthesis of a GO and starch gel that served as a green and hybrid binder, then the preparation of a carbonaceous slurry by adding an active material, AC, and a conductive additive, CB, and finally a controlled coating on a current collector, the rGO paper, immediately followed by a drying process. All slurries were prepared so that the mass ratio of the components is fixed as AC:CB:GO-St = 85:5:10 by using essentially the same method and are termed GO-StC-I, GO-StC-II, GO-StC-III, GO-StC-IV, GO-StC-V, depending on the initial composition of the GO-St-gel (GO amount corresponding to the 2.5, 3.3, 5, 6.7, 7.5 wt%, respectively). Reference samples, with the binder consisting of St only (StC) and of GO only (GO-C), were also manufactured by a similar method. Slurry composition of different GO-StC and reference electrodes are summarised in Table S4-1. It is crucial to note that the physicochemical characterisation was focused on the GO-StC-III electrode (containing 5 wt% GO) that provided optimized electrochemical properties.

As shown in Figure P4-1 – a, when mixed in water, GO sheets intercalates between starch granules thanks to the formation of hydrogen bonds between the molecules of the two components [33, 36]. After heating the blend at a temperature of 70 °C, starch granules swell releasing amylose, mostly, and amylopectin molecules that can generate an amorphous network (i.e., gelation) and thus give the aqueous blend a viscoelastic behaviour [37]. On cooling, the disrupted chains usually tend to reassociate forming microcrystalline regions (i.e., retrogradation) [38]. However, due to the presence of GO intercalated sheets and their interaction through hydrogen bonds, the retrogradation can be inhibited [33]. Additionally, it was recently found that chemical reactions between starch molecules and oxygen functionalities attached to GO can lead to the partial restoration of the conjugated network of the sp^2 lattice of carbon atoms and, consequently, the recovery of graphene electronic properties (i.e., reduction) [34, 39, 40]. The latter is believed to provide for a reduced electrical resistance and an improved electrochemical capacitance of fabricated electrodes [29, 41, 42]. Upon adding CB and AC particles, a homogeneous slurry is obtained, with the key role of linear amylose chains and GO sheets as dispersing agents [11, 29, 43, 44].

GO-StC electrodes are finally obtained with the subsequent coating and drying, as schematised in Figure P4-1 – b. The resulting surface morphology can be observed from Scanning Electron Microscopy (SEM) images (Figure P4-1 – c and Figure S4-1 – a), where the effective role of branched amylopectin chains to build homogeneous coatings with limited shrinkage is proved [15]. Moreover, GO presence determines a more 3D structured morphology with respect of the reference StC coating (Figure P4-1 – d and Figure S4-1 – b), that also shows some lumps due to a poorer dispersion of carbon particles. Higher magnification SEM images ultimately confirm the even distribution of CB particles among AC in GO-StC coatings

(Figure P4-1 – e-f), whether CB clusters near “clean” AC particles are found in StC (Figure P4-1 – g-h). Transmission Electron Microscopy (TEM) images show how Starch, AC and CB particles are distributed to form an StC agglomerate (Figure P4-1 – i-j), with GO sheets being found at its base (Figure P4-1 – k). Higher magnification TEM images of AC, Starch, CB and GO picture their distinctive structures (Figure P4-1 – l-o).

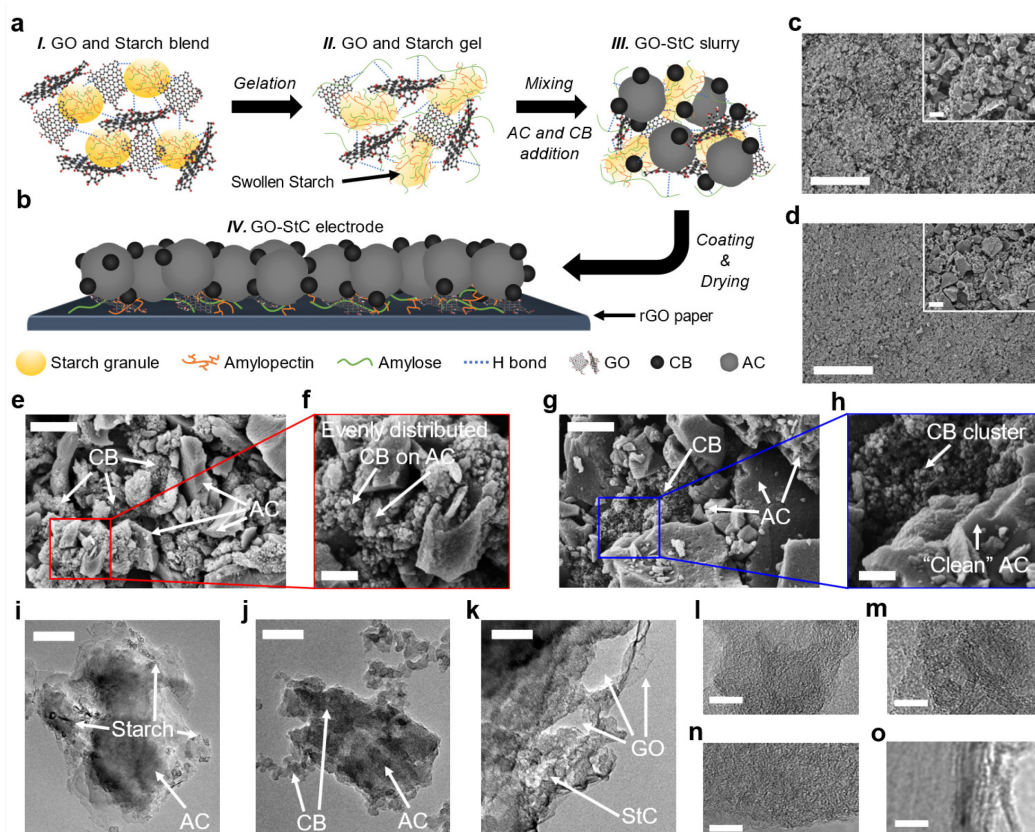


Figure P4-1 – Schematic representation and electronic microscope imaging of GO-StC electrodes. (a) Schematic of GO-StC slurry preparation and of (b) GO-StC electrode. (c-h) SEM images showing: surface morphology of (c) GO-StC and (d) StC coatings (scale bar 100 μm) with higher magnification inset (scale bar 5 μm); AC and CB particles distribution in (e,f) GO-StC and (g,h) StC electrode materials (scale bars 2 μm and 500 nm). (i-o) TEM images of GO-StC electrode material showing: (i) starch particles attached to AC, (j) AC and CB particles distribution, (k) GO sheets at the base of the StC agglomerate (scale bars 200 nm), and (l) AC, (m) Starch, (n) CB and (o) GO magnified structures (scale bars 10 nm).

In X-ray diffraction (XRD) patterns (Figure P4-2 – a), GO shows the characteristic (001) peak associated to the carbon crystalline phase and the

(100) peak related to the lateral dimension of basal planes at 10.80° and 42.57° , respectively [45, 46]. St has instead the typical features of the B-type crystalline form, commonly found in potato starches with high contents of amylose (~20 %) [47]. When GO is mixed with St (GO-St) the (001) peak disappears, indicating the absence of any ordered structure, usually due to the re-stacking of GO sheets driven from Van der Waals interactions, and thus suggesting their intercalation between starch granules [48]. Moreover, after the gelation process the main features of starch are absent. This confirms the formation of an amorphous phase due to the release of amylose from swollen granules [49], and with GO inhibiting the retrogradation into a crystalline matrix [33].

XRD patterns of GO-StC electrode active material show the characteristic (002) and (10) peaks at 21.89° and 43.73° , respectively. The first derives from the interlayer spacing of graphene sheets (d) and is downshifted with respect of both StC (22.24°) and pure AC (22.13°), indicating, according to Bragg's law, a slightly more expanded carbon structure (4.06 Å against 3.99 and 4.01 Å, respectively). The (10) peak derives instead from the merging of (100) and (101) lattice peaks typically shown in ordered graphite, as a consequence of turbostratic arrangements of graphene layers [50]. From Scherrer's formula [51], (10) and (100) peaks data related to AC and GO, respectively, are processed to estimate crystallites lateral size (L_a). The reduction observed from GO (128 Å) to GO-St (109.6 Å) and GO-St-gel (86.9 Å) can be attributed to the rupture of GO sheets during the processing. On the other hand, GO-StC electrode material shows a smaller value (37.6 Å) with respect of both reference StC (43 Å) and starting AC (44.6 Å), explainable with a finer particle distribution due to GO sheets interactions. A summary of main peaks position and calculated structural parameters can be found in Figure S4-2.

Comparing main starch features in Fourier-Transform Infrared Spectroscopies (FT-IR) of GO-St-gel to GO-St and St (Figure P4-2 – b), with particular regards in the disappearance of the 1642 cm^{-1} band (5, associated to water absorbed in the amorphous region), the disappearance of the 1042 cm^{-1} band (14, typical of crystalline phase), and the increase of the intensity ratio between the 1016 and 995 cm^{-1} bands (16 and 17, respectively due to C-OH bending and C-O-C skeletal vibrations) [52], together with the shift of GO band at 1615 cm^{-1} (6, due to stretching and bending of OH groups in absorbed H_2O molecules) [53], ultimately provides for a successful gelation [49, 54]. Moreover, a shift of OH related features for starch at 3310 cm^{-1} (1) and for GO at 1373 , 1219 and 1165 cm^{-1} (7, 9 and 11, respectively) confirms the formation of hydrogen bonds between OH groups of both amylose and amylopectin and the oxygen functionalities on GO sheets [33, 36]. Finally, from FT-IR spectra of GO-St before and after the gelation, the decrease of GO oxygen functional groups between 3586 and 3216 cm^{-1} (1' and 1'', associated to OH stretching), and at 1720 , 1038 and 975 cm^{-1} (4, 15 and 18, respectively attributed to C=O stretching of Carbonyl groups, C-O stretching of Alkoxy groups and C-O-C stretching of Epoxy groups) [55] can be interpreted as a partial reduction of GO by its reaction with starch molecules [39]. A summary of all the features of the discussed materials can be found in Table S4-3. Both GO-StC and StC shows no significant variation with respect of pure AC (Figure P4-2 – b).

The absence of starch features (amylose and amylopectin vibrational modes between 1100 and 1500 cm^{-1} , and C-H vibrations at 2915 cm^{-1}) [52] in Raman Spectroscopies (RS) before and after GO-St blend gelation (Figure P4-2 – c) is mainly due to the stronger excitation of carbon features of intercalated GO sheet, but can also be attributed to structural changes caused by the rearrangement of hydrogen bonds between water and starch molecules [56]. All carbonaceous samples show the typical D ($\sim 1348\text{ cm}^{-1}$)

and G ($\sim 1607 \text{ cm}^{-1}$) bands associated to A_{1g} breathing mode due to structural disorder and E_{2g} vibrating mode of crystalline Graphite [57] as well as 2nd order scatterings ($\sim 2550\text{--}3300 \text{ cm}^{-1}$) caused by turbostratic arrangements of graphene layers [58], however a distinction has to be made in their interpretation due to different material nature. Focusing on D and G bands with the aim to calculate the $I_D/(I_D + I_G)$ ratio expressing carbons' structural disorder [46], both GO-St-gel and GO-St have been deconvoluted considering three additional interbands accounting for disorder (D^* , D'' and D' , associated to sp^2 - sp^3 bonds at the edges of networks, interstitial defects in amorphous lattices and phonon mode due to crystal defects, respectively) following Claramut et al. method for GO [59] (Figure P4-2 – d). The resulting $I_D/(I_D + I_G)$ value for GO-St-gel is 61.33%, increased with respect of both GO-St and GO (58.43% and 58.56%, respectively) and thus corroborates the partial GO reduction previously deduced from FT-IR results [40]. GO-StC and StC have instead been deconvoluted considering only two additional interbands (I , associated to impurity ions, and D'' again) following Cuesta et al. method for AC [60] (Figure P4-2 – e). The smaller $I_D/(I_D + I_G)$ value for GO-StC (51.72%) compared to both StC and AC (52.43% and 53.42%, respectively) can be ascribed to an improved disaggregation and stabilisation of AC and CB particles thanks to their interactions with GO sheets [29, 43], as previously suggested from XRD results. Figure P4-2 – f pictures the described trend for $I_D/(I_D + I_G)$ and its relationship with L_a . A summary of deconvolution parameters and resulting $I_D/(I_D + I_G)$ ratios for the carbonaceous materials can be found in Table S4-4.

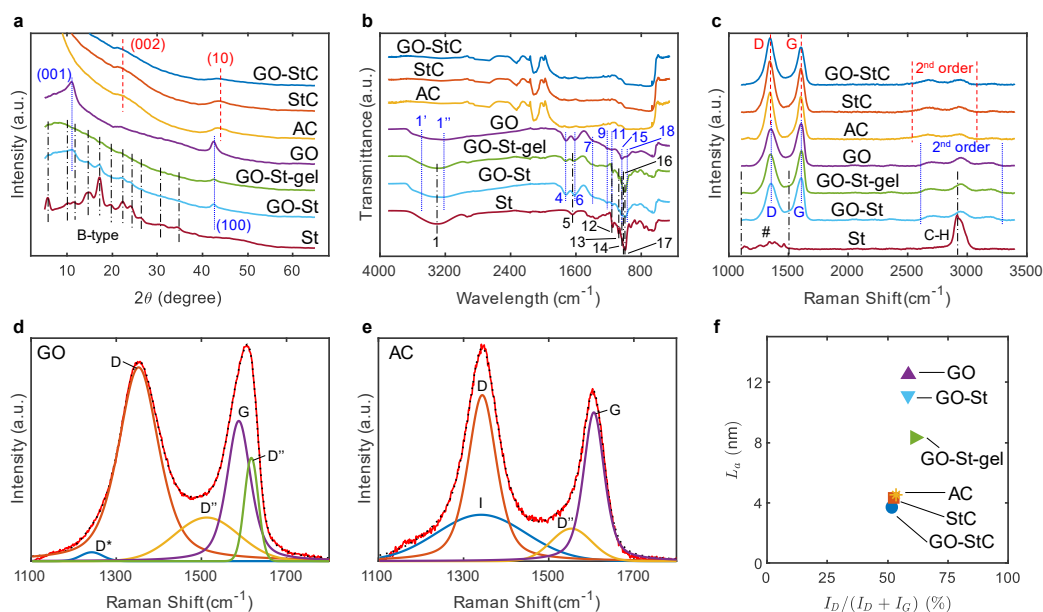


Figure P4-2 – Physicochemical characterisation (a) XRD patterns, (b) FT-IR and (c) RS spectra of GO-StC electrode material and GO-St-gel binder compared with reference materials. Red dashed, blue dotted and black dashed and dotted lines refer to AC, GO and St related features, respectively. “#” stands for “Amylose and Amylopectin”. (d) GO and (e) AC deconvolution results. Red solid and black dotted lines indicate experimental measurements and fitting results, respectively. (f) Variation of L_a with $I_D/(I_D+I_G)$ ratio.

2.2. Thermal behaviour of GO-StC coatings

Thermogravimetric analysis (TGA) and derivative (dTGA) curves for the GO-St binder before and after the gelation and of GO-StC coatings with the relative reference materials are presented in Figure P4-3 – a-b. Thermal reduction of GO in the gelled binder starts at a lower temperature (122 °C) with respect of pure GO (150 °C) and with a quicker kinetic with respect of GO-St. This behaviour is also followed by GO-StC (starting at 132 °C) and is attributable to chemical reactions between starch and GO molecules previously described. Starch, and thus binder, degradation starting is shifted to higher temperature from pure St (255 °C) to its blend with GO (286 °C), but it is anticipated after gelation (start at 250 and 240 °C for GO-St-gel and StC, respectively). The starting point of the degradation is not clear in GO-StC, although it can be estimated being in a range between 250 and 300 °C with a kinetic that is nevertheless slower with respect of the electrode

material fabricated without GO (StC). These results provide for a reciprocal beneficial effect of the interactions between GO and Starch, with a boost of GO reduction and an improvement of the thermal stability of the binder.

The thermal behaviour of the GO-StC coating was further analysed with XRD, FT-IR and RS (Figure S4-2 – a-c), after their thermal treatment at a temperature ranging from 150 to 550 °C for a total duration of 1 h under inert atmosphere. While FT-IR did not provide additional information, mainly because the material is mostly composed of inert carbons with strong absorbance bands, XRD and RS data were processed to evaluate the variation of $I_D/(I_D + I_G)$ and L_a with the thermal treatment temperature. The results are presented in Figure P4-3 – c and show that the disorder ratio, after an initial decrease (from 51.72% to 49.94% at 80 and 150 °C, respectively), reaches a maximum at 250 °C (53.02%) and then a minimum at 350 °C (44.37%), before increasing again for higher temperatures. L_a shows an inverse trend with respect of $I_D/(I_D + I_G)$ at all temperatures but 350 °C and presents a minimum at 450 °C (32 Å). Such behaviour can be attributed to the subsequent processes of GO reduction and Starch degradation, which are superimposed in the range of 250–300 °C. A summary of main XRD peaks position and calculated structural parameters, and of RS deconvolution parameters and resulting $I_D/(I_D + I_G)$ ratios for the thermally treated materials can be found in Table S4-6-7. Changes in coatings morphology with temperature were also observed with SEM imaging, with development of small of cracks at 350 °C (Figure P4-3 – d) and their enlargement at 550 °C (Figure P4-3 – e). Finally, TEM imaging shows the recovery of the graphitic structure of reduced GO after the treatment at 350 °C. As a result of the evaluation of the thermal behaviour of the GO-StC electrodes, the temperature of 350 °C appear to be the highest possible without affecting the structural integrity of the coatings. This is allowed by the residual oxygen functionalities in rGO after its partial

reduction which preserve the bonding sites between rGO and Starch molecules, as indirectly confirmed by the evaluation of the resulting electrochemical properties discussed in the following paragraphs.

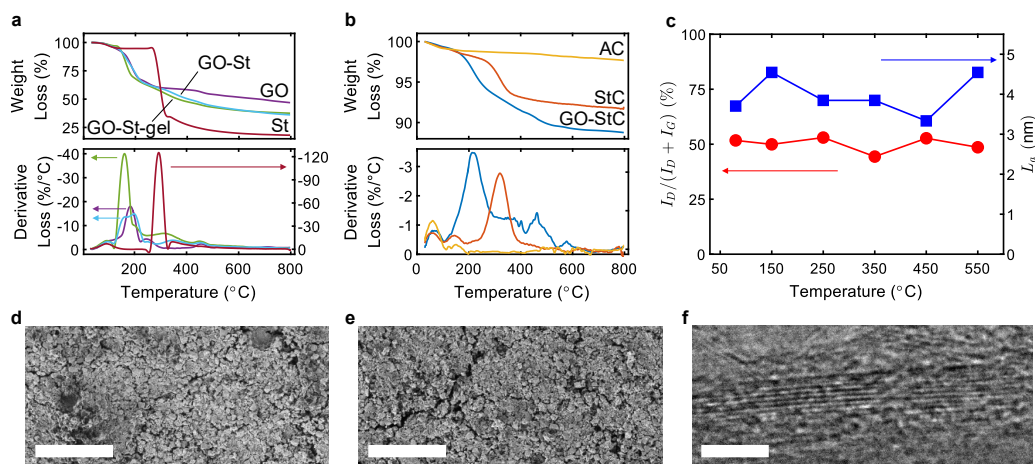


Figure P4-3 – Thermal behaviour of GO-StC coatings. TGA and dTGA of (a) GO-St-gel, GO-St, GO, St and (b) GO-StC, StC, AC. (c) Variation of $I_D/(I_D + I_C)$ ratio and L_a with the temperature. SEM images showing development of cracks after thermal treatment of GO-StC electrodes at (d) 350 and (e) 550 °C (scale bars 100 μm). (f) TEM image showing reduced GO after thermal treatment at 350 °C (scale bar 2 nm).

2.3. Electrochemical performance of GO-StC electrodes

To understand the role of GO amount on electrochemical performance of GO-StC electrodes, all-solid-state supercapacitors were assembled as symmetrical cells using poly(vinyl alcohol) (PVA)/ H_3PO_4 as electrolyte gel, which also behaves as separator, and the rGO paper as current collector. Cyclic voltammetry scans (CVs) at 100 mV s^{-1} for GO-StC electrodes with different GO contents ranging from 0% (StC) to 7.5% are shown in Figure P4-4 – a. Electrodes with GO content of 10% (GO-C) have been excluded as the coatings did not possess acceptable structural robustness. Quasi-rectangular CVs can be observed from the 3.3%, as well as a progressive widening of subtended area up to the 5%. This is directly linked to an improved electrochemical capacitance and a reduced electrical resistance of the electrodes. The beneficial effect of GO on electrochemical performance of assembled supercapacitors is confirmed by the triangular

and symmetric galvanostatic charge-discharge cycles (GCDs) at a current density of 1 A g^{-1} presented in Figure P4-4 – b. The specific capacitance, calculated from GCDs discharge profile at 0.5 A g^{-1} (Figure S4-3), increased from 91.8 F g^{-1} of StC (without GO) to 111.2 F g^{-1} of the cell with 5% GO, and decreased for higher GO inclusions (Figure P4-4 – c). On the other hand, the equivalent series resistance (ESR), calculated from the initial potential drop of GCDs discharge profile at 4 A g^{-1} (Figure S4-3), initially increased from 6.62Ω of StC to 8.02Ω for 2% GO, and then dropped to $\sim 5.07 \Omega$ for GO amount between 3.3 and 6.67% (Figure P4-4 – c). The improved performance with the increase in GO content up to 5%, where it is present in the GO-St-gel binder in equal amount with starch, can be attributed to an indirect contribution of the optimised binder. Particularly, it promotes a transition from a planar and not perfectly homogeneous coating with poorly distributed CB clusters to a 3D structured morphology with evenly distributed CB particles among ACs, as previously discussed. Moreover, the enhanced charge storage capability upon GO inclusion could also derive from a direct contribution of fast red-ox reactions taking place near GO sheets due to the presence of oxygen functional groups [61]. The decrease in specific capacitance and increase in ESR occurred when GO amount was increased to 6.7 and 7.5%, respectively. As a consequence of the latter, St amount was reduced to only the 3.3 and 2.5%, respectively, of the electrode material leading to an insufficient presence of amylose and amylopectin molecules (i.e., the crucial components providing binding capability to the GO-St gel). Subsequently, the observed detrimental effect on both specific capacitance and ESR is likely due to a lack in both cohesion between carbon particles of the coating and in its adhesion on the current collector.

The electrochemical performance of optimised GO-StC electrodes with 5% GO inclusion were further investigated at varying thermal treatment

temperatures from 80 °C (only-dried after coating) to 550 °C. CVs at 100 mV s⁻¹ and GCDs at 1 A g⁻¹ (Figure P4-4 – d-e) describe an improved electrochemical behaviour up to 350 °C, and a clear drop in performance at higher temperatures. In particular, Figure P4-4 – f shows the specific capacitance at 0.5 A g⁻¹ reaching a maximum of 149.5 F g⁻¹ at 350 °C before sharply decreasing to 113 and 98.12 F g⁻¹ at 450 and 550 °C, respectively. The ESR at 4 A g⁻¹ also reaches its optimum at 350 °C, with a value of 3.92 Ω (Figure S4-4). Performance improvement with thermal treatment, at temperature up to 350 °C, can be directly linked to the beneficial effects of GO reduction [42]. Upon heating, more oxygen functional groups and intercalated water molecules are released as CO₂, CO and vapour, complementing the recovery of sp² carbons lattice and, consequently, of electronic properties of graphene started during the gelation of the binder [40]. This directly accounts for the optimisation of both specific capacitance, due to the enhanced charge transfer process [42, 62], and ESR, thanks to the improved electrical conductivity [63]. Conversely, the decrease of electrochemical properties after a thermal treatment at higher temperatures, namely 450 and 550 °C, can be ascribed to multiple factors affecting charge transfer. The first is undoubtedly starch degradation, which starting temperature was estimated at ~250–300 °C from TGA results and with clear evidence of coating structure cracking at 550 °C from SEM imaging, as previously described. Additionally, the exposure at higher temperatures leads to a more extensive reduction of GO and thus to a removal of all the residual oxygen functionalities that positively contributes to charge storage capabilities [61, 64]. This explains the sharp drop in specific capacitance, while the less severe impact on ESR is likely due to a balance between the negative effect caused by the loss of cohesion and adhesion due to starch degradation, and the increased electrical conductivity thanks to GO reduction.

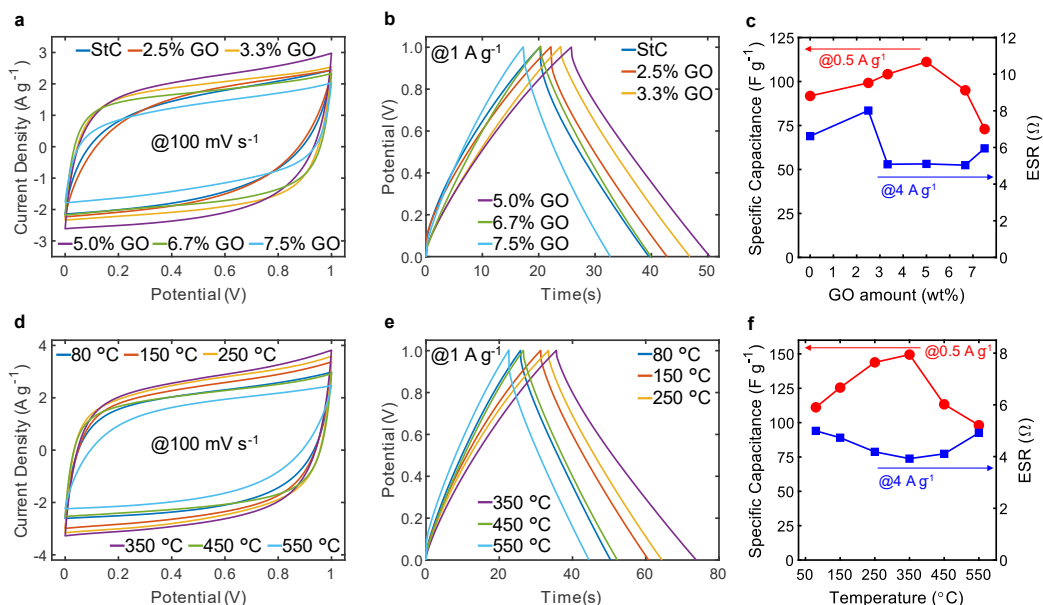


Figure P4-4 – Electrochemical characterisation of supercapacitors. (a) CV curves at a scan rate of 100 mV s⁻¹ and **(b)** GCD curves at a current density of 1 A g⁻¹ for GO-StC electrodes with varying GO amounts. **(c)** Variation of specific capacitance and equivalent series resistance (ESR) with GO amount. **(d)** CV curves at a scan rate of 100 mV s⁻¹ and **(e)** GCD curves at a current density of 1 A g⁻¹ for GO-StC electrodes with varying thermal treatment temperatures. **(f)** Variation of specific capacitance and ESR with the temperature.

2.4. High electrochemical performance of thermally treated GO-StC electrodes

The symmetrical cell assembled with GO-StC electrodes containing 5% GO and thermally treated at 350 °C (rGO-StC@350) resulted as the best performing supercapacitor. It was further evaluated through a full electrochemical characterisation, while dried-only GO-StC and StC electrodes (GO-StC@80 and StC@80, respectively) were considered for comparison. The rGO-StC@350 cell exhibits desirable charge storage capabilities and rate performance, as shown in quasi-rectangular CVs from 10 to 400 mV s⁻¹ and symmetric triangular GCDs from 0.2 to 6 A g⁻¹ (Figure P4-5 – a-b). It also provides a high specific capacitance of 173.8 F g⁻¹ at 0.2 A g⁻¹ with a capacitance retention of 60.5% (105.2 F g⁻¹) at the high scan rate of 6 A g⁻¹ (Figure P4-5 – c), where the minimum recorded ESR value of

3.89 Ω is found. GO-StC@80 and StC@80 cells both provides lower charge storage capabilities over all the tested currents, having a specific capacitance of 125 and 105.9 F g⁻¹ at 0.2 A g⁻¹ and of 78.5 and 51.2 F g⁻¹ at 6 A g⁻¹ (with ESRs of 4.94 and 6.18 Ω), respectively. It is also worth noting the increased rate performance from StC@80 to GO-StC@80, with capacitance retentions of 48.3 and 62.8%, respectively. According to equation (P4-60) and (P4-61), the increase of specific capacitance and the reduction of ESR upon GO inclusion and its subsequent reduction at 350 °C determine the increase of the maximum gravimetric energy and power densities from 14.71 Wh kg⁻¹ and 7.75 kW kg⁻¹ (StC@80) to 24.14 Wh kg⁻¹ and 14.48 kW kg⁻¹ (rGO-StC@350) (values are summarised in the Ragone plot in Figure S4-5). Further details of the coatings and the resulting volumetric capacitance are summarised in Table S4-8.

Electrochemical impedance spectroscopy (EIS) measurements were performed on selected electrodes at open circuit potential. The impedance behaviour of the symmetric cells (schematised in Figure S4-6 – a) was successfully modelled with the simplified equivalent circuit proposed in Figure S4-6 – b (fitting parameters are summarised in Table S4-9). The resulting Nyquist plots (Figure P4-5 – d) show the development of a depressed semi-circle in the high frequency region in both GO-StC@80 and rGO-StC@350, which is attributed to charge building up at the interface of the current collector with the coating. The straight line with slope of $\sim 45^\circ$ at middle frequencies can instead be related to charge transport within the porous electrodes (i.e., transmission line behaviour) [65], with a much quicker transition toward the capacitive behaviour (almost vertical straight line at low frequencies) for rGO-StC@350 (occurring at 6.31 Hz, compared to 0.32 Hz of both StC@80 and GO-StC@80). As shown in Bode and complex impedance plots (Figure S4-6 – c-f), the middle frequency transition is consistent with the improved capacitor time response assessed

from the frequencies leading to a phase angle of -45° in Bode plots and from relaxation frequencies corresponding to local maxima of the imaginary part of capacitance (frequencies value are reported in Table S4-9). For all the tested symmetric cells, the low frequency values of the real part of capacitance is in agreement with results from GCDs. From fitted values of the simplified equivalent circuit elements, it is worth noting the decreasing trend of the series resistance (R_s) from StC@80 (6.83 Ω) to GO-StC@80 (4.43 Ω) and rGO-StC@350 (4.12 Ω), as well as the increasing coefficient related to the phase and the parameter accounting for the capacitance of the constant phase element representing the double layer capacitance (C_{dl-P} and C_{dl-T} , respectively). In particular, a phase value of 1 corresponding to an ideal capacitor behaviour was obtained for rGO-StC@350. EIS analysis thus further confirms the enhanced charge transfer dynamic upon inclusion and subsequent reduction of GO, and consequently proves a direct contribution of the binder to the electrochemical performances.

The rGO-StC@350 supercapacitor also possesses a remarkable cycling stability, with a capacitance retention of 93.1% after 17,000 GCDs at 4 Ag^{-1} (Figure P4-5 – e). Its cycling performance after 5,000 cycles (97.1%) outperformed both GO-StC@80 (92.5%) and StC@80 (92%). Such behaviour confirms the structural integrity of the coatings is not affected by the heating at the designed temperature with reduced GO sheets capable of maintaining a fast and efficient charge storage process upon long-term cycling. Moreover, it is possible to speculate that the fluctuation observed in the capacitance retention could be due to the ability of graphene sheets and residual oxygen functionalities to generate optimised ion diffusion paths during the charge and discharge phases when electrolyte ions intercalate through the pores [66, 67].

All latter results confirm previous assumptions of the beneficial effects on electrochemical performance in GO-StC electrodes with an optimised inclusion of 5% GO into the gelled GO-St binder, which can further be enhanced by an optimised thermal treatment at 350 °C. Finally, the bar chart in Figure P4-5 – f shows that the specific capacitance of the optimised rGO-StC@350 cell is the highest value reported for supercapacitors assembled with alternative green binders processable in water, also outperforming conventional binders used for commercially available devices and other non-biomaterial based greener alternatives (Table S4-10) [14, 15, 18, 68-72].

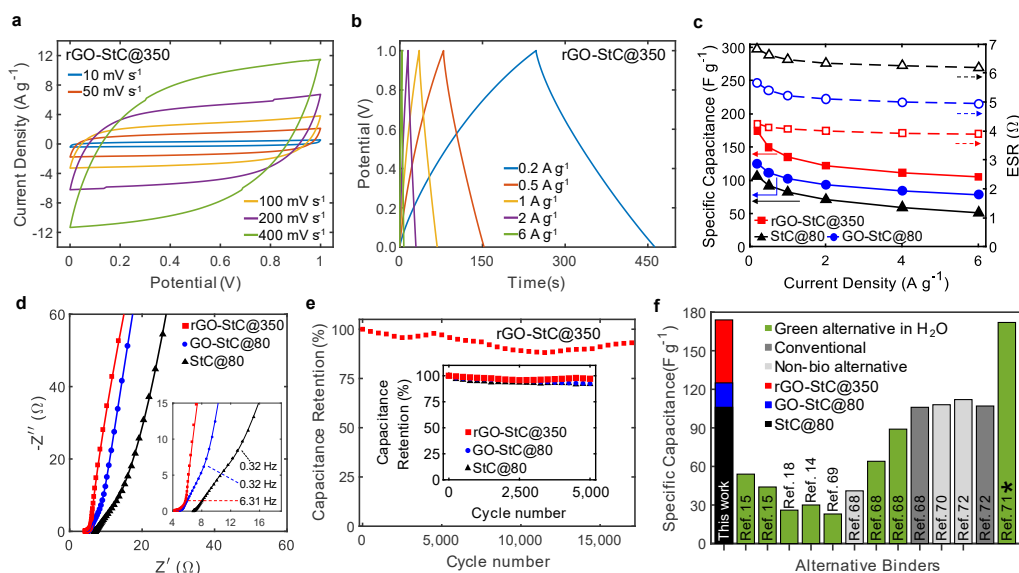


Figure P4-5 – Electrochemical characterisation of optimised GO-StC electrodes. **(a)** CVs at scan rates of 10 to 400 mV s⁻¹ and **(b)** GCDs at current densities of 0.2 to 6 A g⁻¹ for GO-StC electrodes with 5% GO after thermal treatment at 350 °C (rGO-StC@350). **(c)** Variation of specific capacitance and ESR with current density and **(d)** Nyquist plots of rGO-StC@350 with dried-only GO-StC and StC electrodes (GO-StC@80 and StC@80) included for comparison. High-frequency region magnified in the inset. Markers represents the experimental points, while solid lines the modelled behaviour with the simplified equivalent circuit (Figure S4-6). **(e)** Capacitance retention during the cycling at 4 A g⁻¹ of rGO-StC@350 °C up to 17,000 cycles. Inset showing the comparison with GO-StC@80 and StC@80 up to 5,000 cycles. **(f)** Comparative bar chart expressing the high performance of the GO-St-gel (stacked bar colored in black, blue and red when referring to StC@80, GO-StC@80 and rGO-StC@350, respectively) among all alternative green binders processable in water (colored in green) and conventional binders of commercially available devices (colored in dark grey). Some non-biomaterial based greener alternatives have also been included as reference (colored in light grey). Water is used as the only solvent unless differently specified between brackets (*water is mixed with acetic acid).

3. Conclusion

This work demonstrates that a hybrid and green binder can be obtained from the gelation of an optimised mixture of a polysaccharide biomaterial, starch, and GO sheets. Supercapacitors electrodes were then manufactured by a conventional and industrial-ready manufacturing process having water as the only ecological solvent and without any hazardous substances being ever involved, including in the polymer electrolyte gel. A further optimisation of the binder was achieved after a thermal treatment of the electrodes, where the reduction of GO sheets fully unlocked their capabilities to actively contribute to electrochemical performances. The physicochemical characterisation revealed the interactions between starch and GO and their positive effects on coatings structure and morphology, as well as thermal treatment consequences at varying temperatures. An extended thermal stability of the GO-St-gel binder was also proved. Nevertheless, the electrochemical characterisation of symmetrical and all-solid-state supercapacitor cells assembled with GO-StC electrodes demonstrated the ability of the studied binder to provide satisfactory cohesion between AC and CB particles and their adhesion on the rGO paper current collector, due to the crucial role of amylose and amylopectin molecules. Furthermore, the beneficial effects of the optimised amount of 5% GO, and of its reduction after the thermal treatment at the optimised temperature of 350 °C, on a fast and efficient charge storage process were clearly evidenced. The rGO-StC@350 cell presented in this manuscript provided a high specific capacitance of 173.8 F g⁻¹ at 0.2 A g⁻¹ (that is the highest ever reported when alternative green binders processable in water were used), good rate capabilities up to 6 A g⁻¹ and a remarkable long-term stability with a capacitance retention of 93.1% after 17,000 charge/discharge cycles at 4 A g⁻¹. For this reason, the adoption of the GO-St-gel as a hybrid and green binder is envisaged for the

manufacturing of environmentally friendly and high-performance supercapacitors as a potential solution for the continuous growth of energy consumption and global pollution.

4. Methods

4.1. Materials

Graphite Oxide (GtO) powder (SE2430) was purchased from Xiamen TOB New Energy. AC powder (HCE 202) was acquired from Haycarb PLC. Starch, PVA (98-99% hydrolyzed, medium molecular weight) and H₃PO₄ (ACS reagent, 85 wt% in H₂O) were purchased from Sigma Aldrich. CB powder (Black Pearls 2000) was supplied by Cabot Corporation. Deionized water (MilliQ) was used throughout all the experiments. All materials were used without further purification.

4.2. Fabrication of GO-StC electrodes.

GO-St gel synthesis

A GO aqueous dispersion (8 mg mL⁻¹) was first obtained as follows: GtO powder (500 mg) and 50 mL of water were mixed thoroughly and probe ultrasonicated (Dr. Hielscher GmbH UP100H, with an amplitude of 80% and continuous pulsing) for 40 min, vigorous magnetic stirring and an ice bath ensured a homogeneous process with controlled temperature. Then, St granules (500 mg) were added into the GO dispersion and mixed thoroughly with bath ultrasonication for 10 minutes. Finally, the gelation was promoted by heating at 80 °C for 30 min with mild magnetic stirring. After cooling down, the gel was sealed in a vial and preserved at ambient conditions for further use. Samples of GO dispersion, GO-St blends before and after gelation and of the final gel were drop casted onto quartz glass slides and dried at ambient conditions for their physicochemical characterisation.

GO-StC slurry preparation

Well-ground CB powder (500 mg) and 50 mL of GO-St hydrogel were mixed thoroughly with overhead stirring (Heidolph RZR 50) for 1 h. Then, well-ground AC powder (8,500 mg) was slowly added into the black slurry and overhead stirred for 12 h. Finally, the viscous slurry was sealed in a vial and preserved at ambient conditions for further use. The reported amount of materials refers to the optimized GO 5-StC slurry. Different amount of St, CB and AC were used to obtain GO-StC slurries with varying GO contents from 2.5 to 7.5 wt% with respect of the total mass of solids. For comparison, a GO-C and a StC slurry were prepared by sequentially adding CB and AC to the GO dispersion (i.e., without starch and with GO accounting for the 10 wt%) and to a St-only hydrogel (i.e., without GO and with starch accounting for the 10 wt%), respectively.

rGO paper preparation

The rGO paper was prepared as previously reported [27]. Briefly, a GO aqueous dispersion was cast on a polymeric film and dried at ambient conditions. Then, the obtained GO film was peeled off and annealed at 1,300 °C for 3 h under inert atmosphere. Finally, the obtained rGO film was calendered to obtain a freestanding paper with a thickness of 40 µm and a density of 1.18 g cm⁻³.

GO-StC electrode fabrication

The GO-StC slurry was coated on the rGO paper using an adjustable film applicator with a set thickness of 200 µm and vacuum dried at 80 °C for 1 h. Thermally treated electrodes were obtained with further heating at varying temperatures from 150 to 550 °C for 1 h under Argon atmosphere. Finally, the resulting electrodes, having a mass loading of ~2.8 mg cm⁻² and a thickness of ~114 µm, were cut to squares of 2 cm side and preserved in a dry atmosphere for further use. Powder samples of the coatings were

scraped from the substrate and used for their physicochemical characterisation.

4.3. Physicochemical characterisation

Physicochemical testing

The surface morphology and microstructure of GO-StC and StC electrodes was observed using SEM (JEOL JSM-7900F) and TEM (JEOL JEM-2100Plus). The crystal phase composition was analysed by transmission powder XRD (STOE STADI P) using a CuK α generator. The chemical structure was investigated with FT-IR (Perkin-Elmer Frontier FTIR Spectrometer) using a MCT detector and with RS (Renishaw inVia Raman microscope) using a 532 nm laser source (IK Series He-Cd). The thermal stability was evaluated by TGA (Setaram SETSYS Evolution 16 TGA-DTA/DSC).

Physical and chemical parameters calculations

XRD data were used to estimate d from the (100) or (200) bands and L_a from the (10) or (100) bands, using Bragg's law [73] and Scherrer's formula [51], respectively:

$$d = \frac{\lambda}{2 \sin \theta} \quad (\text{P4-55})$$

$$L_a = \frac{K \lambda}{B \cos \theta} \quad (\text{P4-56})$$

where λ is the radiation wavelength, θ is the corresponding scattering angle of the lattice (depending on carbon material's nature), K is a shape factor (equal to 1.84 for carbon materials [74]), and B is the line broadening at half-maximum intensity of the peak. Raman spectra were processed with multiple interbands deconvolution, as discussed in the manuscript, to obtain the $I_D/(I_D + I_G)$ index expressing carbons' structural disorder [46].

4.4. Electrochemical characterisation

Supercapacitor assembly

A typical symmetrical cell was assembled with two identical GO-StC electrodes with the rGO paper serving as the current collector. A PVA/H₃PO₄ gel was employed as both the separator and the electrolyte. First, a PVA solution (10 wt%) was prepared dissolving PVA granules (5 g) in water (50 mL) with continuous stirring and heating up to 90 °C for 4 h. Then, H₃PO₄ (7.5 g) was added to the clear solution and stirred for 12 h to obtain the PVA/H₃PO₄ electrolyte gel. Electrical connections were provided by copper tape attached to the end of each electrode using silver paste and protected with Kapton tape masking, so that an active area of 1 cm² was obtained. Then, a drop of the electrolyte gel was casted on the electrodes and dried for 4 h. Finally, two identical electrodes were sandwiched with a drop of the electrolyte gel and dried overnight.

Electrochemical testing

Electrochemical performances were measured using an electrochemical workstation (Solartron ModuLab XM MTS) in two-electrode configuration. CVs, with scanning rates ranging from 10 to 400 mV s⁻¹, and GCDs, at current densities ranging from 0.2 to 6 A g⁻¹, were performed with a potential ranging from 0 to 1 V. Cycling stability tests were conducted by GCDs at a current density of 4 A g⁻¹. EIS measurements were acquired over a frequency range of 10 mHz to 100 kHz with an amplitude of 10 mV at the open circuit potential.

Electrochemical performance calculations

Electrochemical performance calculations were all performed from discharge profiles of GCDs. In particular, the specific and volumetric capacitance (C , F g⁻¹, and C_v , F cm⁻³, respectively) of GO-StC electrodes were calculated from GCDs as follows:

$$C = \frac{4 I \Delta t}{m \Delta E} \quad (\text{P4-57})$$

$$C_v = \rho C \quad (\text{P4-58})$$

where I is the current (A), Δt is the discharge time (s), m is the total mass of both electrodes (g), ΔE is the potential window (V), and ρ is the density of the coating (g cm^{-3}). The ESR (Ω) was estimated from the initial potential drop (δE) as follows:

$$ESR = \frac{\delta E}{2 I} \quad (\text{P4-59})$$

The gravimetric energy density (U , Wh kg^{-1}) and the gravimetric power density (P , W kg^{-1}) were obtained from the following equations:

$$U = \frac{C E^2}{2 \times 3.6} \quad (\text{P4-60})$$

$$P = \frac{U}{\Delta t} \quad (\text{P4-61})$$

EIS data were fitted by an equivalent circuit model approach using the software “ZView[®]” from Scribner Associates. An evaluation on the variation of the complex capacitance ($C(\omega)$) with the frequency was also performed as follows [75]:

$$C(\omega) = C'(\omega) - jC''(\omega) \quad (\text{P4-62})$$

$$C'(\omega) = \frac{-Z''(\omega)}{\omega |Z(\omega)|^2}; \quad C''(\omega) = \frac{Z'(\omega)}{\omega |Z(\omega)|^2} \quad (\text{P4-63})$$

where $C'(\omega)$ and $C''(\omega)$ are the real and imaginary part of $C(\omega)$, respectively, and ω is the angular frequency. $Z'(\omega)$, $Z''(\omega)$, and $|Z(\omega)|$ are the real and imaginary part and the magnitude of the impedance.

Acknowledgements

The authors acknowledge the Material and Chemical Characterisation Facility (MC2) at the University of Bath (<https://doi.org/10.15125/mx6j-3r54>) for technical support and assistance in this work.

References

1. Larcher, D. and J.M. Tarascon, Towards greener and more sustainable batteries for electrical energy storage. *Nature Chemistry*, 2015. **7**(1): p. 19-29.
2. Abbate, G., E. Saraceno, and A. Damasco, Supercapacitor for Future Energy Storage, in *Sustaining Resources for Tomorrow*, J.A. Stagner and D.S.K. Ting, Editors. 2020, Springer International Publishing: Cham. p. 205-243.
3. Zhu, Y., et al., Carbon-Based Supercapacitors Produced by Activation of Graphene. *Science*, 2011. **332**(6037): p. 1537-1541.
4. Gao, X., et al., Maximizing ion accessibility in MXene-knotted carbon nanotube composite electrodes for high-rate electrochemical energy storage. *Nature Communications*, 2020. **11**(1): p. 6160.
5. Ko, Y., et al., Flexible supercapacitor electrodes based on real metal-like cellulose papers. *Nature Communications*, 2017. **8**(1): p. 536.
6. Zhou, T., et al., Super-tough MXene-functionalized graphene sheets. *Nature Communications*, 2020. **11**(1): p. 2077.
7. Dura, H., et al. Cost analysis of supercapacitor cell production. in *2013 International Conference on Clean Electrical Power (ICCEP)*. 2013.
8. Lohmann, R., et al., Are Fluoropolymers Really of Low Concern for Human and Environmental Health and Separate from Other PFAS? *Environmental Science & Technology*, 2020. **54**(20): p. 12820-12828.
9. Malek, D.E., et al., Repeated Dose Toxicity Study (28 Days) in Rats and Mice with N-Methylpyrrolidone (NMP). *Drug and Chemical Toxicology*, 1997. **20**(1-2): p. 63-77.
10. Capello, C., U. Fischer, and K. Hungerbühler, What is a green solvent? A comprehensive framework for the environmental assessment of solvents. *Green Chemistry*, 2007. **9**(9): p. 927-934.

11. Bresser, D., et al., Alternative binders for sustainable electrochemical energy storage – the transition to aqueous electrode processing and bio-derived polymers. *Energy & Environmental Science*, 2018. **11**(11): p. 3096-3127.
12. Selvaraj, T., et al., The recent development of polysaccharides biomaterials and their performance for supercapacitor applications. *Materials Research Bulletin*, 2020. **126**: p. 110839.
13. Hovenkamp-Hermelink, J.H.M., et al., Rapid estimation of the amylose/amylopectin ratio in small amounts of tuber and leaf tissue of the potato. *Potato Research*, 1988. **31**(2): p. 241-246.
14. Jeżowski, P. and P.Ł. Kowalczewski, Starch as a Green Binder for the Formulation of Conducting Glue in Supercapacitors. *Polymers*, 2019. **11**(10): p. 1648.
15. Varzi, A. and S. Passerini, Enabling high areal capacitance in electrochemical double layer capacitors by means of the environmentally friendly starch binder. *Journal of Power Sources*, 2015. **300**: p. 216-222.
16. Xu, X., et al., Binding interaction between rice glutelin and amylose: Hydrophobic interaction and conformational changes. *International Journal of Biological Macromolecules*, 2015. **81**: p. 942-950.
17. Morris, V.J., Starch gelation and retrogradation. *Trends in Food Science & Technology*, 1990. **1**: p. 2-6.
18. Ruschhaupt, P., A. Varzi, and S. Passerini, Natural Polymers as Green Binders for High-Loading Supercapacitor Electrodes. *ChemSusChem*, 2020. **13**(4): p. 763-770.
19. Raza, W., et al., Recent advancements in supercapacitor technology. *Nano Energy*, 2018. **52**: p. 441-473.
20. Lerf, A., et al., Structure of Graphite Oxide Revisited. *The Journal of Physical Chemistry B*, 1998. **102**(23): p. 4477-4482.
21. Dreyer, D.R., et al., The chemistry of graphene oxide. *Chemical Society Reviews*, 2010. **39**(1): p. 228-240.
22. Novoselov, K.S., et al., Electric Field Effect in Atomically Thin Carbon Films. *Science*, 2004. **306**(5696): p. 666.
23. Balandin, A.A., Thermal properties of graphene and nanostructured carbon materials. *Nat Mater*, 2011. **10**(8): p. 569-81.
24. Zhu, Y., et al., Graphene and Graphene Oxide: Synthesis, Properties, and Applications. *Advanced Materials*, 2010. **22**(35): p. 3906-3924.

25. Rapisarda, M., G.-P. Malfense Fierro, and M. Meo, Ultralight graphene oxide/polyvinyl alcohol aerogel for broadband and tuneable acoustic properties. *Scientific Reports*, 2021. **11**(1): p. 10572.
26. Chen, C., X. Zhu, and B. Chen, Covalently cross-linked graphene oxide aerogel with stable structure for high-efficiency water purification. *Chemical Engineering Journal*, 2018. **354**: p. 896-904.
27. Rapisarda, M. and M. Meo, Multifunctional reduced graphene oxide coating on laminated composites. *Materials Today: Proceedings*, 2021. **34**: p. 149-155.
28. Yan, D.-X., et al., Structured Reduced Graphene Oxide/Polymer Composites for Ultra-Efficient Electromagnetic Interference Shielding. *Advanced Functional Materials*, 2015. **25**(4): p. 559-566.
29. Rapisarda, M., et al., Carbon Black and Reduced Graphene Oxide Nanocomposite for Binder-Free Supercapacitors with Reduced Graphene Oxide Paper as the Current Collector. *ACS Omega*, 2020. **5**(50): p. 32426-32435.
30. Choi, J.-H., et al., High capacitance and energy density supercapacitor based on biomass-derived activated carbons with reduced graphene oxide binder. *Carbon*, 2018. **132**: p. 16-24.
31. Zang, J., et al., Stretchable and High-Performance Supercapacitors with Crumpled Graphene Papers. *Scientific Reports*, 2014. **4**(1): p. 6492.
32. Ahmad, H., M. Fan, and D. Hui, Graphene oxide incorporated functional materials: A review. *Composites Part B: Engineering*, 2018. **145**: p. 270-280.
33. Li, R., C. Liu, and J. Ma, Studies on the properties of graphene oxide-reinforced starch biocomposites. *Carbohydrate Polymers*, 2011. **84**(1): p. 631-637.
34. Cruz-Benítez, M.M., et al., Covalent Functionalization of Graphene Oxide with Fructose, Starch, and Micro-Cellulose by Sonochemistry. *Polymers*, 2021. **13**(4): p. 490.
35. Ma, T., et al., The composites based on plasticized starch and graphene oxide/reduced graphene oxide. *Carbohydrate Polymers*, 2013. **94**(1): p. 63-70.
36. Xu, H., et al., Immobilized Graphene Oxide Nanosheets as Thin but Strong Nanointerfaces in Biocomposites. *ACS Sustainable Chemistry & Engineering*, 2016. **4**(4): p. 2211-2222.

37. Miles, M.J., V.J. Morris, and S.G. Ring, Gelation of amylose. *Carbohydrate Research*, 1985. **135**(2): p. 257-269.
38. Wang, S., et al., Starch Retrogradation: A Comprehensive Review. *Comprehensive Reviews in Food Science and Food Safety*, 2015. **14**(5): p. 568-585.
39. Feng, Y., N. Feng, and G. Du, A green reduction of graphene oxide via starch-based materials. *RSC Advances*, 2013. **3**(44): p. 21466-21474.
40. Schniepp, H.C., et al., Functionalized Single Graphene Sheets Derived from Splitting Graphite Oxide. *The Journal of Physical Chemistry B*, 2006. **110**(17): p. 8535-8539.
41. Galhena, D.T.L., et al., Reduced Graphene Oxide as a Monolithic Multifunctional Conductive Binder for Activated Carbon Supercapacitors. *ACS Omega*, 2018. **3**(8): p. 9246-9255.
42. Xu, B., et al., Reduced graphene oxide as a multi-functional conductive binder for supercapacitor electrodes. *Energy Storage Materials*, 2018. **12**: p. 128-136.
43. Rapisarda, M., et al., The Temperature Role in the Manufacturing of an Electrode for Supercapacitors with Carbon Black and Graphene Oxide. *CHEMICAL ENGINEERING TRANSACTIONS*, 2021. **84**: p. 133-138.
44. Qiu, L., et al., Dispersing Carbon Nanotubes with Graphene Oxide in Water and Synergistic Effects between Graphene Derivatives. *Chemistry – A European Journal*, 2010. **16**(35): p. 10653-10658.
45. Krishnamoorthy, K., et al., The chemical and structural analysis of graphene oxide with different degrees of oxidation. *Carbon*, 2013. **53**: p. 38-49.
46. Cuesta, A., et al., Comparative performance of X-ray diffraction and Raman microprobe techniques for the study of carbon materials. *Journal of Materials Chemistry*, 1998. **8**(12): p. 2875-2879.
47. Lopez-Rubio, A., et al., A novel approach for calculating starch crystallinity and its correlation with double helix content: A combined XRD and NMR study. *Biopolymers*, 2008. **89**(9): p. 761-768.
48. Kashyap, S., S. Mishra, and S.K. Behera, Aqueous Colloidal Stability of Graphene Oxide and Chemically Converted Graphene. *Journal of Nanoparticles*, 2014. **2014**: p. 640281.

49. Liu, Q., et al., Phase transition in potato starch–water system I. Starch gelatinization at high moisture level. *Food Research International*, 2002. **35**(4): p. 397-407.
50. Krishnankutty, N. and M.A. Vannice, Effect of Pretreatment on Surface Area, Porosity, and Adsorption Properties of a Carbon Black. *Chemistry of Materials*, 1995. **7**(4): p. 754-763.
51. Scherrer, P., Bestimmung der Größe und der inneren Struktur von Kolloidteilchen mittels Röntgenstrahlen. *Nachrichten von der Gesellschaft der Wissenschaften zu Göttingen, Mathematisch-Physikalische Klasse*, 1918. **1918**: p. 98-100.
52. Cael, J.J., J.L. Koenig, and J. Blackwell, Infrared and Raman spectroscopy of carbohydrates. Part VI: Normal coordinate analysis of V-amylose. *Biopolymers*, 1975. **14**(9): p. 1885-1903.
53. Titelman, G.I., et al., Characteristics and microstructure of aqueous colloidal dispersions of graphite oxide. *Carbon*, 2005. **43**(3): p. 641-649.
54. Capron, I., et al., Starch in rubbery and glassy states by FTIR spectroscopy. *Carbohydrate Polymers*, 2007. **68**(2): p. 249-259.
55. Zhang, J., et al., Reduction of graphene oxide vial-ascorbic acid. *Chemical Communications*, 2010. **46**(7): p. 1112-1114.
56. Kizil, R. and J. Irudayaraj, Discrimination of Irradiated Starch Gels Using FT-Raman Spectroscopy and Chemometrics. *Journal of Agricultural and Food Chemistry*, 2006. **54**(1): p. 13-18.
57. Tuinstra, F. and J.L. Koenig, Raman Spectrum of Graphite. *The Journal of Chemical Physics*, 1970. **53**(3): p. 1126-1130.
58. Pimenta, M.A., et al., Studying disorder in graphite-based systems by Raman spectroscopy. *Physical Chemistry Chemical Physics*, 2007. **9**(11): p. 1276-1290.
59. Claramunt, S., et al., The Importance of Interbands on the Interpretation of the Raman Spectrum of Graphene Oxide. *The Journal of Physical Chemistry C*, 2015. **119**(18): p. 10123-10129.
60. Cuesta, A., et al., Raman microprobe studies on carbon materials. *Carbon*, 1994. **32**(8): p. 1523-1532.
61. Du, Q., et al., Preparation of functionalized graphene sheets by a low-temperature thermal exfoliation approach and their electrochemical supercapacitive behaviors. *Electrochimica Acta*, 2010. **55**(12): p. 3897-3903.

62. Pham, D.T., et al., Carbon Nanotube-Bridged Graphene 3D Building Blocks for Ultrafast Compact Supercapacitors. *ACS Nano*, 2015. **9**(2): p. 2018-2027.
63. Jung, I., et al., Tunable Electrical Conductivity of Individual Graphene Oxide Sheets Reduced at “Low” Temperatures. *Nano Letters*, 2008. **8**(12): p. 4283-4287.
64. Zhao, B., et al., Supercapacitor performances of thermally reduced graphene oxide. *Journal of Power Sources*, 2012. **198**: p. 423-427.
65. Conway, B.E., *Electrochemical Supercapacitors*. 1 ed. 1999, Boston, MA: Springer. XXX, 698.
66. Rajagopalan, B. and J.S. Chung, Reduced chemically modified graphene oxide for supercapacitor electrode. *Nanoscale Research Letters*, 2014. **9**(1): p. 535.
67. Tan, Y., et al., Facile synthesis of functionalized graphene hydrogel for high performance supercapacitor with high volumetric capacitance and ultralong cycling stability. *Applied Surface Science*, 2018. **455**: p. 683-695.
68. Dyatkin, B., et al., Development of a Green Supercapacitor Composed Entirely of Environmentally Friendly Materials. *ChemSusChem*, 2013. **6**(12): p. 2269-2280.
69. Scalia, A., et al., Tragacanth Gum as Green Binder for Sustainable Water-Processable Electrochemical Capacitor. *ChemSusChem*, 2021. **14**(1): p. 356-362.
70. Lee, S., et al., Effect of emulsified polymer binders on the performance of activated carbon electrochemical double-layer capacitors. *Korean Journal of Chemical Engineering*, 2019. **36**(11): p. 1940-1947.
71. Raja, M., et al., A chitosan/poly(ethylene glycol)-ran-poly(propylene glycol) blend as an eco-benign separator and binder for quasi-solid-state supercapacitor applications. *Sustainable Energy & Fuels*, 2019. **3**(3): p. 760-773.
72. Aslan, M., et al., Polyvinylpyrrolidone as binder for castable supercapacitor electrodes with high electrochemical performance in organic electrolytes. *Journal of Power Sources*, 2014. **266**: p. 374-383.
73. Bragg, W.H. and W.L. Bragg, *The Reflection of X-rays by Crystals*. *Proceedings of the Royal Society of London Series A*, 1913. **88**: p. 428.

74. Biscoe, J. and B.E. Warren, An X-Ray Study of Carbon Black. *Journal of Applied Physics*, 1942. **13**(6): p. 364-371.
75. Taberna, P.L., P. Simon, and J.F. Fauvarque, Electrochemical Characteristics and Impedance Spectroscopy Studies of Carbon-Carbon Supercapacitors. *Journal of The Electrochemical Society*, 2003. **150**(3): p. A292.

Supplementary Information

Supplementary Tables

Table S4-1 – Slurry composition of different GO-StC and reference electrodes.

Slurry name	AC (wt%)	CB (wt%)	St (wt%)	GO (wt%)
StC	85	5	10.00	0
GO-StC-I	85	5	7.50	2.50
GO-StC-II	85	5	6.67	3.33
GO-StC-III	85	5	5.00	5.00
GO-StC-IV	85	5	3.33	6.67
GO-StC-V	85	5	2.50	7.50
GO-C	85	5	0	10

Table S4-2 – Main peaks positions and calculated structural parameters from XRD patterns of GO-StC, StC, AC, GO, GO-St-gel, GO-St, and St (Figure P4-2 – a of the manuscript). d , B and L_a are interplanar spacing in crystal lattice, line broadening at half-maximum intensity of the peak and crystallite lateral size, respectively

Sample	(001) 2 θ (°)	(002) 2 θ (°)	(100) 2 θ (°)	(10) 2 θ (°)	$d_{(001)}$ or (002) (Å)	$B_{(100)}$ or (10) (°)	L_a (Å)
GO-StC	\	21.89	\	43.73	4.03	4.66	37.6
StC	\	22.24	\	43.49	3.99	4.07	43.0
AC	\	22.13	\	43.68	4.01	3.93	44.6
GO	10.85	\	42.57	\	8.15	1.36	128.0
GO-St-gel	\	\	42.62	\	\	2.01	86.9
GO-St	11.07	\	42.50	\	7.99	1.59	109.6

Table S4-3 – Main features and relative assignment from FT-IR spectra of GO, GO-St-gel, GO-St, and St (Figure P4-2 – b of the manuscript).

Code	Wavenumber (cm ⁻¹)				Assignment [1-3]
	GO	GO-St-gel	GO-St	St	
1'	3586	-	3586	\	
1''	3216	-	3233	\	OH stretching
1	\	3286	-	3310	
2		\		2931	
3		\		2894	CH ₂ bending
4	1720	1726	1722	\	C=O stretching (Carbonyl)
5		\		1642	OH bending and stretching of absorbed H ₂ O
6	1615	1627	1615	\	
7	1373	1356	1360	\	OH bending
8		\		1241	C-OH bending
9	1219	1230	1225	\	C-OH stretching
10		\		1207	CH ₂ and C-OH bending
11	1165	-		\	C-OH stretching
12	\	1148	1150	1150	C-O/C-C/OH stretching and bending of glycosidic bridge
13		\		1078	
14		\		1042	C-OH bending
15	1038	-	1038	\	C-O stretching (Alkoxy)
16	\	1014	1015	1016	C-OH bending
17	\	998	993	995	C-O-C (Skeletal starch)
18	975	-		\	C-O-C stretching (Epoxy)

Table S4-4 – Interbands deconvolution of Raman spectra and resulting $I_D/(I_D+I_G)$ ratio of GO-StC, StC, AC, GO, GO-St-gel, and GO-St. Deconvolution result for GO is shown in Figure P4-2 – d of the manuscript, GO-St-gel and GO-St show similar fittings. Deconvolution result for AC is shown in Figure P4-2 – e of the manuscript, GO-StC and StC show similar fittings. x_c , w and I are peak position, full width at half height and peak height, respectively.

Band [Fitting model]	Param.	Sample					
		GO-StC	StC	AC	GO	GO-St	GO-St-gel
D^* [Gaussian]	x_c (cm ⁻¹)				1231.5	1230.5	1243.6
	w (cm ⁻¹)		\		88.7	81.9	61.8
	I (counts)				874.4	943.0	1022.6
I [Gaussian]	x_c (cm ⁻¹)	1360.2	1350.1	1334.9			
	w (cm ⁻¹)	234.2	251.2	324.3		\	
	I (counts)	991.7	781.7	916.1			
D [Ps-Voigt]	x_c (cm ⁻¹)	1345.6	1345.5	1343.9	1353.4	1354.8	1351.0
	w (cm ⁻¹)	74.8	79.1	82.1	114.1	116.0	104.8
	I (counts)	2817.5	2560.4	3252.3	19953.7	23368.8	21706.5
D'' [Gaussian]	x_c (cm ⁻¹)	1557.6	1553.0	1554.2	1508.5	1510.0	1508.8
	w (cm ⁻¹)	105.2	108.3	109.3	149.1	145.6	148.4
	I (counts)	639.2	497.8	556.0	4381.8	5313.6	4051.0
G [Ps-Voigt]	x_c (cm ⁻¹)	1607.8	1606.8	1606.1	1587.9	1587.6	1591.0
	w (cm ⁻¹)	63.3	61.9	58.9	65.8	66.4	62.4
	I (counts)	2629.8	2323.0	2835.5	14119.8	16627.3	13686.1
D' [Gaussian]	x_c (cm ⁻¹)				1617.1	1617.6	1618.4
	w (cm ⁻¹)		\		38.8	39.0	38.1
	I (counts)				11505.5	13023.1	12741.6
$I_D/(I_D+I_G)$ ratio (%)		51.72	52.43	53.42	58.56	58.43	61.33

Table S4-5 – Starting, ending and peak temperatures of GO reduction and Starch degradation for GO-StC electrode material and GO-St-gel binder compared with reference materials (from TGA and dTGA analysis presented in Figure P4-3 – a-b of the manuscript).

Parameter	Sample						
	GO-StC	StC	AC	GO	GO-St-gel	GO-St	St
<i>Reduction start (°C)</i>	132			150	122	121	
<i>Reduction end (°C)</i>	-			300	-	-	
<i>Reduction peak (°C)</i>	216			184	161	180	
<i>Maximum red. rate (% / °C)</i>	3.5			18	40	15	
<i>Degradation start (°C)</i>	~250–300	240			250	286	255
<i>Degradation end (°C)</i>	418	385			423	421	329
<i>Degradation peak (°C)</i>	No	320			313	347	293
<i>Maximum deg. rate (%/°C)</i>	~1.2	2.8			6.7	3.9	125.2

Table S4-6 – Main peaks positions and calculated structural parameters from XRD patterns of GO-StC coatings thermally treated at varying temperatures (a). *d*, *B* and *L_a* are interplanar spacing in crystal lattice, line broadening at half-maximum intensity of the peak and crystallite lateral size, respectively.

Treatment temperature (°C)	(002) 2θ (°)	(10) 2θ (°)	<i>d</i> ₍₀₀₂₎ (Å)	<i>B</i> ₍₁₀₎ (°)	<i>L_a</i> (Å)
80	21.89	43.73	4.06	4.66	37.6
150	22.17	43.86	4.01	3.88	45.1
250	21.72	43.52	4.09	4.63	37.8
350	21.84	43.72	4.07	4.52	38.7
450	21.67	43.88	4.10	5.27	33.2
550	22.24	43.66	3.99	3.81	45.9

Table S4-7 – Interbands deconvolution of Raman spectra and resulting $I_D/(I_D+I_G)$ ratio of GO-StC coatings thermally treated at varying temperatures (Figure S4-1 – c). x_c , w and I are peak position, full width at half height and peak height, respectively.

Band [Fitting model]	Param.	Treatment temperature (°C)					
		80	150	250	350	450	550
<i>I</i> [Gaussian]	x_c (cm ⁻¹)	1360.2	1343.6	1350.4	1365.0	1343.6	1342.9
	w (cm ⁻¹)	234.2	224.3	222.6	264.2	237.1	250.6
	I (counts)	991.7	967.8	630.9	1185.4	947.1	1052.3
<i>D</i> [Ps-Voigt]	x_c (cm ⁻¹)	1345.6	1345.2	1344.7	1346.3	1344.7	1344.3
	w (cm ⁻¹)	74.8	78.7	74.4	88.1	76.1	80.7
	I (counts)	2817.5	3156.9	2273.8	2216.0	3023.5	2980.2
<i>D''</i> [Gaussian]	x_c (cm ⁻¹)	1557.6	1539.2	1547.1	1552.4	1551.5	1544.7
	w (cm ⁻¹)	105.2	100.4	112.7	114.0	111.6	107.3
	I (counts)	639.2	783.1	440.5	949.1	610.5	597.6
<i>G</i> [Ps-Voigt]	x_c (cm ⁻¹)	1607.8	1606.5	1606.8	1606.8	1606.1	1606.4
	w (cm ⁻¹)	63.3	58.7	61.8	64.3	59.9	60.2
	I (counts)	2629.8	3164.4	2014.8	2778.5	2713.9	3150.1
<i>I_D/(I_D+I_G) ratio (%)</i>		51.72%	49.94 %	53.02 %	44.37 %	52.70 %	48.61 %

Table S4-8 – Electrodes coating specifications (mass loading, m_i ; thickness, h ; density, ρ) and resulting specific and volumetric capacitance (C and C_v , respectively; calculated at 0.2 A g⁻¹).

Electrode	m_i (mg cm ⁻²)	h (µm)	ρ (g cm ⁻³)	C (F g ⁻¹)	C_v (F cm ⁻³)
StC@80	2.94	117.52	0.25	105.9	26.5
GO-StC@80	2.81	114.17	0.25	125.0	30.7
rGO-StC@350	2.80	114.56	0.22	173.8	38.2

Table S4-9 – Fitted values of the simplified equivalent circuit model (Figure S4-4 – b) and capacitor properties extrapolated from experimental data for StC@80, GO-StC@80, and rGO-StC@350 supercapacitor symmetric cells.

Parameter	Supercapacitor symmetric cell		
	StC@80	GO-StC@80	rGO-StC@350
R_s [Ω]	6.83	4.43	4.12
C_{int-T} [$s^n \Omega^{-1}$]	0.02	0.01	0.01
C_{int-P}	0.59	0.45	0.45
<i>Simplified model fitting values</i> R_{ct} [Ω]	0.29	0.78	0.70
W_R [Ω]	4.45	8.24	3.25
W_T [s]	1.62	3.01	0.33
W_P	0.62	0.53	0.47
C_{dl-T} [$s^n \Omega^{-1}$]	0.08	0.13	0.27
C_{dl-P}	0.61	0.83	1.00
C' at 0.01 Hz [$F g^{-1}$]	84.6	93.9	118.5
Phase angle at 0.01 Hz [$^\circ$]	-72.9	-77.2	-77.1
<i>Capacitor properties</i> Mid frequency transition [Hz]	0.32	0.32	6.31
Response frequency at -45° [Hz]	0.14	0.21	0.31
Relaxation frequency [Hz]	0.05	0.13	0.32

Table S4-10 – Comparison of specific capacitance and capacitance retention for different supercapacitors obtained using alternative green binder processable in water and conventional binders of commercially available devices. Some non-biomaterial based alternatives have also been included as reference. Water is used as the only solvent unless differently specified between brackets.

*main manuscript reference number

Binder	Electrolyte	Potential window	Specific capacitance	Capacitance retention	Ref.*
<i>rGO-St-gel</i> (350 °C)	PVA/H ₃ PO ₄ gel (60 wt%)	0–1 V	174 F g ⁻¹ at 0.2 A g ⁻¹	93.1% [97.1%] after 17,000 [5,000] cycles at 4 A g ⁻¹	This work
<i>GO-St-gel</i> (80 °C)	PVA/H ₃ PO ₄ gel (60 wt%)	0–1 V	125 F g ⁻¹ at 0.2 A g ⁻¹	92.5% after 5,000 cycles at 4 A g ⁻¹	This work
<i>St only</i> (80 °C)	PVA/H ₃ PO ₄ gel (60 wt%)	0–1 V	106 F g ⁻¹ at 0.2 A g ⁻¹	92% after 5,000 cycles at 4 A g ⁻¹	This work
<i>Potato Starch</i>	1 M Et ₄ NBF ₄ in PC	0–1 V	54 F g ⁻¹ at ~0.5 A g ⁻¹	97.2% after 5,000 cycles at ~1 A g ⁻¹	15
<i>CMC</i>	1 M Et ₄ NBF ₄ in PC	0–5 V	44 F g ⁻¹ at ~0.7 A g ⁻¹	97.4% after 5,000 cycles at ~1.5 A g ⁻¹	15
<i>Potato Starch/ Guar Gum</i>	1 M TEABF ₄ in PC	0–2.5 V	26 F g ⁻¹ at 0.2 A g ⁻¹	\	18
<i>Starch glue</i>	1 M TEABF ₄ in ACN	0–2.5 V	~30 F g ⁻¹ at 0.5 A g ⁻¹	~90% after 2,000 cycles at 0.5 A g ⁻¹	14
<i>Tragacanth Gum</i>	1 M TEABF ₄ in PC	0–2.75 V	23 F g ⁻¹ at 1 A g ⁻¹	97% after 15,000 cycles at ~2 A g ⁻¹	69
<i>PVAc/poly(isoprene)</i> [Xylene]	1 M Na ₂ SO ₄ in H ₂ O	0–1 V	41 F g ⁻¹ at ~0.1 A g ⁻¹	\	68
<i>PVA/PVAc</i> (crosslinked with Na ₂ B ₄ O ₇)	1 M Na ₂ SO ₄ in H ₂ O	0–1 V	64 F g ⁻¹ at ~0.1 A g ⁻¹	\	68
<i>Egg white</i>	1 M Na ₂ SO ₄ in H ₂ O	0–1 V	89 F g ⁻¹ at ~0.1 A g ⁻¹	\	68
<i>PTFE [Ethanol]</i>	1 M Na ₂ SO ₄ in H ₂ O	0–1 V	106 F g ⁻¹ at ~0.1 A g ⁻¹	\	68
<i>SBR/PTFE</i>	1 M TEABF ₄ in ACN	0–2.7 V	108 F g ⁻¹ at 0.2 A g ⁻¹	~80% after 20,000 cycles at ~1 A g ⁻¹	65- 70
<i>PVP [Ethanol]</i>	1 M TEABF ₄ in PC	0–2.7 V	112 F g ⁻¹ at 0.1 A g ⁻¹	~81% after 10,000 cycles at 1 A g ⁻¹	66- 72
<i>PTFE [NMP]</i>	1 M TEABF ₄ in PC	0–2.7 V	107 F g ⁻¹ at 0.1 A g ⁻¹	~81% after 10,000 cycles at 1 A g ⁻¹	66- 72
<i>Ch/poly(EG-ran-PG)</i> [1% acetic acid in H ₂ O]	1 M H ₂ SO ₄ in H ₂ O	0–1 V	172 F g ⁻¹ at 0.5 A g ⁻¹	~99% after 6,000 cycles at 3.5 A g ⁻¹	67- 71

Supplementary Figures

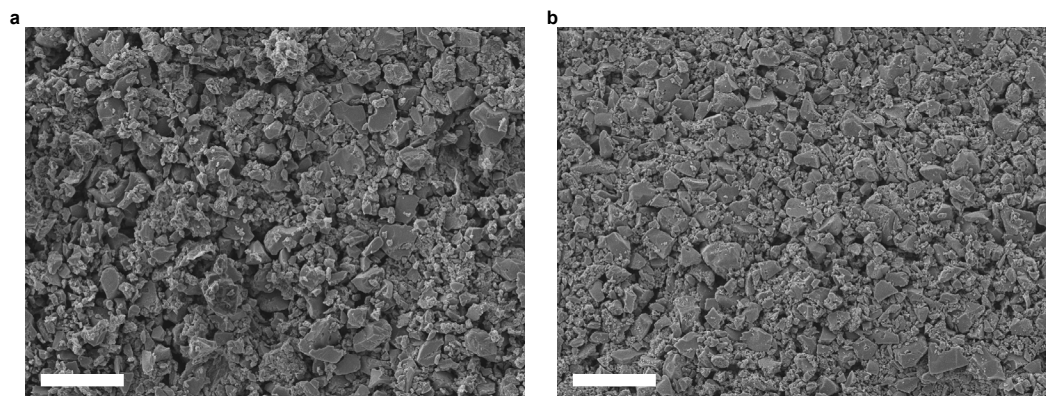


Figure S4-1 – Electronic microscope imaging of GO-StC electrodes. (a-b) SEM images showing: surface morphology of (c) GO-StC and (d) StC coatings (scale bar 20 μm).

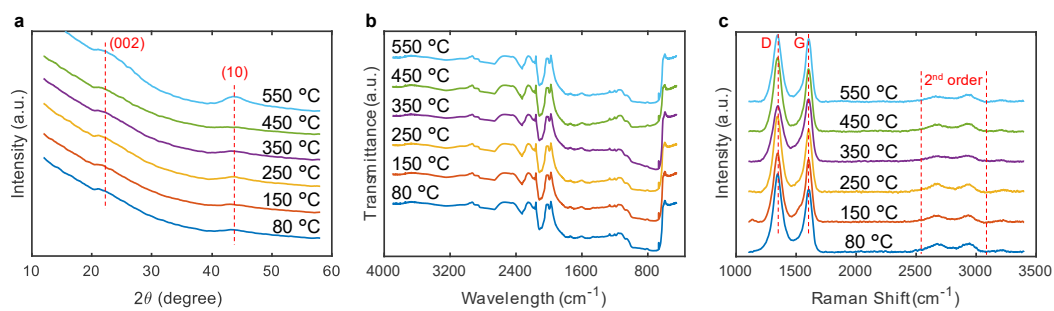


Figure S4-2 – Physicochemical characterisation of GO-StC coatings at varying thermal treatment temperatures. (a) XRD patterns, **(b)** FT-IR and **(c)** RS spectra.

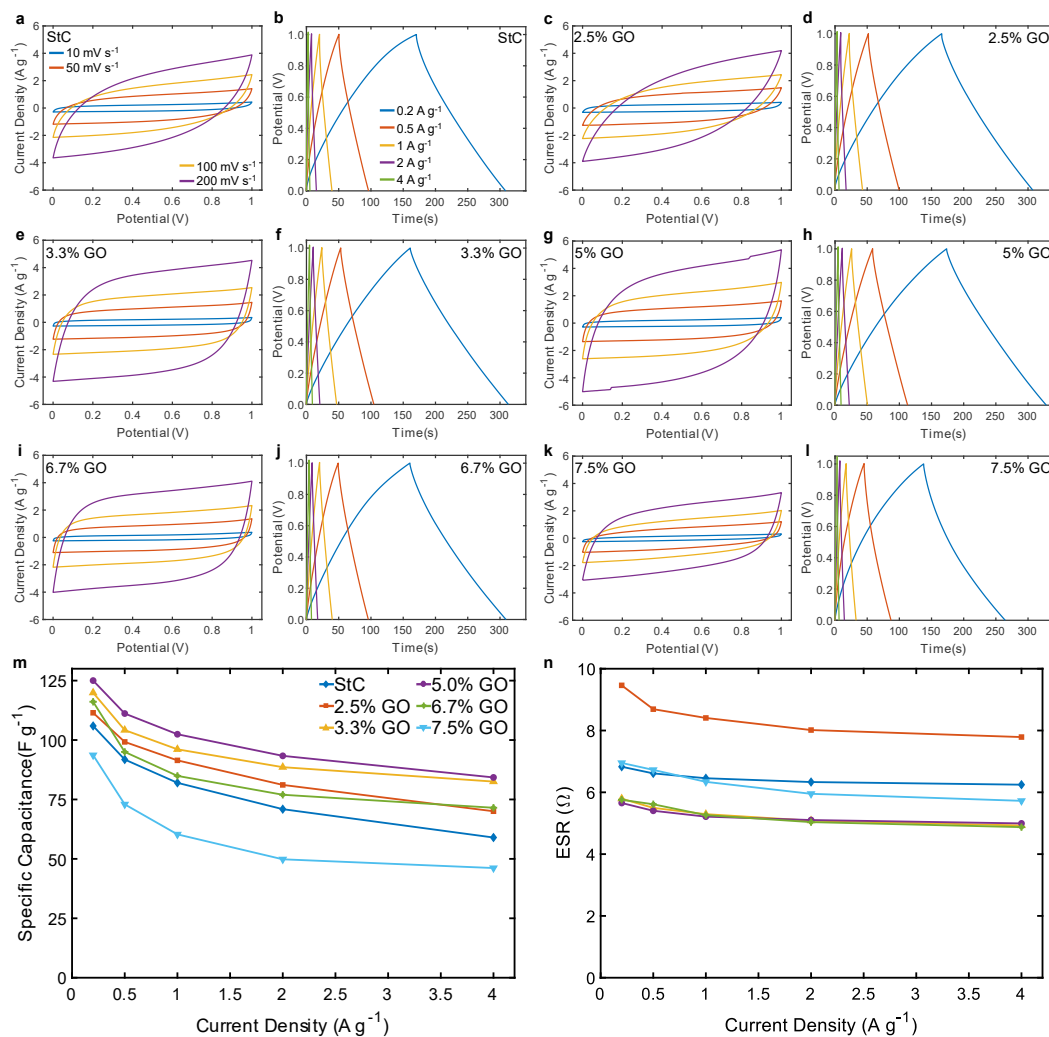


Figure S4-3 – Electrochemical characterisation of GO-StC electrodes with GO amount varying from 0 (StC) to 7.5%. (a, c, e, g, i, k) Cyclic Voltammetry Scans (CVs) and (b, d, f, h, j, l) Galvanostatic Charge Discharge Cycles (GCDs). Same legend applies for all CVs and all GCDs. Variation of (m) specific capacitance and (n) Equivalent Series Resistance (ESR) with current density. Same legend applies for both panels.

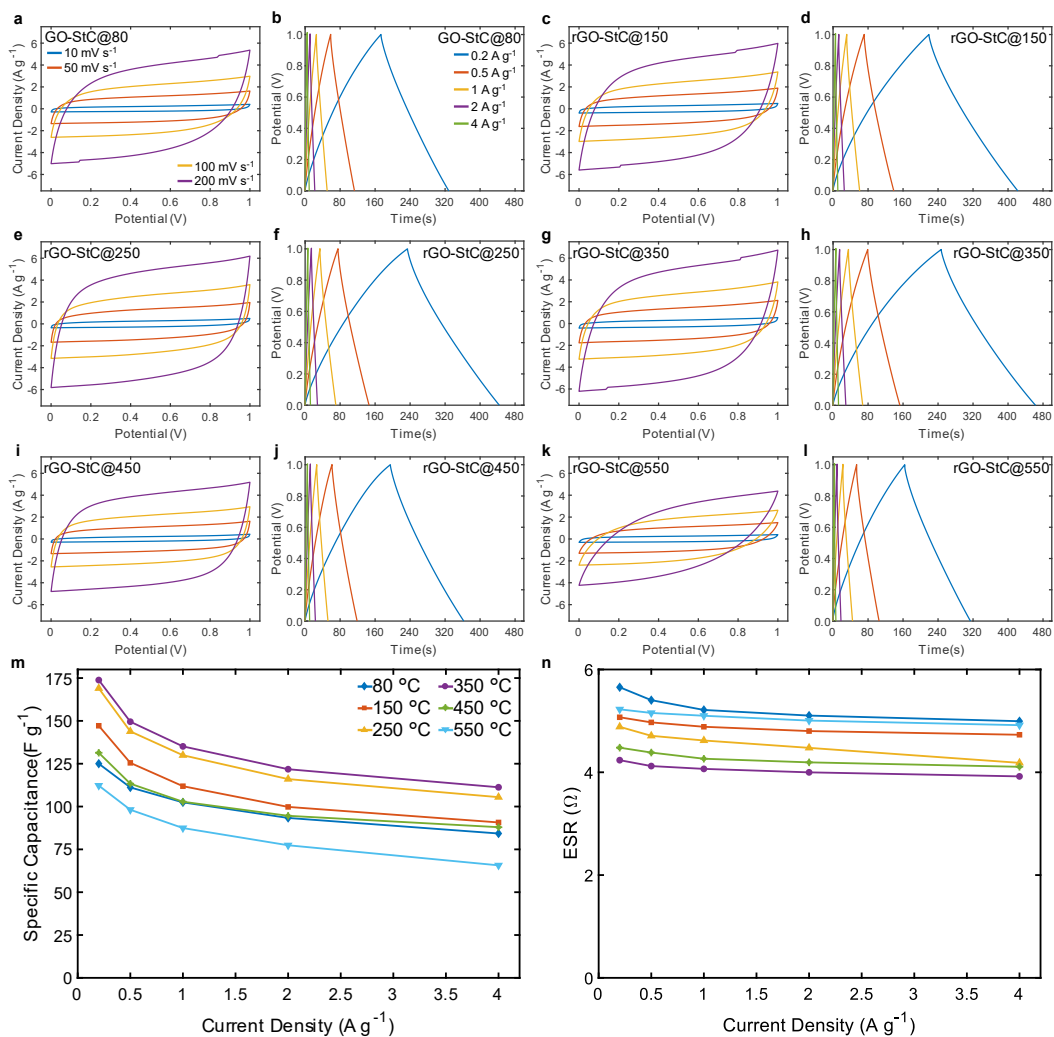


Figure S4-4 – Electrochemical characterisation of GO-StC electrodes with thermal treatment temperatures varying from 80 to 550 °C. (a, c, e, g, i, k) Cyclic Voltammetry Scans (CVs) and (b, d, f, h, j, l) Galvanostatic Charge Discharge Cycles (GCDs). Same legend applies for all CVs and all GCDs. Variation of (m) specific capacitance and (n) Equivalent Series Resistance (ESR) with current density. Same legend applies for both panels.

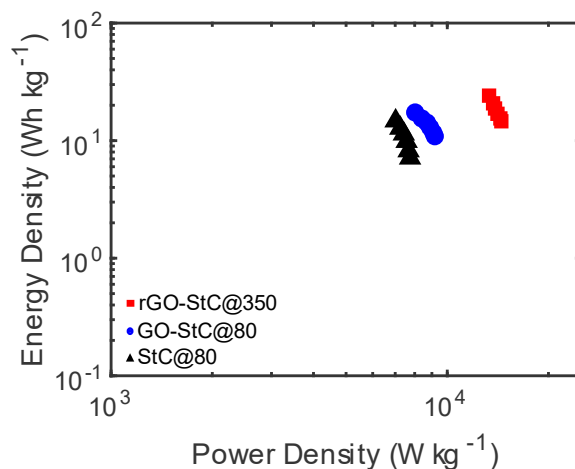


Figure S4-5 – Ragone plot of assembled SCs.

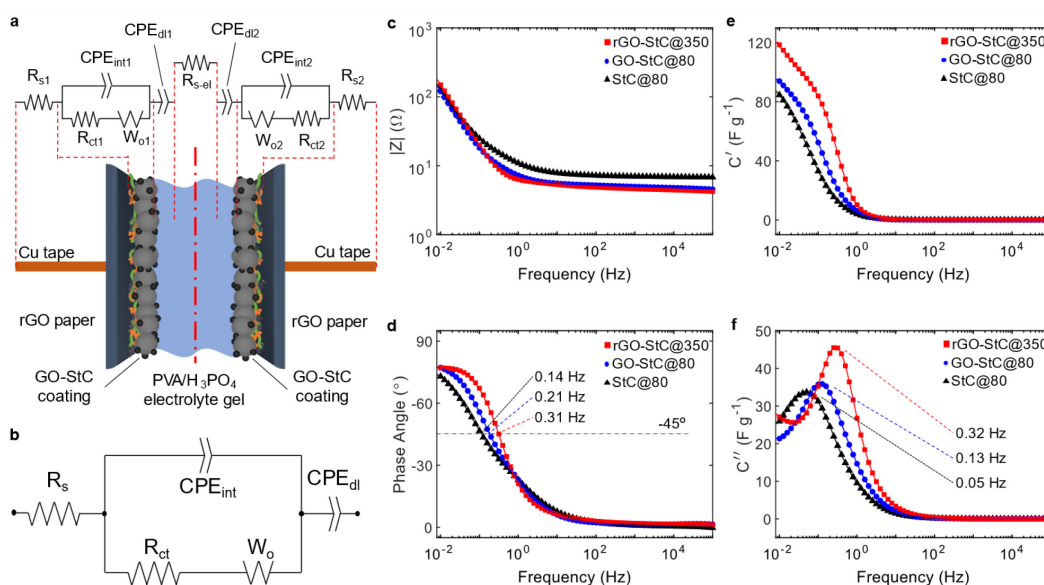


Figure S4-6 – Impedance characterisation of supercapacitors. (a) Schematic of GO-StC symmetric cell with equivalent circuit elements assignment (R_{s1-2} are resistors accounting for leads, current collectors and interparticle series resistances; R_{s-el} accounts for the electrolyte series resistance; CPE_{int1-2} are constant phase elements accounting for interfacial non-ideal capacitances; R_{ct1-2} account for charge-transfer resistances at interfaces; W_{o1-2} are finite length-open Warburg elements accounting for the transmission-line behaviour of porous materials; CPE_{dl1-2} account for non-ideal double-layer capacitances [4]). **(b)** Simplified equivalent circuit for EIS fittings where $R_s = R_{s1} + R_{s2} + R_{s-el}$, $CPE_{dl} = (CPE_{dl1} + CPE_{dl2})/2$, $Z(R_{ct} - CPE_{int} - W_o) = Z(R_{ct1} - CPE_{int1} - W_{o1}) + Z(R_{ct2} - CPE_{int2} - W_{o2})$. **(c-d)** Bode plots of rGO-StC@350 with dried-only GO-StC and StC electrodes (GO-StC@80 and StC@80) included for comparison. Markers represent the experimental points, while solid lines represent the modelled behaviour with the simplified equivalent circuit. Capacitors response frequency at a phase angle of -45° are specified. Variation of **(e)** Real and **(f)** imaginary part of complex capacitance for StC@80, GO-StC@80, and rGO-StC@350. Capacitors relaxation frequency (local maxima of C'') are specified.

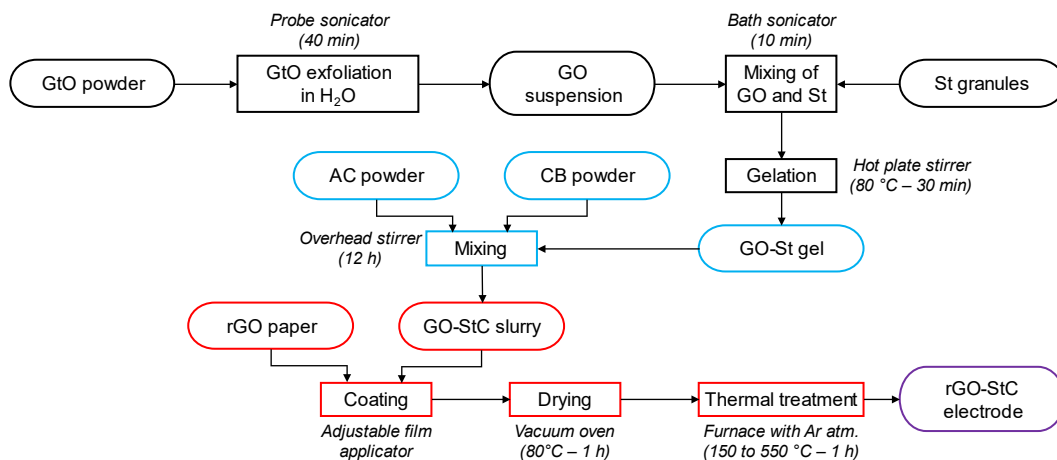


Figure S4-7 – Flow diagram of rGO-StC electrodes fabrication process.

Supplementary References

1. Cael, J.J., J.L. Koenig, and J. Blackwell, Infrared and Raman spectroscopy of carbohydrates. Part VI: Normal coordinate analysis of V-amylose. *Biopolymers*, 1975. **14**(9): p. 1885-1903.
2. Titelman, G.I., et al., Characteristics and microstructure of aqueous colloidal dispersions of graphite oxide. *Carbon*, 2005. **43**(3): p. 641-649.
3. Zhang, J., et al., Reduction of graphene oxide vial-ascorbic acid. *Chemical Communications*, 2010. **46**(7): p. 1112-1114.
4. Conway, B.E., *Electrochemical Supercapacitors*. 1 ed. 1999, Boston, MA: Springer. XXX, 698.

Chapter 7

CONCLUSIONS AND FUTURE WORKS

7.1 Conclusions

Nowadays graphene-based materials have attracted the attention of many researchers for the development of advanced engineering applications, where features such as low density, high surface area, high chemical, thermal and mechanical stability, and tuneable electrical properties could be exploited. Those derive from the peculiar chemical structure of graphene, consisting of a hexagonal lattice of sp^2 -hybridised carbon atoms. GO, in particular, is a promising candidate to be used as a precursor for industrial-scale processes. This is allowed by the introduction of oxygen containing

functional groups during its synthesis from graphite, and consequently by the ability of water and other organic polar solvents to intercalate between interlayers spacings. In addition, although initially behaving as a thermal and electrical insulator, electronic properties of GO can be restored with its reduction. During the latter, oxygen groups are partially stripped, and the conjugated network of carbon atoms is consequently restored.

The main scope of this thesis was to investigate the versatility of exploiting GO as precursor for the manufacturing of graphene-based materials in multiple engineering applications, namely aerogels as porous sound absorbers and supercapacitors as energy storage devices. In order to evaluate the effects of GO processing to the properties of the resulting materials, the research work is in its first part related to the background and literature review of graphene-based materials obtained from GO. It was found that every step of the processing is crucial for the final performance of the resulting graphene-based material, starting from the oxidation from Graphite to Graphite Oxide, its exfoliation to Graphene Oxide, and eventually its reduction to Reduced Graphene Oxide. For this reason, a proper chemico-physical analysis is a fundamental tool to understand the underlying mechanism leading to the final performance of the prototype under investigation. While a trivial visual inspection permits, to some extent, to establish if the reduction was successful, microscopy (such as SEM, TEM, and AFM) and spectroscopy (such as Raman, FT-IR, and XPS) techniques can be used to observe morphological changes and the evolution of the chemical-structure, respectively. Moreover, XRD can be used for crystalline phases individuation and analysis.

The thesis then proceeded toward the practical evaluation of prototypes for the two mentioned engineering areas, through a collection of two journal papers for each. Regarding porous absorbers, the first work presented a

novel ultralight aerogel for the design of compact acoustic materials. An environmentally friendly process allowed to embed templated GO and PVA blends in structural honeycomb cores. The hydrogen bonds between the two components resulted crucial to achieve the hierarchical porosity responsible for the low density and the tuneable sound absorption and transmission functionalities. Specifically, the reported average sound absorption coefficient over the 400 – 2500 Hz reached a value of 0.79 (sample with a density of 2.10 kg m^{-3} and a thickness of 35 mm), while the average sound transmission loss was as high as 15.8 dB (sample with a density of 7.41 kg m^{-3} and a thickness of 35 mm). Moreover, a semi-analytical approach was employed to evaluate the effect of different processing times on the acoustic properties and their relationships with the non-acoustic properties of the material.

The second work proposed instead a chemical modification of the same aerogel derived from GO and PVA blends, with the aim to obtain multifunctional materials readily applicable for the automotive and aerospace industries. Glycerol and Glutaraldehyde were used as plasticising and cross-linking agent, respectively, leading to a more robust structure. The attention was then focused not only on the acoustic, but also on the thermal and mechanical properties. The modified aerogel showed an average absorption coefficient in the critical range of 500 – 1500 Hz of 0.72 (sample with a density of 6.51 kg m^{-3} and a thickness of 25 mm), a thermal conductivity of 0.0424 W mK^{-1} , and most importantly, a three-fold improvement, with respect of the un-modified aerogel, of the compressive strength and energy loss coefficient during mechanical testing. Moreover, an additional prototype where the in-situ reduction of GO was chemically promoted by Ascorbic Acid, showed piezoresistive capabilities.

The first journal of the collection related to SCs demonstrates the possibility to use rGO as an alternative active binder to fabricate EDLC electrodes. A homogeneous carbonaceous composite with CB was obtained having water as the only cheap and ecological solvent and GO as dispersing agent. Afterward, the electrodes were thermally treated to promote the reduction to rGO and thus unlocking its ability to actively contribute to the electrochemical performances. Furthermore, an innovative current collector deriving as well from GO reduction was exploited to manufacture “all-graphene based” devices. rGO sheets wrapping CB particles generated an interconnected 3D network that allowed to reach a high specific power of 32.1 kW kg^{-1} and a specific energy of 8.8 Wh kg^{-1} , with a 1 M TEMA-BF₄ in AC electrolyte.

Such intriguing results drove the research toward the green and hybrid binder developed in the second work of the collection, where the main goal was to develop materials and a fabrication procedure immediately transferrable to the industry. Particularly, a water-based blend of GO and a biopolymer, starch, was gelled and used as binder to fabricate EDLC electrodes. AC, CB, and rGO paper were used, respectively, as active material, conductive additive, and current collector, while a PVA/H₃PO₄ gel was adopted as electrolyte. The interactions between rGO sheets and starch molecules improved the morphology and structure of the material, as well as its thermal stability, leading to the specific capacitance of 112.2 F g^{-1} . Moreover, a subsequent thermal treatment at $350 \text{ }^\circ\text{C}$ determined a higher degree of reduction of rGO, which further improved its contribution for a fast and efficient charge storage process. As a result, the high specific capacitance of 173.8 F g^{-1} could be obtained, together with a high-rate capability and a remarkable cycling stability (capacitance retention of 93.1% after 17,000 charge/discharge cycles).

7.2 Future Works

This doctoral research thesis documented the ability to exploit GO as precursor for the manufacturing of graphene-based materials applicable in two different engineering fields: ultra-light porous sound absorbers and supercapacitors with active binders. Despite the promising results achieved for both the cases, further developments are still required before such materials could be transferred from laboratory scale to the industry.

Concerning porous sound absorbers, the following goal would be the design for a specific application. Particularly, the GPA aerogel described in the first journal paper attracted the attention of different manufacturers involved in the commercial business for the aerospace industry. Thanks to their feedbacks, important improvements were already achieved as described for the modified aerogels of the second publication. The next step would then be the scale-up of the manufacturable volume to reach the desired size of insulating panels for secondary structures in planes cabin. In addition, a further optimisation of the chemical modifications of the multifunctional rGOP aerogel presented as the last prototype of graphene-based acoustic materials could mitigate the negative impact of the process on the fabricated material weight.

On the other hand, the effectiveness of rGO as active binder for supercapacitors markedly increased when used in conjunction with the biopolymer starch. Although the manufacturing process, thanks to its simplicity, is already scalable to a bigger batch size and the specific capacitance is among the highest ever reported for alternative green binders processable in water, the ESR of the prototypes still needs to be dramatically reduced. Major improvements could already be achieved with an improved design of the pouch cells, but another factor where the attention will be focused for the next studies is an improvement at the

interface between the current collector and the active material. While ESR reduction would guarantee a boost to the maximum power deliverable from an EDLC, studies on non-organic electrolytes capable to operate at higher rated voltages would allow to reach a dramatic increase also of the maximum stored energy.

Finally, the broader vision of this research work is the possibility, in future, to combine the two assessed engineering solutions in an integrated and innovative structure possessing multifunctional abilities, such as: sound and thermal insulation, piezo-resistivity, and electrical energy storage. Its crucial components would be Graphene-based materials derived from GO, allowing thus for large scale, low cost and environmentally friendly manufacturing processes.

References

1. Novoselov, K.S., et al., *Electric Field Effect in Atomically Thin Carbon Films*. Science, 2004. **306**(5696): p. 666.
2. Kroto, H.W., et al., *C60: Buckminsterfullerene*. Nature, 1985. **318**(6042): p. 162-163.
3. Iijima, S., *Helical microtubules of graphitic carbon*. Nature, 1991. **354**(6348): p. 56-58.
4. Lee, C., et al., *Measurement of the Elastic Properties and Intrinsic Strength of Monolayer Graphene*. Science, 2008. **321**(5887): p. 385-388.
5. Kiew, S.F., et al., *Assessing biocompatibility of graphene oxide-based nanocarriers: A review*. J Control Release, 2016. **226**: p. 217-28.
6. Balandin, A.A., *Thermal properties of graphene and nanostructured carbon materials*. Nature Materials, 2011. **10**: p. 569.
7. Du, X., et al., *Approaching ballistic transport in suspended graphene*. Nature Nanotechnology, 2008. **3**: p. 491.

8. Stoller, M.D., et al., *Graphene-Based Ultracapacitors*. Nano Letters, 2008. **8**(10): p. 3498-3502.
9. Nine, M.J., et al., *Graphene Oxide-Based Lamella Network for Enhanced Sound Absorption*. Advanced Functional Materials, 2017. **27**(46): p. 1703820.
10. Cui, X., et al., *Thermal Conductive and Mechanical Properties of Polymeric Composites Based on Solution-Exfoliated Boron Nitride and Graphene Nanosheets: A Morphology-Promoted Synergistic Effect*. ACS Applied Materials & Interfaces, 2015. **7**(34): p. 19068-19075.
11. Lu, C.-H., et al., *A Graphene Platform for Sensing Biomolecules*. Angewandte Chemie International Edition, 2009. **48**(26): p. 4785-4787.
12. Wang, J., et al., *Graphene Oxide as an Effective Barrier on a Porous Nanofibrous Membrane for Water Treatment*. ACS Applied Materials & Interfaces, 2016. **8**(9): p. 6211-6218.
13. Kuilla, T., et al., *Recent advances in graphene based polymer composites*. Progress in Polymer Science, 2010. **35**(11): p. 1350-1375.
14. Park, S. and R.S. Ruoff, *Chemical methods for the production of graphenes*. Nature Nanotechnology, 2009. **4**: p. 217.
15. Stankovich, S., et al., *Synthesis of graphene-based nanosheets via chemical reduction of exfoliated graphite oxide*. Carbon, 2007. **45**(7): p. 1558-1565.
16. Paredes, J.I., et al., *Graphene Oxide Dispersions in Organic Solvents*. Langmuir, 2008. **24**(19): p. 10560-10564.
17. Guerrero-Contreras, J. and F. Caballero-Briones, *Graphene oxide powders with different oxidation degree, prepared by synthesis variations of the Hummers method*. Materials Chemistry and Physics, 2015. **153**: p. 209-220.
18. Liu, F., et al., *Facile Synthetic Method for Pristine Graphene Quantum Dots and Graphene Oxide Quantum Dots: Origin of Blue and Green Luminescence*. Advanced Materials, 2013. **25**(27): p. 3657-3662.
19. Higginbotham, A.L., et al., *Lower-Defect Graphene Oxide Nanoribbons from Multiwalled Carbon Nanotubes*. ACS Nano, 2010. **4**(4): p. 2059-2069.

20. Wang, C., et al., *Preparation and characterization of graphene oxide/poly(vinyl alcohol) composite nanofibers via electrospinning*. Journal of Applied Polymer Science, 2013. **127**(4): p. 3026-3032.
21. Yao, Y., et al., *Graphene oxide thin film coated quartz crystal microbalance for humidity detection*. Applied Surface Science, 2011. **257**(17): p. 7778-7782.
22. Dikin, D.A., et al., *Preparation and characterization of graphene oxide paper*. Nature, 2007. **448**: p. 457.
23. Wang, J. and M. Ellsworth, *Graphene Aerogels*. ECS Transactions, 2019. **19**(5): p. 241-247.
24. Chen, J.-T., et al., *Enhancing polymer/graphene oxide gas barrier film properties by introducing new crystals*. Carbon, 2014. **75**: p. 443-451.
25. Park, J., et al., *Characteristics tuning of graphene-oxide-based-graphene to various end-uses*. Energy Storage Materials, 2018. **14**: p. 8-21.
26. Bianco, A., et al., *All in the graphene family – A recommended nomenclature for two-dimensional carbon materials*. Carbon, 2013. **65**: p. 1-6.
27. Brodie, B.C., *XIII. On the atomic weight of graphite*. Philosophical Transactions of the Royal Society of London, 1859. **149**: p. 249-259.
28. Staudenmaier, L., *Verfahren zur Darstellung der Graphitsäure*. Berichte der deutschen chemischen Gesellschaft, 1898. **31**(2): p. 1481-1487.
29. Hummers, W.S. and R.E. Offeman, *Preparation of Graphitic Oxide*. Journal of the American Chemical Society, 1958. **80**(6): p. 1339-1339.
30. Marcano, D.C., et al., *Improved Synthesis of Graphene Oxide*. ACS Nano, 2010. **4**(8): p. 4806-4814.
31. Lerf, A., et al., *Structure of Graphite Oxide Revisited*. The Journal of Physical Chemistry B, 1998. **102**(23): p. 4477-4482.
32. Szabó, T., et al., *Evolution of Surface Functional Groups in a Series of Progressively Oxidized Graphite Oxides*. Chem. Mater., 2006. **18**(11): p. 2740-2749.

33. Bagri, A., et al., *Structural evolution during the reduction of chemically derived graphene oxide*. *Nature Chemistry*, 2010. **2**: p. 581.
34. Dreyer, D.R., et al., *The chemistry of graphene oxide*. *Chemical Society Reviews*, 2010. **39**(1): p. 228-240.
35. He, H., et al., *Solid-State NMR Studies of the Structure of Graphite Oxide*. *The Journal of Physical Chemistry*, 1996. **100**(51): p. 19954-19958.
36. Krishnamoorthy, K., et al., *The chemical and structural analysis of graphene oxide with different degrees of oxidation*. *Carbon*, 2013. **53**: p. 38-49.
37. Erickson, K., et al., *Determination of the Local Chemical Structure of Graphene Oxide and Reduced Graphene Oxide*. *Advanced Materials*, 2010. **22**(40): p. 4467-4472.
38. Mermoux, M., Y. Chabre, and A. Rousseau, *FTIR and 13C NMR study of graphite oxide*. *Carbon*, 1991. **29**(3): p. 469-474.
39. Buchsteiner, A., A. Lerf, and J. Pieper, *Water Dynamics in Graphite Oxide Investigated with Neutron Scattering*. *The Journal of Physical Chemistry B*, 2006. **110**(45): p. 22328-22338.
40. Chen, J. and L. Li, *Effect of oxidation degree on the thermal properties of graphene oxide*. *Journal of Materials Research and Technology*, 2020. **9**(6): p. 13740-13748.
41. Boehm, H.P., et al., *Das Adsorptionsverhalten sehr dünner Kohlenstoff-Folien*. *Zeitschrift für anorganische und allgemeine Chemie*, 1962. **316**(3-4): p. 119-127.
42. Compton, O.C. and S.T. Nguyen, *Graphene Oxide, Highly Reduced Graphene Oxide, and Graphene: Versatile Building Blocks for Carbon-Based Materials*. *Small*, 2010. **6**(6): p. 711-723.
43. Georgakilas, V., et al., *Functionalization of Graphene: Covalent and Non-Covalent Approaches, Derivatives and Applications*. *Chemical Reviews*, 2012. **112**(11): p. 6156-6214.
44. Chen, S., et al., *Graphene Oxide-MnO₂ Nanocomposites for Supercapacitors*. *ACS Nano*, 2010. **4**(5): p. 2822-2830.
45. Zhu, Y., et al., *Graphene and Graphene Oxide: Synthesis, Properties, and Applications*. *Advanced Materials*, 2010. **22**(35): p. 3906-3924.

46. Liu, J., J. Tang, and J.J. Gooding, *Strategies for chemical modification of graphene and applications of chemically modified graphene*. Journal of Materials Chemistry, 2012. **22**(25): p. 12435-12452.
47. Jauregui, L.A., et al., *Thermal Transport in Graphene Nanostructures: Experiments and Simulations*. ECS Transactions, 2010. **28**(5): p. 73-83.
48. Pei, S. and H.-M. Cheng, *The reduction of graphene oxide*. Carbon, 2012. **50**(9): p. 3210-3228.
49. Edgar Jimenez-Cervantes Amieva, et al., *Graphene-Based Materials Functionalization with Natural Polymeric Biomolecules*, in *Recent Advances in Graphene Research*. 2016, IntechOpen.
50. Schniepp, H.C., et al., *Functionalized Single Graphene Sheets Derived from Splitting Graphite Oxide*. The Journal of Physical Chemistry B, 2006. **110**(17): p. 8535-8539.
51. McAllister, M.J., et al., *Single Sheet Functionalized Graphene by Oxidation and Thermal Expansion of Graphite*. Chemistry of Materials, 2007. **19**(18): p. 4396-4404.
52. Zhu, Y., et al., *Exfoliation of Graphite Oxide in Propylene Carbonate and Thermal Reduction of the Resulting Graphene Oxide Platelets*. ACS Nano, 2010. **4**(2): p. 1227-1233.
53. Jung, I., et al., *Tunable Electrical Conductivity of Individual Graphene Oxide Sheets Reduced at "Low" Temperatures*. Nano Letters, 2008. **8**(12): p. 4283-4287.
54. Lu, G., L.E. Ocola, and J. Chen, *Gas detection using low-temperature reduced graphene oxide sheets*. Applied Physics Letters, 2009. **94**(8): p. 083111.
55. Wei, Z., et al., *Nanoscale Tunable Reduction of Graphene Oxide for Graphene Electronics*. Science, 2010. **328**(5984): p. 1373-1376.
56. Mattevi, C., et al., *Evolution of Electrical, Chemical, and Structural Properties of Transparent and Conducting Chemically Derived Graphene Thin Films*. Advanced Functional Materials, 2009. **19**(16): p. 2577-2583.
57. Falcao, E.H.L., et al., *Microwave exfoliation of a graphite intercalation compound*. Carbon, 2007. **45**(6): p. 1367-1369.

58. Fozooni, S. and A.M. Tikdari, *Microwave-Assisted Graphite-Support Synthesis of Imidazolones*. *Catalysis Letters*, 2008. **120**(3): p. 303-306.
59. Zhu, Y., et al., *Microwave assisted exfoliation and reduction of graphite oxide for ultracapacitors*. *Carbon*, 2010. **48**(7): p. 2118-2122.
60. Chen, W., L. Yan, and P.R. Bangal, *Preparation of graphene by the rapid and mild thermal reduction of graphene oxide induced by microwaves*. *Carbon*, 2010. **48**(4): p. 1146-1152.
61. Gilje, S., et al., *Photothermal Deoxygenation of Graphene Oxide for Patterning and Distributed Ignition Applications*. *Advanced Materials*, 2010. **22**(3): p. 419-423.
62. Zhang, Y., et al., *Direct imprinting of microcircuits on graphene oxides film by femtosecond laser reduction*. *Nano Today*, 2010. **5**(1): p. 15-20.
63. Abdelsayed, V., et al., *Photothermal Deoxygenation of Graphite Oxide with Laser Excitation in Solution and Graphene-Aided Increase in Water Temperature*. *The Journal of Physical Chemistry Letters*, 2010. **1**(19): p. 2804-2809.
64. Sokolov, D.A., K.R. Shepperd, and T.M. Orlando, *Formation of Graphene Features from Direct Laser-Induced Reduction of Graphite Oxide*. *The Journal of Physical Chemistry Letters*, 2010. **1**(18): p. 2633-2636.
65. Trusovas, R., et al., *Reduction of graphite oxide to graphene with laser irradiation*. *Carbon*, 2013. **52**: p. 574-582.
66. Kotov, N.A., I. Dékány, and J.H. Fendler, *Ultrathin graphite oxide–polyelectrolyte composites prepared by self-assembly: Transition between conductive and non-conductive states*. *Advanced Materials*, 1996. **8**(8): p. 637-641.
67. Shin, H.-J., et al., *Efficient Reduction of Graphite Oxide by Sodium Borohydride and Its Effect on Electrical Conductance*. *Advanced Functional Materials*, 2009. **19**(12): p. 1987-1992.
68. Moon, I.K., et al., *Reduced graphene oxide by chemical graphitization*. *Nature Communications*, 2010. **1**: p. 73.
69. Zhang, J., et al., *Reduction of graphene oxide via ascorbic acid*. *Chemical Communications*, 2010. **46**(7): p. 1112-1114.

70. Fernández-Merino, M.J., et al., *Vitamin C Is an Ideal Substitute for Hydrazine in the Reduction of Graphene Oxide Suspensions*. The Journal of Physical Chemistry C, 2010. **114**(14): p. 6426-6432.
71. Williams, G., B. Seger, and P.V. Kamat, *TiO₂-Graphene Nanocomposites. UV-Assisted Photocatalytic Reduction of Graphene Oxide*. ACS Nano, 2008. **2**(7): p. 1487-1491.
72. Ramesha, G.K. and S. Sampath, *Electrochemical Reduction of Oriented Graphene Oxide Films: An in Situ Raman Spectroelectrochemical Study*. The Journal of Physical Chemistry C, 2009. **113**(19): p. 7985-7989.
73. An, S.J., et al., *Thin Film Fabrication and Simultaneous Anodic Reduction of Deposited Graphene Oxide Platelets by Electrophoretic Deposition*. The Journal of Physical Chemistry Letters, 2010. **1**(8): p. 1259-1263.
74. Zhou, Y., et al., *Hydrothermal Dehydration for the "Green" Reduction of Exfoliated Graphene Oxide to Graphene and Demonstration of Tunable Optical Limiting Properties*. Chemistry of Materials, 2009. **21**(13): p. 2950-2956.
75. El-Kady, M.F., et al., *Laser Scribing of High-Performance and Flexible Graphene-Based Electrochemical Capacitors*. Science, 2012. **335**(6074): p. 1326-1330.
76. Pei, S., et al., *Direct reduction of graphene oxide films into highly conductive and flexible graphene films by hydrohalic acids*. Carbon, 2010. **48**(15): p. 4466-4474.
77. Gao, W., et al., *Direct laser writing of micro-supercapacitors on hydrated graphite oxide films*. Nature Nanotechnology, 2011. **6**: p. 496.
78. Chen, H., et al., *Mechanically Strong, Electrically Conductive, and Biocompatible Graphene Paper*. Advanced Materials, 2008. **20**(18): p. 3557-3561.
79. Wang, C., et al., *Freeze-Casting Produces a Graphene Oxide Aerogel with a Radial and Centrosymmetric Structure*. ACS Nano, 2018. **12**(6): p. 5816-5825.
80. Shao, Y., et al., *Facile and controllable electrochemical reduction of graphene oxide and its applications*. Journal of Materials Chemistry, 2010. **20**(4): p. 743-748.

81. Stobinski, L., et al., *Graphene oxide and reduced graphene oxide studied by the XRD, TEM and electron spectroscopy methods*. Journal of Electron Spectroscopy and Related Phenomena, 2014. **195**: p. 145-154.
82. Paredes, J.I., et al., *Atomic Force and Scanning Tunneling Microscopy Imaging of Graphene Nanosheets Derived from Graphite Oxide*. Langmuir, 2009. **25**(10): p. 5957-5968.
83. Luo, D., et al., *Evaluation Criteria for Reduced Graphene Oxide*. The Journal of Physical Chemistry C, 2011. **115**(23): p. 11327-11335.
84. Poot, M. and H.S.J.v.d. Zant, *Nanomechanical properties of few-layer graphene membranes*. Applied Physics Letters, 2008. **92**(6): p. 063111.
85. Meer, F.v.d., *Near-infrared laboratory spectroscopy of mineral chemistry: A review*. International Journal of Applied Earth Observation and Geoinformation, 2018. **65**: p. 71-78.
86. Briggs, D. and M.P. Seah, *Practical Surface Analysis. Volume 1 – Auger and X-ray Photoelectron Spectroscopy*. Second ed. Vol. 1. 1990: Wiley-Blackwell.
87. Hontoria-Lucas, C., et al., *Study of oxygen-containing groups in a series of graphite oxides: Physical and chemical characterization*. Carbon, 1995. **33**(11): p. 1585-1592.
88. Guo, H.-L., et al., *A Green Approach to the Synthesis of Graphene Nanosheets*. ACS Nano, 2009. **3**(9): p. 2653-2659.
89. Titelman, G.I., et al., *Characteristics and microstructure of aqueous colloidal dispersions of graphite oxide*. Carbon, 2005. **43**(3): p. 641-649.
90. Faniyi, I.O., et al., *The comparative analyses of reduced graphene oxide (RGO) prepared via green, mild and chemical approaches*. SN Applied Sciences, 2019. **1**(10): p. 1181.
91. Xu, L.Q., et al., *Dopamine-Induced Reduction and Functionalization of Graphene Oxide Nanosheets*. Macromolecules, 2010. **43**(20): p. 8336-8339.
92. Ferrari, A.C., *Raman spectroscopy of graphene and graphite: Disorder, electron–phonon coupling, doping and nonadiabatic effects*. Solid State Communications, 2007. **143**(1): p. 47-57.

93. Claramunt, S., et al., *The Importance of Interbands on the Interpretation of the Raman Spectrum of Graphene Oxide*. The Journal of Physical Chemistry C, 2015. **119**(18): p. 10123-10129.
94. Ferrari, A.C. and D.M. Basko, *Raman spectroscopy as a versatile tool for studying the properties of graphene*. Nature Nanotechnology, 2013. **8**(4): p. 235-246.
95. Gupta, A., et al., *Raman Scattering from High-Frequency Phonons in Supported n-Graphene Layer Films*. Nano Letters, 2006. **6**(12): p. 2667-2673.
96. Wang, H., et al., *Vibrational properties of graphene and graphene layers*. Journal of Raman Spectroscopy, 2009. **40**(12): p. 1791-1796.
97. Ni, Z.H., et al., *Uniaxial Strain on Graphene: Raman Spectroscopy Study and Band-Gap Opening*. ACS Nano, 2008. **2**(11): p. 2301-2305.
98. Zhou, H., et al., *Raman scattering of monolayer graphene: the temperature and oxygen doping effects*. Journal of Physics D: Applied Physics, 2011. **44**(18): p. 185404.
99. Bragg William, H. and L. Bragg William, *The reflection of X-rays by crystals*. Proceedings of the Royal Society of London. Series A, Containing Papers of a Mathematical and Physical Character, 1913. **88**(605): p. 428-438.
100. Krishnankutty, N. and M.A. Vannice, *Effect of Pretreatment on Surface Area, Porosity, and Adsorption Properties of a Carbon Black*. Chemistry of Materials, 1995. **7**(4): p. 754-763.
101. Johra, F.T., J.-W. Lee, and W.-G. Jung, *Facile and safe graphene preparation on solution based platform*. Journal of Industrial and Engineering Chemistry, 2014. **20**(5): p. 2883-2887.
102. Scherrer, P., *Bestimmung der Größe und der inneren Struktur von Kolloidteilchen mittels Röntgenstrahlen*. Nachrichten von der Gesellschaft der Wissenschaften zu Göttingen, Mathematisch-Physikalische Klasse, 1918. **1918**: p. 98-100.
103. Biscoe, J. and B.E. Warren, *An X-Ray Study of Carbon Black*. Journal of Applied Physics, 1942. **13**(6): p. 364-371.
104. Tuinstra, F. and J.L. Koenig, *Raman Spectrum of Graphite*. The Journal of Chemical Physics, 1970. **53**(3): p. 1126-1130.

105. Ziegler, C., et al., *Modern Inorganic Aerogels*. Angewandte Chemie International Edition, 2017. **56**(43): p. 13200-13221.
106. Bobrovnikskii, Y.I. and T.M. Tomilina, *Sound Absorption and Metamaterials: A Review*. Acoustical Physics, 2018. **64**(5): p. 519-526.
107. Sabine, W.C., *Collected Papers on Acoustics*. Acoustical Society of America Journal, 1994. **95**: p. 3679.
108. Arenas, J. and M. Crocker, *Recent Trends in Porous Sound-Absorbing Materials*. Sound & vibration, 2010. **44**: p. 12-17.
109. Cox, T. and P. D'Antonio, *Acoustic absorbers and diffusers: theory, design and application*. 2009: Routledge Taylor & Francis. 496.
110. Yang, M. and P. Sheng, *Sound Absorption Structures: From Porous Media to Acoustic Metamaterials*. Annual Review of Materials Research, 2017. **47**(1): p. 83-114.
111. Engel, Z., *Notes on Sound Absorption Technology, K.U. INGARD*. 2014. Vol. 21. 2014.
112. Cao, L., et al., *Porous materials for sound absorption*. Composites Communications, 2018. **10**: p. 25-35.
113. Mazrouei-Sebdani, Z., et al., *A review on silica aerogel-based materials for acoustic applications*. Journal of Non-Crystalline Solids, 2021. **562**: p. 120770.
114. Xu, Z., et al., *Sound propagation in porous materials containing rough tubes*. Physics of Fluids, 2020. **32**(9): p. 093604.
115. Stinson, M.R. and Y. Champoux, *Propagation of sound and the assignment of shape factors in model porous materials having simple pore geometries*. The Journal of the Acoustical Society of America, 1992. **91**(2): p. 685-695.
116. Champoux, Y. and J.F. Allard, *Dynamic tortuosity and bulk modulus in air-saturated porous media*. Journal of Applied Physics, 1991. **70**(4): p. 1975-1979.
117. Bonfiglio, P. and F. Pompoli, *A single measurement approach for the determination of the normal incidence transmission loss*. The Journal of the Acoustical Society of America, 2008. **124**(3): p. 1577-1583.

118. Han, F., et al., *Acoustic absorption behaviour of an open-celled aluminium foam*. Journal of Physics D: Applied Physics, 2003. **36**(3): p. 294-302.
119. Johnson, D.L., J. Koplik, and R. Dashen, *Theory of dynamic permeability and tortuosity in fluid-saturated porous media*. Journal of Fluid Mechanics, 1987. **176**: p. 379-402.
120. Bheekhun, N., A.R. Abu Talib, and M.R. Hassan, *Aerogels in Aerospace: An Overview*. Advances in Materials Science and Engineering, 2013. **2013**: p. 406065.
121. Alwin, S. and X. Sahaya Shajan, *Aerogels: promising nanostructured materials for energy conversion and storage applications*. Materials for Renewable and Sustainable Energy, 2020. **9**(2): p. 7.
122. Hyuk Park, J., et al., *Cell openness manipulation of low density polyurethane foam for efficient sound absorption*. Journal of Sound and Vibration, 2017. **406**: p. 224-236.
123. Xue, B., J. Deng, and J. Zhang, *Multiporous open-cell poly(vinyl formal) foams for sound absorption*. RSC Advances, 2016. **6**(9): p. 7653-7660.
124. Gong, R., et al., *A simple preparation method and characterization of epoxy reinforced microporous phenolic open-cell sound absorbent foam*. RSC Advances, 2015. **5**(83): p. 68003-68013.
125. Liu, Y., X. Zhao, and L. Ye, *A Novel Elastic Urea–Melamine–Formaldehyde Foam: Structure and Properties*. Industrial & Engineering Chemistry Research, 2016. **55**(32): p. 8743-8750.
126. Ghaffari Mosanenzadeh, S., et al., *Design and development of novel bio-based functionally graded foams for enhanced acoustic capabilities*. Journal of Materials Science, 2015. **50**(3): p. 1248-1256.
127. Ke, H., et al., *Acoustic absorption properties of open-cell Al alloy foams with graded pore size*. Journal of Physics D: Applied Physics, 2011. **44**(36): p. 365405.
128. Gao, N., et al., *Mesophase pitch based carbon foams as sound absorbers*. Materials Letters, 2018. **212**: p. 243-246.
129. Chen, J.H., P.S. Liu, and J.X. Sun, *Sound absorption performance of a lightweight ceramic foam*. Ceramics International, 2020. **46**(14): p. 22699-22708.

130. Statharas, E.C., et al., *Polyurethane/poly(vinylidene fluoride)/MWCNT composite foam for broadband airborne sound absorption*. Journal of Applied Polymer Science, 2019. **136**(33): p. 47868.
131. Shen, L., et al., *Hierarchical pore structure based on cellulose nanofiber/melamine composite foam with enhanced sound absorption performance*. Carbohydrate Polymers, 2021. **255**: p. 117405.
132. Wu, Y., et al., *Graphene foam/carbon nanotube/poly(dimethyl siloxane) composites as excellent sound absorber*. Composites Part A: Applied Science and Manufacturing, 2017. **102**: p. 391-399.
133. Liu, L., et al., *A graphene oxide and functionalized carbon nanotube based semi-open cellular network for sound absorption*. Soft Matter, 2019. **15**(10): p. 2269-2276.
134. Oh, J.-H., et al., *Directionally Antagonistic Graphene Oxide-Polyurethane Hybrid Aerogel as a Sound Absorber*. ACS Applied Materials & Interfaces, 2018. **10**(26): p. 22650-22660.
135. Oh, J.-H., et al., *Auxetic graphene oxide-porous foam for acoustic wave and shock energy dissipation*. Composites Part B: Engineering, 2020. **186**: p. 107817.
136. Lee, J. and I. Jung, *Tuning sound absorbing properties of open cell polyurethane foam by impregnating graphene oxide*. Applied Acoustics, 2019. **151**: p. 10-21.
137. Pinto, S.C., et al., *Hybrid Structures Made of Polyurethane/Graphene Nanocomposite Foams Embedded within Aluminum Open-Cell Foam*. Metals, 2020. **10**(6): p. 768.
138. He, C., et al., *Enhanced Sound Absorption Properties of Ceramics with Graphene Oxide Composites*. ACS Omega, 2021. **6**(50): p. 34242-34249.
139. Lu, B., et al., *High performance broadband acoustic absorption and sound sensing of a bubbled graphene monolith*. Journal of Materials Chemistry A, 2019. **7**(18): p. 11423-11429.
140. Helmholtz, *ON THE MODERN DEVELOPMENT OF FARADAY'S CONCEPTION OF ELECTRICITY*. Science, 1881. **os-2**(44): p. 182-185.
141. Becker, H.I., *Low voltage electrolytic capacitor*. 1957.

142. Rightmire, R.A., *Electrical Energy Storage Apparatus*. 1966, Standard Oil Co.
143. M. Endo , T.T., Y. J. Kim , K. Koshiba , K. Ishii, *High power electric double layer capacitor (EDLC's); from operating principles to pore size control in advanced activated carbons*. *Carbon Science* 2001. Carbon Science, 2001.
144. Ragone, D.V., *Review of Battery Systems for Electrically Powered Vehicles*. 1968, SAE International.
145. Kötz, R. and M. Carlen, *Principles and applications of electrochemical capacitors*. *Electrochimica Acta*, 2000. **45**(15): p. 2483-2498.
146. Conway, B.E., *Electrochemical Supercapacitors - Scientific Fundamentals and Technological Applications*. 1999: Springer US.
147. P. Simon, A.B., *Nanostructured carbon; Double-layer capacitance and more*. *The Electrochemical Society Interface*, 2008. **17**: p. 38 - 43.
148. Du, H., et al., *Electric double-layer transistors: a review of recent progress*. *Journal of Materials Science*, 2015. **50**(17): p. 5641-5673.
149. Miller, J.R. and P. Simon, *Electrochemical Capacitors for Energy Management*. *Science*, 2008. **321**(5889): p. 651-652.
150. Kim, M.-H., et al., *Hierarchically structured activated carbon for ultracapacitors*. *Scientific Reports*, 2016. **6**: p. 21182.
151. Jäckel, N., et al., *Performance evaluation of conductive additives for activated carbon supercapacitors in organic electrolyte*. *Electrochimica Acta*, 2016. **191**: p. 284-298.
152. Oschatz, M., et al., *Carbide-derived carbon aerogels with tunable pore structure as versatile electrode material in high power supercapacitors*. *Carbon*, 2017. **113**: p. 283-291.
153. Zeiger, M., et al., *Review: carbon onions for electrochemical energy storage*. *Journal of Materials Chemistry A*, 2016. **4**(9): p. 3172-3196.
154. Gao, Y., et al., *Chemical activation of carbon nano-onions for high-rate supercapacitor electrodes*. *Carbon*, 2013. **51**: p. 52-58.
155. Pan, H., J. Li, and Y. Feng, *Carbon Nanotubes for Supercapacitor*. *Nanoscale Research Letters*, 2010. **5**(3): p. 654.

156. Ran, F., X. Yang, and L. Shao, *Recent progress in carbon-based nanoarchitectures for advanced supercapacitors*. *Advanced Composites and Hybrid Materials*, 2018. **1**(1): p. 32-55.
157. El-Kady, M.F., Y. Shao, and R.B. Kaner, *Graphene for batteries, supercapacitors and beyond*. *Nature Reviews Materials*, 2016. **1**: p. 16033.
158. Yan, J., et al., *Recent Advances in Design and Fabrication of Electrochemical Supercapacitors with High Energy Densities*. *Advanced Energy Materials*, 2014. **4**(4): p. 1300816.
159. Yang, Z., et al., *Carbon nanotube- and graphene-based nanomaterials and applications in high-voltage supercapacitor: A review*. *Carbon*, 2019. **141**: p. 467-480.
160. Maxwell Technologies, I. *Datasheets*. [cited 2019; Available from: <https://www.maxwell.com/>].
161. Corporation, P. *Lithium-ion Batteries - Overview and Features*. [cited 2019; Available from: <https://industrial.panasonic.com/ww/products/batteries/secondary-batteries/lithium-ion>].
162. Burke, A., *R&D considerations for the performance and application of electrochemical capacitors*. *Electrochimica Acta*, 2007. **53**(3): p. 1083-1091.
163. Yao, L., et al., *Scalable 2D Hierarchical Porous Carbon Nanosheets for Flexible Supercapacitors with Ultrahigh Energy Density*. *Advanced Materials*, 2018. **30**(11): p. 1706054.
164. Vindt, S.T. and E.M. Skou, *The buffer effect in neutral electrolyte supercapacitors*. *Applied Physics A*, 2016. **122**(2): p. 64.
165. Brandt, A., et al., *Ionic liquids in supercapacitors*. *MRS Bulletin*, 2013. **38**(7): p. 554-559.
166. Mauger, A., et al., *Challenges and issues facing lithium metal for solid-state rechargeable batteries*. *Journal of Power Sources*, 2017. **353**: p. 333-342.
167. Wu, Z.S., et al., *Graphene-based in-plane micro-supercapacitors with high power and energy densities*. *Nature Communications*, 2013. **4**: p. 2487.

168. Kang, Y.J., et al., *All-solid-state flexible supercapacitors based on papers coated with carbon nanotubes and ionic-liquid-based gel electrolytes*. *Nanotechnology*, 2012. **23**(6): p. 065401.
169. Li, L., et al., *Recent Advances in Flexible/Stretchable Supercapacitors for Wearable Electronics*. *Small*, 2018. **14**(43): p. 1702829.
170. Inagaki, M., H. Konno, and O. Tanaike, *Carbon materials for electrochemical capacitors*. *Journal of Power Sources*, 2010. **195**(24): p. 7880-7903.
171. Xia, J., et al., *Measurement of the quantum capacitance of graphene*. *Nature Nanotechnology*, 2009. **4**(8): p. 505-509.
172. Ke, Q. and J. Wang, *Graphene-based materials for supercapacitor electrodes – A review*. *Journal of Materiomics*, 2016. **2**(1): p. 37-54.
173. Ramachandran, R., et al., *Effect of reducing agent on graphene synthesis and its influence on charge storage towards supercapacitor applications*. *Applied Energy*, 2015. **153**: p. 22-31.
174. Jin, Y., et al., *A green and efficient method to produce graphene for electrochemical capacitors from graphene oxide using sodium carbonate as a reducing agent*. *Applied Surface Science*, 2013. **268**: p. 541-546.
175. Vivekchand, S.R.C., et al., *Graphene-based electrochemical supercapacitors*. *Journal of Chemical Sciences*, 2008. **120**(1): p. 9-13.
176. Lv, W., et al., *Low-Temperature Exfoliated Graphenes: Vacuum-Promoted Exfoliation and Electrochemical Energy Storage*. *ACS Nano*, 2009. **3**(11): p. 3730-3736.
177. Shi, W., et al., *Achieving high specific charge capacitances in Fe₃O₄/reduced graphene oxide nanocomposites*. *Journal of Materials Chemistry*, 2011. **21**(10): p. 3422-3427.
178. Hassan, H.M.A., et al., *Microwave synthesis of graphene sheets supporting metal nanocrystals in aqueous and organic media*. *Journal of Materials Chemistry*, 2009. **19**(23): p. 3832-3837.
179. Zhu, Y., et al., *Carbon-Based Supercapacitors Produced by Activation of Graphene*. *Science*, 2011. **332**(6037): p. 1537-1541.
180. Tan, Y.B. and J.-M. Lee, *Graphene for supercapacitor applications*. *Journal of Materials Chemistry A*, 2013. **1**(47): p. 14814-14843.

181. Si, Y. and E.T. Samulski, *Exfoliated Graphene Separated by Platinum Nanoparticles*. Chemistry of Materials, 2008. **20**(21): p. 6792-6797.
182. Zhang, K., et al., *Surfactant-intercalated, chemically reduced graphene oxide for high performance supercapacitor electrodes*. Journal of Materials Chemistry, 2011. **21**(20): p. 7302-7307.
183. Fan, Z., et al., *A Three-Dimensional Carbon Nanotube/Graphene Sandwich and Its Application as Electrode in Supercapacitors*. Advanced Materials, 2010. **22**(33): p. 3723-3728.
184. Yan, J., et al., *Electrochemical properties of graphene nanosheet/carbon black composites as electrodes for supercapacitors*. Carbon, 2010. **48**(6): p. 1731-1737.
185. Lei, Z., N. Christov, and X.S. Zhao, *Intercalation of mesoporous carbon spheres between reduced graphene oxide sheets for preparing high-rate supercapacitor electrodes*. Energy & Environmental Science, 2011. **4**(5): p. 1866-1873.
186. Chen, L., et al., *Graphene-based fibers for supercapacitor applications*. Nanotechnology, 2015. **27**(3): p. 032001.
187. Korkmaz, S. and İ.A. Kariper, *Graphene and graphene oxide based aerogels: Synthesis, characteristics and supercapacitor applications*. Journal of Energy Storage, 2020. **27**: p. 101038.
188. Niu, Z., et al., *A Leavening Strategy to Prepare Reduced Graphene Oxide Foams*. Advanced Materials, 2012. **24**(30): p. 4144-4150.
189. Chee, W.K., et al., *Flexible Graphene-Based Supercapacitors: A Review*. The Journal of Physical Chemistry C, 2016. **120**(8): p. 4153-4172.
190. Velasco, A., et al., *Recent trends in graphene supercapacitors: from large area to microsupercapacitors*. Sustainable Energy & Fuels, 2021. **5**(5): p. 1235-1254.
191. Gao, Y., *Graphene and Polymer Composites for Supercapacitor Applications: a Review*. Nanoscale Research Letters, 2017. **12**(1): p. 387.
192. Wang, S., et al., *Highly Stretchable and Self-Healable Supercapacitor with Reduced Graphene Oxide Based Fiber Springs*. ACS Nano, 2017. **11**(2): p. 2066-2074.

193. Jung, S.M., et al., *Controlled porous structures of graphene aerogels and their effect on supercapacitor performance*. *Nanoscale*, 2015. **7**(10): p. 4386-4393.
194. Lee, S.P., et al., *Optimizing Reduced Graphene Oxide Aerogel for a Supercapacitor*. *Energy & Fuels*, 2021. **35**(5): p. 4559-4569.
195. Wang, S., et al., *Room-temperature fast assembly of 3D macroscopically porous graphene frameworks for binder-free compact supercapacitors with high gravimetric and volumetric capacitances*. *Journal of Energy Chemistry*, 2021. **61**: p. 23-28.
196. Liu, T. and Y. Li, *Addressing the Achilles' heel of pseudocapacitive materials: Long-term stability*. *InfoMat*, 2020. **2**(5): p. 807-842.
197. Xu, B., et al., *Reduced graphene oxide as a multi-functional conductive binder for supercapacitor electrodes*. *Energy Storage Materials*, 2018. **12**: p. 128-136.
198. Choi, J.-H., et al., *High capacitance and energy density supercapacitor based on biomass-derived activated carbons with reduced graphene oxide binder*. *Carbon*, 2018. **132**: p. 16-24.
199. Galhena, D.T.L., et al., *Reduced Graphene Oxide as a Monolithic Multifunctional Conductive Binder for Activated Carbon Supercapacitors*. *ACS Omega*, 2018. **3**(8): p. 9246-9255.
200. Skrypnichuk, V., et al., *Aqueous Activated Graphene Dispersions for Deposition of High-Surface Area Supercapacitor Electrodes*. *The Journal of Physical Chemistry Letters*, 2020. **11**(8): p. 3032-3038.
201. Yang, C., et al., *High-Performance All-Solid-State Supercapacitor Based on Activated Carbon Coated Fiberglass Cloth Using Asphalt as Active Binder*. *Journal of The Electrochemical Society*, 2020. **167**(2): p. 020540.